

Development of transition metal sulfide composites as the anode materials for sodium-ion batteries

**by
Yang He**

Graduate School of Science and Technology

HIROSAKI UNIVERSITY

2023

ABSTRACT

Sodium-ion batteries (SIBs) have similar energy storage mechanisms as lithium-ion batteries (LIBs), and possess the advantages of high abundance, wide distribution, and low cost of sodium resources, it has become the most promising alternative to LIBs. However, given the larger ionic radius of Na-ion (Na^+ , 1.02 Å) compared to that of Li-ion (Li^+ , 0.76 Å). The electrode materials of SIBs face larger volume expansion and more sluggish reaction kinetics than those of LIBs in the charge/discharge operation, thereby hindering the stability of SIBs. Transition metal sulfides (TMSs) possess considerable theoretical capacities as the material of anode in SIBs, but their application is limited by their large volume expansion, sluggish charge transfer kinetics, and poor cycling performance. Although, many strategies have been put forward to solve those issues, including carbon modification, nanostructure design, construction of heterostructures and electrolyte optimization, etc., it is still full of challenges to design TMSs-based anodes with superior reversibility capacity and excellent cycling stability for SIBs. In this dissertation, TMSs with carbon framework and/or heterostructure are designed as the anode materials for SIBs, which exhibit excellent electrochemical performances.

Firstly, different from the traditional co-precipitation method to prepare the Prussian blue analog (PBA), the PBA with a tremella-like micro-flower structure is firstly synthesized by the hydrothermal method under the synergistic effect of trisodium citrate dihydrate (TSC, $\text{Na}_3\text{C}_6\text{H}_5\text{O}_7 \cdot 2\text{H}_2\text{O}$) and $\text{K}_3[\text{Co}(\text{CN})_6]$, and two kinds of cobalt sulfide nanoparticles embedded in N/S co-doped carbon frameworks (namely, $\text{Co}_3\text{S}_4@\text{C-N/S}$ and $\text{Co}_9\text{S}_8@\text{C-N/S}$) are successfully synthesized by a subsequent solid sulfidation process. Herein, N/S co-doped carbon frameworks improve the electronic conductivity and provide more active sites for sodium storage. As the material for the

anode in SIBs, the $\text{Co}_3\text{S}_4@\text{C-N/S}$ -based anode exhibits excellent initial charge/discharge specific capacities of $685.3/745.2 \text{ mA h g}^{-1}$ with a high initial Coulombic efficiency of 91.97% at 0.1 A g^{-1} and a superior cycling performance ($599.1 \text{ mA h g}^{-1}$ in the 600th cycle at 1 A g^{-1} with a capacity retention of 89.4%). While the $\text{Co}_9\text{S}_8@\text{C-N/S}$ -based anode also delivers considerable initial Coulombic efficiency (86.1% at 0.1 A g^{-1}) with high cycling stability ($391.9 \text{ mA h g}^{-1}$ even in the 1200th cycle at 2 A g^{-1} with a capacity retention of 78.1%). It provides a material synthesis route for high-performance anode materials used in SIBs and other alkali metal ion batteries.

Secondly, micro-flower-like MoS_2 -modified Co_9S_8 ($\text{Co}_9\text{S}_8/\text{MoS}_2$) with a three-dimensional (3D) heterostructure is first obtained via a simple solvothermal synthesis followed by a solid sulfidation treatment process. As a material for the anode of SIBs, the $\text{Co}_9\text{S}_8/\text{MoS}_2$ -based electrode with an initial Co/Mo molar ratio of 1/1 (denoted as CM55-S) exhibits the best sodium storage performance with a boosted capacity, superior reversibility ($424.5 \text{ mAh g}^{-1}@2 \text{ A g}^{-1}$ at the 1600th cycle, $401.1 \text{ mAh g}^{-1}@5 \text{ A g}^{-1}$ at the 800th cycle), and an excellent rate capacity ($210.1 \text{ mAh g}^{-1}@20 \text{ A g}^{-1}$). Density functional theory (DFT) calculations confirm that the $\text{Co}_9\text{S}_8/\text{MoS}_2$ heterostructure has a lower energy barrier (0.30 eV) than the pure Co_9S_8 (0.53 eV). It is expected that such a heterostructured material could be an attractive candidate as the material of the anode for SIBs.

Finally, cobalt sulfide/molybdenum disulfide with heterostructure is fabricated as the anode for SIBs, which can be constructed by combining a one-pot hydrothermal route with a solid-state sulfidation step. Compared with the anodes based on pure cobalt sulfide and pure molybdenum disulfide materials, the cobalt sulfide/molybdenum

disulfide-based one displays superior cycling stability (e.g., 510.9 mAh g⁻¹ @1 A g⁻¹ at the 1000th cycle), and an extraordinary rate performance (341 mAh g⁻¹ @10 A g⁻¹). The material characterizations show that the obtained cobalt sulfide/molybdenum disulfide material with abundance of mesopores. The kinetics analysis further confirms the decreasing of charge transfer resistance and the increasing of Na⁺ diffusion coefficient with cycling for this material. As a result, the reasonable design of cobalt sulfide/molybdenum disulfide heterostructure can provide abundant active sites for the storage of Na⁺ ions and facilitate surface capacity-controlled behavior. It offers useful insights into the utilization of those heterostructured materials for SIBs.

ACKNOWLEDGEMENTS

With the Ph.D. course nearing completion, which also means the end of my student career, but it is also the beginning of another journey. Looking back on my study and life at Hirosaki University in Japan over the past three years, I have benefited a lot from the care of my supervisor, classmates, and family members.

First of all, I would like to express my deepest gratitude to my supervisor Professor Dr. Abuliti Abudula, who gave me the opportunity to continue my research in the Ph.D. course at Hirosaki University. In addition, I sincerely thank him for his help in my experiments and support in my daily life.

My deepest appreciation is also given to Professor Dr. Guoqing Guan, for his careful guidance, valuable suggestions, and encouragement for my research and daily life. It's my honor to be one of his students.

I would like to thank Associate Professor Dr. Gang Chen, Institute of Metallurgical Physical Chemistry, Northeastern University (China), for teaching me how to conduct scientific experiments during my master's degree, and for recommending me to study for a doctorate at Hirosaki University.

I am also thankful to all the members in our group, all the professors and staffs at the Institute of Regional Innovation (IRI) and the Graduated School of Science and Technology, Hirosaki University, for your kind help and support.

Finally, I would like to thank my family for their care and support over the years.

Thank you all very much.

Yang He

TABLE OF CONTENTS

ABSTRACT.....	I
ACKNOWLEDGEMENTS.....	IV
TABLE OF CONTENTS.....	V
LIST OF TABLES	IX
LIST OF FIGURES	X
Chapter 1. Introduction	1
1.1 General Introduction.....	1
1.2 Sodium-ion batteries overview.....	3
1.3 Cathode materials for sodium-ion batteries.....	4
1.4 Anode materials for sodium-ion batteries	7
1.4.1 Intercalation-type anode materials for sodium-ion batteries	8
1.4.2 Alloy-type anode materials for sodium-ion batteries.....	11
1.4.3 Conversion reaction-type anode materials for sodium-ion batteries	13
1.4.4 Optimization Strategies of Transition Metal Sulfides-Based Anodes for SIBs	17
1.5 Objectives of this study	19
1.6 Contents of this dissertation	20
References	22
Chapter 2. Experimental	33
2.1 Reagents information	33
2.2 Characterizations	33
2.2.1 X-ray diffractometer (XRD)	33
2.2.2 Raman spectra.....	34
2.2.2 X-ray photoelectron spectrometer (XPS).....	34

2.2.3 Field-emission scanning electron microscopy (FE-SEM)	35
2.2.4 Transmission electron microscope (TEM).....	35
2.2.5 Inductively coupled plasma emission optical spectrometry (ICP-OES).....	36
2.2.6 Brunauer-Emmett-Teller (BET).....	36
2.3 Electrochemical measurements	36
Chapter 3 Prussian Blue Analog Derived Cobalt Sulfide Nanoparticles Embedded in N/S Co-doped Carbon Frameworks as a High-Performance Anode Material for Sodium-ion Batteries	38
3.1 Introduction	38
3.2. Experimental	40
3.2.1 Synthesis precursor	40
3.2.2 Synthesis of $\text{Co}_3\text{S}_4@\text{C-N/S}$	41
3.2.3 Synthesis of $\text{Co}_3\text{S}_4@\text{C-N/S}$	41
3.2.4 Materials characterization.....	41
3.2.5 Electrochemical measurements.....	42
3.3. Results and discussion.....	43
3.3.1 Characterization of $\text{Co}_3\text{S}_4@\text{C-N/S}$ and $\text{Co}_9\text{S}_8@\text{C-N/S}$	43
3.3.2 Electrochemical performance	52
3.3.3 Electrochemical kinetics	63
3.4. Conclusions	67
References	68
Chapter 4 Micro-flower-like MoS_2 -modified Co_9S_8 Heterostructure as Anode Material for Sodium-ion Batteries with Superior Reversibility and Rate Capacity.	76
4.1. Introduction	76
4.2 Experimental	77

4.2.1. Synthesis of precursor	77
4.2.2. Synthesis of Co ₉ S ₈ /MoS ₂	78
4.2.3. Computational methods	78
4.2.4 Characterizations.....	79
4.2.5 Electrochemical performance	79
4.3. Results and discussion.....	80
4.3.1. Characterizations of as-prepared materials	80
4.3.2. Electrochemical performance	88
4.3.3. Electrochemical kinetics	98
4.4. Conclusions	102
References	104
Chapter 5 Construction of Cobalt Sulfide/Molybdenum Disulfide Heterostructure as the Anode Material for Sodium Ion Batteries.....	110
5.1 Introduction	110
5.2 Experimental	112
5.2.1 Synthesis of CoS/MoS ₂	112
5.2.2 Synthesis of pure CoS and pure MoS ₂	112
5.2.3 Characterizations.....	113
5.2.4 Electrochemical measurements.....	113
5.3 Results and discussion.....	114
5.3.1 Characterizations.....	114
5.3.2 Electrochemical performance	120
5.3.3 Electrochemical kinetics	128
5.1 Conclusion.....	135
References	136

Chapter 6 Conclusion and Prospects.....	145
6.1 Conclusion.....	145
6.2 Prospects.....	146
List of publications and presentations.....	148

LIST OF TABLES

Table 1.1 The main features of lithium (Li) and sodium (Na)	2
Table 1.2 Electrochemical performances of reported carbon anode materials for SIBs.....	9
Table 1.3 The parameters of alloy-type anode materials for SIBs.	12
Table 1.4 Calculated theoretical capacities of the M_aX_b compounds[60].	15
Table 2.1 Main chemical reagents for this research.	33
Table 3.1 Table 3.1 Comparison of electrochemical performances of Co_3S_4 -based and Co_9S_8 -based anodes for Na-ion batteries.	58
Table 3.2 Table 3.2 Fitting results of Nyquist plots based on the equivalent circuit after 20 cycles.	62
Table 4.1 ICP-OES analysis results of the precursors with different molar ratios of Co/Mo.	82
Table 4.2 Fitting results of Nyquist plots based on the equivalent circuit after 1, 20 and 50 cycles.....	96
Table 5.1 Fitting results of Nyquist plots based on the equivalent circuit after 1, 20 and 50 cycles.....	130

LIST OF FIGURES

Figure 1.1 Schematic diagram of the working principle and configuration of sodium-ion batteries.....	3
Figure 1.2 The classification of Na–Me–O layered materials with the sheets of edge-sharing MeO_6 octahedra and phase transition processes induced by sodium extraction[4].	4
Figure 1.3 Schematic crystal structures of PBAs framework[5].....	5
Figure 1.4 Crystal structure of $\text{Na}_3\text{V}_2(\text{PO}_4)_3$ (100-plane)[9].	6
Figure 1.5 Schematic representation of reaction mechanisms occurring during storage of Na^+ in various classes of anode materials[11].	7
Figure 1.6 The schematic illustration of conversion reactions with sodium[60].	13
Figure 1.7 The specific capacity and theoretical potentials vs Na/Na^+ for conversion-type materials for sodium storage[66].	16
Figure 3.1 Schematically illustration of formations of $\text{Co}_3\text{S}_4@\text{C-N/S}$ and $\text{Co}_9\text{S}_8@\text{C-N/S}$ anode materials.....	43
Figure 3.2 XRD patterns of as-prepared Co-precursors with different contents of TSC (0.0, 1.8, 3.6 mmol).	44
Figure 3.3 SEM images of $\text{Co}_3\text{S}_4@\text{C-N/S}$ composites prepared using the precursors with different contents of TSC (a-b) 0.0, (c-d) 1.8 and (e-f) 3.6 mmol.	44
Figure 3.4 SEM images of $\text{Co}_9\text{S}_8@\text{C-N/S}$ composites with different contents of TSC (a-b) 0.0 mmol, (c-d) 1.8 mmol and (e-f) 3.6 mmol.....	45
Figure 3.5 (a-b) TEM images, (c-e) HRTEM images, (f) SAED pattern and (g-k) EDX elemental mapping of $\text{Co}_3\text{S}_4@\text{C-N/S}$ 1.8.	46
Figure 3.6 (a-b) TEM images, (c-d) HRTEM images, (e) SAED pattern and (f-j) EDX elemental mapping of $\text{Co}_3\text{S}_4@\text{C-N/S}$ 0.0.	47
Figure 3.7 (a-b) TEM images, (c-e) HRTEM images, (f) SAED pattern and (g-k) EDX elemental mapping of $\text{Co}_3\text{S}_4@\text{C-N/S}$ 3.6.	48
Figure 3.8 (a) XRD patterns of $\text{Co}_3\text{S}_4@\text{C-N/S}$ 0.0, 1.8 and 3.6; (b) High-resolution	

XPS spectra of (c) Co 2p, (d) C 1s, (e) N 1s and (f) S 2p; BET curves of (g) Co ₃ S ₄ @C-N/S 0.0, (h) Co ₃ S ₄ @C-N/S 1.8 and (i) Co ₃ S ₄ @C-N/S 3.6.....	49
Figure 3.9 (a) XRD patterns of Co ₉ S ₈ @C-N/S (0.0, 1.8 and 3.6); (b) High-resolution XPS spectra of (c) Co 2p, (d) C 1s, (e) N 1s and (f) S 2p for Co ₉ S ₈ @C-N/S 0.0, 1.8 and 3.6.	50
Figure 3.10 (a) CV curves of Co ₃ S ₄ @C-N/S 1.8 based anode at a scan rate of 0.1 mV s ⁻¹ in the potential window of 0.3-3V; (b) Ex-situ XRD patterns of Co ₃ S ₄ @C-N/S 1.8 at different charge/discharge states.....	53
Figure 3.11 CV curves of (a) Co ₃ S ₄ @C-N/S 0.0 and (b) Co ₃ S ₄ @C-N/S 3.6 based anodes at a scan rate of 0.1 mV s ⁻¹ in the potential window of 0.3-3 V.	53
Figure 3.12 (a) Typical galvanostatic charge/discharge profiles of Co ₃ S ₄ @C-N/S 1.8 based anode at 0.1 A g ⁻¹ at different cycles (1 st , 2 nd , 5 th , 10 th and 20 th); Cycling performance of Co ₃ S ₄ @C-N/S 1.8 based anode at current densities of (b) 0.1 A g ⁻¹ and (d) 2 A g ⁻¹ ; (c) Cycling performances of Co ₃ S ₄ @C-N/S 0.0, 1.8 and 3.6 based anodes at a current density of 1 A g ⁻¹ ; (e) Rate performances and (f) Nyquist plots of Co ₃ S ₄ @C-N/S 0.0, 1.8 and 3.6 based anodes.....	55
Figure 3.13 Typical galvanostatic charge/discharge profiles of (a) Co ₃ S ₄ @C-N/S 0.0, (b) Co ₃ S ₄ @C-N/S 3.6, (c) Co ₉ S ₈ @C-N/S 0.0 and (d) Co ₉ S ₈ @C-N/S 3.6 based anodes at a current density of 0.1 A g ⁻¹ for different cycles (1 st , 2 nd , 5 th , 10 th and 20 th).	57
Figure 3.14 (a) Typical galvanostatic charge/discharge profiles of Co ₉ S ₈ @C-N/S 1.8 based anode at 0.1 A g ⁻¹ for different cycles (1 st , 2 nd , 5 th , 10 th and 20 th); (b) Cycling performance of Co ₉ S ₈ @C-N/S 0.0, 1.8 and 3.6 based anodes at 1 A g ⁻¹ ; (c) Cycling performance of Co ₉ S ₈ @C-N/S 1.8 based anode at 2 A g ⁻¹ ; (d) Rate performances of Co ₉ S ₈ @C-N/S 0.0, 1.8 and 3.6 based anodes.....	60
Figure 3.15 (a) The equivalent circuit used for the analysis of the impedance plots; Fitted straight lines between z' and $\omega^{-1/2}$ at the low-frequency region for (b) Co ₃ S ₄ @C-N/S 0.0, 1.8 and 3.6 based anodes and (d) Co ₉ S ₈ @C-N/S 0.0, 1.8 and 3.6 based anodes after 20 cycles; (c) Nyquist plots of Co ₉ S ₈ @C-N/S 0.0, 1.8 and 3.6 based anodes.....	61

Figure 3.16 (a) CV curves of $\text{Co}_3\text{S}_4@\text{C-N/S}$ 1.8 based anode in a voltage range of 0.3-3 V at different scan rates from 0.1-1.2 mV s^{-1} ; (b) The fitting lines of $\log i$ vs $\log v$ of peaks 1, 2 and 3; (c) Capacitive contribution of $\text{Co}_3\text{S}_4@\text{C-N/S}$ 1.8 based anode compared with the total current at 1.2 mV s^{-1} ; (d) The capacitive contribution of $\text{Co}_3\text{S}_4@\text{C-N/S}$ 1.8 based anode at different scan rates from 0.1 to 1.2 mV s^{-1}	63
Figure 3.17 (a) CV curves of $\text{Co}_3\text{S}_4@\text{C-N/S}$ 0.0 based anode in a voltage range of 0.3-3 V at different scan rates from 0.1 to 1.2 mV s^{-1} ; (b) The fitting lines of $\log i$ vs $\log v$ of peaks 1, 2 and 3; (c) Capacitive contribution of $\text{Co}_3\text{S}_4@\text{C-N/S}$ 0.0 based anode compared with the total current at 1.2 mV s^{-1} ; (d) The capacitive contribution of $\text{Co}_3\text{S}_4@\text{C-N/S}$ 0.0 based anode at different scan rates from 0.1 to 1.2 mV s^{-1}	64
Figure 3.18 (a) CV curves of $\text{Co}_3\text{S}_4@\text{C-N/S}$ 3.6 based anode in a voltage range of 0.3-3V at different scan rates from 0.1 to 1.2 mV s^{-1} ; (b) The fitting lines of $\log i$ vs $\log v$ of peaks 1, 2 and 3; (c) Capacitive contribution of $\text{Co}_3\text{S}_4@\text{C-N/S}$ 3.6 based anode compared with the total current at 1.2 mV s^{-1} ; (d) The capacitive contribution of $\text{Co}_3\text{S}_4@\text{C-N/S}$ 3.6 based anode at different scan rates from 0.1 to 1.2 mV s^{-1}	65
Figure 3.19 The discharge/charge profiles in GITT measurements of the (a) $\text{Co}_3\text{S}_4@\text{C-N/S}$ 0.0, (a) $\text{Co}_3\text{S}_4@\text{C-N/S}$ 1.8 and (c) $\text{Co}_3\text{S}_4@\text{C-N/S}$ 3.6; The diffusion coefficient of Na^+ in (d) discharge and (e) charge processes of the $\text{Co}_3\text{S}_4@\text{C-N/S}$ 0.0, 1.8 and 3.6 based anodes.	66
Figure 4.1 Schematic illustration of the synthesis of micro-flower-like $\text{Co}_9\text{S}_8/\text{MoS}_2$ heterostructure.....	80
Figure 4.2 SEM images of precursors with different molar ratios of Co and Mo. (a) CM50, (b) CM51, (c) CM53, and (d) CM55.	81
Figure 4.3 SEM images of sulfurization products with different molar ratios of Co and Mo, (a-b) CM50-S, (c-d) CM51-S and (e-f) CM55-S.	82
Figure 4.4 (a-b) TEM images; (c-f) HRTEM images; (g) SAED pattern; and (h) EDS elements mapping of CM55-S.....	83

Figure 4.5 (a) XRD patterns of CM50-S, CM51-S, and CM55-S; High-resolution XPS spectra of (b) full XPS survey, (c) Co 2p, (d) Mo 3d, (e) S 2p for CM55-S; (f) Nitrogen desorption-adsorption isotherm and pore size distribution of CM55-S.....	84
Figure 4.6 High-resolution XPS spectra of (a) full XPS survey, (b) Co 2p, and (c) S 2p for CM50-S.....	85
Figure 4.7 High-resolution XPS spectra of (a) full XPS survey, (b) Co 2p, (c) Mo 3d, and (d) S 2p for CM51-S.	87
Figure 4.8 Nitrogen desorption-adsorption isotherms and pore size distributions of (a) CM50-S and (b)CM51-S.	87
Figure 4.9 (a) CV curves of CM55-S-based anode at a scan rate of 0.1 mV s ⁻¹ in the potential window of 0.3-3V; (b) <i>Ex situ</i> XRD patterns of CM55-S-based anode at different charge/discharge states.....	88
Figure 4.10 CV curves of (a) CM50-S- and (b) CM51-S-based anodes at a scan rate of 0.1 mV s ⁻¹ in the potential window of 0.3-3V.....	89
Figure 4.11 (a) Typical galvanostatic charge-discharge profiles of CM55-S-based anode at 0.1 A g ⁻¹ with different cycles (1 st , 2 nd , 5 th , 10 th , and 20 th); Cycling performance of CM55-S-based anode at current densities of (b) 0.1A g ⁻¹ and (d) 2 A g ⁻¹ ; (c) Cycling performances of CM50-S-, CM51-S- and CM55-S-based anodes at the current density of 1 A g ⁻¹ ; (e) Rate performances of CM50-S-, CM51-S- and CM55-S-based anodes; (f) Comparison of rate performance of the CM55-S-based anode with other Co ₉ S ₈ - and MoS ₂ -based anodes.....	90
Figure 4.12 Typical galvanostatic charge/discharge profiles of (a) CM50-S- and (b) CM51-S-based anodes at 0.1 A g ⁻¹ with different cycles (1 st , 2 nd , 5 th , 10 th , and 20 th).	91
Figure 4.13 Cycling performance of CM55-S-based anode at a current density of 5 A g ⁻¹ (the first ten cycles were tested at 1A g ⁻¹).	92
Figure 4.14 (a) HRTEM image and (b) SAED pattern of CM55-S-based anode after 150 cycles at the current density of 0.2 A g ⁻¹	93
Figure 4.15 Typical galvanostatic charge/discharge profiles corresponding to rate	

performance for CM55-S-based anode.....	94
Figure 4.16 Nyquist plots of (a) CM50-S, (b) CM51-S, and (c) CM55-S based anodes after different cycles (1, 20, and 50); (d) Fitted straight lines between z' and $\omega^{-1/2}$ at the low-frequency region for CM50-S-, CM51-S- and CM55-S-based anodes after 50 cycles; The discharge/charge profiles and corresponding Na^+ diffusion coefficients of CM55-S-based anode in GITT measurements of (e) the first cycle, and (f) the 20 th cycle.	95
Figure 4.17 The discharge/charge profiles and corresponding Na^+ diffusion coefficients of (a) CM50-S-, and (b) CM51-S-based anodes in GITT measurements of the first cycle.....	97
Figure 4.18 Schematic illustration of the diffusion path for Na^+ in (a) Co_9S_8 and (b) $\text{Co}_9\text{S}_8/\text{MoS}_2$ heterostructure, and (c) corresponding energy profiles between adjacent lowing-energy sites.....	98
Figure 4.19 CV curves of (a) CM50-S-, (d) CM51-S-, and (g) CM55-S-based anodes in a voltage range of 0.3-3 V at different scan rates from 0.1 to 1.5 mV s^{-1} ; Capacitive contributions of (b) CM50-S-, (e) CM51-S- and (h) CM55-S-based anodes compared with the total current at 1.5 mV s^{-1} ; The capacitive contributions of (c) CM50-S-, (f) CM51-S- and (i) CM55-S-based anodes at different scan rates from 0.1 to 1.5 mV s^{-1}	99
Figure 4.20 The fitting lines of $\log i$ vs $\log v$ of peaks in CV curves for (a) CM50-S, (b) CM51-S, and (c) CM55-S.....	102
Figure 5.1 Schematic illustration of the fabrication CoS/MoS_2 heterostructure.	115
Figure 5.2 XRD patterns of (a) CoS/MoS_2 heterostructure, (b) pure CoS and pure MoS_2 ; and SEM images of (c) pure CoS, (d) pure MoS_2 , and (e-f) CoS/MoS_2 composite.	116
Figure 5.3 Raman spectrum of CoS/MoS_2	116
Figure 5.4 Nitrogen desorption-adsorption isotherms and pore size distributions of (a-b) pure CoS, (c-d) CoS/MoS_2 , and (e-f) pure MoS_2	117
Figure 5.5 (a-b) TEM images; (c) HRTEM images; (d) SAED pattern; and (e) the	

area for EDS analysis of CoS/MoS ₂ powder.....	118
Figure 5.6 High-resolution XPS spectra of (a) full XPS survey, (b) Co 2p, (c) Mo 3d, (d) S 2p, and (e) C 1s for CoS/MoS ₂ composite.	119
Figure 5.7 (a) CV curves of CoS/MoS ₂ -based anode at a scan rate of 0.1 mV s ⁻¹ in the potential window of 0.3-3V; (b) galvanostatic charge/discharge profiles of CoS/MoS ₂ -based anode at 0.1 A g ⁻¹ ; (c) Cycling performance of CoS/MoS ₂ -based anode at 0.1 A g ⁻¹ ; (d) Cycling performances of pure CoS-, pure MoS ₂ - and CoS/MoS ₂ -based anodes at the current density of 1 A g ⁻¹ ; (e) The long-term cycling stability of CoS/MoS ₂ -based anode at a higher current density of 2 A g ⁻¹	122
Figure 5.8 CV curves of (a) pure CoS- and (b) pure MoS ₂ -based anodes at a scan rate of 0.1 mV s ⁻¹ in the potential window of 0.3-3V.....	123
Figure 5.9 Typical galvanostatic charge/discharge profiles of (a) pure CoS- and (b) pure MoS ₂ -based anodes at 0.1 A g ⁻¹ with different cycles (1 st , 2 nd , 5 th , 10 th , and 20 th).	123
Figure 5.10 Cycling performance of the CoS/MoS ₂ -based anode at a current density of 5 A g ⁻¹ (the first ten cycles were tested at 1 A g ⁻¹).	124
Figure 5.11 SEM images of CoS/MoS ₂ -based anode (a) after 5 cycles and (b) after 20 cycles at a current density of 0.2 A g ⁻¹	124
Figure 5.12 (a) HRTEM images of (a) the CoS/MoS ₂ composite after 100 cycles, (b) the CoS/MoS ₂ composite after 500 cycles, and (c) pure MoS ₂ after 100 cycles at the current density of 0.2 A g ⁻¹	125
Figure 5.13 (a) Rate performances of pure CoS-, pure MoS ₂ - and CoS/MoS ₂ -based anodes; (b) Charge-discharge curves corresponding to rate performance for CoS/MoS ₂ -based anode; (c) Cycling performance of CoS/MoS ₂ -based anode after rate performance test at 0.1 A g ⁻¹ . (d) Comparison of rate performance of the CoS/MoS ₂ -based anode with other CoS- and MoS ₂ -based anodes reported in the literatures.....	127
Figure 5.14 Nyquist plots of (a) CoS-, (b) MoS ₂ -, and (c) CoS/MoS ₂ -based anodes after different cycles (1, 20, and 50); (d) Fitted straight lines between z' and ω ⁻¹	

^{1/2} at the low-frequency region for the CoS/MoS₂-based anode after different cycles (1, 20, and 50); The discharge/charge profiles and corresponding Na⁺ diffusion coefficients of the CoS/MoS₂-based anode in GITT measurements of (e) the first cycle, and (f) the 100th cycle. 129

Figure 5.15 (a) CV curves of the CoS/MoS₂-based anode in a voltage range of 0.3-3 V at different scan rates from 0.1 to 1.5 mV s⁻¹; (b) The fitting lines of log *i* vs log *v* of peaks in CV curves for the CoS/MoS₂-based anode; (c) Capacitive contributions of CoS/MoS₂-based anode compared with the total current at 1.5 mV s⁻¹; The capacitive contributions of the CoS/MoS₂-based anode at different scan rates from 0.1 to 1.5 mV s⁻¹. 131

Figure 5.16 (a) CV curves of pure CoS-based anode in a voltage range of 0.3-3 V at different scan rates from 0.1 to 1.5 mV s⁻¹; (b) The fitting lines of log *i* vs log *v* of peaks in CV curves for the pure CoS-based anode; (c) Capacitive contribution of the pure CoS-based anode compared with the total current at 1.5 mV s⁻¹; The capacitive contributions of pure CoS-based anode at different scan rates from 0.1 to 1.5 mV s⁻¹. 133

Figure 5.17 (a) CV curves of pure MoS₂-based anode in a voltage range of 0.3-3 V at different scan rates from 0.1 to 1.5 mV s⁻¹; (b) The fitting lines of log *i* vs log *v* of peaks in CV curves for the pure MoS₂-based anode; (c) Capacitive contributions of the pure MoS₂-based anode compared with the total current at 1.5 mV s⁻¹; The capacitive contributions of the pure MoS₂-based anode at different scan rates from 0.1 to 1.5 mV s⁻¹. 134

Chapter 1. Introduction

1.1 General Introduction

With the development of society, the demand of energy for human beings continues to expand. However, the combustion of fossil fuels (coal, oil, natural gas, etc., as the main source of energy) has led to serious environmental problems, and its non-renewable characteristics have also raised human concerns about the depletion of energy in the future. Therefore, it is imminent to develop renewable energy and change the existing energy structure. Wind-, solar-, geothermal-, tidal- and hydro- powers are all renewable energy sources with huge reserves. However, due to the characteristics of timeliness and intermittency, those new energies cannot be directly used in our daily life. Therefore, it is necessary to develop and use energy conversion/storage devices including water splitting, carbon dioxide reduction, supercapacitors, and secondary batteries becomes more and more important. Among them, the secondary batteries, as an energy storage medium with high energy density, have made great progress since the advent of lithium-ion batteries (LIBs) in 1991, and are widely used in our daily life, such as mobile electronic devices, and medical and transportation power systems. However, due to the uneven distribution (70% in South America) and limited reserves (the crustal content is about 20 ppm) of lithium resources on the earth, the cost of lithium-ion batteries continues to rise under the growing market demand. Therefore, the development of high-safety, low-cost, and environmentally friendly secondary batteries has become a research hotspot for many researchers.

Table 1.1 The main features of lithium (Li) and sodium (Na)

	${}^3\text{Li}$	${}^{11}\text{Na}$
Ionic radius (\AA)	0.76	1.02
Atomic mass (g mol^{-1})	6.9	23
E° vs SHE (V)	-3.04	-2.71
Melting point ($^\circ\text{C}$)	180.5	97.7
Resource abundance (ppm)	≤ 20	≥ 23000
Price (\$ /ton)	≈ 5800	≈ 280
Distribution	South America	Everywhere

Sodium has a higher crustal abundance, wider distribution, and lower cost compared to lithium. In addition, sodium and lithium are both alkali metal elements with similar physical and chemical properties and sodium-ion batteries (SIBs) have a similar energy storage mechanism to LIBs. Based on the above advantages, SIBs have received extensive attention worldwide in recent years. However, there are also some drawbacks for SIBs. Table 1 shows the main features of lithium (Li) and sodium (Na). The sodium-ion (Na^+ , 1.02 \AA) has a larger radius compared to the lithium-ion (Li^+ , 0.76 \AA). As a result, the diffusion kinetics of Na^+ will be slower, and more energy will be required to drive thermodynamically, which will affect the electrochemical performance of the battery, such as capacity, rate performance, cycle life, etc. Furthermore, a larger radius causes greater structural damage to the electrode active material during the process of intercalation/desorption of Na^+ , which requires a more stable structure of the electrode material, and there should have larger channels in its structure to facilitate the transmission of Na^+ . Finally, since the standard electrode potential of sodium (-2.7 V vs. SHE) is slightly higher than that of lithium (-3.04 V vs. SHE), the energy density of SIBs is much lower than that of LIBs, thus, it is difficult to satisfy the areas of high energy density application such as electric vehicles and portable

devices.[1-3] Therefore, the development of high-performance electrode materials for SIBs is one of the keys to the commercialization of SIBs in the future.

1.2 Sodium-ion batteries overview

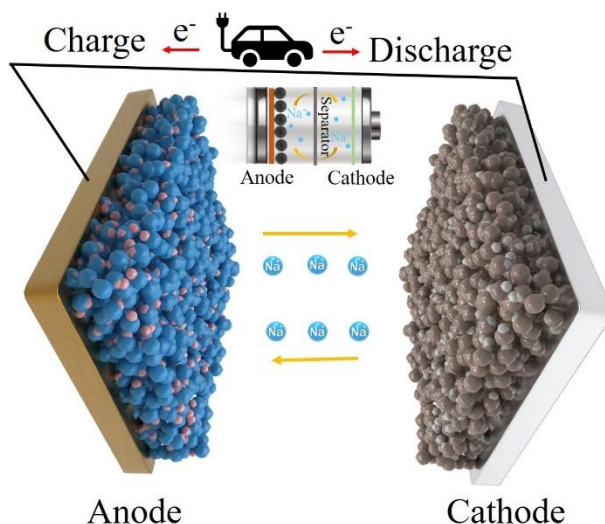


Figure 1.1 Schematic diagram of the working principle and configuration of sodium-ion batteries.

SIBs are composed of five parts: cathode, anode, electrolyte, separator, and cell case, which has the same structure as LIBs. The charging/discharging process of the SIBs is achieved by reversible insertion/extraction of Na^+ between the anode and cathode. Fig. 1.1 exhibits the schematic diagram of the working principle and configuration of sodium-ion batteries. Typically, aluminum (Al) and copper (Cu) are used as current collectors for cathode and anode, respectively, since neither forms an alloy with Na^+ . Cathode/anode active materials are mixed with conductive additives and binders to make a slurry and coated on Al/Cu foil to prepare the electrodes. The composition of electrolytes is generally sodium salt ($NaClO_4$, $NaPF_6$, and CF_3NaO_3S , etc.) dissolved in carbonate/ether solvent. The function of the separator is to separate the cathode and anode to avoid contact, and it can also pass through Na^+ and electrolytes. Generally, glass fiber or PP, PE membranes are used as the separator.

1.3 Cathode materials for sodium-ion batteries

Cathode materials, as an important part of SIBs, have a significant impact on battery performance. At present, the cathode materials of SIBs are mainly divided into three categories such as layered metal oxides, Prussian blue analogs, and polyanion-type.

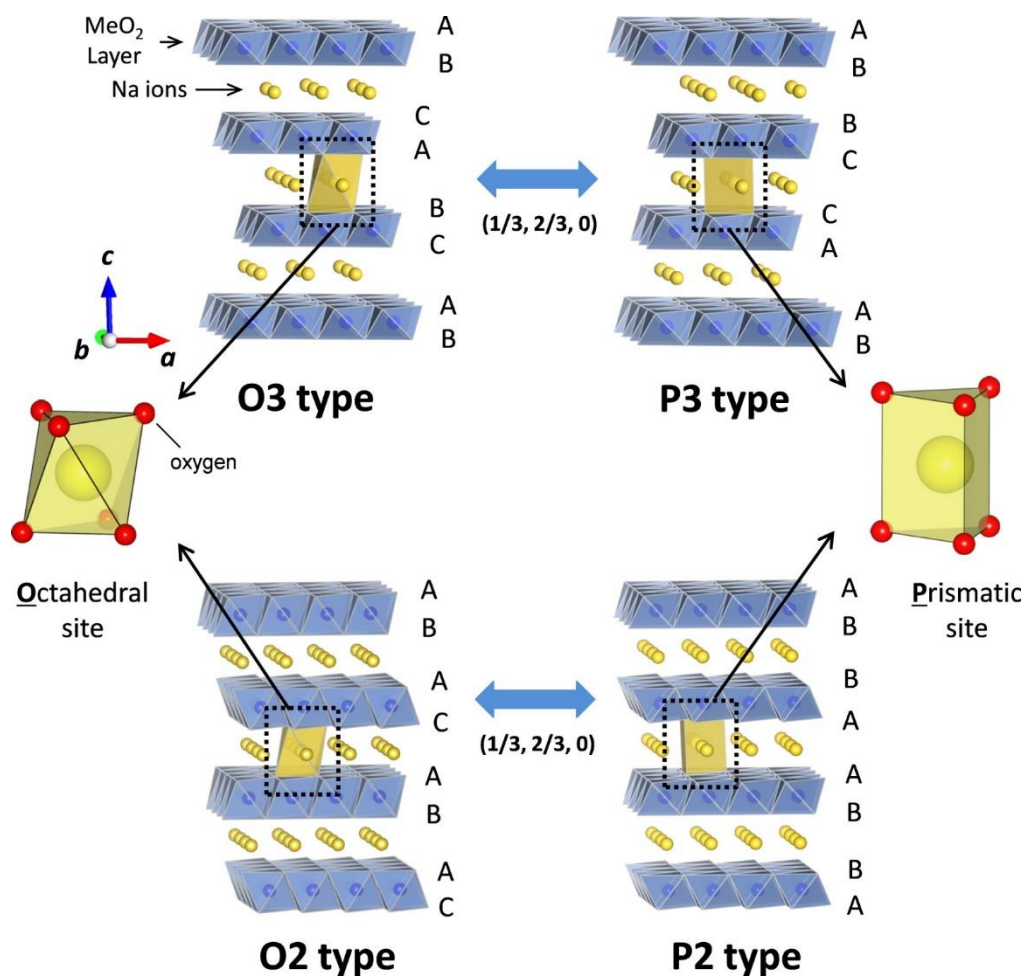


Figure 1.2 The classification of Na-Me-O layered materials with the sheets of edge-sharing MeO₆ octahedra and phase transition processes induced by sodium extraction.[4]

Layered metal oxides NaTMO₂ (TM = Fe, Co, Ni, Mn, Cr, V, Ti, and a mixture of 2 or 3 elements) exhibit excellent sodium ion storage capacity as the cathodes for SIBs, and can be divided into the following four types according to the coordination environment of sodium ions in the compound: P2, P3, O2, and O3. As shown in Fig.1.2,

sodium ions are intercalated at the octahedral site (O) or tetrahedral site (P), and the numbers 2 and 3 represent different packing methods. O-type and P-type materials can be transformed into each other during the charge/discharge process, while the number of unit layers of the material will not change. For example, O3-type material can be converted into P3-type, and P2-type can be converted into O2-type. Typical P2-type layered oxides are Na_xCoO_2 ($0.76 > x > 0.68$) and Na_xMnO_2 ($0.85 > x > 0.45$), and the typical representative of O3-type layered oxides is NaMeO_2 (Me = Fe, Mn, Ni, Cr). Among these different types of layered metal oxides, many studies have demonstrated that O2 and P3 types usually exhibit relatively excellent electrochemical performance.

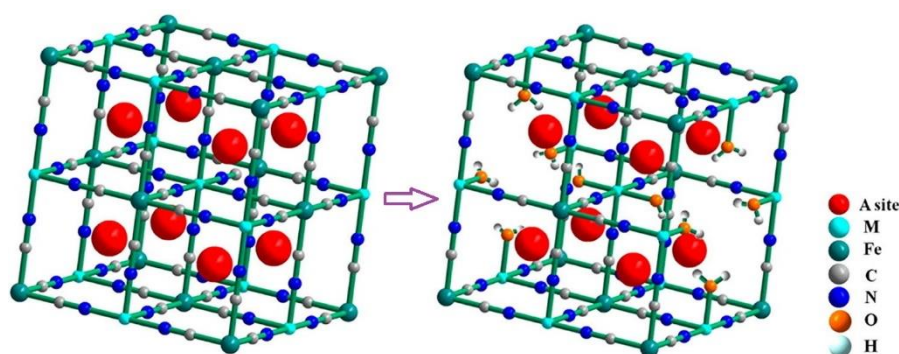


Figure 1.3 Schematic crystal structures of PBAs framework.[5]

Prussian blue analogs (PBAs) $\text{Na}_x\text{M}_\text{I}[\text{M}_\text{II}(\text{CN})_6]$ ($\text{M}_\text{I}, \text{M}_\text{II} = \text{Fe}, \text{Co}, \text{Mn}, \text{etc.}$), as the cathode materials for SIBs, have attracted extensive attention from researchers because of their simple preparation and low toxicity. As shown in Fig. 1.3, M and Fe are located at the cubic vertices, and (CN) anions are located at the edges, which can provide a stable crystal structure and high cycle stability as an electrode material. However, the precipitation reaction is often very rapid, and $\text{Fe}(\text{CN})_6$ vacancies will appear randomly with the loss of $\text{Fe}(\text{CN})_6$ ionic groups. Therefore, to reduce $\text{Fe}(\text{CN})_6$ vacancies, it is necessary to add a large amount of chelating agent (sodium citrate, EDTA, and NaC_2O_4 , etc.) to slow down the nucleation and growth rate[6-8].

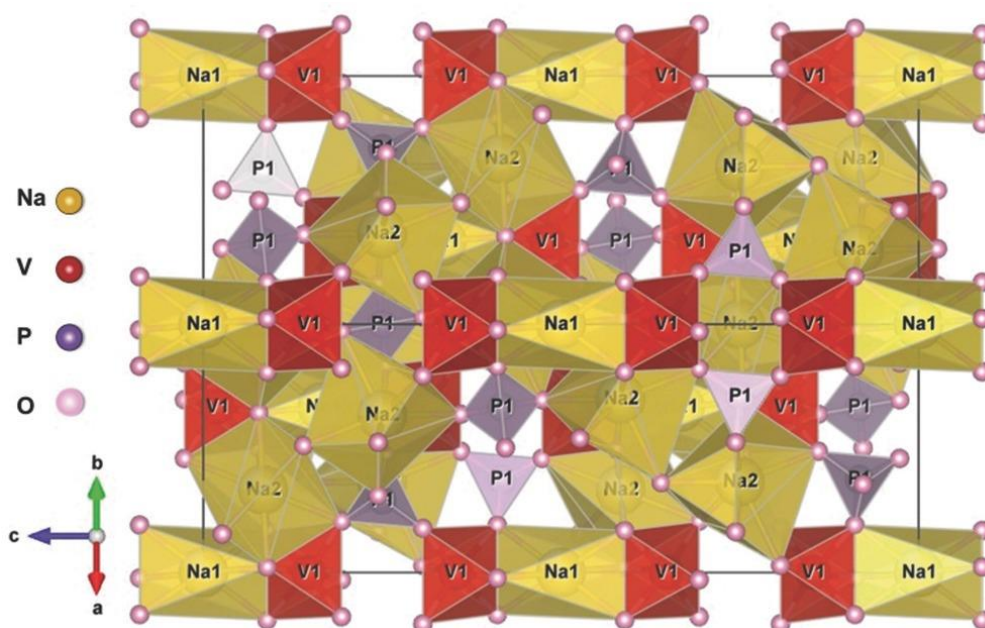


Figure 1.4 Crystal structure of $\text{Na}_3\text{V}_2(\text{PO}_4)_3$ (100-plane)[9].

Polyanion-type materials mainly include NaMPO_4 , NaMPO_4F ($\text{M} = \text{metal}$), and sodium super ion conductor (NASICON), etc., which have the characteristics of diverse structures and stable performance. As anode materials for SIBs, they often exhibit three-dimensional channels for Na^+ transportation, among which NASICON has received widespread attention for its excellent rate performance and cycling performance. Fig. 1.4 displays the crystal structure of $\text{Na}_3\text{V}_2(\text{PO}_4)_3$, as a typical representative of NASICON, which consists of $[\text{VO}_6]$ octahedrons and $[\text{PO}_4]$ tetrahedra connected by shared corners to form a basic framework. $\text{Na}_3\text{V}_2(\text{PO}_4)_3$ has a high voltage platform and fast Na^+ transfer rate, but there is a problem of cycle performance degradation. Studies have shown that carbon coating on the surface of nano-scale $\text{Na}_3\text{V}_2(\text{PO}_4)_3$ can effectively improve its electrochemical performance[10].

1.4 Anode materials for sodium-ion batteries

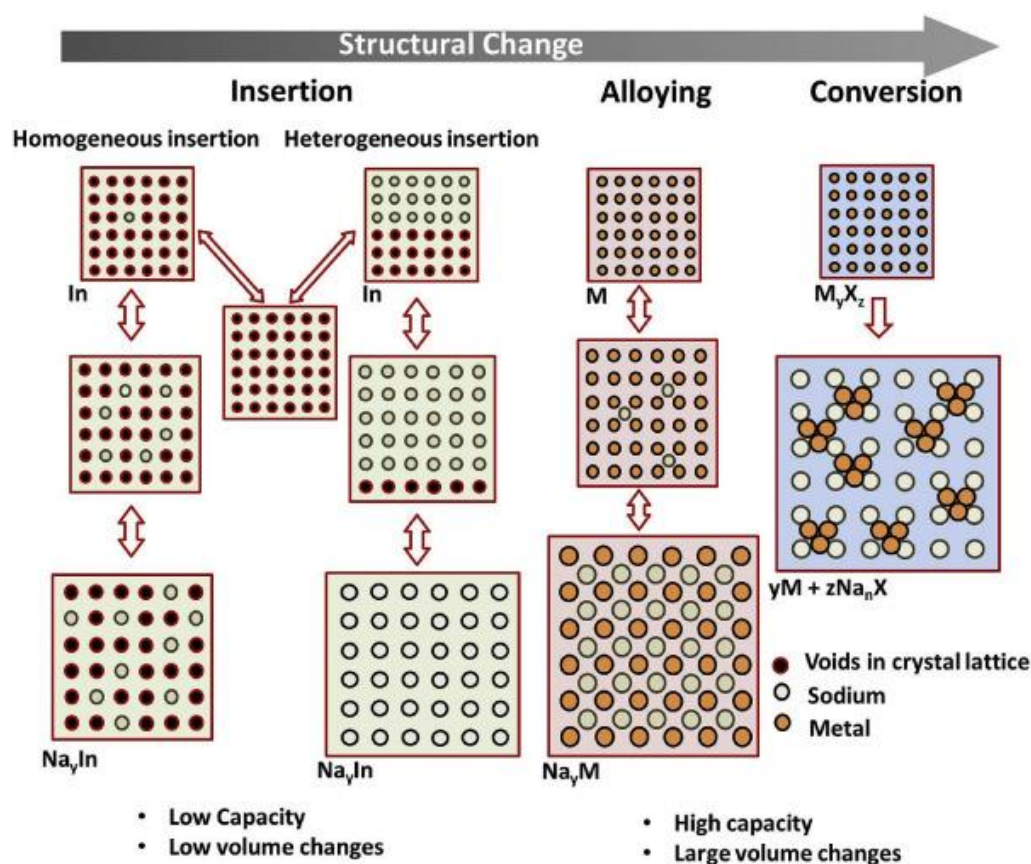


Figure 1.5 Schematic representation of reaction mechanisms occurring during storage of Na⁺ in various classes of anode materials[11].

Lithium-ion batteries widely use graphite materials as anodes, but due to the inherent characteristics of Na⁺ (ion radius 1.02 Å for Na⁺ vs 0.59 Å for Li⁺; molar mass 22.99 g/mol for Na⁺ vs 6.94 g/mol for Li⁺), it is not suitable for SIBs. Theoretically, metal Na is the most ideal choice as the anode material of SIBs because of its high theoretical capacity (1166 mAh g⁻¹), but the sodium dendrites caused by the uneven deposition of Na will pierce the separator and cause short circuit of the battery. Generally speaking, the anode materials for SIBs should have the following characteristics:

1. Large sodium ion storage capacity and excellent cycle reversibility;
2. Lower Na⁺ insertion/extraction potential;
3. Fast conduction of sodium ions and electrons;

4. Good chemical and structural stability;
5. High performance and environment friendly.

Similar to the classification of anode materials for LIBs, as shown in Fig. 1.5, according to the storage mechanism of Na^+ in the anode materials of SIBs, it can also be divided into intercalation-, alloy-, and conversion reaction-type materials.

1.4.1 Intercalation-type anode materials for sodium-ion batteries

Intercalation-type materials can topologically embed Na^+ in the material lattice during the charge/discharge process, and the main structure of the material will not change significantly after the intercalation/deintercalation of Na^+ . Therefore, when used as anode materials for SIBs, they often exhibit excellent cycle reversibility and long-term cycle life. However, the amount of Na^+ accommodated in the material lattice is limited, so the charge/discharge capacity of intercalation-type anode materials is low. There are mainly two kinds of intercalation-type anode materials including carbon materials and titanium-based materials.

(1) Carbon materials

Carbon materials can be divided into graphite and amorphous carbon according to their intrinsic structure differences. Among them, graphite material has always been the first choice for LIBs anode materials based on its excellent comprehensive performance and was successfully commercialized by Sony in 1991.[12, 13] However, graphite materials hardly deliver Na^+ storage capacity as the anode for SIBs due to the large ionic radius of Na^+ . Therefore, researchers have attempted to improve the sodium storage performance of graphite materials by modifying them. Wen et al. [14] reported the expanded graphite as a superior anode material, which exhibited an interlayer distance of 0.43 nm and delivered a high reversible capacity of 284 mAh g⁻¹ at the current density of 20 mA g⁻¹.

In recent years, the research on carbon material anodes for SIBs has mainly focused on amorphous carbon materials, including soft carbon and hard carbon materials. Doeff et al. [15] first reported the Na^+ storage performance of amorphous

soft carbon prepared from petroleum coke in 1993. Subsequently, in 2000, Stevens et al. [16] used amorphous hard carbon as the anode for SIBs and delivered a high reversible capacity of 300 mAh g⁻¹, which is comparable to the charge/discharge capacity of LIBs using graphite as the anode. As a result, it has attracted the attention of many scholars, who believe that hard carbon has excellent commercial potential as an anode material for sodium-ion batteries. To explore the sodium storage mechanism of hard carbon, researchers have prepared hard carbon materials with different structures around different precursors and heat treatment methods. A series of sodium storage mechanisms including intercalation-filling, defect, adsorption-filling and adsorption-intercalation were proposed through systematic analysis of its electrochemical test and material characterization results[17-21]. Apart from the carbon materials mentioned above, the electrochemical performance of other carbon materials for SIBs are listed in table 1.2.

Table 1.2 Electrochemical performances of reported carbon anode materials for SIBs.

Materials	Voltage (V)	Initial C. E.	Rate capability (mAh g ⁻¹)	Cyclability (mAh g ⁻¹)	Ref.
Templated carbon	0.0 ~ 1.6	20%	140 at 0.074 A g ⁻¹ ; 100 at 1.85 A g ⁻¹	120 @ 40cycles at 0.074 A g ⁻¹	[22]
Nanoporous hard carbon	0.01 ~ 2.0	77%	307 at 0.2 A g ⁻¹ ; 95 at 0.5 A g ⁻¹	289 @ 100 cycles at 0.02 A g ⁻¹	[23]
Hard carbon from PVC	0.01 ~ 2.5	69.9%	271 at 0.012 A g ⁻¹ ; 147 at 0.24 A g ⁻¹	215 @ 120 cycles at 0.012 A g ⁻¹	[24]
S doped carbon	0.01 ~ 2.0	73.6%	192.5 at 2 A g ⁻¹ ; 119.5 at 5 A g ⁻¹	302.2 @ 700 cycles at 0.5 A g ⁻¹	[25]
N-doped carbon nanofiber films	0.01 ~ 3.0	35.5%	315 at 0.5 A g ⁻¹ ; 154 at 15 A g ⁻¹	210 @ 7000 cycles at 5 A g ⁻¹	[26]
P-doped carbon nanosheets	0.01 ~ 3.0	46.7%	269 at 0.2 A g ⁻¹ ; 108 at 20 A g ⁻¹	108.8 @ 5000 cycles at 5 A g ⁻¹	[27]

Hard carbon microtubes	0.0 ~ 2.0	83%	275 at 0.15 A g ⁻¹ ; 180 at 0.3 A g ⁻¹	305 @ 100 cycles at 0.03 A g ⁻¹	[20]
Hard carbon nanoparticles	0.0 ~ 1.2	51.6%	270 at 0.05 A g ⁻¹ ; 45 at 2.5 A g ⁻¹	207 @ 500 cycles at 0.05 A g ⁻¹	[28]
Coal-based carbon	0.001 ~ 3.0	82.9%	356 at 0.03 A g ⁻¹ ; 207 at 0.2 A g ⁻¹	225 @ 1400 cycles 0.3 A g ⁻¹	[29]
Mesoporous soft carbon	0.01 ~ 3.0	45%	331 at 0.03 A g ⁻¹ ; 62 at 5 A g ⁻¹	103 @ 3000 cycles at 0.5 A g ⁻¹	[30]
Self-supported hard carbon	0.01 ~ 3.0	88.2%	292 at 0.02 A g ⁻¹ ; 175.6 at 0.4 A g ⁻¹	256.5 @ 536 cycles at 0.2 A g ⁻¹	[31]

Ref., References; C.E., Coulombic efficiency; PVC, Polyvinyl Chloride;

(2) Titanium-based materials

Titanium-based materials, such as TiO₂ and sodium super ion conductor (NASICON, such as NaTi₂(PO₄)₃ and NaZr₂(PO₄)₃), have been widely studied as anode materials for SIBs, in which the Ti⁴⁺/Ti³⁺ redox couple plays a key role[32, 33]. There are various TiO₂ crystal structures including anatase, brookite, rutile, and bronze phases, among which anatase has attracted enormous attention due to its lower activation barrier for Na⁺ intercalation[34-37]. Xu et al. [38] fabricated anatase TiO₂ nanocrystals as the anode materials for SIBs for the first time, which exhibited excellent cycling stability (150 mAh g⁻¹ @ over 100 cycles at 50 mA g⁻¹) and rate performance. To further improve the stability of the anatase TiO₂-based anode, the researchers also tried atomic doping. Wang et al. synthesized boron-doped anatase TiO₂ via a facile sol-gel and the hydrothermal method as the anode for SIBs, which demonstrated that the boron doping can result in lattice expansion was the main reason for its remarkable electrochemical performance (150 mAh g⁻¹ @ over 400 cycles at 2C)[39].

The NASICON-type material NaTi₂(PO₄)₃ is a three-dimensional (3D) framework material composed of TiO₆ octahedra and PO₄ tetrahedra connected at vertices. As a typical representative of intercalation materials, NaTi₂(PO₄)₃ has attracted much attention because of its stable charge/discharge platform, broad Na⁺ transport channels, and good thermodynamic stability. It delivers two stable discharge plateaus of 2.1 and

0.4 V within the voltage range of 0-3 V, which can be well corresponded to $\text{Ti}^{4+}/\text{Ti}^{3+}$ and $\text{Ti}^{3+}/\text{Ti}^{2+}$ transformations, respectively[40]. For the first time, Delmas et al. [41] successfully synthesized $\text{NaTi}_2(\text{PO}_4)_3$, which can reversibly storage Na^+ at room temperature. However, limited by the poor conductivity of $\text{NaTi}_2(\text{PO}_4)_3$, researchers subsequently proposed many improvement measures including particle size reduction, morphology, structure design, composite conductive materials, etc.[42-44]. Man et al. [43] reported a carbon-coated porous $\text{NaTi}_2(\text{PO}_4)_3$ olive-like nanospheres as the anode for SIBs with facilitated electron/ Na^+ diffusion kinetics, excellent reversible capacity (127 mAh g^{-1} at 0.1 C) and superior cycling stability (84.8% capacity retention after 10000 cycles at 5 C).

1.4.2 Alloy-type anode materials for sodium-ion batteries

Intercalation-type materials often exhibit excellent cycling stability, however, limited by the internal structure of the materials, the energy density is low when used as the anode for SIBs. Alloy-type materials (P, Si, Ge, Sn, Sb, Bi, and In et al.) refer to the storage of Na^+ by reversibly forming alloys between Na^+ and anode materials, which usually exhibit high specific capacity. Table 1.3 summarizes the parameters of alloy-type anode materials for SIBs. Its alloy reaction can be mainly expressed as $\text{M} + x\text{Na}^+ + xe^- \leftrightarrow \text{Na}_x\text{M}$. However, due to the large radius of Na^+ , alloy-type anode materials are often accompanied by huge volume expansion/contraction during the alloying/de-alloying process with Na^+ , resulting in pulverization of the active material and/or shedding, and battery capacity decay or even fail. To deal with these problems, researchers have proposed many solutions, such as structural design and interface modification[45].

The hollow structure design is considered to be an effective method to alleviate the volume expansion of alloy-type materials. Pu et al. [46] fabricated Bi nanotubes by a facile iodide-ion-assisted galvanic displacement method for high-capacity, high-rate, and long-term stability sodium storage, which can be resulted from its excellent structural merits including hollow tubular structure, large specific surface area, and thin

wall. In addition to metal-based alloy materials, the researchers also designed hollow silicon materials to improve the electrochemical performance of batteries. Hollow Si@void@C yolk-shell microspheres were successfully synthesized by Zhou et al. [47] via low-temperature aluminothermic reduction, which exhibited excellent cycling stability and rate capacity for lithium storage.

Table 1.3 The parameters of alloy-type anode materials for SIBs.

Alloy materials	Alloy phase	Theoretical capacity (mAh g ⁻¹)	Electrical conductivity (S cm ⁻¹)	Volume expansion (%)
P	Na ₃ P	2596	1×10^{-14} [48]	305 [49]
Si	NaSi	954	/	114 [50]
Ge	NaGe	369	1×10^{-2} [48]	305 [51]
Sn	Na ₁₅ Sn ₄	847	9×10^4 [52]	420 [53]
Sb	Na ₃ Sb	660	2.5×10^4 [54]	390 [55]
Bi	Na ₃ Bi	385	/	250 [56]
In	Na ₂ In	467	/	297 [57]

Constructing an interfacial buffer layer is another effective way to improve the electrochemical performance of alloy-type anode materials. The electrode/electrolyte interface can often form a solid electrolyte interface layer (SEI), which can avoid electrolyte decomposition caused by direct contact between the electrode and the electrolyte. However, the SEI layer is easily destroyed and a new SEI layer is re-formed during battery charging/discharging, resulting in continuous consumption of electrolytes, which in turn leads to battery capacity attenuation or even failure. Therefore, it is necessary to construct an artificial SEI layer, which is also applicable to other types of electrode materials[58, 59].

1.4.3 Conversion reaction-type anode materials for sodium-ion batteries

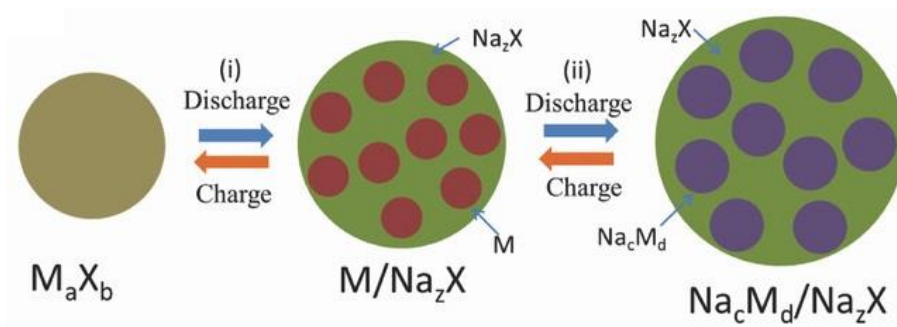


Figure 1.6 The schematic illustration of conversion reactions with sodium.[60]

Different from intercalation-type and alloy-type anode materials, conversion reaction-type anode materials undergo phase transition during the sodiation/desodiation process, and the conversion reaction formula can be expressed as follows:



Herein, M and X represent metals and non-metal elements, respectively. M is the main transition metals including Fe, Co, Ni, Mo, Cu, etc., and X is mainly including O, S, Se, P, and F, etc.[61-63] It is worth noting that if M is an alloy-type anode element (eg. Sn, Bi, and Sb, etc.), as shown in Fig. 1.6, the reaction process includes both conversion reactions and alloy reactions, which can often provide higher sodium storage capacity than a single reaction process. Furthermore, as depicted in Fig. 1.7, metal-oxides, -phosphides, and -sulfides deliver lower theoretical potentials and higher specific capacities compared with other conversion-type materials, which have great advantages as anode materials for SIBs.[64-66]

Table 1.4 summarizes the theoretical capacities of M_aX_b compounds (metal-oxides, -phosphides, -selenides, and -sulfides), where transition metal compounds with high oxidation valence release higher capacities upon conversion reactions. In addition, the strength of the bond energy of M-X can affect the potential of the conversion reaction, and the M_aX_b compound with a weak metal bond is more likely to undergo the conversion reaction at a lower potential. In recent years, the research on conversion

reaction materials as anodes for SIBs has attracted extensive attention due to their higher specific capacity than intercalation-type materials and better stability than alloy-type materials. However, there are still some shortcomings that need to be solved urgently for conversion-type anode materials, including voltage hysteresis, low initial Coulombic efficiency, and low cycle stability.

Table 1.4 Calculated theoretical capacities of the M_aX_b compounds. [60]

Metal	X = O		X = P		X = Se		X = S	
	Phase	Specific Capacity (mAh g ⁻¹)	Phase	Specific Capacity (mAh g ⁻¹)	Phase	Specific Capacity (mAh g ⁻¹)	Phase	Specific Capacity (mAh g ⁻¹)
M = Fe	FeO	746	Fe ₂ P	564	FeSe	397	FeS	610
	Fe ₂ O ₃	1007	FeP	926	FeSe ₂	502	FeS ₂	894
	Fe ₃ S ₄	924	FeP ₂	1365	/	/	Fe ₃ S ₄	725
M = Co	CoS	716	Co ₂ P	540	CoSe	389	CoS	589
	Co ₂ O ₃	967	CoP	894	CoSe ₂	494	CoS ₂	870
	Co ₃ S ₄	890	CoP ₂	1330	Co ₉ Se ₈	369	Co ₉ S ₈	544
M = Ni	NiO	718	Ni ₂ P	542	NiSe	389	NiS	591
	/	/	NiP	897	NiSe ₂	495	NiS ₂	879
	/	/	NiP ₂	1333	/	/	Ni ₃ S ₂	446
M = Mo	MoO ₂	838	MoP	633	MoSe ₂	422	MoS ₂	669
	MoO ₃	1117	/	/	/	/	/	/

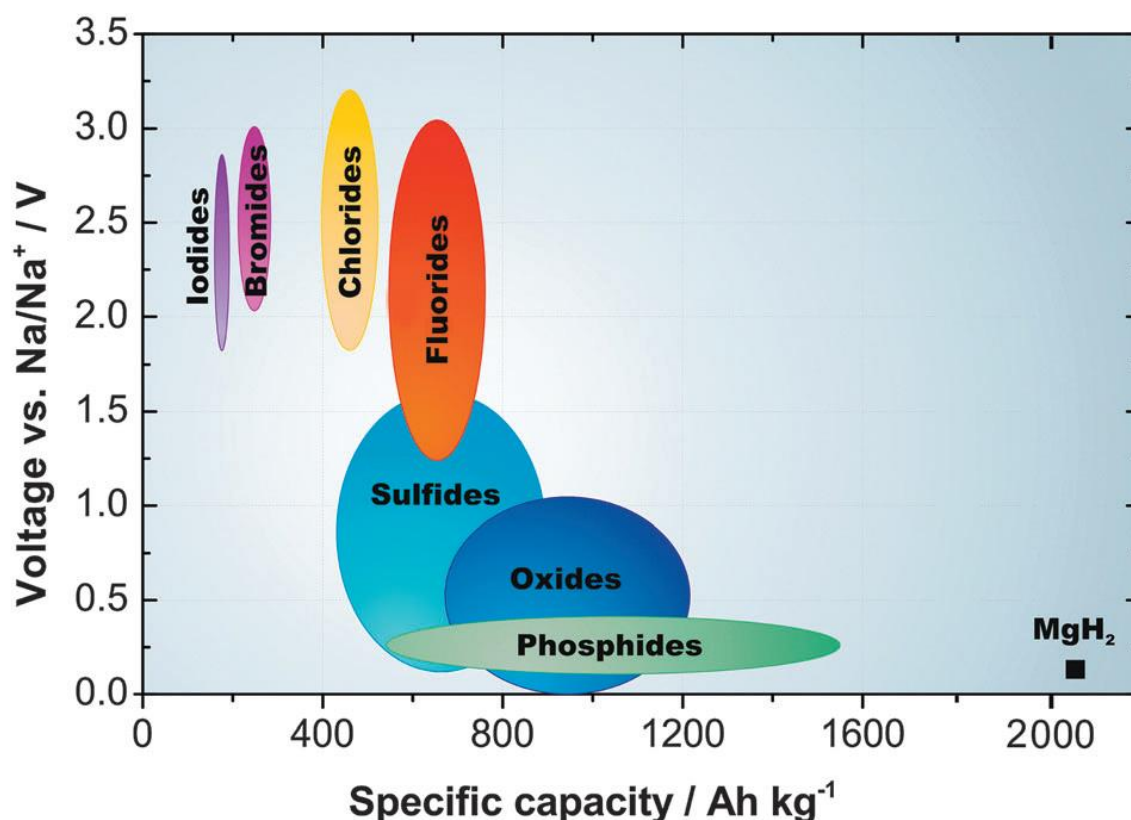


Figure 1.7 The specific capacity and theoretical potentials vs Na/Na^+ for conversion-type materials for sodium storage.[66]

Among many conversion reaction anode materials, metal oxides have attracted extensive attention due to their environmental friendliness, easy preparation, and low cost, etc. However, due to its strong M-O bond energy, the conversion reaction potential is usually as high as 0.96 V, which greatly limits its electrochemical reaction kinetics. Although metal phosphides deliver the lowest sodiation/desodiation potential and ultrahigh theoretical capacity, the common use of flammable red phosphorus and the generation of toxic PH_3 gas in the preparation process limit its practical application in reality. Metal selenides have similar physicochemical properties to metal sulfides, and they all exhibit weaker M-S/Se bonds than M-O and higher electrical conductivity than metal oxides. However, compared with metal selenides, the natural abundance of sulfur is high and the toxicity of metal sulfides is much lower than that of metal selenides, which greatly limits the application of metal selenides in SIBs. Therefore, metal sulfides are expected to become the most potential candidate anode materials for SIBs.

1.4.4 Optimization Strategies of Transition Metal Sulfides-Based Anodes for SIBs

In recent years, with the rapid development of SIBs and their huge potential to replace LIBs, metal sulfides, especially transition metal sulfides (TMSs), have attracted extensive attention due to their high ionic conductivity, environmental friendliness, and easily-controlled structure.[67] For example, iron sulfides, cobalt sulfides, and nickel sulfides as typical representatives of TMSs have been explored as anodes for SIBs, which exhibit high theoretical charge-discharge capacity due to their conversion reaction mechanism.[68-73] In particular, FeS_2 has the merits of abundant resources, low cost, and a high theoretical specific capacity of 894 mAh g^{-1} . Shadike et al. [74] reported the hydrothermal synthesis of FeS_2 as the anode for SIBs for the first time, revealing the formation of the new phase of NaFeS_2 during the charge/discharge process, which is also the main reason for the large irreversible capacity in the first cycle. In addition, layered transition metal sulfides (MS_2 , $\text{M}=\text{Ti, V, W, and Mo}$) are also frequently used as anodes for SIBs due to their larger interlayer spacing and weaker van der Waals forces between S-M-S layers, which are beneficial to improve the electrochemical kinetics during Na^+ storage.[75-79] MoS_2 nanoflowers were fabricated as anodes for SIBs by Hu et al. [76], which exhibited a high specific capacity and superior rate performance due to its expanded interlayer space during the repeated intercalation/deintercalation of Na^+ .

It is worth noting that, in addition to the advantages of TMSs mentioned above, they also face challenges brought about by their essential properties. First of all, voltage hysteresis refers to the phenomenon of slow voltage response during battery charge/discharge, which will reduce energy efficiency and affect the output voltage of the battery. Although TMSs exhibit faster kinetics, they still have a voltage hysteresis greater than 0.4 V [80]. In addition, initial Coulombic efficiency (ICE) is an important parameter to evaluate the performance of electrode materials while TMSs can usually provide 80% of ICE, which is not enough for the commercial application of such a secondary battery.[81] The main reasons for the low ICE of TMSs include incomplete

electrode reaction (kinetic factors) and electrolyte decomposition (caused by irreversible reactions). Furthermore, volume expansion is another key factor restricting the commercialization of TMSs anode materials for SIBs. Large volume expansion will cause active material pulverization, stripping from the current collector, and re-forming SEI film, which will lead to poor cycle performance of the battery.[82, 83] Last but not least, cycling stability is an important criterion for evaluating the commercial potential of electrode materials, and the phenomenon that conversion-type anode materials decay rapidly during cycling is common. For example, bulk MoS_2 can deliver a high initial discharge capacity of about 940 mAh g^{-1} , while only 148 mAh g^{-1} can be obtained after 100 cycles[84]. To deal with the above challenges, researchers have proposed many effective methods, such as carbon modification, nanostructure design, construction of heterostructures and electrolyte optimization, etc.

(1) Carbon modification

Coating carbonaceous materials onto active particles is a common route to stabilize interfaces, reduce the formation of SEI film and enhance electronic conductivity.[85-88] Zhu et al. [89] fabricated carbon-coated 3D porous interconnected metal sulfides (SnS/C) for both lithium/sodium storage, which exhibited excellent reversible capacity and cycling stability due to its unique structure and morphology. Furthermore, there is another approach to incorporate TMSs with flexible carbon materials (carbon nanotubes and graphene) to construct a 3D interconnected framework, which can not only effectively buffer mechanical stress but also facilitate the kinetics of electrode reactions[90-94]. Chen et al. [95] synthesized the anode for SIBs with 3D graphene-wrapped Co_9S_8 , which delivered superior cycling stability with a high capacity retention of 92.6% after 500 cycles at 0.3 A g^{-1} . Although carbon-modified materials effectively improved the stability of materials, part of the capacity was sacrificed due to the introduction of inactive carbon materials.

(2) Nanostructure design

TMSs with nanostructural features have excellent physicochemical properties as anodes for SIBs. Firstly, the large specific surface area provides abundant active sites for Na^+ storage. Secondly, nanostructured materials can shorten the diffusion distance

of ions/electrons, which can effectively improve the kinetics of electrode reactions. Finally, well-designed nanostructures (i.e., hollow, core-shell, hierarchical structures, etc.) can even effectively alleviate the volume expansion of anode active materials during the charge/discharge process.[96, 97] However, the larger specific surface area means that more SEI films are formed in the first cycle, so the ICE of nanostructured materials is generally lower.

(3) Construction of heterostructures

Compared with single-component TMSs, multi-component TMSs with heterostructures exhibit better electrochemical performance[98, 99]. When different types of materials (p-type and n-type semiconductors) are coupled to each other, a built-in electric field is formed at the interface, which can accelerate the transport of carriers and thus improve the kinetics of the electrode reaction[100]. $\text{Bi}_2\text{S}_3/\text{MoS}_2$ heterostructures were successfully synthesized by Yang et al. [101], which delivered excellent cycling stability (323.4 mAh g^{-1} after 1200 cycles) at a high current density of 10 A g^{-1} . It can be assigned to the rational design of $\text{Bi}_2\text{S}_3/\text{MoS}_2$ heterostructures.

(4) Electrolyte optimization

As an important part of the battery, the electrolyte plays a key role in the electrochemical performance of the battery. The electrolyte systems currently used in SIBs are mainly carbonates and ethers. Numerous studies have demonstrated that ether electrolytes can improve the reversible capacity and cycle stability of TMSs compared with carbonate electrolytes[102, 103]. Su et al. [102] conducted the density functional theory (DFT) calculations and demonstrated that the intercalation of Na^+ in ZnS nanocrystals has lower activation energy in ether electrolytes. Currently, the mechanism of sodiation/desodiation for TMSs-based anodes in ether electrolytes is unclear, but their good compatibility with each other may be an important factor.

1.5 Objectives of this study

Compared with LIBs, sodium used in SIBs is rich, widely distributed, low-cost, and the SIBs have a similar working mechanism to LIBs, making it possible to replace

LIBs. However, the performance of current electrode materials is still unstable, which hinders the process of its commercial application. Compared with other types of anode materials (intercalation-type, alloy-type, and other conversion-type materials), TMSs have greater advantages, including higher theoretical capacity, excellent electrical conductivity, environmental friendliness, an easily-controlled structure, etc. Although TMSs have obvious advantages as anode materials for SIBs, there are still full of challenges that need to be solved, such as voltage hysteresis, low initial Coulombic efficiency, volume expansion, and cycle stability, etc.

In recent years, researchers have proposed many solutions to the defects of TMSs, including carbon modification, nanostructure design, heterostructure construction, and electrolyte optimization. Although it can achieve some effects, it is still not used on a large scale due to factors such as cost, sacrifice capacity, and complex preparation process. The main objectives of this research are to propose a relatively simple preparation process of TMSs (hydrothermal synthesis followed with solid state sulfidation), and meanwhile, taking into account on the modification by the carbon framework and heterostructure design. Finally, they are used as the anodes for SIBs, and it is expected to show excellent reversible capacity, good rate performance, and outstanding cycle stability.

1.6 Contents of this dissertation

This dissertation contains six chapters.

Chapter 1: The systematic summary of the various anode materials currently available for sodium-ion batteries, and a detailed analysis of the challenges and optimization strategies encountered in the research of transition metal sulfides as the anode materials for sodium-ion batteries.

Chapter 2: The introduction of the used chemical reagents, characterization, and electrochemical testing methods.

Chapter 3: The Prussian blue analogs (PBAs) were synthesized by the hydrothermal method under the synergistic effect of trisodium citrate dihydrate (TSC,

$\text{Na}_3\text{C}_6\text{H}_5\text{O}_7 \cdot 2\text{H}_2\text{O}$) and $\text{K}_3[\text{Co}(\text{CN})_6]$, and two kinds of cobalt sulfide nanoparticles embedded in N/S co-doped carbon frameworks (namely, $\text{Co}_3\text{S}_4@\text{C-N/S}$ and $\text{Co}_9\text{S}_8@\text{C-N/S}$) are successfully fabricated by a subsequent solid-state sulfidation process. The morphology and electrochemical performance of the as-prepared products with different content of TSC were explored.

Chapter 4: Micro-flower-like MoS_2 -modified Co_9S_8 ($\text{Co}_9\text{S}_8/\text{MoS}_2$) with a three-dimensional (3D) heterostructure was obtained via a simple solvothermal synthesis followed by a solid sulfidation treatment process. The formation mechanism and properties of the micro-flower morphology are explored through various material characterizations. The electrochemical performances of as-prepared samples were tested and analyzed. In addition, density functional theory (DFT) calculations were conducted to analysis the Na^+ diffusion energy barrier in $\text{Co}_9\text{S}_8/\text{MoS}_2$ heterostructure and Co_9S_8 .

Chapter 5: CoS/MoS_2 with heterostructure was fabricated as anode material for sodium-ion batteries, which can be constructed by combining a one-pot hydrothermal route with a solid-state sulfidation step. In addition, pure CoS and pure MoS_2 were also synthesized following the reported methods. The materials characterizations and kinetics analysis were conducted to investigate the mechanism of the excellent electrochemical performance of CoS/MoS_2 heterostructure materials.

Chapter 6: The general conclusions of this study and challenges for the future commercial application of sodium-ion batteries are introduced.

References

- [1] V. Palomares, P. Serras, I. Villaluenga, K.B. Hueso, J. Carretero-Gonzalez, T. Rojo, Na-ion batteries, recent advances and present challenges to become low cost energy storage systems, *Energ. Environ. Sci.* 5 (2012) 5884-5901.
- [2] S.W. Kim, D.H. Seo, X.H. Ma, G. Ceder, K. Kang, Electrode Materials for Rechargeable Sodium-Ion Batteries: Potential Alternatives to Current Lithium-Ion Batteries, *Adv. Energy Mater.* 2 (2012) 710-721.
- [3] H.L. Pan, Y.S. Hu, L.Q. Chen, Room-temperature stationary sodium-ion batteries for large-scale electric energy storage, *Energ. Environ. Sci.* 6 (2013) 2338-2360.
- [4] N. Yabuuchi, S. Komaba, Recent research progress on iron- and manganese-based positive electrode materials for rechargeable sodium batteries, *Sci. Technol. Adv. Mat.* 15 (2014) 043501.
- [5] B.X. Xie, B.Y. Sun, T.Y. Gao, Y.L. Ma, G.P. Yin, P.J. Zuo, Recent progress of Prussian blue analogues as cathode materials for nonaqueous sodium-ion batteries, *Coord. Chem. Rev.* 460 (2022).
- [6] Y. Shang, X.X. Li, J.J. Song, S.Z. Huang, Z. Yang, Z.C.J. Xu, H.Y. Yang, Unconventional Mn Vacancies in Mn-Fe Prussian Blue Analogs: Suppressing Jahn-Teller Distortion for Ultrastable Sodium Storage, *Chem* 6 (2020) 1804-1818.
- [7] Z. Xu, Y. Sun, J. Xie, Y. Nie, X.W. Xu, J. Tu, J. Zhang, L.C. Qiu, T.J. Zhu, X.B. Zhao, Scalable Preparation of Mn/Ni Binary Prussian Blue as Sustainable Cathode for Harsh-Condition-Tolerant Sodium-Ion Batteries, *Acs Sustainable Che. Eng.* 10 (2022) 13277-13287.
- [8] W.L. Wang, Y. Gang, Z. Hu, Z.C. Yan, W.J. Li, Y.C. Li, Q.F. Gu, Z.X. Wang, S.L. Chou, H.K. Liu, S.X. Dou, Reversible structural evolution of sodium-rich rhombohedral Prussian blue for sodium-ion batteries, *Nat. Commun.* 11 (2020).
- [9] S.Q. Chen, C. Wu, L.F. Shen, C.B. Zhu, Y.Y. Huang, K. Xi, J. Maier, Y. Yu, Challenges and Perspectives for NASICON-Type Electrode Materials for Advanced Sodium-Ion Batteries, *Adv. Mater.* 29 (2017).
- [10] Z. Jian, L. Zhao, H. Pan, Y.-S. Hu, H. Li, W. Chen, L. Chen, Carbon coated

Na₃V₂(PO₄)₃ as novel electrode material for sodium ion batteries, *Electrochem. Commun.* 14 (2012) 86-89.

[11] T. Perveen, M. Siddiq, N. Shahzad, R. Ihsan, A. Ahmad, M.I. Shahzad, Prospects in anode materials for sodium ion batteries - A review, *Renew. Sust. Energ. Rev.* 119 (2020) 109549.

[12] B. Scrosati, History of lithium batteries, *J. Solid State Electr.* 15 (2011) 1623-1630.

[13] H. Zhang, Y. Yang, D. Ren, L. Wang, X. He, Graphite as anode materials: Fundamental mechanism, recent progress and advances, *Energy Storage Mater.* 36 (2021) 147-170.

[14] Y. Wen, K. He, Y.J. Zhu, F.D. Han, Y.H. Xu, I. Matsuda, Y. Ishii, J. Cumings, C.S. Wang, Expanded graphite as superior anode for sodium-ion batteries, *Nat. Commun.* 5 (2014).

[15] M.M. Doeff, Y. Ma, S.J. Visco, L.C. De Jonghe, Electrochemical Insertion of Sodium into Carbon, *J. Electrochem. Soc.* 140 (1993) L169.

[16] D.A. Stevens, J.R. Dahn, High Capacity Anode Materials for Rechargeable Sodium-Ion Batteries, *J. Electrochem. Soc.* 147 (2000) 1271.

[17] C. Bommier, T.W. Surta, M. Dolgos, X. Ji, New Mechanistic Insights on Na-Ion Storage in Nongraphitizable Carbon, *Nano Lett.* 15 (2015) 5888-5892.

[18] D.A. Stevens, J.R. Dahn, An In Situ Small-Angle X-Ray Scattering Study of Sodium Insertion into a Nanoporous Carbon Anode Material within an Operating Electrochemical Cell, *J. Electrochem. Soc.* 147 (2000) 4428.

[19] B. Zhang, C.M. Ghimbeu, C. Laberty, C. Vix-Guterl, J.-M. Tarascon, Correlation Between Microstructure and Na Storage Behavior in Hard Carbon, *Adv. Energy Mater.* 6 (2016) 1501588.

[20] Y. Li, Y.-S. Hu, M.-M. Titirici, L. Chen, X. Huang, Hard Carbon Microtubes Made from Renewable Cotton as High-Performance Anode Material for Sodium-Ion Batteries, *Adv. Energy Mater.* 6 (2016) 1600659.

[21] S. Qiu, L. Xiao, M.L. Sushko, K.S. Han, Y. Shao, M. Yan, X. Liang, L. Mai, J. Feng, Y. Cao, X. Ai, H. Yang, J. Liu, Manipulating Adsorption–Insertion Mechanisms in Nanostructured Carbon Materials for High-Efficiency Sodium Ion Storage, *Adv.*

Energy Mater. 7 (2017) 1700403.

[22] S. Wenzel, T. Hara, J. Janek, P. Adelhelm, Room-temperature sodium-ion batteries: Improving the rate capability of carbon anode materials by templating strategies, *Energ. Environ. Sci.* 4 (2011) 3342-3345.

[23] S.J.R. Prabakar, J. Jeong, M. Pyo, Nanoporous hard carbon anodes for improved electrochemical performance in sodium ion batteries, *Electrochim. Acta* 161 (2015) 23-31.

[24] Y. Bai, Z. Wang, C. Wu, R. Xu, F. Wu, Y.C. Liu, H. Li, Y. Li, J. Lu, K. Amine, Hard Carbon Originated from Polyvinyl Chloride Nanofibers As High-Performance Anode Material for Na-Ion Battery, *Acs Appl. Mater. Interfaces* 7 (2015) 5598-5604.

[25] L. Qie, W. Chen, X. Xiong, C. Hu, F. Zou, P. Hu, Y. Huang, Sulfur-Doped Carbon with Enlarged Interlayer Distance as a High-Performance Anode Material for Sodium-Ion Batteries, *Adv. Sci.* 2 (2015).

[26] S. Wang, L. Xia, L. Yu, L. Zhang, H. Wang, X.W. Lou, Free-Standing Nitrogen-Doped Carbon Nanofiber Films: Integrated Electrodes for Sodium-Ion Batteries with Ultralong Cycle Life and Superior Rate Capability, *Adv. Energy Mater.* 6 (2016) 1502217.

[27] H. Hou, L. Shao, Y. Zhang, G. Zou, J. Chen, X. Ji, Large-Area Carbon Nanosheets Doped with Phosphorus: A High-Performance Anode Material for Sodium-Ion Batteries, *Adv. Sci.* 4 (2017) 1600243.

[28] L. Xiao, Y. Cao, W.A. Henderson, M.L. Sushko, Y. Shao, J. Xiao, W. Wang, M.H. Engelhard, Z. Nie, J. Liu, Hard carbon nanoparticles as high-capacity, high-stability anodic materials for Na-ion batteries, *Nano Energy* 19 (2016) 279-288.

[29] H. Chen, N. Sun, Q. Zhu, R.A. Soomro, B. Xu, Microcrystalline Hybridization Enhanced Coal-Based Carbon Anode for Advanced Sodium-Ion Batteries, *Adv. Sci.* 9 (2022) 2200023.

[30] B. Cao, H. Liu, B. Xu, Y.F. Lei, X.H. Chen, H.H. Song, Mesoporous soft carbon as an anode material for sodium ion batteries with superior rate and cycling performance, *J. Mater. Chem. A* 4 (2016) 6472-6478.

[31] P. Wang, Y.J. Guo, W.P. Chen, H. Duan, H. Ye, H.R. Yao, Y.X. Yin, F.F. Cao, Self-

supported hard carbon anode from fungus-treated basswood towards sodium-ion batteries, Nano Res..

[32] M. Sondergaard, K.J. Dalgaard, E.D. Bojesen, K. Wonsyld, S. Dahl, B.B. Iversen, In situ monitoring of $\text{TiO}_2(\text{B})$ /anatase nanoparticle formation and application in Li-ion and Na-ion batteries, J. Mater. Chem. A 3 (2015) 18667-18674.

[33] H. Li, H.L. Fei, X. Liu, J. Yang, M.D. Wei, In situ synthesis of $\text{Na}_2\text{Ti}_7\text{O}_{15}$ nanotubes on a Ti net substrate as a high performance anode for Na-ion batteries, Chem. Commun. 51 (2015) 9298-9300.

[34] Y. Zhang, C.W. Foster, C.E. Banks, L. Shao, H. Hou, G. Zou, J. Chen, Z. Huang, X. Ji, Graphene-Rich Wrapped Petal-Like Rutile TiO_2 tuned by Carbon Dots for High-Performance Sodium Storage, 28 (2016) 9391-9399.

[35] Y. Xu, M. Zhou, L. Wen, C. Wang, H. Zhao, Y. Mi, L. Liang, Q. Fu, M. Wu, Y. Lei, Highly Ordered Three-Dimensional Ni- TiO_2 Nanoarrays as Sodium Ion Battery Anodes, Chem. Mater. 27 (2015) 4274-4280.

[36] L.M. Wu, D. Bresser, D. Buchholz, S. Passerini, Nanocrystalline $\text{TiO}_2(\text{B})$ as Anode Material for Sodium-Ion Batteries, J. Electrochem. Soc. 162 (2015) A3052-A3058.

[37] C.X. Chu, J. Yang, Q.Q. Zhang, N.N. Wang, F.E. Niu, X.N. Xu, J. Yang, W.L. Fan, Y.T. Qian, Biphasic-Interface Enhanced Sodium Storage and Accelerated Charge Transfer: Flower-Like Anatase/Bronze TiO_2/C as an Advanced Anode Material for Na-Ion Batteries, Acs Appl. Mater. Interfaces 9 (2017) 43648-43656.

[38] Y. Xu, E.M. Lotfabad, H.L. Wang, B. Farbod, Z.W. Xu, A. Kohandehghan, D. Mitlin, Nanocrystalline anatase TiO_2 : a new anode material for rechargeable sodium ion batteries, Chem. Commun. 49 (2013) 8973-8975.

[39] B. Wang, F. Zhao, G. Du, S. Porter, Y. Liu, P. Zhang, Z. Cheng, H.K. Liu, Z. Huang, Boron-Doped Anatase TiO_2 as a High-Performance Anode Material for Sodium-Ion Batteries, ACS Appl. Mater. Interfaces 8 (2016) 16009-16015.

[40] P. Senguttuvan, G. Rousse, M.E. Arroyo y de Dompablo, H. Vezin, J.M. Tarascon, M.R. Palacín, Low-Potential Sodium Insertion in a NASICON-Type Structure through the Ti(III)/Ti(II) Redox Couple, J. Am. Chem. Soc. 135 (2013) 3897-3903.

[41] C. Delmas, F. Cherkaoui, A. Nadiri, P. Hagemuller, A nasicon-type phase as

intercalation electrode: $\text{NaTi}_2(\text{PO}_4)_3$, Mater. Res. Bull. 22 (1987) 631-639.

[42] Y. Wang, Z. Peng, Y. Li, H. Li, H. Jiang, L. Chen, An interconnected $\text{NaTi}_2(\text{PO}_4)_3$ /carbon composite from an all-integrated framework with chelating Ti in a cross-linked citric acid-organic phosphonic acid skeleton for high-performance sodium storage, J. Colloid Interf. Sci. 626 (2022) 1-12.

[43] Y. Man, J. Sun, X. Zhao, L. Duan, Y. Fei, J. Bao, X. Mo, X. Zhou, An ultrastable sodium-ion battery anode enabled by carbon-coated porous $\text{NaTi}_2(\text{PO}_4)_3$ olive-like nanospheres, J. Colloid Interf. Sci. 635 (2023) 417-426.

[44] P. Wei, Y. Liu, Z. Wang, Y. Huang, Y. Jin, Y. Liu, S. Sun, Y. Qiu, J. Peng, Y. Xu, X. Sun, C. Fang, J. Han, Y. Huang, Porous $\text{NaTi}_2(\text{PO}_4)_3/\text{C}$ Hierarchical Nanofibers for Ultrafast Electrochemical Energy Storage, ACS Appl. Mater. Interfaces 10 (2018) 27039-27046.

[45] M.Q. Peng, K. Shin, L.X. Jiang, Y. Jin, K. Zeng, X.L. Zhou, Y.B. Tang, Alloy-Type Anodes for High-Performance Rechargeable Batteries, Angew. Chem. Int. Edit. 61 (2022).

[46] B. Pu, Y. Liu, J. Bai, X. Chu, X. Zhou, Y. Qing, Y. Wang, M. Zhang, Q. Ma, Z. Xu, B. Zhou, W. Yang, Iodine-Ion-Assisted Galvanic Replacement Synthesis of Bismuth Nanotubes for Ultrafast and Ultrastable Sodium Storage, ACS Nano 16 (2022) 18746-18756.

[47] Z. Zhou, L. Pan, Y. Liu, X. Zhu, X. Xie, From sand to fast and stable silicon anode: Synthesis of hollow Si@void@C yolk-shell microspheres by aluminothermic reduction for lithium storage, Chinese Chem. Lett. 30 (2019) 610-617.

[48] J. Sun, G. Zheng, H.-W. Lee, N. Liu, H. Wang, H. Yao, W. Yang, Y. Cui, Formation of Stable Phosphorus-Carbon Bond for Enhanced Performance in Black Phosphorus Nanoparticle-Graphite Composite Battery Anodes, Nano Letters 14 (2014) 4573-4580.

[49] Y. Fu, Q. Wei, G. Zhang, S. Sun, Advanced Phosphorus-Based Materials for Lithium/Sodium-Ion Batteries: Recent Developments and Future Perspectives, Adv. Energy Mater. 8 (2018) 1703058.

[50] S.C. Jung, D.S. Jung, J.W. Choi, Y.-K. Han, Atom-Level Understanding of the Sodiation Process in Silicon Anode Material, J. Phys. Chem. Lett. 5 (2014) 1283-1288.

- [51] H. Kim, H. Kim, Z. Ding, M.H. Lee, K. Lim, G. Yoon, K. Kang, Recent Progress in Electrode Materials for Sodium-Ion Batteries, *Adv. Energy Mater.* 6 (2016) 1600943.
- [52] H.-X. Yang, J.-S. Li, T. Guo, W.-Y. Wang, H.-C. Kou, J. Wang, Evolution of microstructure and hardness in a dual-phase $\text{Al}_{0.5}\text{CoCrFeNi}$ high-entropy alloy with different grain sizes, *Rare Metals* 39 (2020) 156-161.
- [53] Y. Liu, Y. Xu, Y. Zhu, J.N. Culver, C.A. Lundgren, K. Xu, C. Wang, Tin-Coated Viral Nanoforests as Sodium-Ion Battery Anodes, *ACS Nano* 7 (2013) 3627-3634.
- [54] L. Wu, X.H. Hu, J.F. Qian, F. Pei, F.Y. Wu, R.J. Mao, X.P. Ai, H.X. Yang, Y.L. Cao, Sb-C nanofibers with long cycle life as an anode material for high-performance sodium-ion batteries, *Energy Environ. Sci.* 7 (2014) 323-328.
- [55] L. Wu, H. Lu, L. Xiao, X. Ai, H. Yang, Y. Cao, Electrochemical properties and morphological evolution of pitaya-like Sb@C microspheres as high-performance anode for sodium ion batteries, *J. Mater. Chem. A* 3 (2015) 5708-5713.
- [56] L.D. Ellis, B.N. Wilkes, T.D. Hatchard, M.N. Obrovac, In Situ XRD Study of Silicon, Lead and Bismuth Negative Electrodes in Nonaqueous Sodium Cells, *J. Electrochem. Soc.* 161 (2014) A416.
- [57] S.A. Webb, L. Baggetto, C.A. Bridges, G.M. Veith, The electrochemical reactions of pure indium with Li and Na: Anomalous electrolyte decomposition, benefits of FEC additive, phase transitions and electrode performance, *J. Power Sources* 248 (2014) 1105-1117.
- [58] L. Wang, S. Fu, T. Zhao, J. Qian, N. Chen, L. Li, F. Wu, R. Chen, In situ formation of a LiF and Li-Al alloy anode protected layer on a Li metal anode with enhanced cycle life, *J. Mater. Chem. A* 8 (2020) 1247-1253.
- [59] Y. Xu, S. Zhao, G. Zhou, W. Chen, F. Zhou, Z. Rong, Y. Wu, J. Li, J. Guo, Y. Zhang, Solubility-Dependent Protective Effects of Binary Alloys for Lithium Anode, *ACS Appl. Energy Mater.* 3 (2020) 2278-2284.
- [60] C. Wu, S.-X. Dou, Y. Yu, The State and Challenges of Anode Materials Based on Conversion Reactions for Sodium Storage, *Small* 14 (2018) 1703671.
- [61] H. Zhang, I. Hasa, S. Passerini, Beyond Insertion for Na-Ion Batteries: Nanostructured Alloying and Conversion Anode Materials, *Adv. Energy Mater.* 8 (2018)

1702582.

- [62] J. Li, X. Li, P. Liu, X. Zhu, R.N. Ali, H. Naz, Y. Yu, B. Xiang, Self-Supporting Hybrid Fiber Mats of Cu_3P – Co_2P /N–C Endowed with Enhanced Lithium/Sodium Ions Storage Performances, *ACS Appl. Mater. Interfaces* 11 (2019) 11442-11450.
- [63] Y. Fang, D. Luan, X.W. Lou, Recent Advances on Mixed Metal Sulfides for Advanced Sodium-Ion Batteries, *Adv. Mater.* 32 (2020) 2002976.
- [64] W. Luo, F. Shen, C. Bommier, H. Zhu, X. Ji, L. Hu, Na-Ion Battery Anodes: Materials and Electrochemistry, *Acc. Chem. Res.* 49 (2016) 231-240.
- [65] Z. Li, J. Ding, D. Mitlin, Tin and Tin Compounds for Sodium Ion Battery Anodes: Phase Transformations and Performance, *Acc. Chem. Res.* 48 (2015) 1657-1665.
- [66] F. Klein, B. Jache, A. Bhide, P. Adelhelm, Conversion reactions for sodium-ion batteries, *Phys. Chem. Chem. Phys.* 15 (2013) 15876-15887.
- [67] J. Zhou, Y. Liu, S. Zhang, T. Zhou, Z. Guo, Metal chalcogenides for potassium storage, *InfoMat* 2 (2020) 437-465.
- [68] X. Wei, W. Li, J.-a. Shi, L. Gu, Y. Yu, $\text{FeS}@C$ on Carbon Cloth as Flexible Electrode for Both Lithium and Sodium Storage, *ACS Appl. Mater. Interfaces* 7 (2015) 27804-27809.
- [69] T. Wang, W.H. Lv, D.D. Meng, Q.A. Liu, Z.Y. Rong, H.L. Qiu, A novelty strategy for preparing ternary FeS_2 - Fe_7S_8 - FeCl_2 composite as anode materials for sodium-ion batteries, *J. Alloy. Compd.* 925 (2022).
- [70] F. Wang, W.L. Zhang, H.H. Zhou, H. Chen, Z.Y. Huang, Z.H. Yan, R.J. Jiang, C.Q. Wang, Z. Tan, Y.F. Kuang, Preparation of porous FeS_2 -C/RG composite for sodium ion batteries, *Chem. Eng. J.* 380 (2020).
- [71] Y.Y. He, C.F. Dong, S.J. He, H. Li, X.P. Sun, Y. Cheng, G.W. Zhou, L.Q. Xu, Bimetallic nickel cobalt sulfides with hierarchical coralliform architecture for ultrafast and stable Na-ion storage, *Nano Res.* 14 (2021) 4014-4024.
- [72] M.M. Yin, D. Zhao, C.H. Feng, W. Zhou, Q.Z. Jiao, X.T. Feng, S.S. Wang, Y. Zhao, H.S. Li, T.Y. Feng, Construction of Porous Co_9S_8 Hollow Boxes with Double Open Ends toward High-Performance Half/Full Sodium-Ion Batteries, *Acs Sustainable Chem. Eng.* 8 (2020) 6305-6314.

- [73] R. Sun, S. Liu, Q. Wei, J. Sheng, S. Zhu, Q. An, L. Mai, Mesoporous NiS₂ Nanospheres Anode with Pseudocapacitance for High-Rate and Long-Life Sodium-Ion Battery, *Small* 13 (2017) 1701744.
- [74] Z. Shadike, Y.-N. Zhou, F. Ding, L. Sang, K.-W. Nam, X.-Q. Yang, Z.-W. Fu, The new electrochemical reaction mechanism of Na/FeS₂ cell at ambient temperature, *J. Power Sources* 260 (2014) 72-76.
- [75] X.Q. Zhang, X.N. Li, J.W. Liang, Y.C. Zhu, Y.T. Qian, Synthesis of MoS₂@C Nanotubes Via the Kirkendall Effect with Enhanced Electrochemical Performance for Lithium Ion and Sodium Ion Batteries, *Small* 12 (2016) 2484-2491.
- [76] Z. Hu, L.X. Wang, K. Zhang, J.B. Wang, F.Y. Cheng, Z.L. Tao, J. Chen, MoS₂ Nanoflowers with Expanded Interlayers as High-Performance Anodes for Sodium-Ion Batteries, *Angew. Chem. Int. Edit.* 53 (2014) 12794-12798.
- [77] Y.B. Xu, K. Wang, Z.P. Yao, J. Kang, D. Lam, D. Yang, W. Ai, C. Wolverton, M.C. Hersam, Y. Huang, W. Huang, V.P. Dravid, J.S. Wu, In Situ, Atomic-Resolution Observation of Lithiation and Sodiation of WS₂ Nanoflakes: Implications for Lithium-Ion and Sodium-Ion Batteries, *Small* 17 (2021).
- [78] S. Hwang, Z.P. Yao, L. Zhang, M.S. Fu, K. He, L.Q. Mai, C. Wolverton, D. Su, Multistep Lithiation of Tin Sulfide: An Investigation Using in Situ Electron Microscopy, *Acs Nano* 12 (2018) 3638-3645.
- [79] M.S. Fu, Z.P. Yao, X. Ma, H. Dong, K. Sun, S. Hwang, E.Y. Hu, H. Gan, Y. Yao, E.A. Stach, C. Wolverton, D. Su, Expanded lithiation of titanium disulfide: Reaction kinetics of multi-step conversion reaction, *Nano Energy* 63 (2019).
- [80] J.S. Cho, J.-S. Park, Y.C. Kang, Porous FeS nanofibers with numerous nanovoids obtained by Kirkendall diffusion effect for use as anode materials for sodium-ion batteries, *Nano Res.* 10 (2017) 897-907.
- [81] P. Chandra Rath, J. Patra, D. Saikia, M. Mishra, J.-K. Chang, H.-M. Kao, Highly enhanced electrochemical performance of ultrafine CuO nanoparticles confined in ordered mesoporous carbons as anode materials for sodium-ion batteries, *J. Mater. Chem. A* 4 (2016) 14222-14233.
- [82] Y. Sun, N. Liu, Y. Cui, Promises and challenges of nanomaterials for lithium-based

rechargeable batteries, *Nat. Energy* 1 (2016) 16071.

[83] F. Wu, G. Yushin, Conversion cathodes for rechargeable lithium and lithium-ion batteries, *Energ. Environ. Sci.* 10 (2017) 435-459.

[84] D.W. Su, S.X. Dou, G.X. Wang, Ultrathin MoS₂ Nanosheets as Anode Materials for Sodium-Ion Batteries with Superior Performance, *Adv. Energy Mater.* 5 (2015).

[85] Z. Liu, T. Lu, T. Song, X.-Y. Yu, X.W. Lou, U. Paik, Structure-designed synthesis of FeS₂@C yolk-shell nanoboxes as a high-performance anode for sodium-ion batteries, *Energ. Environ. Sci.* 10 (2017) 1576-1580.

[86] Y.-X. Wang, J. Yang, S.-L. Chou, H.K. Liu, W.-x. Zhang, D. Zhao, S.X. Dou, Uniform yolk-shell iron sulfide-carbon nanospheres for superior sodium-iron sulfide batteries, *Nat. Commun.* 6 (2015) 8689.

[87] L. Wu, H. Lu, L. Xiao, J. Qian, X. Ai, H. Yang, Y. Cao, A tin(ii) sulfide-carbon anode material based on combined conversion and alloying reactions for sodium-ion batteries, *J. Mater. Chem. A* 2 (2014) 16424-16428.

[88] X. Ma, X. Xiong, P. Zou, W. Liu, F. Wang, L. Liang, Y. Liu, C. Yuan, Z. Lin, General and Scalable Fabrication of Core-Shell Metal Sulfides@C Anchored on 3D N-Doped Foam toward Flexible Sodium Ion Batteries, 15 (2019) 1903259.

[89] C. Zhu, P. Kopold, W. Li, P.A. van Aken, J. Maier, Y. Yu, A General Strategy to Fabricate Carbon-Coated 3D Porous Interconnected Metal Sulfides: Case Study of SnS/C Nanocomposite for High-Performance Lithium and Sodium Ion Batteries, 2 (2015) 1500200.

[90] S.J. Peng, X.P. Han, L.L. Li, Z.Q. Zhu, F.Y. Cheng, M. Srinivansan, S. Adams, S. Ramakrishna, Unique Cobalt Sulfide/Reduced Graphene Oxide Composite as an Anode for Sodium-Ion Batteries with Superior Rate Capability and Long Cycling Stability, *Small* 12 (2016) 1359-1368.

[91] H. Ye, L. Wang, S. Deng, X. Zeng, K. Nie, P.N. Duchesne, B. Wang, S. Liu, J. Zhou, F. Zhao, N. Han, P. Zhang, J. Zhong, X. Sun, Y. Li, Y. Li, J. Lu, Amorphous MoS₃ Infiltrated with Carbon Nanotubes as an Advanced Anode Material of Sodium-Ion Batteries with Large Gravimetric, Areal, and Volumetric Capacities, 7 (2017) 1601602.

[92] Q. Wang, W. Zhang, C. Guo, Y. Liu, C. Wang, Z. Guo, In Situ Construction of 3D

Interconnected FeS@Fe₃C@Graphitic Carbon Networks for High-Performance Sodium-Ion Batteries, *Adv. Funct. Mater.* 27 (2017) 1703390.

[93] Y. Liu, Y. Yang, X. Wang, Y. Dong, Y. Tang, Z. Yu, Z. Zhao, J. Qiu, Flexible Paper-like Free-Standing Electrodes by Anchoring Ultrafine SnS₂ Nanocrystals on Graphene Nanoribbons for High-Performance Sodium Ion Batteries, *ACS Appl. Mater. Interfaces* 9 (2017) 15484-15491.

[94] Y. Lu, N. Zhang, S. Jiang, Y. Zhang, M. Zhou, Z. Tao, L.A. Archer, J. Chen, High-Capacity and Ultrafast Na-Ion Storage of a Self-Supported 3D Porous Antimony Persulfide–Graphene Foam Architecture, *Nano Lett.* 17 (2017) 3668-3674.

[95] Z.L. Chen, R.B. Wu, M. Liu, H. Wang, H.B. Xu, Y.H. Guo, Y. Song, F. Fang, X.B. Yu, D.L. Sun, General Synthesis of Dual Carbon-Confined Metal Sulfides Quantum Dots Toward High-Performance Anodes for Sodium-Ion Batteries, *Adv. Funct. Mater.* 27 (2017).

[96] X. Wei, X. Wang, X. Tan, Q. An, L. Mai, Nanostructured Conversion-Type Negative Electrode Materials for Low-Cost and High-Performance Sodium-Ion Batteries, *Adv. Funct. Mater.* 28 (2018) 1804458.

[97] P.G. Bruce, B. Scrosati, J.-M. Tarascon, Nanomaterials for Rechargeable Lithium Batteries, *Angew. Chem. Int. Edit.* 47 (2008) 2930-2946.

[98] Y. Zheng, T. Zhou, C. Zhang, J. Mao, H. Liu, Z. Guo, Boosted Charge Transfer in SnS/SnO₂ Heterostructures: Toward High Rate Capability for Sodium-Ion Batteries, *Angew. Chem. Int. Edit.* 55 (2016) 3408-3413.

[99] X. Xiang, K. Zhang, J. Chen, Recent Advances and Prospects of Cathode Materials for Sodium-Ion Batteries, *Adv. Mater.* 27 (2015) 5343-5364.

[100] C. Zhang, F. Han, F. Wang, Q. Liu, D. Zhou, F. Zhang, S. Xu, C. Fan, X. Li, J. Liu, Improving compactness and reaction kinetics of MoS₂@C anodes by introducing Fe₉S₁₀ core for superior volumetric sodium/potassium storage, *Energy Storage Mater.* 24 (2020) 208-219.

[101] L. Cao, X.H. Liang, X. Ou, X.F. Yang, Y.Z. Li, C.H. Yang, Z. Lin, M.L. Liu, Heterointerface Engineering of Hierarchical Bi₂S₃/MoS₂ with Self-Generated Rich Phase Boundaries for Superior Sodium Storage Performance, *Adv. Funct. Mater.* 30

(2020).

[102] D. Su, K. Kretschmer, G. Wang, Improved Electrochemical Performance of Na-Ion Batteries in Ether-Based Electrolytes: A Case Study of ZnS Nanospheres, *Adv. Energy Mater.* 6 (2016) 1501785.

[103] Z. Hu, Z. Zhu, F. Cheng, K. Zhang, J. Wang, C. Chen, J. Chen, Pyrite FeS₂ for high-rate and long-life rechargeable sodium batteries, *Energy Environ. Sci.* 8 (2015) 1309-1316.

Chapter 2. Experimental

2.1 Reagents information

Table 2.1 Main chemical reagents for this research.

Reagents	Grade	Company
Sodium	99.9%	Sigma-Aldrich
Super P		MTI Corp.
Polyvinylidene Fluoride (PVDF)		MTI Corp.
1-Methyl-2-pyrrolidinone (NMP)		MTI Corp.
NaCF_3SO_3	98.0%	Sigma-Aldrich
Diglyme (DGM)	Anhydrous	Sigma-Aldrich
$\text{K}_3[\text{Co}(\text{CN})_6]$	$\geq 97\%$	Sigma-Aldrich
$\text{C}_6\text{H}_5\text{Na}_3\text{O}_7 \cdot 2\text{H}_2\text{O}$	$\geq 99.0\%$	Sigma-Aldrich
$\text{Na}_2\text{MoO}_4 \cdot 2\text{H}_2\text{O}$	$\geq 99.5\%$	Sigma-Aldrich
Deionized water	18.2 M Ω	Homemade
$\text{C}_2\text{H}_5\text{NS}$ (TAA)	99%	Wako
$\text{CoCl}_2 \cdot 6\text{H}_2\text{O}$	99%	Wako
$\text{CH}_4\text{N}_2\text{S}$	98%	Wako

2.2 Characterizations

2.2.1 X-ray diffractometer (XRD)

XRD analyzes the crystal structure of materials based on the principle of Bragg

diffraction, which can accurately characterize the phase of materials. Since the interplanar spacing of each crystal plane in a crystal material is close to the wavelength of X-rays, diffraction will occur when X-rays act on the crystal. With the change of the angle between the X-ray and the sample to be measured, the XRD pattern shows diffraction peaks with different intensities. The phase and structure information of the sample can be analyzed by comparing the XRD pattern with the PDF card. The structures and compositions of the as-prepared materials in this dissertation were determined with a Smartlab X-ray diffractometer (XRD, Japan) with CuK α ($\lambda = 1.5418$ Å) as the radiation source. Step scanning is adopted, and the scanning speed is 5°/min.

2.2.2 Raman spectra

Raman spectroscopy was discovered by Indian scientist C.V. Raman in 1928. It analyzes molecular vibration (rotation) information through Raman scattering, and then characterizes molecules and chemical bonds in samples. Raman spectra were collected with a Renishaw inVia Raman spectrometer using an excitation wavelength of 532 nm.

2.2.2 X-ray photoelectron spectrometer (XPS)

Based on the principle of the photoelectric effect, XPS uses X-rays to irradiate the sample to excite electrons at a specific energy level to form photoelectrons. According to the equation: $h\nu = E_b + E_c + W_s$, the energy $h\nu$ of X-ray photons is fixed, the kinetic energy E_c and work function W_s of the escaped photoelectrons can be measured, and the binding energy E_b of electrons at this energy level can be obtained. The elemental compositions and chemical valence states were analyzed by XPS (VG ESCALAB 250,

Thermo Electron, UK) using an Al K α X-ray source (1486 eV) in this dissertation.

2.2.3 Field-emission scanning electron microscopy (FE-SEM)

FE-SEM is a device for observing samples based on the principle of electrical signal imaging, that is when high-energy electron beams bombard the surface of the sample, signals such as secondary electrons and backscattered electrons will escape from the surface of the sample. Among them, the resolution of secondary electrons is high, which can well reflect the sample morphology in the scanning area. However, the backscattered electron signal becomes stronger with the increase of the atomic number of the sample, specifically manifested as brighter (larger average atomic number, stronger signal) and darker (lower average atomic number, weaker signal) regions. In this dissertation, morphology, and nanostructure were investigated the S-4800 FE-SEM of Hitachi, Japan.

2.2.4 Transmission electron microscope (TEM)

Similar to the principle of FE-SEM, TEM is also a device that uses electronic signal imaging to observe the morphology of materials. However, unlike SEM, the electron beam of TEM can penetrate the sample to reflect the structural information inside the sample. Furthermore, the sample can be characterized by selected area electron diffraction (SAED), thus analyzing the composition of the sample. Energy-dispersive X-ray spectroscopy (EDS or EDX) matched with TEM is used to analyze the elemental composition, distribution, and content of the micro-region of the material. A high-resolution transmission electron microscope (TEM, HRTEM, JEM-2100F, JEOL,

Japan) at 200 kV was used to investigate the morphology and nanostructure of the samples in this dissertation.

2.2.5 Inductively coupled plasma emission optical spectrometry (ICP-OES)

The ratio of metal elements in the samples of this dissertation was detected by inductively coupled plasma emission optical spectrometry (ICP-OES).

2.2.6 Brunauer-Emmett-Teller (BET)

Based on the BET equation, the nitrogen equilibrium adsorption amount can be calculated according to the pressure difference before and after the sample absorbs nitrogen, and then the specific surface area of the sample can be analyzed. In this dissertation, the nitrogen adsorption-desorption isotherm was obtained at 77.3 K on a Nova 4200 equipment (Quantachrome Inc., USA) after the sample was evacuated at 300 °C for 12 h.

2.3 Electrochemical measurements

Galvanostatic charge/discharge measurement, cycling stability test, rate performance test, and galvanostatic intermittent titration technique (GITT) were conducted on a battery testing system (LAND CT2001A model, Wuhan LAND Electronic., Ltd.) in a voltage range of 0.3-3 V. Cyclic voltammetry (CV) curve was obtained from an electrochemical workstation VersaSTAT 4. The electrochemical impedance spectrum (EIS) was determined on an electrochemical workstation (RST

5090F) in a frequency range of 0.01 Hz-100 kHz.

Chapter 3 Prussian Blue Analog Derived Cobalt Sulfide Nanoparticles Embedded in N/S Co-doped Carbon Frameworks as a High-Performance Anode Material for Sodium-ion Batteries

3.1 Introduction

To date, lithium-ion batteries (LIBs) have been widely used as the rechargeable energy source in various electric vehicles and portable electronic devices owing to their high energy densities and long-term cycle life. However, uneven distribution and limitation of lithium resources have led to increasing manufacturing costs of LIBs, which prompts researchers to explore new sustainable alternatives to replace them. Sodium-ion batteries (SIBs), which have features of similar energy storage mechanisms as LIBs with natural abundance in sodium resources, are considered to be the most suitable candidate [1-4]. Unfortunately, due to the limitation of the inherent characteristics of the sodium ion with a larger radius and heavier mass (ion radius: 1.02 Å, molar mass: 22.99 g/mol) than the lithium-ion (ion radius: 0.59 Å, molar mass: 6.94 g/mol), the typical graphite-based anode materials commonly used in LIBs are no longer suitable for SIBs [5, 6]. Therefore, it is a necessity to develop more effective anode materials to meet the practical application of SIBs.

Currently, carbon-, alloy-, metal sulfide- and metal oxide-based anode materials have been widely studied [7-17]. Among those reported anode materials, metal sulfides, especially transition metal sulfides (TMS), have attracted great attention owing to their high-power densities, abundant resources, and low cost. For example, cobalt sulfides (CoS_x) have highly theoretical capacities according to their conversion reaction mechanism (i.e., 589 mA h g⁻¹ for CoS; 872 mA h g⁻¹ for CoS₂; 702 mA h g⁻¹ for Co₃S₄ and 544 mA h g⁻¹ for Co₉S₈) [18-21]. Nonetheless, the single-component TMS always has poor electronic conductivity with pulverization problems aroused by the huge volume expansion/shrinkage during the repeated insertion/extraction of sodium ions

(Na⁺), which always results in poor cycling and rate performance.

Some effective strategies have been put forward to solve the above shortcomings, for instance, by using carbon-matrix materials, composite materials with multi-component, and metal atom-modified materials [22-27]. Especially, the combination of TMS and carbon materials could achieve satisfactory electrochemical performance. For example, Zhao et al. [26] prepared highly dispersed NiS₂ nanoparticles in carbon nanofiber-composed porous materials for the anode, which exhibited an excellent specific capacity (500 mA h g⁻¹ at 0.1 A g⁻¹) as well as stability (200 mA h g⁻¹ at 2 A g⁻¹ even after 1000 cycles). Zhang et al. [25] made ultrathin MoS₂ nanosheets growth on carbon nanotubes (CNTs) as anode material, which showed a specific capacity of 495.9 mAh g⁻¹ at 0.2 A g⁻¹ with a capacity retention of 84.8% after 80 cycles. Generally, carbon-matrix materials can build a highway for ion/electron transmission, which can effectively improve the kinetics of electrochemical reactions. Furthermore, it can effectively accommodate the volume changes in the charging/discharging process. This ultimately results in superior unfading capacity and high-rate performance.

While the incorporation of heteroatoms into carbon material can improve conductivity and provide more active sites for sodium storage [9, 24, 28, 29]. Liu et al. [30] prepared one-dimensional (1D) CoSe₂@nitrogen-doped carbon driven from the PBA with hierarchical microcube structure for SIBs, which exhibited excellent reversible capacity with a very long cycling lifespan even at a high rate of 2.0 A g⁻¹ (384.3 mAh g⁻¹ after 1800 cycles). Jiang et al. [31] synthesized nitrogen (N)-rich carbon coated Co₃S₄ nanocrystal (Co₃S₄@NC) driven from zeolitic imidazolate frameworks-67 (ZIF-67, a metal-organic framework (MOF)), which delivered a remarkable cycling performance with a specific capacity of 420.9 mAh g⁻¹ at 0.1 A g⁻¹ after 100 cycles. Herein, the PBA and ZIF-67 are mainly formed by inorganic metal ions and organic ligands, and their precursors usually form regular polyhedral morphologies by the co-precipitation method. Although the in-situ formation of N-doped carbon coating during the calcination process can effectively enhance the cycling performance of the batteries, the capacity performance is always much lower than the theoretical capacity of metal sulfide due to the sluggish ion transport kinetics caused by few defects inside the bulk

phase of the material.

In this work, the PBA precursor with $C\equiv N$ ligands was prepared in a hydrothermal way. Then, two kinds of cobalt-based sulfide nanoparticles (i.e., Co_3S_4 and Co_9S_8) embedded in N/S co-doped carbon frameworks with hierarchical tremella-like micro-flower structure were successfully obtained with the same precursor but using two different solid sulfidation processes. It is found that the obtained special structure enhanced the stability of cobalt-based sulfide particles, the abundant defects facilitated rapid charge transfer and improved the storage of sodium ions due to the enhanced electronegativity of the material. As a result, both anode materials exhibited higher capacities with longer stability when used as the anodes for SIBs. Especially, the optimum $Co_3S_4@C-N/S$ 1.8-based anode delivered a good performance for Na^+ storage and a high initial Coulombic efficiency (91.97% at 0.1 A g^{-1}) with long-term cycling stability (599.1 mA h g^{-1} even in the 600th cycle at 1 A g^{-1}). While the optimum $Co_9S_8@C-N/S$ 1.8-based anode also delivered a considerable initial Coulombic efficiency (86.1% at 0.1 A g^{-1}) and long-term cycling stability (391.9 mA h g^{-1} even in the 1200th cycle at 2 A g^{-1}).

3.2. Experimental

3.2.1 Synthesis precursor

$Co_3S_4@C-N/S$ was synthesized in two steps, namely, synthesis of precursor was firstly performed via a facile hydrothermal method and then a solid sulfurization process was carried out. Typically, a solution A was prepared by dissolving of X mmol ($X=0, 1.8, 3.6$) of TSC in 30 mL of deionized (DI) water, and a solution B was obtained by dissolving 2 mmol of $K_3[Co(CN)_6]$ in 30 mL of DI water. After stirring vigorously for 30 minutes, solution B was mixed with solution A and stirred for another 1 h until achieving a transparent solution. Subsequently, the above-mixed solution was put into a Teflon-lined stainless steel autoclave (100 mL) after sonicating for 10 minutes, which was sealed and heated at $200\text{ }^\circ\text{C}$ for 16 h in an oven. The product collected by centrifugation was washed successively with ethanol and DI water several times, and

freeze-dried for 24 hours.

3.2.2 Synthesis of $\text{Co}_3\text{S}_4@\text{C-N/S}$

The obtained precursor product and $\text{C}_2\text{H}_5\text{NS}$ (TAA) powder with a mass ratio of 1:8 were put into two ceramic boats, respectively. Then, the ceramic boats were put into the tube furnace in turn and kept the argon (Ar) gas flowing continuously to replace the air in the tube. After the Ar gas was introduced for 30 minutes, the intake valve was closed and the vacuum pump was turned on at the same time. When the pressure in the tube reached a certain negative pressure value, the outlet valve and the vacuum pump were closed in turn. The tube furnace was heated to 500 °C at a heating rate of 5 °C/min and maintained at this temperature for 3 h. Finally, the black powder of $\text{Co}_3\text{S}_4@\text{C-N/S}$ can be obtained after cooling down to the ambient temperature. Hereafter, the products based on the precursors prepared with 0.0, 1.8, and 3.6 mmol of TSC were denoted as $\text{Co}_3\text{S}_4@\text{C-N/S X}$ ($X=0.0, 1.8, \text{ and } 3.6$).

3.2.3 Synthesis of $\text{Co}_3\text{S}_4@\text{C-N/S}$

Similar to the preparation of $\text{Co}_3\text{S}_4@\text{C-N/S}$, the obtained precursor in section 2.1 and sulfur (S) powder with a mass ratio of 1:8 were separately put into two ceramic boats. Subsequently, they were placed in a tube furnace, and the mixed gas of Ar/ H_2 (20/5 mL/min) was continuously passed through the tube, where the sulfur powder was placed at the upstream side and the precursor was placed at the downstream side. The samples were heated at 500 °C for 3 h in a tube furnace with a heating rate of 5 °C/min. As such, $\text{Co}_9\text{S}_8@\text{C-N/S}$ black powders were obtained. Hereafter, the products based on the precursors prepared with 0.0, 1.8, 3.6 mmol of TSC were denoted as $\text{Co}_9\text{S}_8@\text{C-N/S X}$ ($X=0.0, 1.8, \text{ and } 3.6$).

3.2.4 Materials characterization

Morphology and nanostructure were investigated by a field-emission scanning electron microscopy (FESEM, SU8010, Hitachi, Japan) and a high-resolution

transmission electron microscope (TEM, HRTEM, JEM-2100F, JEOL, Japan) at 200 kV, respectively. Distributions of Co, S, C, and N elements on the surface of the sample were characterized by an energy-dispersive spectroscopy (EDS) analysis instrument. The crystalline structure was analyzed by an X-ray diffractometer (XRD, Smartlab 9 kW, Rigaku, Japan) with CuK α ($\lambda = 1.5418 \text{ \AA}$) as the radiation source. Nitrogen adsorption-desorption isotherm was obtained at 77.3 K on a Nova 4200 equipment (Quantachrome Inc., USA) after the sample was evacuated at 300 °C for 12 h. The elemental compositions and chemical valence states were analyzed by an X-ray photoelectron spectrometer (XPS) (VG ESCALAB 250, Thermo Electron, UK) using an Al K α X-ray source (1486 eV).

3.2.5 Electrochemical measurements

The working electrode was fabricated by fully mixing 75 wt% of active material, 15 wt% of super P, and 10 wt% polyvinylidene fluoride (PVDF) with N-methyl pyrrolidone (NMP) to form a slurry at first. Then, the obtained slurry was coated on copper foil and dried in a vacuum oven at 80 °C overnight. Subsequently, the copper foil coated with the active material was cut into a piece with a diameter of 12 mm as the electrode. Herein, the loading amount of active material on the copper foil was around $1.0 \text{ mg}\cdot\text{cm}^{-2}$. In the two-electrode coin cell, sodium metal and glass fiber were used as the counter electrode and separator, respectively. A solution of 1 M sodium trifluoromethanesulfonate (NaSO_3CF_3) in diglyme (DGM) was used as the electrolyte. The battery was assembled with CR2032 coin-type cases in an argon-filled glove box. The galvanostatic charge/discharge curve, cycling performance, and rate performance of the as-prepared electrode were tested on a battery testing system (LAND CT2001A model, Wuhan LAND Electronic. Ltd) over a voltage range of 0.3-3 V. Cyclic voltammetry (CV, 0.3-3 V with a scan rate of 0.1 mV s^{-1}) and electrochemical impedance spectrum (EIS, frequency range of 0.01 Hz-100 kHz) were recorded on an electrochemical workstation.

3.3. Results and discussion

3.3.1 Characterization of $\text{Co}_3\text{S}_4@\text{C-N/S}$ and $\text{Co}_9\text{S}_8@\text{C-N/S}$

In the present synthesis, as shown in Fig. 3.1, two steps are involved to synthesize both $\text{Co}_3\text{S}_4@\text{C-N/S}$ and $\text{Co}_9\text{S}_8@\text{C-N/S}$. Specifically, the precursors are converted into $\text{Co}_3\text{S}_4@\text{C-N/S}$ and $\text{Co}_9\text{S}_8@\text{C-N/S}$ by the solid sulfidation at 500 °C using TAA and sulfur powder as sulfur sources, respectively. The morphologies of all samples show a tremella-like micro-flower structure assembled by nanosheets, which are composed of numerous Co_3S_4 or Co_9S_8 nanoparticles encapsulated by N/S co-doped amorphous carbon frameworks.

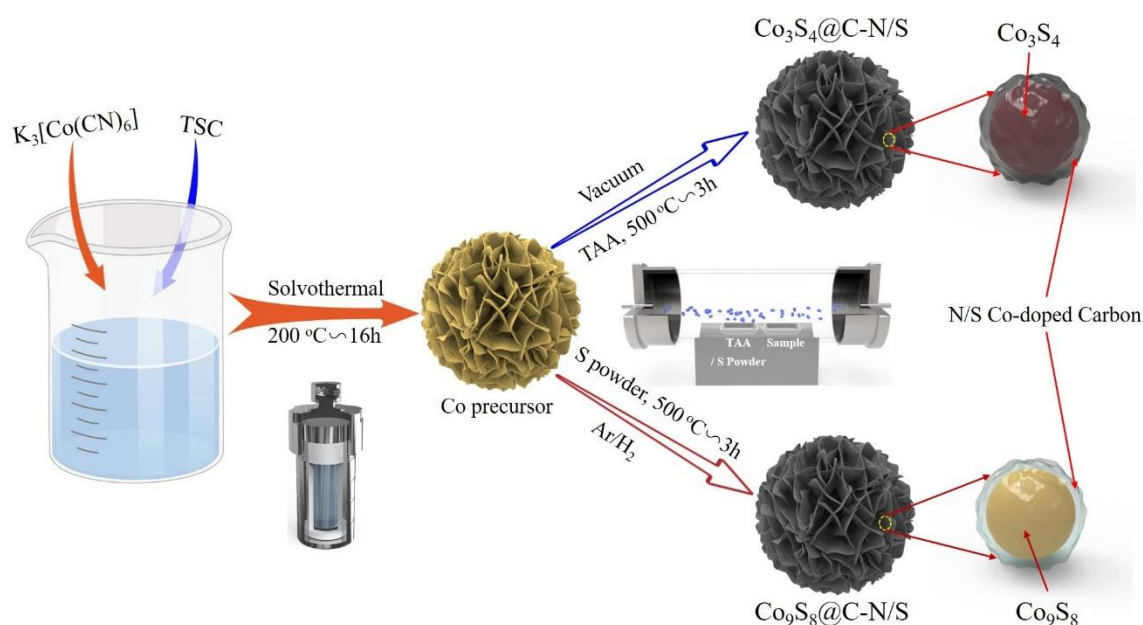


Figure 3.1 Schematically illustration of formations of $\text{Co}_3\text{S}_4@\text{C-N/S}$ and $\text{Co}_9\text{S}_8@\text{C-N/S}$ anode materials.

The precursors prepared with different contents of TSC (0.0, 1.8, 3.6 mmol) were analyzed by XRD patterns. As displayed in Figure 3.2, those peaks of precursor prepared without TSC (0.0 mmol) are much stronger and sharper than those precursors prepared with 1.8 and 3.6 mmol of TCS. Herein, the lower crystallinity of Co-precursors (TCS=1.8 and 3.6 mmol) indicates more amorphous phases on the surfaces of the samples. It is found that the main peaks are well corresponding to the diffraction

pattern of cobalt cyanide hydrate ($\text{Co}_3[\text{Co}(\text{CN})_6]_2 \cdot x\text{H}_2\text{O}$, JSPDS No. 22-0215), i.e., PBA.

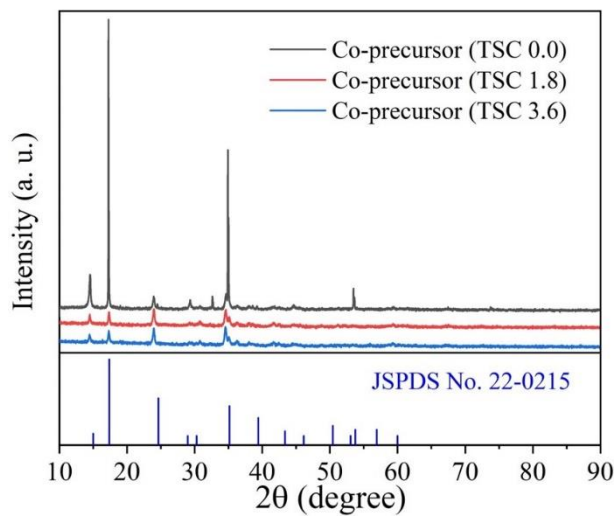


Figure 3.2 XRD patterns of as-prepared Co-precursors with different contents of TSC (0.0, 1.8, 3.6 mmol).

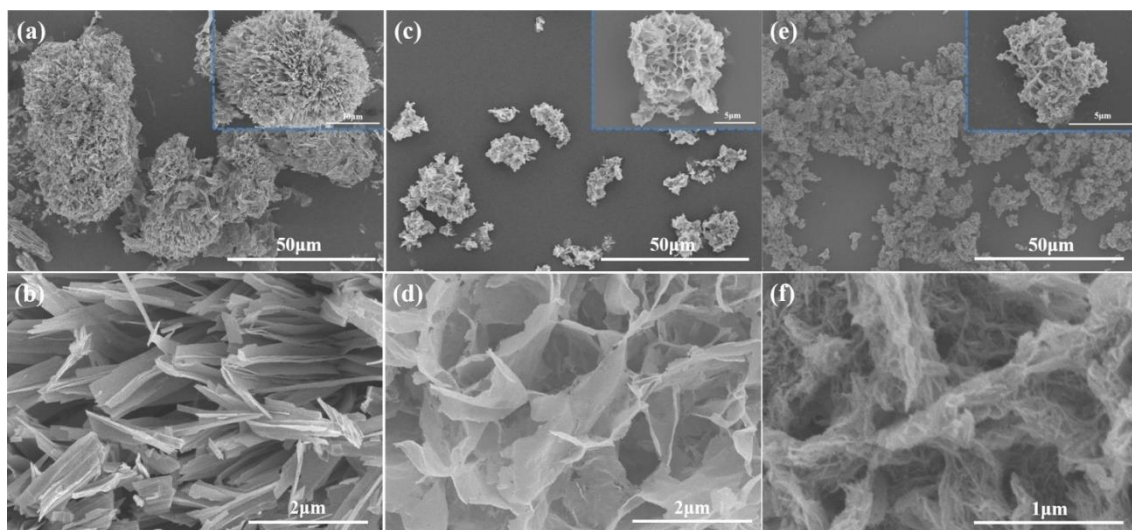


Figure 3.3 SEM images of $\text{Co}_3\text{S}_4@\text{C-N/S}$ composites prepared using the precursors with different contents of TSC (a-b) 0.0, (c-d) 1.8 and (e-f) 3.6 mmol.

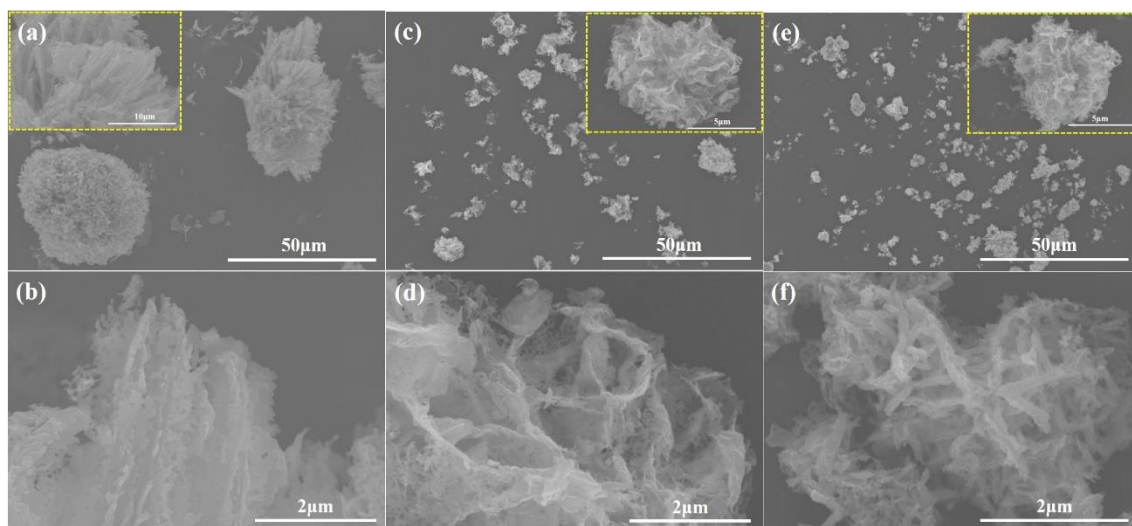


Figure 3.4 SEM images of $\text{Co}_9\text{S}_8@\text{C-N/S}$ composites with different contents of TSC (a-b) 0.0 mmol, (c-d) 1.8 mmol and (e-f) 3.6 mmol.

Figure 3.3 shows the morphologies of the as-prepared $\text{Co}_3\text{S}_4@\text{C-N/S}$ and $\text{Co}_9\text{S}_8@\text{C-N/S}$. It can be seen from Figures 3.3a-b that the sample prepared using the precursor without TSC ($\text{Co}_3\text{S}_4@\text{C-N/S}$ 0.0) has a particle size of 30-50 μm and exhibits a sea urchin-like structure assembled by independent nanobelts. In comparison, with the increase of TSC content to 1.8 mM ($\text{Co}_3\text{S}_4@\text{C-N/S}$ 1.8), as shown in Figure 3.3c-d, the nanosheets with a longitudinal length of 1-2 μm are interconnected to form a tremella-like micro-flower structure with particle sizes in the range of 5-15 μm . Further increasing of the TSC content to 3.6 mM, the sample ($\text{Co}_3\text{S}_4@\text{C-N/S}$ 3.6) still maintains a micro-flower structure, but agglomeration phenomenon occurs on each particle and nanosheet. It indicates that the TSC as an additive for material synthesis plays an important role in the formation of tremella-like micro-flower structure. Specifically, TSC could bridge those independent nanosheets to form a micro-flower morphology during the hydrothermal synthesis process, but the excessive addition of TSC can cause agglomeration. While, Figure 3.4 shows SEM images of $\text{Co}_9\text{S}_8@\text{C-N/S}$ with the precursors using different contents of TSC ($\text{Co}_9\text{S}_8@\text{C-N/S}$ 0.0, $\text{Co}_9\text{S}_8@\text{C-N/S}$ 1.8 and $\text{Co}_9\text{S}_8@\text{C-N/S}$ 3.6). One can see that the $\text{Co}_9\text{S}_8@\text{C-N/S}$ samples exhibit almost the same morphologies as those of $\text{Co}_3\text{S}_4@\text{C-N/S}$ samples, but with many pores on the nanosheets, which will be discussed in the following section.

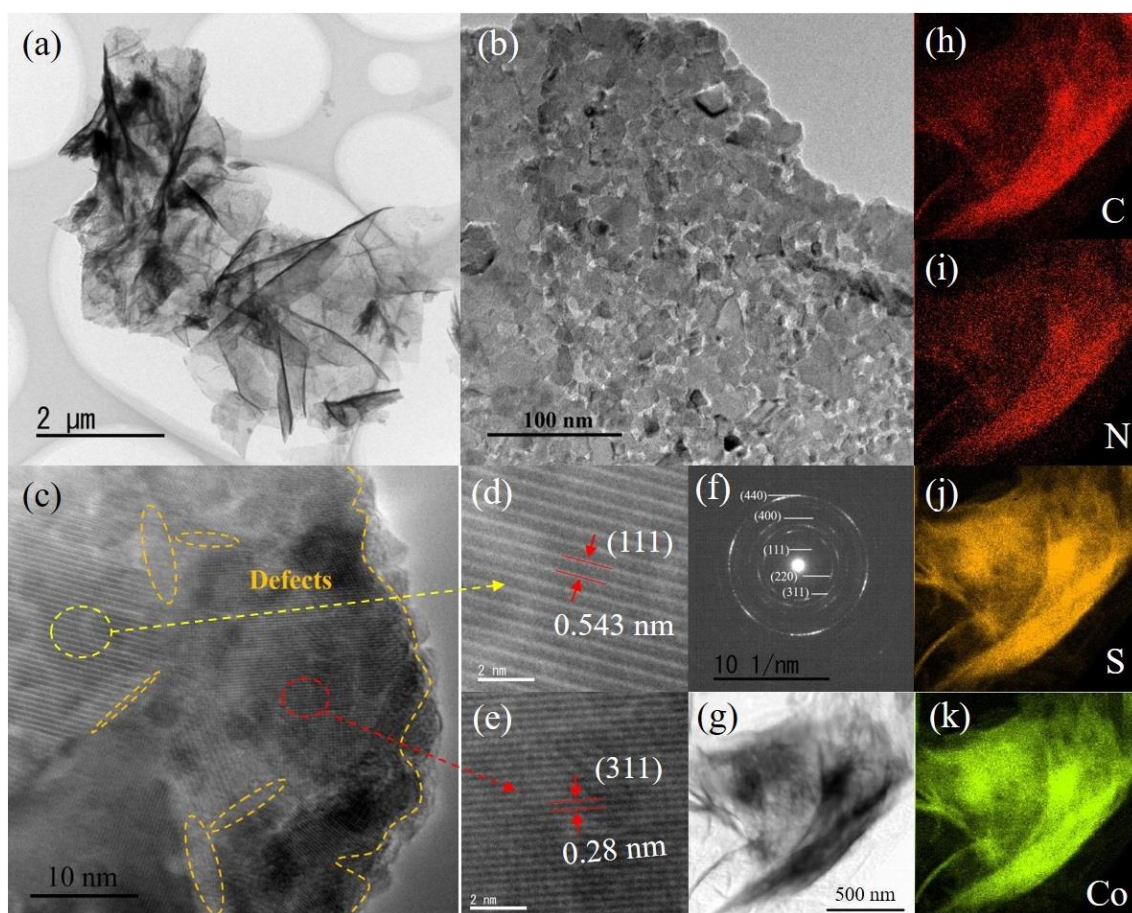


Figure 3.5 (a-b) TEM images, (c-e) HRTEM images, (f) SAED pattern and (g-k) EDX elemental mapping of $\text{Co}_3\text{S}_4@\text{C-N/S 1.8}$.

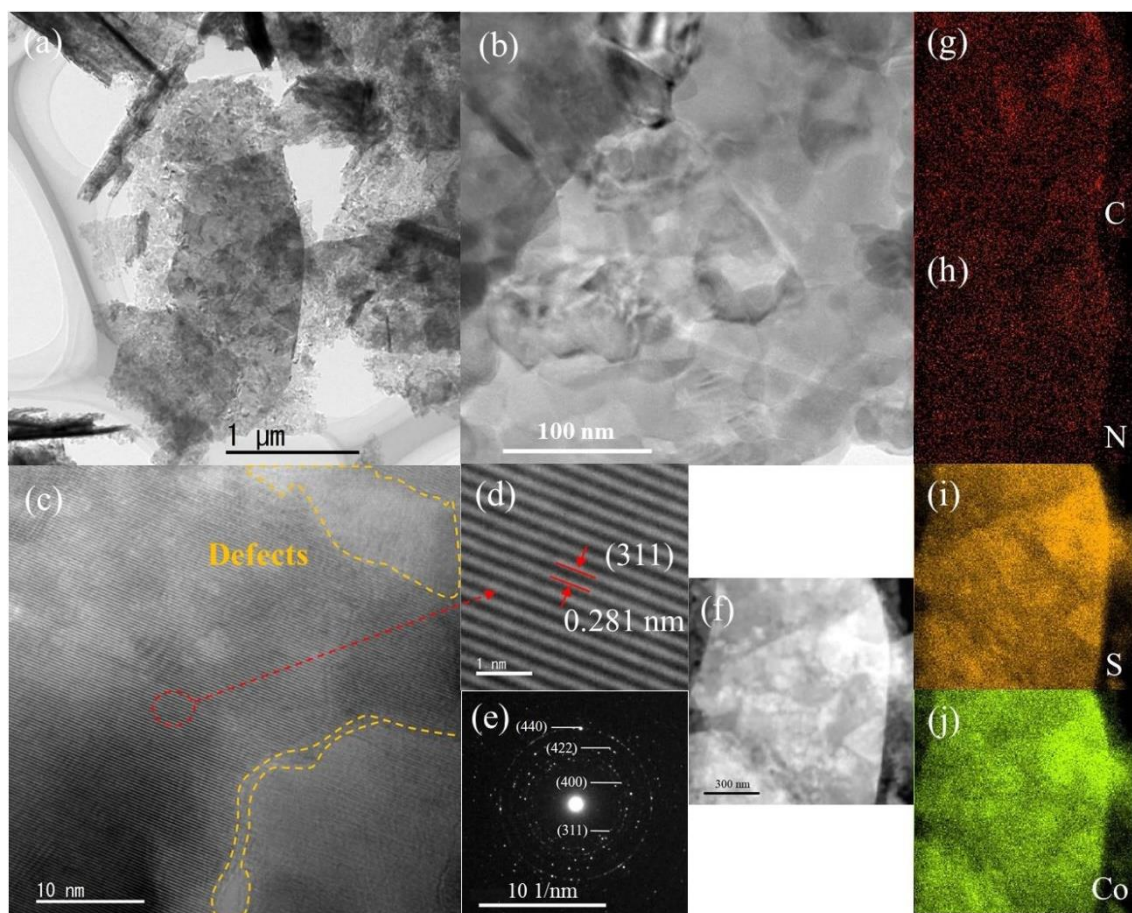


Figure 3.6 (a-b) TEM images, (c-d) HRTEM images, (e) SAED pattern and (f-j) EDX elemental mapping of $\text{Co}_3\text{S}_4@\text{C-N/S}$ 0.0.

To further analyze the nanostructure of $\text{Co}_3\text{S}_4@\text{C-N/S}$, TEM observation is performed. As shown in Figure 3.5a, as the SEM observation, low-magnification TEM morphology also displays that the ultra-thin nanosheets are interconnected and uniformly dispersed, where the nanosheets are composed of abundant nanoparticles (Figure 3.5b). The high-resolution TEM (HRTEM, Figure 3.5c) image displays that there are many defects in the periphery of nanosheets and between the nanoparticles, which should be derived from those amorphous carbons attached on the nanoparticle surface. A series of distinct lattice fringes (Figure 3.5 d, e) with a spacing of 0.28 and 0.543 nm correspond to the (311) and (111) planes of Co_3S_4 , respectively.[31, 32] While, the SAED exhibits a pattern of several concentric circles, indicating the polycrystalline characteristics of $\text{Co}_3\text{S}_4@\text{C-N/S}$ 1.8 (Figure 3.5f). EDX element mapping demonstrates the uniform distributions of C, N, S and Co on the nanosheets of $\text{Co}_3\text{S}_4@\text{C-N/S}$ 1.8

(Figure 3.5g-i). For comparison, the TEM images of $\text{Co}_3\text{S}_4@\text{C-N/S}$ 0.0 and 3.6 are shown in Figures 3.6 and 3.7, respectively. Notably, the HRTEM image of $\text{Co}_3\text{S}_4@\text{C-N/S}$ 0.0 is significantly different from those prepared with the precursors using TSC, which has a larger grain size and long-range ordered lattice fringes with fewer internal defects.

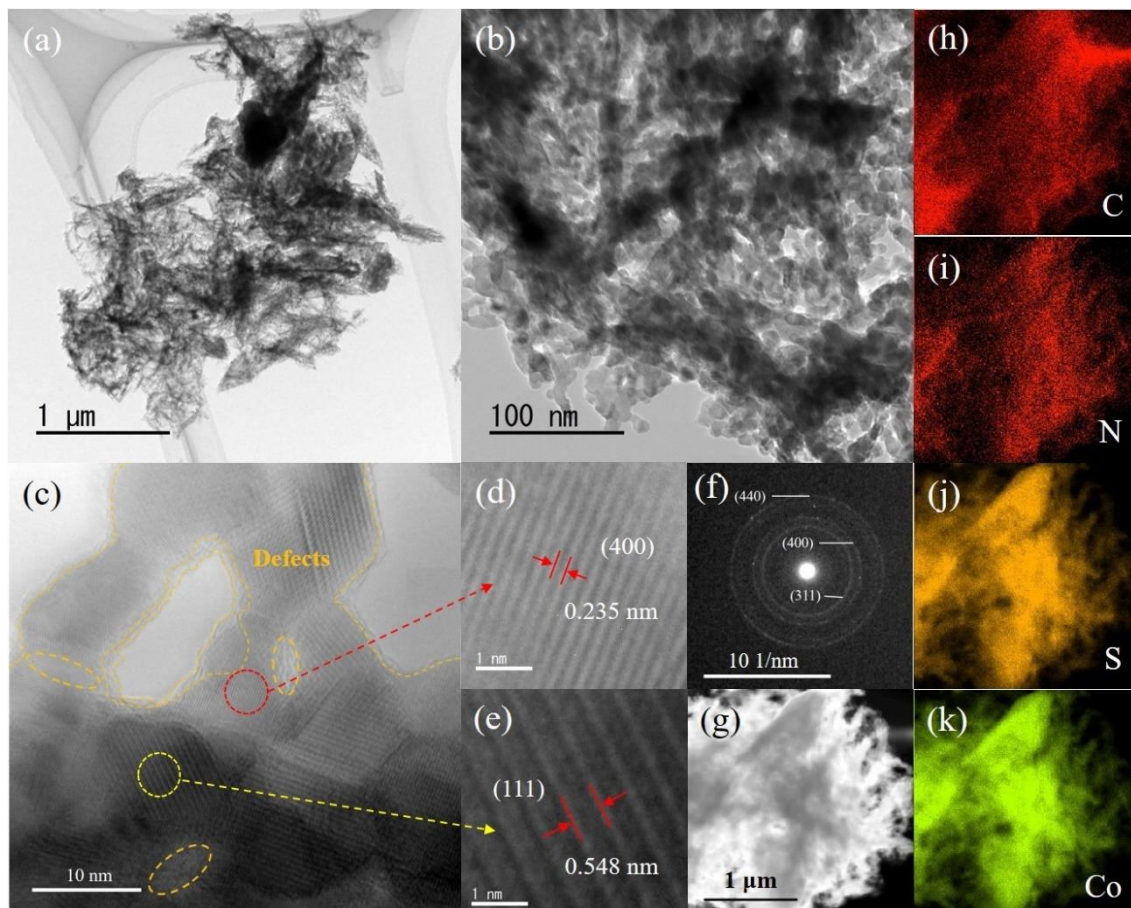


Figure 3.7 (a-b) TEM images, (c-e) HRTEM images, (f) SAED pattern and (g-k) EDX elemental mapping of $\text{Co}_3\text{S}_4@\text{C-N/S}$ 3.6.

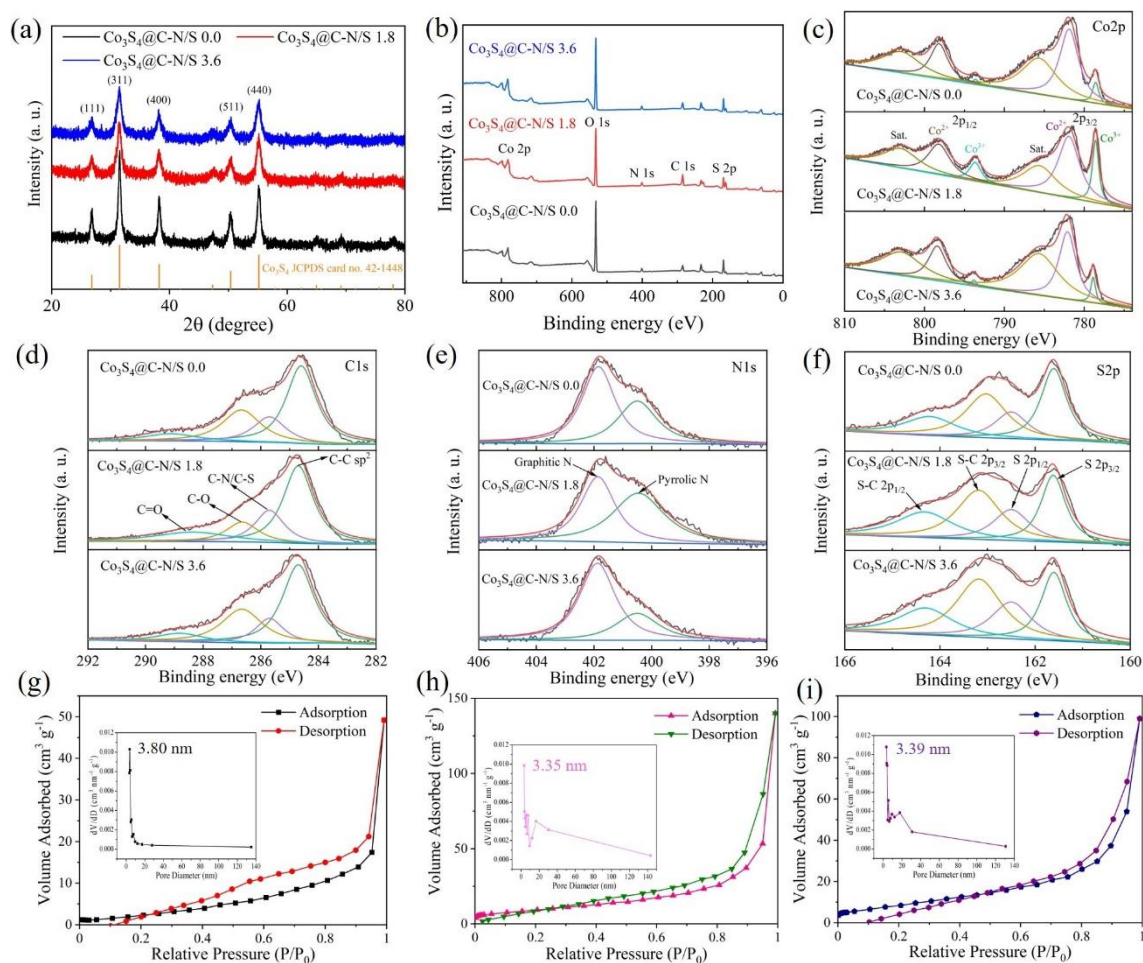


Figure 3.8 (a) XRD patterns of Co₃S₄@C-N/S 0.0, 1.8 and 3.6; (b) High-resolution XPS spectra of (c) Co 2p, (d) C 1s, (e) N 1s and (f) S 2p; BET curves of (g) Co₃S₄@C-N/S 0.0, (h) Co₃S₄@C-N/S 1.8 and (i) Co₃S₄@C-N/S 3.6.

As shown in Figure 3.8a, XRD peaks of Co₃S₄@C-N/S are well corresponding to those in the diffraction pattern of Co₃S₄ (JCPDS Card No. 42-1448). The main peaks located at 26.8, 31.5, 38.2, 50.4, and 55.2° are ascribed to (220), (311), (400), (511), and (440) planes of Co₃S₄, which reveals that Co precursors have been completely transformed into Co₃S₄ without the formation of impurity. Since N/S co-doped carbon frameworks are amorphous, no diffraction peak indexed to it is found.[33] In addition, the diffraction peaks gradually become weaker with the increase of TSC content in the precursors for the preparation of Co₃S₄@C-N/S (0.0, 1.8, 3.6), which is also consistent with the XRD patterns of the precursors. The decrease in crystallinity of Co₃S₄@C-N/S with more TSC in the precursor may be related to the increase of amorphous carbon

content in the sample. While, Figure 3.9a shows the XRD peaks of $\text{Co}_9\text{S}_8@\text{C-N/S}$ samples, in which the main peaks located at 14.5° , 29.8° , 47.6° , and 52.1° are ascribed to (111), (311), (511) and (440) planes of Co_9S_8 (JCPDS Card No. 86-2273) without the formation of impurity phases.

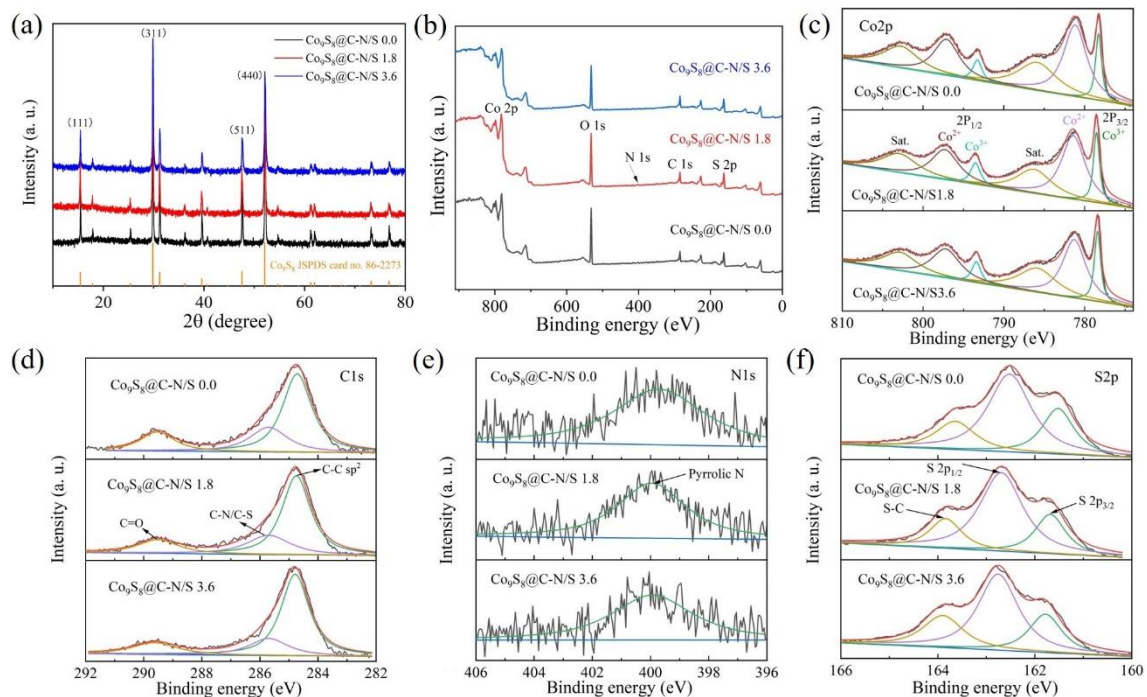


Figure 3.9 (a) XRD patterns of $\text{Co}_9\text{S}_8@\text{C-N/S}$ (0.0, 1.8 and 3.6); (b) High-resolution XPS spectra of (c) Co 2p, (d) C 1s, (e) N 1s and (f) S 2p for $\text{Co}_9\text{S}_8@\text{C-N/S}$ 0.0, 1.8 and 3.6.

Figure 3.8b-f shows the XPS spectra of the $\text{Co}_3\text{S}_4@\text{C-N/S}$ composite. The full-survey-scan spectrum (Figure 3.8b) confirms the existence of Co, S, C, N, and O elements together. The high-resolution spectrum of Co 2p (Figure 3.8c) exhibits two predominant peaks ($\text{Co } 2p_{3/2}$ and $\text{Co } 2p_{1/2}$) with an energy separation of about ~ 15.2 eV, indicating the existence of Co^{2+} together with Co^{3+} . The pair peaks at 778.6 and 793.6 eV are related to Co^{3+} while the pair at 781.9 and 798.2 eV are assigned to Co^{2+} . [34-36] The two broad peaks centered at 785.6 and 802.9 eV are related to the shake-up satellite peaks of $\text{Co } 2p_{3/2}$ and $\text{Co } 2p_{1/2}$, separately. The binding energies of two pairs of Co 2p and two shake-up satellites are also consistent with the characteristic peaks of Co_3S_4 . [36] Figure 3.8d exhibits the high-resolution C 1s spectrum with four fitted peaks of C-C

(284.7 eV), C-N/C-S (285.7 eV), C-O (286.6 eV), and C=O (288.4 eV), respectively.[30, 37-39] Furthermore, there are two different peaks of the high-resolution XPS spectrum of N1s (Figure 3.8e), including pyrrolic N (400.5 eV) and graphitic N (401.9eV) that doped on the carbon matrix.[30, 39-41] It is well known that Pyrrolic N exists at the defective sites of carbon, which can enhance the electrochemical performance of the material due to the conjugation of lone electron pairs to the p-conjugated ring of Pyrrolic N.[42] While, graphitic N could substitute the carbon atom of the graphene structure, which can improve the conductivity of the sample because of the difference in electronegativity between C and N.[43] Both C 1s and N 1s XPS spectra indicate that N has been doped into the carbon matrix. The formation of these N-doped carbon frameworks should be attributed to the breakage of the triple bond of $C\equiv N$ in the precursor during the solid sulfidation at 500 °C. While, the high-resolution S 2p spectrum (Figure 3.8f) with three fitted peaks at 161.6, 162.5, 163.1, and 164.4 eV corresponding to Co-S $2p_{3/2}$, Co-S $2p_{1/2}$, S-C $2p_{3/2}$ and S-C $2p_{1/2}$ respectively is observed.[9, 39, 44, 45] The presence of the S-C peak can be attributed to the partial substitution of N in C-N by S and/or the insertion of S in the amorphous carbon during the solid sulfidation process. Herein, N/S co-doping carbon frameworks could introduce more active sites and abundant defects, which can enhance the interaction between carbon and Na^+ due to the increased electronegativity, beneficial to store more Na^+ ions by adsorption.[30, 46, 47] What's more, N/S co-doping carbon on the surface of the active material plays a key role in maintaining the structural stability of the electrode material. It serves as both protective layer and a buffer layer, which can adapt to the strain related to the volume change during the charge/discharge process. The XPS spectra of the $Co_9S_8@C-N/S$ composite are shown in Figure 3.9b-f with the similar C1s, Co2p, and S2p XPS spectra as those of $Co_3S_4@C-N/S$ with little difference in peak band energies. However, as shown in Figure 3.9e, only one small peak centered at 399.9 eV in the N1s XPS spectrum is ascribed to pyrrolic N, indicating that a small amount of N doped carbons remain in the $Co_9S_8@C-N/S$ composite. The reduction of N-doped carbon content may be attributed to the reaction of $C\equiv N$ in the precursor with excessive H_2 to generate NH_3 and CH_4 during the solid sulfidation process, which is also the main

reason for the formation of many pores on the nanosheets after the solid sulfidation process.

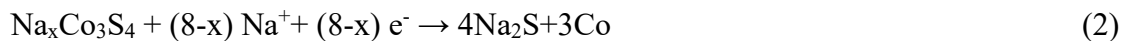
Figure 3.8g-i shows the specific surface areas and pore size distributions of $\text{Co}_3\text{S}_4@\text{C-N/S}$ samples. One can see that all curves exhibit a typical type-IV isothermal mode with a representative H3 hysteresis loop, which indicates that all these $\text{Co}_3\text{S}_4@\text{C-N/S}$ composites possess rich mesopores.[33, 39] While, the pore size distributions mainly locate at 3.80, 3.35, and 3.39 nm for the $\text{Co}_3\text{S}_4@\text{C-N/S}$ 0.0, 1.8, and 3.6, respectively. The Brunauer-Emmett-Teller (BET) specific surface areas of the $\text{Co}_3\text{S}_4@\text{C-N/S}$ 0.0, $\text{Co}_3\text{S}_4@\text{C-N/S}$ 1.8, and $\text{Co}_3\text{S}_4@\text{C-N/S}$ 3.6 are 10.3, 34.5 and 32.9 $\text{m}^2 \text{g}^{-1}$, respectively. It is well known that the large specific surface area can provide a more effective contact area between electrode and electrolyte with additional space for reducing the volume change during the insertion/desertion of Na^+ . In addition, the mesoporous structure could effectively shorten the Na^+ /electron diffusion distance, making it easier for the transferring of ions/electrons between active materials. Based on the above structural and compositional analysis results, it is expected that the $\text{Co}_3\text{S}_4@\text{C-N/S}$ 1.8 should exhibit excellent sodium ion storage performance.

3.3.2 Electrochemical performance

Figure 3.10a displays CV curves of $\text{Co}_3\text{S}_4@\text{C-N/S}$ 1.8-based anode at a scan rate of 0.1 mV s^{-1} in the potential window of 0.3-3 V (VS Na^+/Na). In the first cathodic sweep, the peak that appeared at 1.0 V could be assigned to Na^+ insertion into Co_3S_4 to form $\text{Na}_x\text{Co}_3\text{S}_4$, which results in a shift of 1.35 V in the subsequent cycle.[31, 48, 49] While, the sharp peak centered at 0.72 V should be attributed to the generation of a solid electrolyte interphase (SEI) layer with the conversion process, which divided into two peaks at 0.55 and 0.95 V in the following two cycles.[48] During the anodic process, the peaks located at 1.73 and 2.0 V represent the above reversible reactions. Notably, the later CV curves of $\text{Co}_3\text{S}_4@\text{C-N/S}$ 1.8 are almost overlapped after the first cycle, indicating the high reversibility of $\text{Co}_3\text{S}_4@\text{C-N/S}$ 1.8 composite during the cycling. In comparison, the CV curves of the $\text{Co}_3\text{S}_4@\text{C-N/S}$ 0.0 and $\text{Co}_3\text{S}_4@\text{C-N/S}$ 3.6-based

anodes are also shown in Figure 3.11. Herein, the corresponding electrochemical reactions can be described by the following equations:

Discharging process:



Charging process:

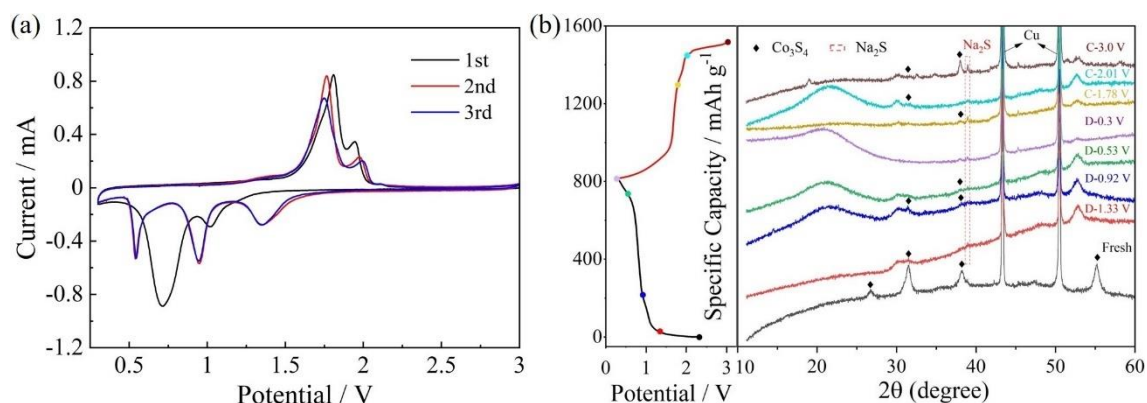
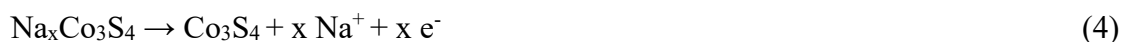
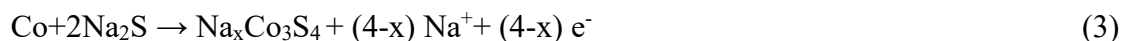


Figure 3.10 (a) CV curves of $\text{Co}_3\text{S}_4@\text{C-N/S}$ 1.8 based anode at a scan rate of 0.1 mV s^{-1} in the potential window of 0.3-3V; (b) Ex-situ XRD patterns of $\text{Co}_3\text{S}_4@\text{C-N/S}$ 1.8 at different charge/discharge states.

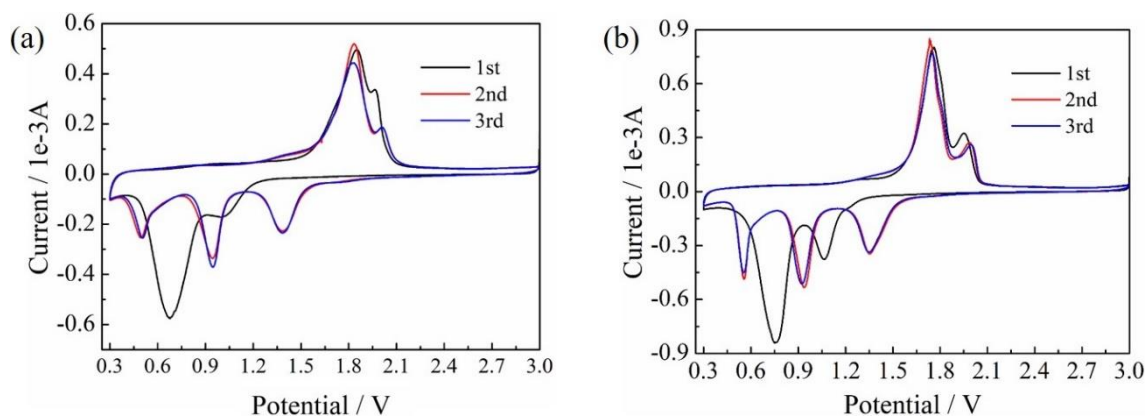


Figure 3.11 CV curves of (a) $\text{Co}_3\text{S}_4@\text{C-N/S}$ 0.0 and (b) $\text{Co}_3\text{S}_4@\text{C-N/S}$ 3.6 based anodes at a scan rate of 0.1 mV s^{-1} in the potential window of 0.3-3 V.

To further investigate the sodium-ion storage mechanism, ex-situ XRD

measurements are carried out for the $\text{Co}_3\text{S}_4@\text{C-N/S}$ 1.8-based anode at different charge/discharge (C/D) states. Figure 3.10 b shows the XRD patterns of fresh $\text{Co}_3\text{S}_4@\text{C-N/S}$ 1.8 based anode and the anode at different states of D-1.33 V, D-0.92 V, D-0.53 V, D-0.3 V, C-1.78 V, C-2.01 V, and C-3.0 V. For the fresh one, the Co_3S_4 phase can be clearly observed in the XRD pattern. The peak intensity of Co_3S_4 is significantly weakened during the subsequent charge/discharge process. When the battery is discharged to voltage levels of 1.33 and 0.92 V, a diffraction peak concentrated at 39.01° attributed to the (220) crystal plane of Na_2S phase (JSPDS Card No.77-2149) can be observed. This transition agrees with the reactions relating to the conversion from the Co_3S_4 phase to Na_2S and Co phases during the discharge process. After further discharging to 0.53 and 0.3 V, the peaks of the Co_3S_4 phase are weakened or even disappear, but the peaks corresponding to Na_2S phases are significantly enhanced, indicating that Na_2S phases should be one of the final products of discharge. Conversely, the peak intensity of Co_3S_4 is gradually increased during the battery charging process, indicating the high reversibility of the sodiation/desodiation processes of Co_3S_4 in the $\text{Co}_3\text{S}_4@\text{C-N/S}$ 1.8-based anode.

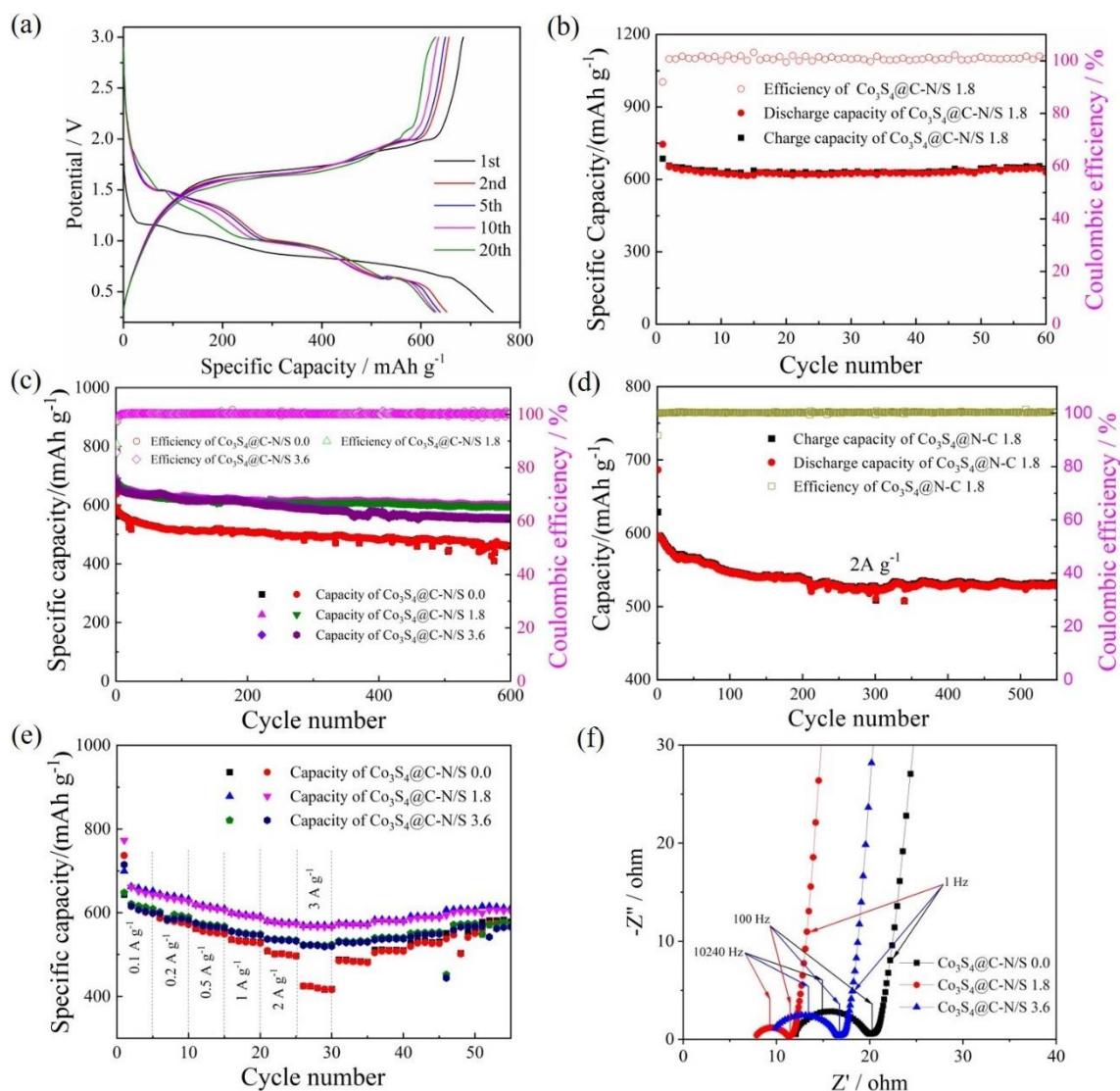


Figure 3.12 (a) Typical galvanostatic charge/discharge profiles of $\text{Co}_3\text{S}_4@\text{C-N/S} 1.8$ based anode at 0.1 A g^{-1} at different cycles (1st, 2nd, 5th, 10th and 20th); Cycling performance of $\text{Co}_3\text{S}_4@\text{C-N/S} 1.8$ based anode at current densities of (b) 0.1 A g^{-1} and (d) 2 A g^{-1} ; (c) Cycling performances of $\text{Co}_3\text{S}_4@\text{C-N/S}$ 0.0, 1.8 and 3.6 based anodes at a current density of 1 A g^{-1} ; (e) Rate performances and (f) Nyquist plots of $\text{Co}_3\text{S}_4@\text{C-N/S}$ 0.0, 1.8 and 3.6 based anodes.

The galvanostatic charge/discharge profiles of $\text{Co}_3\text{S}_4@\text{C-N/S}$ based anodes are investigated at a current density of 0.1 A g^{-1} in a voltage range of 0.3-3V also for different cycles (1st, 2nd, 5th, 10th, and 20th). As displayed in Figure 3.12a, the initial discharge/charge capacities of $\text{Co}_3\text{S}_4@\text{C-N/S} 1.8$ based anode are $745.2/685.3 \text{ mA h g}^{-1}$, corresponding to a high initial Coulombic efficiency (CE) of 91.97%. The capacity

reduction in the first cycle should be ascribed to the generation of SEI film.[50] It is well known that larger specific surface area could result in the formation of more SEIs with a lower initial CE. Co₃S₄@C-N/S 1.8 exhibits a high initial CE. It may be related to the existence of surface amorphous N/S co-doped carbon, which can prevent the side reaction between the electrode/electrolyte interface and reduce the effective contact area between the active material and electrolyte.[51, 52] Subsequently, the discharge/charge capacities of 656.6/651.9 mA h g⁻¹ are obtained in the second cycle with a CE of about 100%. While, the discharge capacity gradually decreased to 645.3, 632.3, and 629.2 mA h g⁻¹ in the following cycles of the 5th, 10th, and 20th, respectively. However, it can be gradually recovered to the discharge capacity of 653.5 mA h g⁻¹ in the 60th cycle, which is displayed in Figure 3.12b on cycling performance at 0.1 A g⁻¹. For comparison, as shown in Figure 3.13 a and b, the initial CEs of 84.9% (729.5/619.6 mA h g⁻¹) and 83.8% (776.7/651 mA h g⁻¹) are achieved for the Co₃S₄@C-N/S 0.0 and 3.6, respectively, which are lower than that of Co₃S₄@C-N/S 1.8. While the galvanostatic charge/discharge profiles of Co₉S₈@C-N/S-based anodes are also studied. As shown in Figures 3.14a and 3.13c-d, the Co₉S₈@C-N/S 0.0-, 1.8-, and 3.6-based anodes exhibit the initial discharge/charge capacities of 606.7/501.4, 626.7/539.4 and 613.6/501.4 mA h g⁻¹, relating to the initial CEs of 82.6%, 86.1%, and 81.7%, respectively. The initial CE of the Co₉S₈@C-N/S-based electrode is lower than that of the Co₃S₄@C-N/S-based electrode under the same preparation condition of precursor, which can be attributed to only a small amount of N/S co-doped carbon remaining on the surface of the Co₉S₈@C-N/S based electrode according to the N1s XPS. Furthermore, since the effective contact area between the active material of the Co₉S₈@C-N/S-based electrode and electrolyte is larger than that of the Co₃S₄@C-N/S-based electrode and the electrolyte, more SEI and lower initial CE on Co₉S₈@C-N/S-based electrode can be obtained.

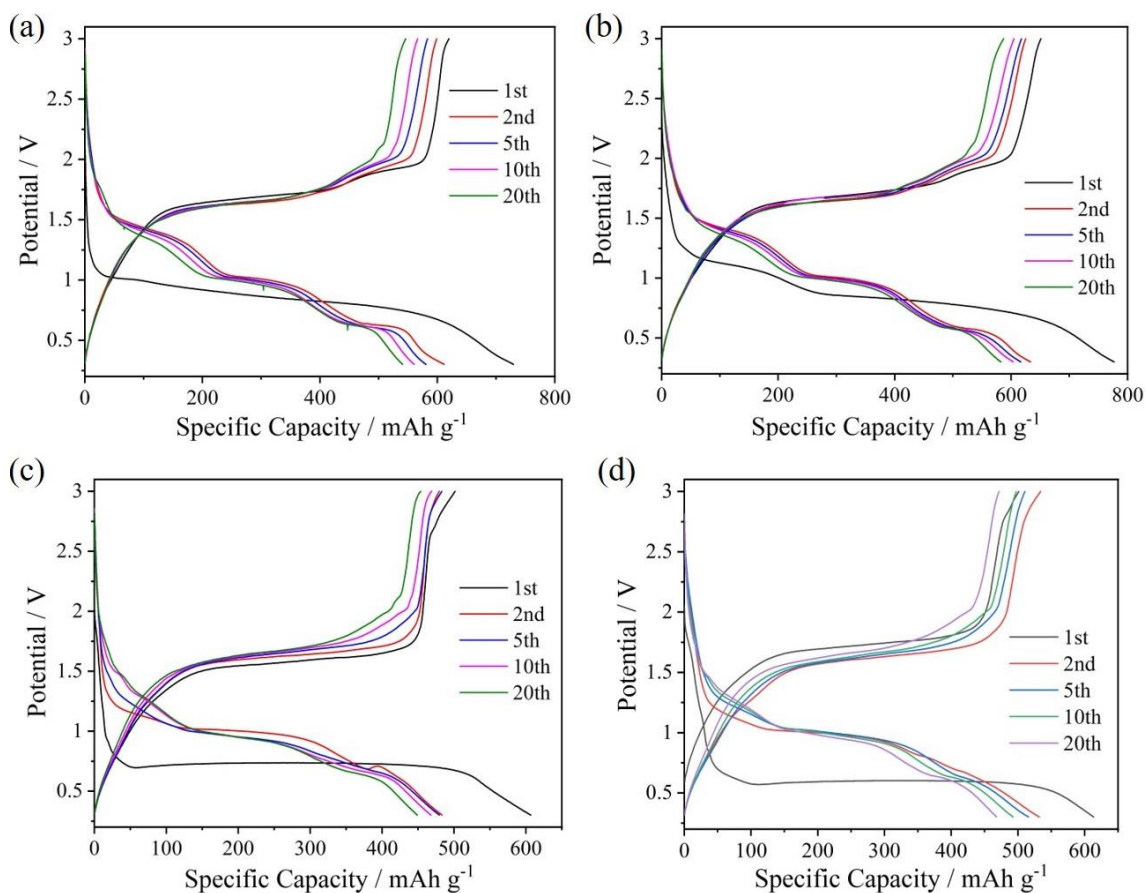


Figure 3.13 Typical galvanostatic charge/discharge profiles of (a) $\text{Co}_3\text{S}_4@\text{C-N/S}$ 0.0, (b) $\text{Co}_3\text{S}_4@\text{C-N/S}$ 3.6, (c) $\text{Co}_9\text{S}_8@\text{C-N/S}$ 0.0 and (d) $\text{Co}_9\text{S}_8@\text{C-N/S}$ 3.6 based anodes at a current density of 0.1 A g^{-1} for different cycles (1st, 2nd, 5th, 10th and 20th).

The long-term cycling performances of $\text{Co}_3\text{S}_4@\text{C-N/S}$ and $\text{Co}_9\text{S}_8@\text{C-N/S}$ based anodes are further investigated at 1 A g^{-1} with a cutoff voltage range of 0.3-3 V. As shown in Figure 3.12c, the $\text{Co}_3\text{S}_4@\text{C-N/S}$ 1.8 based anode exhibits a higher specific capacity with better cycling stability than others, which could be attributed to its robust framework, larger specific surface area with abundant internal defects. It should be noted that the $\text{Co}_3\text{S}_4@\text{C-N/S}$ 1.8-based anode delivers a high reversible charge capacity of $599.1 \text{ mA h g}^{-1}$ in the 600th cycle with a CE of $\sim 100\%$, relating to a capacity retention rate of 89.4% from the 2nd-cycle charge capacity. However, only 459.7 and 552.7 mA h g^{-1} can be obtained for the $\text{Co}_3\text{S}_4@\text{C-N/S}$ 0.0- and 3.6-based anodes after 600 cycles, respectively. Figure 3.12d manifests the long-term cycling performance of the $\text{Co}_3\text{S}_4@\text{C-N/S}$ 1.8-based anode at 2 A g^{-1} , which still maintains a considerable specific

capacity of 529 mA h g⁻¹ after 550 cycles. Figure 3.14b shows the cycle performance of Co₉S₈@C-N/S based anode at 1 A g⁻¹. While, the Co₉S₈@C-N/S 1.8-based anode delivers a reversible charge capacity of 431.9 mA h g⁻¹ in the 400th cycle with a capacity retention rate of 83.4% from the second-cycle charge capacity, which is also a higher than those of Co₉S₈@C-N/S 0.0 (413.7 mA h g⁻¹ / 82.7%), and Co₉S₈@C-N/S 3.6 (399.3 mA h g⁻¹ / 81.9%) based anodes. In addition, as shown in Figure 3.14c, the Co₉S₈@C-N/S 1.8-based anode also maintains a considerable capacity of 391.9 mA h g⁻¹ even at 2 A g⁻¹ after 1200 cycles with a capacity retention of 78.1%. Such a huge capacity difference between Co₃S₄@C-N/S and Co₉S₈@C-N/S based anodes should be related to not only the phase composition of the material (the huge difference in theoretical capacities of Co₃S₄ and Co₉S₈) but also the amount of N/S co-doped carbon attached on the surface of cobalt sulfide. As shown in Table 3.1, the Co₃S₄@C-N/S 1.8- and Co₉S₈@C-N/S 1.8-based anodes exhibit superior cycling performance when compared to those reported other Co₃S₄- and Co₉S₈-based anode materials previously.[28, 31, 33, 49, 53-56]

Table 3.1 Comparison of electrochemical performances of Co₃S₄-based and Co₉S₈-based anodes for Na-ion batteries.

Anode	Electrolyte	Voltage range V	Current density A g ⁻¹	Specific capacity mAh g ⁻¹	Cycle number	Reference
Co ₃ S ₄ - PNS/GS	1 M NaClO ₄ in EC/DEC and FEC	0.005-3	0.5	329	50	28
CoO/Co ₃ S ₄ @ N-C	1 M NaPF ₆ in EC/PC and FEC	0.01-3	0.1 1	577.3 400	60 100	31
Co ₃ S ₄ /CNTs	1 M NaClO ₄ in EC/DMC and FEC	0.01-3	0.1 0.5	469.4 355.9	100 100	33

Co ₃ S ₄ @NC	1 M NaClO ₄ in PC and FEC	0.01-3	0.1	420.9	100	49
ZnS/Co ₃ S ₄	1 M NaClO ₄ in PC/EC and FEC	0.01-2.5	0.5 1	377.3 316.5	1000 1000	53
Co ₉ S ₈ @CHSs	1 M NaCF ₃ SO ₃ in diglyme	0.25-3	0.5 5	492 223	100 10000	54
Co ₉ S ₈ @C nanospheres	1 M NaPF ₆ in DEG/DME	0.01-3	0.5 5	405 305	100 1000	55
Co ₉ S ₈ @S-CF	1 M NaClO ₄ in PC/EC and FEC	0.01-3	0.1	373	1000	56
Co ₉ S ₈ @ C-N/S 1.8	1 M NaCF ₃ SO ₃ in diglyme	0.3-3	1 2	431.9 391.9	400 1200	This Work
Co ₃ S ₄ @ C-N/S 1.8	1 M NaCF ₃ SO ₃ in diglyme	0.3-3	0.1 1	651.9 599.1	60 600	This Work

PNS/GS: porous nanosheet/graphene sheet; CoO/Co₃S₄@N-C: CoO/Co₃S₄ nanoparticles embedded in N-doped carbon frameworks; CNTs: carbon nanotubes; Co₃S₄@NC: N-rich carbon coated Co₃S₄; Co₉S₈@S-CF: Co₉S₈ nanoclusters embedded in sulfur-doped carbon foam; EC: Ethylene carbonate; DEC: Diethyl carbonate; PC: Propylene carbonate; FEC: Fluoroethylene carbonate; DEG: Diethylene glycol; DME: Dimethyl ether.

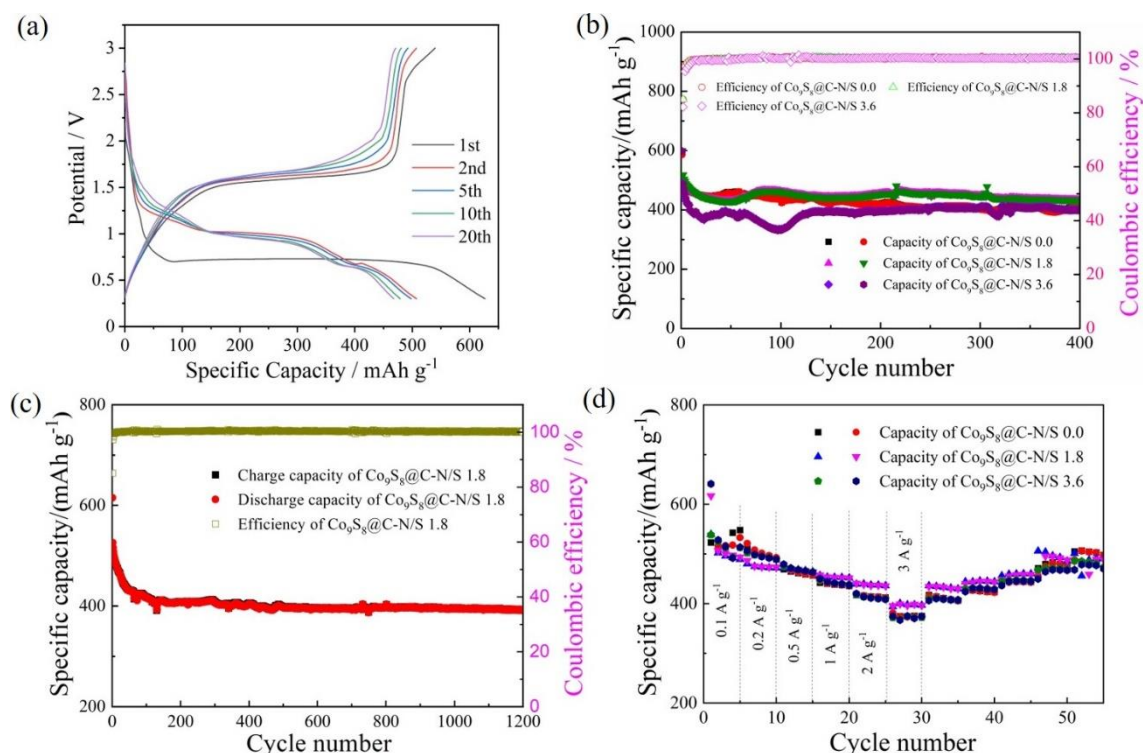


Figure 3.14 (a) Typical galvanostatic charge/discharge profiles of Co₉S₈@C-N/S 1.8 based anode at 0.1 A g⁻¹ for different cycles (1st, 2nd, 5th, 10th and 20th); (b) Cycling performance of Co₉S₈@C-N/S 0.0, 1.8 and 3.6 based anodes at 1 A g⁻¹; (c) Cycling performance of Co₉S₈@C-N/S 1.8 based anode at 2 A g⁻¹; (d) Rate performances of Co₉S₈@C-N/S 0.0, 1.8 and 3.6 based anodes.

The rate performances of as-prepared Co₃S₄@C-N/S-based anodes are depicted in Figure 3.12e. One can see that the Co₃S₄@C-N/S 1.8-based anode shows an excellent rate capacity, which delivers average discharge capacities of 642.8, 626.9, 606.8, 589, 573, and 568 mA h g⁻¹ with the increasing of current density from 0.1 to 0.2, 0.5, 1.0, 2.0 and 3.0 A g⁻¹, respectively. Notably, when the current density is returned to 0.1 A g⁻¹, the reversible capacity is recovered to 611.4 mA h g⁻¹. In contrast, the Co₃S₄@C-N/S 0.0- and 3.6-based anodes show poor rate performances, which only deliver reversible capacities of 416.5 and 519.7 mA h g⁻¹ at 3.0 A g⁻¹, respectively. Furthermore, as shown in Figure 3.14d, the Co₉S₈@C-N/S 1.8-based anode delivers average discharge capacities of 500.3, 474.1, 461.5, 452.8, 437.1, and 396.2 mA h g⁻¹ with the increasing of current density from 0.1 to 0.2, 0.5, 1.0, 2.0 and 3.0 A g⁻¹. While the reversible capacity of 481.7 mA h g⁻¹ is obtained when the current density is returned to 0.1 A g⁻¹.

¹. For comparison, the $\text{Co}_9\text{S}_8@\text{C-N/S-0.0}$ and $\text{Co}_9\text{S}_8@\text{C-N/S 3.6}$ -based anodes only deliver reversible capacities of 373.3 and 374.8 mA h g^{-1} at 3.0 A g^{-1} , respectively.

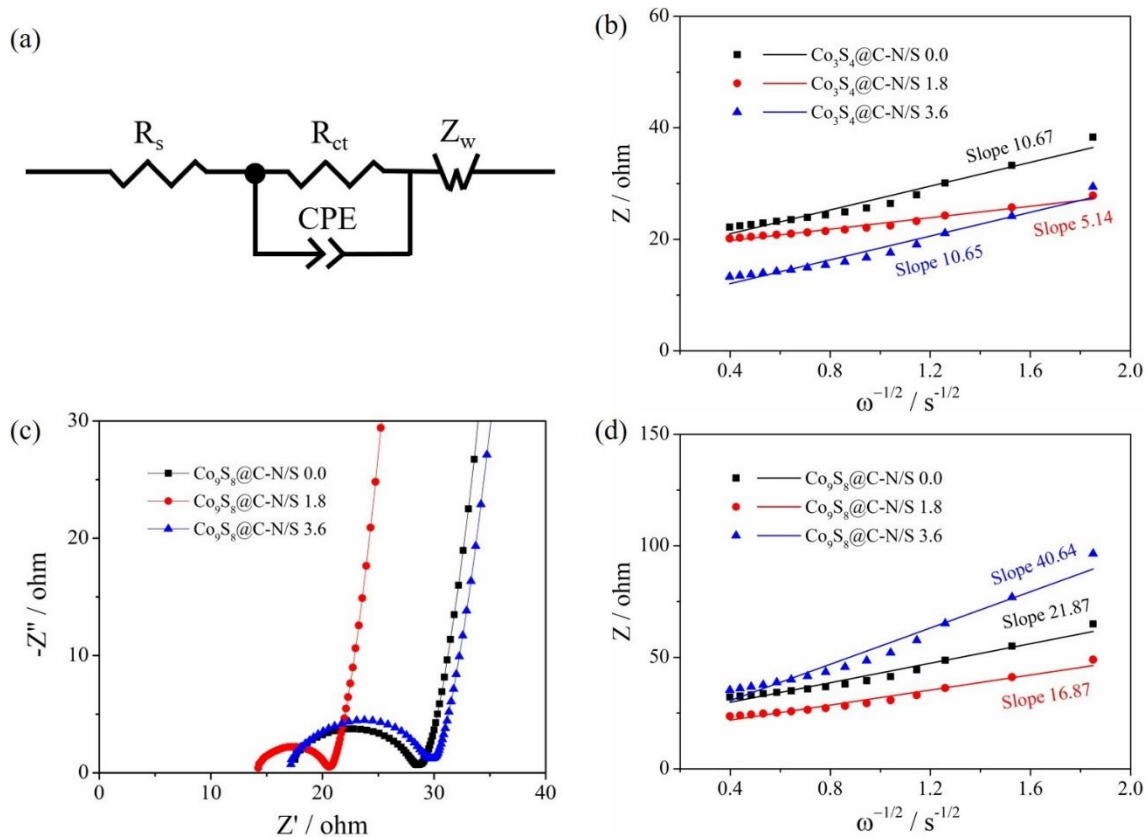


Figure 3.15 (a) The equivalent circuit used for the analysis of the impedance plots; Fitted straight lines between z' and $\omega^{-1/2}$ at the low-frequency region for (b) $\text{Co}_3\text{S}_4@\text{C-N/S}$ 0.0, 1.8 and 3.6 based anodes and (d) $\text{Co}_9\text{S}_8@\text{C-N/S}$ 0.0, 1.8 and 3.6 based anodes after 20 cycles; (c) Nyquist plots of $\text{Co}_9\text{S}_8@\text{C-N/S}$ 0.0, 1.8 and 3.6 based anodes.

In addition, electrochemical impedance spectroscopy (EIS) of the as-prepared anode is employed to analyze the impedance and diffusion coefficient. Figures 3.12f and 3.15c exhibit the Nyquist plot results after 20 cycles at 0.5 A g^{-1} . Herein, the Nyquist plot shows a straight line in the low-frequency region, which relates to the Warburg impedance (Z_w) relating to Na^+ diffusion whereas a semicircle in the high-frequency region displays the charge transfer resistance (R_{ct}) at the interface between electrolyte and electrode.[57, 58] The corresponding resistance values can be obtained by fitting the experimental data with an equivalent circuit model (Figure 3.15 a). As summarized in Table 3.2, the R_{ct} values of $\text{Co}_3\text{S}_4@\text{C-N/S}$ 0.0, 1.8, and 3.6 based anodes

are 7.91, 3.30, and 7.22 Ω , respectively. While, the Co₉S₈@C-N/S 0.0, 1.8, and 3.6 based ones deliver R_{ct} values of 10.58, 5.913, and 12.04 Ω , respectively. The lower R_{ct} value indicates a faster reaction rate, which could be resulted from its high conductivity and rational N/S co-doped carbon frameworks in the anode materials. Herein, the Na⁺ diffusion characteristics of the as-prepared anodes can be investigated by the following equation:[59, 60]

$$Z' = R_s + R_{ct} + \sigma_w \omega^{-0.5} \quad (5)$$

Where Warburg impedance coefficient (σ_w) is obtained by linear fitting the slope of Z' vs $\omega^{-0.5}$. Generally, the smaller σ_w indicates a faster Na⁺ diffusion. As shown in Figs. 3.15 b and d, compared with other Co₃S₄@C-N/S- and Co₉S₈@C-N/S-based anodes, the smaller slopes of Co₃S₄@C-N/S1.8- and Co₉S₈@C-N/S 1.8-based anodes demonstrate their superior Na⁺ diffusion ability.

Table 3.2 Fitting results of Nyquist plots based on the equivalent circuit after 20 cycles.

Electrode	R _s	R _{ct}
Co ₃ S ₄ @C-N/S 0.0	11.73	7.91
Co ₃ S ₄ @C-N/S 1.8	7.753	3.30
Co ₃ S ₄ @C-N/S 3.6	9.256	7.22
Co ₉ S ₈ @C-N/S 0.0	17.44	10.58
Co ₉ S ₈ @C-N/S 1.8	14.18	5.913
Co ₉ S ₈ @C-N/S 3.6	16.92	12.04

3.3.3 Electrochemical kinetics

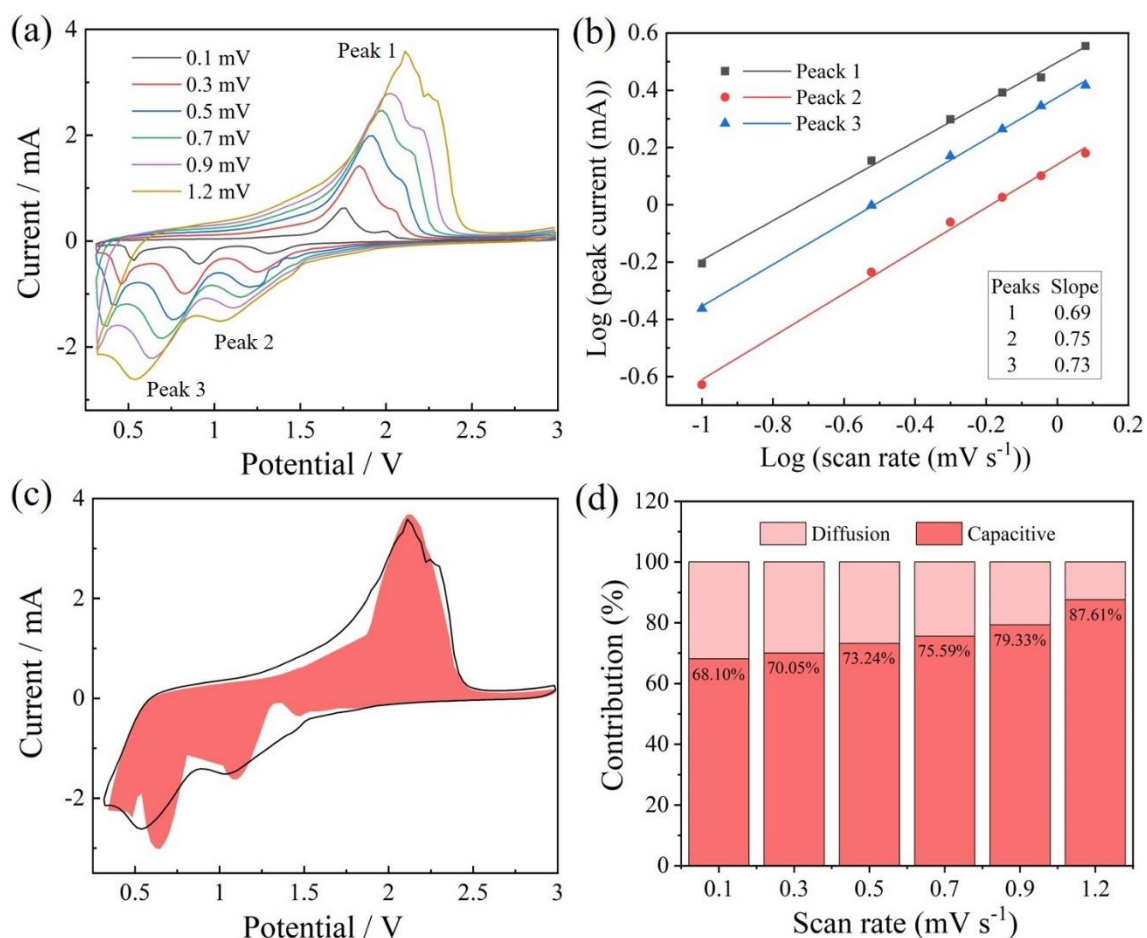


Figure 3.16 (a) CV curves of $\text{Co}_3\text{S}_4@\text{C-N/S}$ 1.8 based anode in a voltage range of 0.3–3 V at different scan rates from 0.1–1.2 mV s^{-1} ; (b) The fitting lines of $\log i$ vs $\log v$ of peaks 1, 2 and 3; (c) Capacitive contribution of $\text{Co}_3\text{S}_4@\text{C-N/S}$ 1.8 based anode compared with the total current at 1.2 mV s^{-1} ; (d) The capacitive contribution of $\text{Co}_3\text{S}_4@\text{C-N/S}$ 1.8 based anode at different scan rates from 0.1 to 1.2 mV s^{-1} .

To further explain the superior Na^+ storage ability of as-prepared samples as the anode material, CV measurements are carried out at various scan rates (0.1, 0.3, 0.5, 0.7, 0.9, and 1.2 mV s^{-1}) for kinetic analysis. As illustrated in Figure 3.16a, all the CV curves' shapes of $\text{Co}_3\text{S}_4@\text{C-N/S}$ 1.8-based anodes are almost preserved well with the increasing scan rate, indicating its small potential polarization and high rate performance.[61] In general, the relationship between the peak current (i) and scan rate (v) obeys the power law as follows:[62, 63]

$$i = av^b \quad (6)$$

Herein, a and b are the adjustable parameters.[24] Typically, the b -value approaches 0.5, indicating a diffusion-controlled charge storage process. Whereas, the b -value closes to 1, suggesting that the charge storage process is surface capacity-controlled. Based on the fitted line of $\log(v)$ - $\log(i)$ curve shown in Figure 3.16b, the b -value of peaks of 1, 2, and 3 are 0.69, 0.75, and 0.73, respectively, revealing that the capacities should be originated from both of the diffusion-controlled and surface capacity-controlled behaviors.[14] What's more, as shown in Figures 3.17b and 3.18b, similar diffusion-controlled and surface capacity-controlled behaviors can also be observed for the $\text{Co}_3\text{S}_4@\text{C-N/S}$ 0.0 and 3.6 based anodes since all of them are Co_3S_4 -based materials.

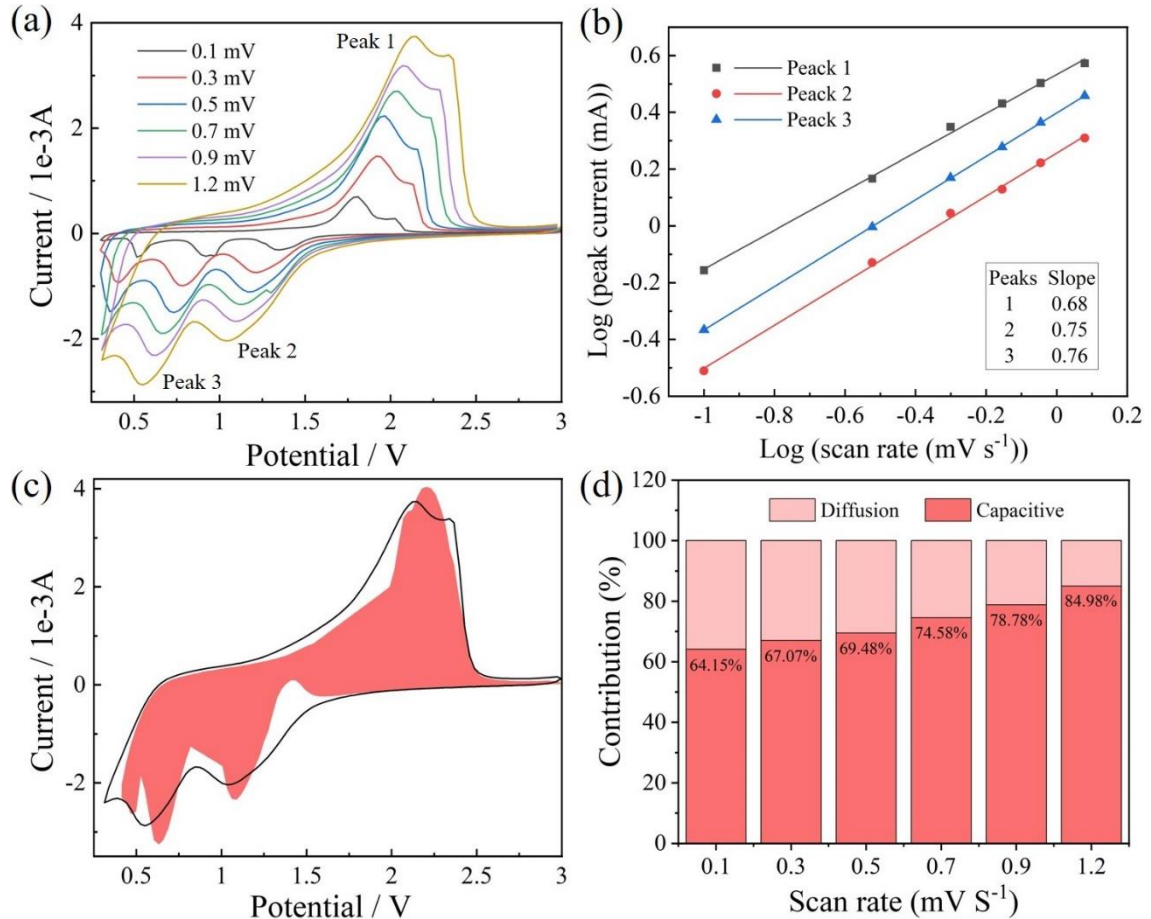


Figure 3.17 (a) CV curves of $\text{Co}_3\text{S}_4@\text{C-N/S}$ 0.0 based anode in a voltage range of 0.3-3 V at different scan rates from 0.1 to 1.2 mV s^{-1} ; (b) The fitting lines of $\log i$ vs $\log v$ of peaks 1, 2 and 3; (c) Capacitive contribution of $\text{Co}_3\text{S}_4@\text{C-N/S}$ 0.0 based anode compared with the total current at 1.2 mV s^{-1} ; (d) The capacitive contribution of

Co₃S₄@C-N/S 0.0 based anode at different scan rates from 0.1 to 1.2 mV s⁻¹.

Furthermore, the percentage of capacity contribution is quantified by fitting the current (*i*) measured at a specific voltage (*V*) through the following equations:

$$i(V) = k_1 v + K_2 v^{1/2} \quad (7)$$

$$i(V)/v^{1/2} = k_1 v^{1/2} + K_2 \quad (8)$$

Where, $k_1 v$ and $K_2 v^{1/2}$ relate to the contributions of capacity and diffusion-controlled process, respectively. As depicted in Figures 3.16c and d, the capacitive contributions of 68.10, 70.05, 73.24, 75.59, 79.33, and 87.61% can be achieved for the Co₃S₄@C-N/S 1.8-based anode at different scan rates from 0.1 to 1.2 mV s⁻¹, respectively. What's more, as shown in Figures 3.17c, d and 3.18c, d, the capacitive contribution of Co₃S₄@C-N/S 0.0- and 3.6-based anodes are slightly lower than that of Co₃S₄@C-N/S 1.8-based one, indicating its superior charge transfer kinetics.

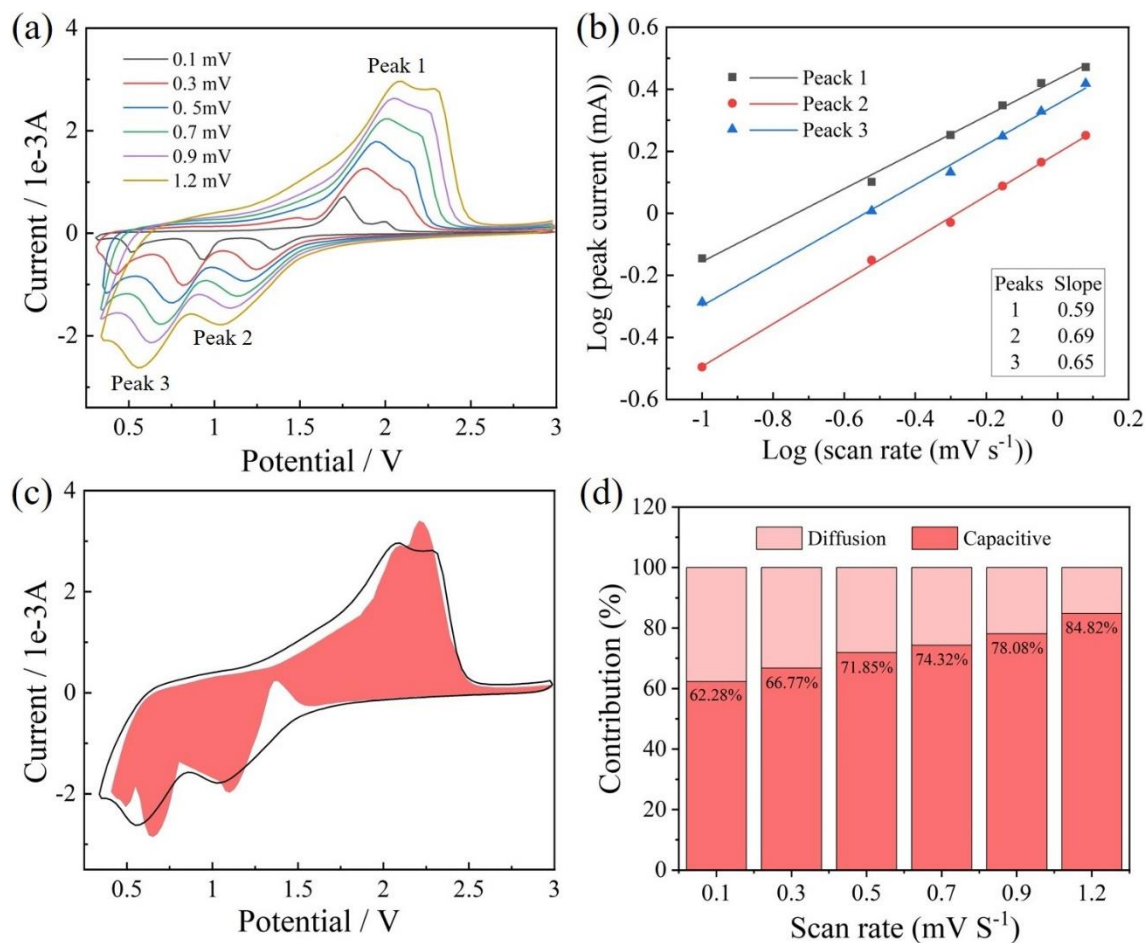


Figure 3.18 (a) CV curves of Co₃S₄@C-N/S 3.6 based anode in a voltage range of 0.3-

3V at different scan rates from 0.1 to 1.2 mV s⁻¹; (b) The fitting lines of log i vs log v of peaks 1, 2 and 3; (c) Capacitive contribution of Co₃S₄@C-N/S 3.6 based anode compared with the total current at 1.2 mV s⁻¹; (d) The capacitive contribution of Co₃S₄@C-N/S 3.6 based anode at different scan rates from 0.1 to 1.2 mV s⁻¹.

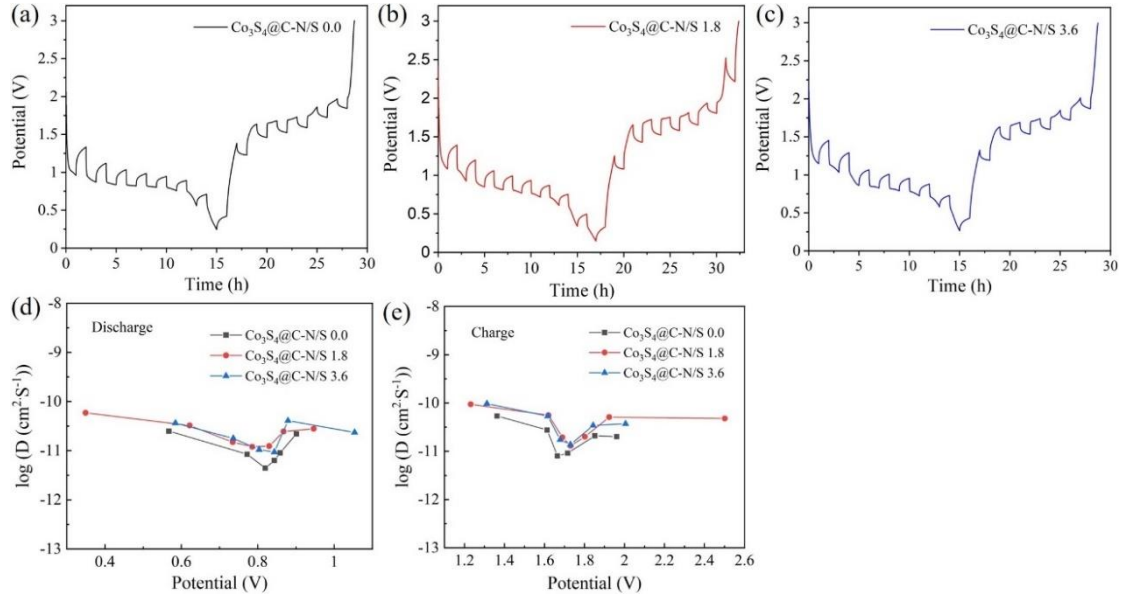


Figure 3.19 The discharge/charge profiles in GITT measurements of the (a) Co₃S₄@C-N/S 0.0, (a) Co₃S₄@C-N/S 1.8 and (c) Co₃S₄@C-N/S 3.6; The diffusion coefficient of Na⁺ in (d) discharge and (e) charge processes of the Co₃S₄@C-N/S 0.0, 1.8 and 3.6 based anodes.

The diffusion coefficients of Na⁺ (D_{Na^+}) during the discharge/charge processes of Co₃S₄@C-N/S 0.0, 1.8 and 3.6 based electrodes are investigated by galvanostatic intermittent titration technique (GITT) measurements. As shown in Figure 3.19 a-c, the cells are tested at 0.1A g⁻¹ with a voltage range of 0.3-3V, and the constant current pulse and open-circuit stand are alternately performed throughout the GITT measurements. As such, the D_{Na^+} can be calculated by the following equation:[64]

$$D_{Na^+} = \frac{4}{\pi\tau} \left(\frac{nV_m}{S} \right)^2 \left(\frac{\Delta E_s}{\Delta E_\tau} \right)^2 \quad (9)$$

where τ , n , V_m , and S are the pulse time of the current, molar number, molar volume of the active material, and the surface area of the electrode, respectively; ΔE_s and ΔE_τ

represent the voltage variation between two adjacent steady states and the voltage change during the time of the current pulse, respectively. As shown in Figure 3.19 (d-e), $\text{Co}_3\text{S}_4@\text{C-N/S}$ 1.8- and 3.6-based anodes exhibit similar D_{Na^+} during the discharge/charge process in the first cycle, which is higher than that of $\text{Co}_3\text{S}_4@\text{C-N/S}$ 0.0-based one. This phenomenon is consistent with those typical galvanostatic charge/discharge profiles of $\text{Co}_3\text{S}_4@\text{C-N/S}$ 0.0, 1.8, and 3.6 based electrodes (Figures 3.12a and 3.13 a, b), indicating faster Na^+ diffusion in $\text{Co}_3\text{S}_4@\text{C-N/S}$ 1.8 and 3.6 based anodes.

3.4. Conclusions

In summary, PBA-derived $\text{Co}_3\text{S}_4@\text{C-N/S}$ and $\text{Co}_9\text{S}_8@\text{C-N/S}$ with tremella-like micro-flower structures have been successfully prepared as the anode materials for SIBs by a successive hydrothermal and solid sulfidation process, which inherits the carbon/nitrogen framework in the precursor to form an N/S co-doped carbon frameworks during the solid sulfidation process. The obtained anode possesses high-speed ion/electron transfer ability and more active sites for sodium storage, ultimately resulting in a high specific capacity as well as cycling stability when used as the anode material for the SIBs. The optimum $\text{Co}_3\text{S}_4@\text{C-N/S}$ -based anode delivers excellent initial charge/discharge specific capacities of 685.3/745.2 mA h g^{-1} with a high initial Coulombic efficiency of 91.97% at 0.1 A g^{-1} and superior cycling performance (599.1 mA h g^{-1} even in the 600th cycle at 1 A g^{-1} with a capacity retention of 89.4%). While the optimum $\text{Co}_9\text{S}_8@\text{C-N/S}$ -based anode also exhibits considerable initial Coulombic efficiency (86.1% at 0.1 A g^{-1}) and cycling stability (391.9 mA h g^{-1} even in the 1200th cycle at 2 A g^{-1} with a capacity retention of 78.1%). This novel hydrothermally synthesized PBA-driven cobalt-based sulfides ($\text{Co}_3\text{S}_4@\text{C-N/S}$ and $\text{Co}_9\text{S}_8@\text{C-N/S}$) provide a new material preparation strategy, and their excellent electrochemical performance indicates that can be promising anodes for SIBs.

References

- [1] G.Q. Zou, H.S. Hou, P. Ge, Z.D. Huang, G.G. Zhao, D.L. Yin, X.B. Ji, Metal-Organic Framework-Derived Materials for Sodium Energy Storage, *Small* 14 (2018) No. 1702648.
- [2] X. Ou, L. Cao, X.H. Liang, F.H. Zheng, H.S. Zheng, X.F. Yang, J.H. Wang, C.H. Yang, M.L. Liu, Fabrication of $\text{SnS}_2/\text{Mn}_2\text{SnS}_4$ /Carbon Heterostructures for Sodium-Ion Batteries with High Initial Coulombic Efficiency and Cycling Stability, *Acs Nano* 13 (2019) 3666-3676.
- [3] Q.C. Pan, Q.B. Zhang, F.H. Zheng, Y.Z. Liu, Y.P. Li, X. Ou, X.H. Xiong, C.H. Yang, M.L. Liu, Construction of MoS_2/C Hierarchical Tubular Heterostructures for High-Performance Sodium Ion Batteries, *Acs Nano* 12 (2018) 12578-12586.
- [4] Y.J. Fang, X.Y. Yu, X.W. Lou, Nanostructured Electrode Materials for Advanced Sodium-Ion Batteries, *Matter* 1 (2019) 90-114.
- [5] Y.C. Liu, N. Zhang, C.M. Yu, L.F. Jiao, J. Chen, $\text{MnFe}_2\text{O}_4@\text{C}$ Nanofibers as High-Performance Anode for Sodium-Ion Batteries, *Nano Letters* 16 (2016) 3321-3328.
- [6] R.P. Zhang, Y. Wang, M.Q. Jia, J.J. Xu, E.Z. Pan, One-pot hydrothermal synthesis of ZnS quantum dots/graphene hybrids as a dual anode for sodium ion and lithium ion batteries, *Appl. Surf. Sci.* 437 (2018) 375-383.
- [7] Y.W. Wang, N. Xiao, Z.Y. Wang, Y.C. Tang, H.Q. Li, M.L. Yu, C. Liu, Y. Zhou, J.S. Qiu, Ultrastable and high-capacity carbon nanofiber anodes derived from pitch/polyacrylonitrile for flexible sodium-ion batteries, *Carbon* 135 (2018) 187-194.
- [8] K. Kim, D.G. Lim, C.W. Han, S. Osswald, V. Ortalan, J.P. Youngblood, V.G. Pol, Tailored Carbon Anodes Derived from Biomass for Sodium-Ion Storage, *Acs Sustain. Chem. Eng.* 5 (2017) 8720-8728.
- [9] Q.B. Guo, Y.F. Ma, T.T. Chen, Q.Y. Xia, M. Yang, H. Xia, Y. Yu, Cobalt Sulfide Quantum Dot Embedded N/S-Doped Carbon Nanosheets with Superior Reversibility and Rate Capability for Sodium-Ion Batteries, *Acs Nano* 11 (2017) 12658-12667.
- [10] Z. Ali, T.Y. Tang, X.X. Huang, Y.Z. Wang, M. Asif, Y.L. Hou, Cobalt selenide decorated carbon spheres for excellent cycling performance of sodium ion batteries,

Energy Stor. Mater. 13 (2018) 19-28.

[11] Y.Y. Wang, W.P. Kang, D.W. Cao, M.H. Zhang, Z.X. Kang, Z.Y. Xiao, R.M. Wang, D.F. Sun, A yolk-shelled Co₉S₈/MoS₂-CN nanocomposite derived from a metal-organic framework as a high performance anode for sodium ion batteries, J. Mater. Chem. A 6 (2018) 4776-4782.

[12] C.T. Zhao, C. Yu, M.D. Zhang, Q. Sun, S.F. Li, M.N. Banis, X.T. Han, Q. Dong, J. Yang, G. Wang, X.L. Sun, J.S. Qiu, Enhanced sodium storage capability enabled by super wide-interlayer-spacing MoS₂ integrated on carbon fibers, Nano Energy 41 (2017) 66-74.

[13] X. Yang, R.Y. Zhang, J. Zhao, Z.X. Wei, D.X. Wang, X.F. Bie, Y. Gao, J. Wang, F. Du, G. Chen, Amorphous Tin-Based Composite Oxide: A High-Rate and Ultralong-Life Sodium-Ion-Storage Material, Adv. Energy Mater. 8 (2018) No. 201701827.

[14] Y. Wang, C.Y. Wang, Y.J. Wang, H.K. Liu, Z.G. Huang, Superior sodium-ion storage performance of Co₃O₄@nitrogen-doped carbon: derived from a metal-organic framework, J. Mater. Chem. A 4 (2016) 5428-5435.

[15] C. Wang, Z.Y. Wang, D.C. Zhao, J.H. Ren, S.P. Liu, H. Tang, P. Xu, F. Gao, X.A. Yue, H. Yang, C.M. Niu, W.S. Chu, D. Wang, X. Liu, Z.L. Wang, Y.T. Wu, Y. Zhang, Core-Shell Co₂VO₄/Carbon Composite Anode for Highly Stable and Fast-Charging Sodium-Ion Batteries, Acs Appl. Mater. Inter. 13 (2021) 55020-55028.

[16] Y. Qi, T. Zhang, N.X. Wu, H.R. Ding, G.X. Yu, J.B.A. Lian, L. Xu, J.X. Qiu, S. Li, Rational Design of the CoS/Co₉S₈@NC Composite Enabling High-Rate Sodium-Ion Storage, Acs Appl. Energy Mater. 4 (2021) 5574-5582.

[17] G. Ali, M.A.R. Anjum, S. Mehboob, Free-Standing Petal-Shaped Metallic 1T-Phase Molybdenum Sulfide Anchored on a Nitrogen-Doped Carbon Cloth for High Rate Na-Ion Batteries, Acs Appl. Energy Mater. 5 (2022) 1106-1113.

[18] Z. Hu, Q.N. Liu, S.L. Chou, S.X. Dou, Advances and Challenges in Metal Sulfides/Selenides for Next-Generation Rechargeable Sodium-Ion Batteries, Adv. Mater. 29 (2017).

[19] F. Han, T.Z. Lv, B. Sun, W. Tang, C.Z. Zhang, X.K. Li, In situ formation of ultrafine CoS₂ nanoparticles uniformly encapsulated in N/S-doped carbon polyhedron for

- advanced sodium-ion batteries, *Rsc Adv.* 7 (2017) 30699-30706.
- [20] Y.N. Ko, Y.C. Kang, Co₉S₈-carbon composite as anode materials with improved Na-storage performance, *Carbon* 94 (2015) 85-90.
- [21] X.Y. Li, K.K. Li, S.C. Zhu, K. Fan, L.L. Lyu, H.M. Yao, Y.Y. Li, J.L. Hu, H.T. Huang, Y.W. Mai, J.B. Goodenough, Fiber-in-Tube Design of Co₉S₈-Carbon/Co₉S₈: Enabling Efficient Sodium Storage, *Angew. Chem. Int. Ed.* 58 (2019) 6239-6243.
- [22] Y.J. Fang, B.Y. Guan, D.Y. Luan, X.W. Lou, Synthesis of CuS@CoS₂ Double-Shelled Nanoboxes with Enhanced Sodium Storage Properties, *Angew. Chem. Int. Ed.* 58 (2019) 7739-7743.
- [23] Q. Liu, S.J. Zhang, C.C. Xiang, C.X. Luo, P.F. Zhang, C.G. Shi, Y. Zhou, J.T. Li, L. Huang, S.G. Sun, Cubic MnS-FeS₂ Composites Derived from a Prussian Blue Analogue as Anode Materials for Sodium-Ion Batteries with Long-Term Cycle Stability, *Acs Appl. Mater. Inter.* 12 (2020) 43624-43633.
- [24] Z.L. Chen, R.B. Wu, M. Liu, H. Wang, H.B. Xu, Y.H. Guo, Y. Song, F. Fang, X.B. Yu, D.L. Sun, General Synthesis of Dual Carbon-Confined Metal Sulfides Quantum Dots Toward High-Performance Anodes for Sodium-Ion Batteries, *Adv. Funct. Mater.* 27 (2017).
- [25] S. Zhang, X.B. Yu, H.L. Yu, Y.J. Chen, P. Gao, C.Y. Li, C.L. Zhu, Growth of Ultrathin MoS₂ Nanosheets with Expanded Spacing of (002) Plane on Carbon Nanotubes for High-Performance Sodium-Ion Battery Anodes, *Acs Appl. Mater. Inter.* 6 (2014) 21880-21885.
- [26] W.X. Zhao, S.Q. Ci, X. Hu, J.X. Chen, Z.H. Wen, Highly dispersed uttrasmall NiS₂ nanoparticles in porous carbon nanofiber anodes for sodium ion batteries, *Nanoscale* 11 (2019) 4688-4695.
- [27] S. Senkale, S. Indris, M. Etter, W. Bensch, CuFeS₂ as a Very Stable High-Capacity Anode Material for Sodium-Ion Batteries: A Multimethod Approach for Elucidation of the Complex Reaction Mechanisms during Discharge and Charge Processes, *Acs Appl. Mater. Inter.* 13 (2021) 26034-26045.
- [28] C. Guo, W.C. Zhang, Y. Liu, J.P. He, S. Yang, M.K. Liu, Q.H. Wang, Z.P. Cuo, Constructing CoO/Co₃S₄ Heterostructures Embedded in N-doped Carbon Frameworks

for High-Performance Sodium-Ion Batteries, *Adv. Funct. Mater.* 29 (2019) No. 201901925.

[29] S.Q. Xing, J. Yang, M. Muska, H.R. Li, Q. Yang, Rock-Salt $\text{MnS}_{0.5}\text{Se}_{0.5}$ Nanocubes Assembled on N-Doped Graphene Forming van der Waals Heterostructured Hybrids as High-Performance Anode for Lithium- and Sodium-Ion Batteries, *Acs Appl. Mater. Inter.* 13 (2021) 22608-22620.

[30] T.Z. Liu, Y.P. Li, S. Hou, C.H. Yang, Y.Y. Guo, S. Tian, L.Z. Zhao, Building Hierarchical Microcubes Composed of One-Dimensional CoSe_2 @Nitrogen-Doped Carbon for Superior Sodium Ion Batteries, *Chem. Eur. J.* 26 (2020) 13716-13724.

[31] Y.L. Jiang, G.Q. Zou, W.W. Hong, Y. Zhang, Y. Zhang, H.L. Shuai, W. Xu, H.S. Hou, X.B. Ji, N-Rich carbon-coated Co_3S_4 ultrafine nanocrystals derived from ZIF-67 as an advanced anode for sodium-ion batteries, *Nanoscale* 10 (2018) 18786-18794.

[32] M. Chauhan, K.P. Reddy, C.S. Gopinath, S. Deka, Copper Cobalt Sulfide Nanosheets Realizing a Promising Electrocatalytic Oxygen Evolution Reaction, *Acs Catal.* 7 (2017) 5871-5879.

[33] Z. Zhang, Y. Huang, X.D. Liu, C. Chen, Z.P. Xu, P.B. Liu, Zeolitic imidazolate frameworks derived $\text{ZnS}/\text{Co}_3\text{S}_4$ composite nanoparticles doping on polyhedral carbon framework for efficient lithium/sodium storage anode materials, *Carbon* 157 (2020) 244-254.

[34] J.W. Zhang, Y. Li, Z. Wang, Y.Q. Wang, F. Wang, M.H. Chen, Three-dimensionally hierarchical $\text{NiCoP}@ \text{PANI}$ architecture for high-performance hydrogen evolution reaction, *Nanotechnology* 31 (2020) No.445401.

[35] X.J. Yang, H.M. Sun, P. Zan, L.J. Zhao, J.S. Lian, Growth of vertically aligned $\text{Co}_3\text{S}_4/\text{CoMo}_2\text{S}_4$ ultrathin nanosheets on reduced graphene oxide as a high-performance supercapacitor electrode, *J. Mater. Chem. A* 4 (2016) 18857-18867.

[36] R.R. Liu, H.M. Zhang, X. Zhang, T.X. Wu, H.J. Zhao, G.Z. Wang, $\text{Co}_9\text{S}_8@ \text{N}$, P-doped porous carbon electrocatalyst using biomass-derived carbon nanodots as a precursor for overall water splitting in alkaline media, *Rsc Adv.* 7 (2017) 19181-19188.

[37] J.L. Li, R.H. Li, C.K. Bulin, R.G. Xing, B.W. Zhang, Facile Synthesis of Silicon Nanoparticles Embedded in 3D N-doped Graphene as Anode Materials for High-

- Performance Lithium Ion Batteries, *Int. J. Electrochem. Sci.* 12 (2017) 4164-4172.
- [38] Y. Zhao, Y.L. Liu, C. Wang, E. Ortega, X.M. Wang, Y.F. Xie, J.N. Shen, C.J. Gao, B. Van der Bruggen, Electric field-based ionic control of selective separation layers, *J. Mater. Chem. A* 8 (2020) 4244-4251.
- [39] F. Luo, D.T. Ma, Y.L. Li, H.W. Mi, P.X. Zhang, S. Luo, Hollow $\text{Co}_3\text{S}_4/\text{C}$ anchored on nitrogen-doped carbon nanofibers as a free-standing anode for high-performance Li-ion batteries, *Electrochim. Acta* 299 (2019) 173-181.
- [40] M. Asif, M. Rashad, Z. Ali, Electrochemical intercalations of divalent ions inside Ni/Zn co-doped cobalt sulfide nanoparticle decorated carbon spheres with superior capacity, *Nanoscale* 12 (2020) 14267-14278.
- [41] G.L. Xia, L.J. Zhang, X.W. Chen, Y.Q. Huang, D.L. Sun, F. Fang, Z.P. Guo, X.B. Yu, Carbon hollow nanobubbles on porous carbon nanofibers: An ideal host for high-performance sodium-sulfur batteries and hydrogen storage, *Energy Stor. Mater.* 14 (2018) 314-323.
- [42] H. Sun, Y.Q. Zhu, B. Yang, Y.F. Wang, Y.P. Wu, J.Z. Du, Template-free fabrication of nitrogen-doped hollow carbon spheres for high-performance supercapacitors based on a scalable homopolymer vesicle, *J. Mater. Chem. A* 4 (2016) 12088-12097.
- [43] E. Samuel, B. Joshi, M.W. Kim, Y.I. Kim, M.T. Swihart, S.S. Yoon, Hierarchical zeolitic imidazolate framework-derived manganese-doped zinc oxide decorated carbon nanofiber electrodes for high performance flexible supercapacitors, *Chem. Eng. J.* 371 (2019) 657-665.
- [44] L. Xia, Z.C. Song, L.X. Zhou, D.M. Lin, Q.J. Zheng, Nitrogen and oxygen dual-doped hierarchical porous carbon derived from rapeseed meal for high performance lithium-sulfur batteries, *J. Solid State Chem.* 270 (2019) 500-508.
- [45] Q. Shi, K.Y. Chen, Z.H. Yu, M.X. Fang, Z.Y. Dai, J.X. Wang, K. Cao, F.H. Tian, Y. Zhang, S. Yang, X. Zhou, Fabrication of N, S co-doped carbon nanofiber matrix with cobalt sulfide nanoparticles enhancing lithium/sodium storage performance, *J. Alloy. Compd.* 902 (2022).
- [46] J.F. Ruan, Y.H. Zhao, S.N. Luo, T. Yuan, J.H. Yang, D.L. Sun, S.Y. Zheng, Fast and stable potassium-ion storage achieved by in situ molecular self-assembling N/O

- dual-doped carbon network, *Energy Stor. Mater.* 23 (2019) 46-54.
- [47] Y.P. Li, C.H. Yang, F.H. Zheng, X. Ou, Q.C. Pan, Y.Z. Liu, G. Wang, High pyridine N-doped porous carbon derived from metal-organic frameworks for boosting potassium-ion storage, *J. Mater. Chem. A* 6 (2018) 17959-17966.
- [48] Q. Zhou, L. Liu, Z.F. Huang, L.G. Yi, X.Y. Wang, G.Z. Cao, Co_3S_4 @polyaniline nanotubes as high-performance anode materials for sodium ion batteries, *J. Mater. Chem. A* 4 (2016) 5505-5516.
- [49] Y.C. Du, X.S. Zhu, X.S. Zhou, L.Y. Hu, Z.H. Dai, J.C. Bao, Co_3S_4 porous nanosheets embedded in graphene sheets as high-performance anode materials for lithium and sodium storage, *J. Mater. Chem. A* 3 (2015) 6787-6791.
- [50] X.J. Hu, X.J. Liu, K. Chen, G. Wang, H. Wang, Core-shell MOF-derived N-doped yolk-shell carbon nanocages homogenously filled with ZnSe and CoSe_2 nanodots as excellent anode materials for lithium- and sodium-ion batteries, *J. Mater. Chem. A* 7 (2019) 11016-11037.
- [51] D. Xie, X.H. Xia, Y.D. Wang, D.H. Wang, Y. Zhong, W.J. Tang, X.L. Wang, J.P. Tu, Nitrogen-Doped Carbon Embedded MoS_2 Microspheres as Advanced Anodes for Lithium- and Sodium-Ion Batteries, *Chem. Eur. J.* 22 (2016) 11617-11623.
- [52] H.N. He, D. Sun, Y.G. Tang, H.Y. Wang, M.H. Shao, Understanding and improving the initial Coulombic efficiency of high-capacity anode materials for practical sodium ion batteries, *Energy Stor. Mater.* 23 (2019) 233-251.
- [53] D.N. Liu, A.P. Hu, Y.F. Zhu, S.P. Zhou, Y. Duan, Q.L. Tang, W.N. Deng, X.H. Chen, Hierarchical microstructure of CNTs interwoven ultrathin Co_3S_4 nanosheets as a high performance anode for sodium-ion battery, *Ceram. Int.* 45 (2019) 3591-3599.
- [54] M.M. Yin, X.T. Feng, D. Zhao, Y. Zhao, H.S. Li, W. Zhou, H.B. Liu, X.P. Bai, H.X. Wang, C.H. Feng, Q.Z. Jiao, Hierarchical Co_9S_8 @Carbon Hollow Microspheres as an Anode for Sodium Ion Batteries with Ultralong Cycling Stability, *Acs Sustain. Chem. Eng.* 7 (2019) 6122-6130.
- [55] Y.H. Zhang, N.N. Wang, P. Xue, Y.L. Liu, B. Tang, Z.C. Bai, S.X. Dou, Co_9S_8 @carbon nanospheres as high-performance anodes for sodium ion battery, *Chem. Eng. J.* 343 (2018) 512-519.

- [56] Y.X. Wang, Y.X. Wang, Y.X. Wang, X.M. Feng, W.H. Chen, J.F. Qian, X.P. Ai, H.X. Yang, Y.L. Cao, In Situ Formation of Co₉S₈ Nanoclusters in Sulfur-Doped Carbon Foam as a Sustainable and High-Rate Sodium-Ion Anode, *Acs Appl. Mater. Inter.* 11 (2019) 19218-19226.
- [57] S.H. Yang, S.K. Park, J.K. Kim, Y.C. Kang, A MOF-mediated strategy for constructing human backbone-like CoMoS₃@N-doped carbon nanostructures with multiple voids as a superior anode for sodium-ion batteries, *J. Mater. Chem. A* 7 (2019) 13751-13761.
- [58] S.Y. Tian, G.N. Zhu, Y.P. Tang, X.H. Xie, Q. Wang, Y.F. Ma, G.Q. Ding, X.M. Xie, Three-dimensional cross-linking composite of graphene, carbon nanotubes and Si nanoparticles for lithium ion battery anode, *Nanotechnology* 29 (2018).
- [59] P. Ge, H.S. Hou, X.Y. Cao, S.J. Li, G.G. Zhao, T.X. Guo, C. Wang, X.B. Ji, Multidimensional Evolution of Carbon Structures Underpinned by Temperature-Induced Intermediate of Chloride for Sodium-Ion Batteries, *Adv. Sci.* 5 (2018) No. 201800080.
- [60] S.P. Zhang, G. Wang, B.B. Wang, J.M. Wang, J.T. Bai, H. Wang, 3D Carbon Nanotube Network Bridged Hetero-Structured Ni-Fe-S Nanocubes toward High-Performance Lithium, Sodium, and Potassium Storage, *Adv. Funct. Mater.* 30 (2020).
- [61] X. Li, Y.G. Sun, X. Xu, Y.X. Wang, S.L. Chou, A.M. Cao, L.B. Chen, S.X. Dou, Lotus rhizome-like S/N-C with embedded WS₂ for superior sodium storage, *J. Mater. Chem. A* 7 (2019) 25932-25943.
- [62] W.H. Chen, X.X. Zhang, L.W. Mi, C.T. Liu, J.M. Zhang, S.Z. Cui, X.M. Feng, Y.L. Cao, C.Y. Shen, High-Performance Flexible Freestanding Anode with Hierarchical 3D Carbon-Networks/Fe₇S₈/Graphene for Applicable Sodium-Ion Batteries, *Adv. Mater.* 31 (2019).
- [63] X.T. Lian, N. Xu, Y.C. Ma, F. Hu, H.X. Wei, H.Y. Chen, Y.Z. Wu, L.L. Li, D.S. Li, S.J. Peng, In-situ formation of Co_{1-x}S hollow polyhedrons anchored on multichannel carbon nanofibers as self-supporting anode for lithium/sodium-ion batteries, *Chem. Eng. J.* 421 (2021).
- [64] S.W. Fan, G.D. Li, F.P. Cai, G. Yang, Synthesis of Porous Ni-Doped CoSe₂/C

Nanospheres towards High-Rate and Long-Term Sodium-Ion Half/Full Batteries, Chem. Eur. J. 26 (2020) 8579-8587.

Chapter 4 Micro-flower-like MoS₂-modified Co₉S₈

Heterostructure as Anode Material for Sodium-ion Batteries

with Superior Reversibility and Rate Capacity

4.1. Introduction

The growing demand for high-capacity and low-cost energy storage devices from wearable electronics to electric vehicles has sparked a research boom on the new types of batteries to replace lithium-ion batteries (LIBs) over the past few decades[1, 2]. Sodium-ion batteries (SIBs) are considered to be the most potential substitute for LIBs due to the abundant sodium resources with a wide regional distribution, similar energy storage mechanism as the LIBs, and low cost[3-5]. Unfortunately, not all electrode materials applied in the LIBs are suitable for the SIBs because sodium ion (Na⁺, 1.06 Å) has a larger ionic radius than lithium-ion (Li⁺, 0.76 Å). To date, more works are concentrated on the development of cathode materials for SIBs cathodes and have reached remarkable achievements, however, further research on the anode materials is necessary.

Nowadays, transition metal sulfides (TMSs) have become critical functional materials and been successfully applied in various fields[6-8]. Especially, they have high theoretical specific capacities and easily controllable morphologies, making them more competitive than other anode materials. Among various TMSs, cobalt sulfides (CoS, CoS₂, Co₃S₄, and Co₉S₈) have more excellent theoretical specific capacities. However, due to poor electrical conductivity, they always exhibit inferior electrochemical capacity and sluggish electrochemical kinetics [9-11]. Furthermore, the electrode could be pulverized by the large volume changes upon the repeatedly charging/discharging process always results in poor rate capability and rapid capacity decay. As such, various strategies for the fabrication of electrode materials such as nanocrystallization, compositing with carbon matrix, constructing of the heterostructure, and introducing of defects have been proposed to overcome these

issues[12-18]. In particular, creating a heterostructure is considered an effective way to lead ultra-fast charge transfer, thereby achieving satisfactory electrochemical performance [19-22]. For example, compared with the electrode material with a pure phase, the heterostructured core-shell $\text{Bi}_2\text{S}_3@\text{Co}_9\text{S}_8$ showed enhanced electrochemical performance with a high sodium storage ability (rate performance: 293 mAh g^{-1} @ 5 A g^{-1} , cycling stability: 354 mAh g^{-1} @ 0.5 A g^{-1} at the 500th cycle)[23]. Qi *et al.* embedded cobalt sulfide heterostructure in N-modified carbon composite ($\text{CoS}/\text{Co}_9\text{S}_8@\text{NC}$), which delivered high-rate sodium-ion storage capacities of 204.2 and 134.9 mAh g^{-1} at 5 and 10 A g^{-1} , respectively[17]. To date, how to further enhance cycling stability and achieve high rate capability of the Co_9S_8 -based electrode is still necessary.

Layered transition-metal dichalcogenides (MS_2 , M=Mo, W, V, Ti, and Sn) with wide interlayer spacings and weak van der Waals forces between each set of S–M–S layer could provide effective diffusion paths during the repeatedly inserting/extracting of Na^+ , thereby improving ion diffusion kinetics [24-29]. Thus, in this study, to further improve Na^+ storage ability with superior reversibility and rate capacity, one of MS_2 materials, i.e., MoS_2 , was used to modify Co_9S_8 , and a micro-flower-like $\text{Co}_9\text{S}_8/\text{MoS}_2$ composite with a three-dimensional (3D) heterostructure was constructed via a simple solvothermal synthesis method followed with a solid sulfidation process.

4.2 Experimental

4.2.1. Synthesis of precursor

All the reagents used in this study did not perform further purification. The precursors were obtained by a facile hydrothermal method. Typically, 1 mmol of $\text{K}_3[\text{Co}(\text{CN})_6]$ was dissolved in 30 mL of deionized (DI) water to obtain a solution A. X mmol ($X = 0, 0.2, 0.6, \text{ and } 1.0$) of $\text{Na}_2\text{MoO}_4 \cdot 2\text{H}_2\text{O}$ was dissolved in another 30 mL of DI water to get a solution B. The solution A was poured into the solution B, and the solution mixture was stirred for 1 h until a transparent solution was obtained. After sonicating for 10 min, the transparent solution was transferred to a stainless steel

autoclave (100 mL) with Teflon-line, which was sealed and heated up to 200°C and maintained at this temperature for 20 h in an oven. The obtained precipitate was centrifugated, washed with DI water and ethanol successively for several times and freeze-dried for 24 h. Hereafter, the precursors obtained with 0, 0.2, 0.6 and 1.0 mmol of $\text{Na}_2\text{MoO}_4 \cdot 2\text{H}_2\text{O}$ are called as CM50, CM51, CM53, and CM55, respectively.

4.2.2. Synthesis of $\text{Co}_9\text{S}_8/\text{MoS}_2$

The above-obtained precursor (0.1 g) and sulfide powder (0.8 g) were placed in a sealed tube furnace with two porcelain boats, where the one with sulfur powder was placed on the upstream side and the other was placed at the downstream side. Then, the mixed gas (Ar/H_2 , $\phi_{\text{H}_2}=5\%$) was continuously passed through the tube reactor at a flow rate of 30 mL/min. The final black powders ($\text{Co}_9\text{S}_8/\text{MoS}_2$) were obtained after calcination at 500 °C for 3 h, where the heating rate was controlled at 5 °C/min. Hereafter, the final powder products from those precursors prepared with 0.0, 0.2, and 1.0 mmol $\text{Na}_2\text{MoO}_4 \cdot 2\text{H}_2\text{O}$ are called as CM50-S, CM51-S, and CM55-S.

4.2.3. Computational methods

The Vienna ab initio simulation package (VASP) was employed to perform all the density functional theory (DFT) calculations within the generalized gradient approximation (GGA) using the Perdew, Burke Enzerhof (PBE) formulation. The projected augmented wave (PAW) potentials were applied to describe the ionic cores and take valence electrons into account using a plane wave basis set with a kinetic energy cutoff of 450 eV. Partial occupancies of the Kohn–Sham orbitals were allowed using the Gaussian smearing method and a width of 0.05 eV. The electronic energy was considered self-consistent when the energy change was smaller than 10^{-5} eV. Geometry optimization was considered convergent when the force change was smaller than 0.03 eV/Å. Grimme’s DFT-D3 methodology was used to describe the dispersion interactions. The equilibrium lattice constants of Si unit cells were optimized when using a $2 \times 2 \times 1$ Monkhorst-Pack k-point grid for Brillouin zone sampling. The climbing-image nudged

elastic band method was employed to calculate the Na^+ diffusion barriers in the $\text{Co}_9\text{S}_8/\text{MoS}_2$ heterostructure and Co_9S_8 pure phase.

4.2.4 Characterizations

Crystalline structure and phase composition were characterized by a Rigaku X-ray diffractometer (XRD, Smartlab 9 kW, Japan) with a Cu K α radiation source ($\lambda = 1.5418$ Å). Morphology, microstructure, and elemental distribution were measured by a Hitachi field-emission scanning electron microscopy (FESEM, SU8010, Japan) with a Horiba energy-dispersive spectroscopy (EDS) analysis instrument. The nanostructure was analyzed by a JEOL high-resolution transmission electron microscope (TEM, JEM-2100F, Japan) with an accelerating voltage of 200 kV. The ratio of metal elements in the precursors was detected by inductively coupled plasma emission optical spectrometry (ICP-OES). The Brunauer-Emmett-Teller (BET) specific surface area and Barret-Joyner-Halenda (BJH) pore size distribution were obtained by analyzing nitrogen adsorption-desorption isotherm with an equipment of NOVA 4200e (Quantachrome Inc., USA). A Thermo Electron X-ray photoelectron spectrometer (XPS) (VG ESCALAB 250, UK) with an Al K α as X-ray source (1486 eV) was applied to investigate the elemental compositions and chemical valence states.

4.2.5 Electrochemical performance

For the fabrication of working electrode, 75 wt% active material, 15 wt% conductive material (super P), and 10 wt% polyvinylidene fluoride (PVDF) binder were mixed in N-methyl pyrrolidone (NMP) to obtain a uniform slurry at first and then, the slurry was painted on a Cu sheet and vacuum dried at 80 °C overnight. Subsequently, a disk (12 mm diameter) was cut from the Cu sheet as the anode, where the active material loaded was about $1.0 \text{ mg}\cdot\text{cm}^{-2}$. The CR2032 coin-type cell was assembled with Na metal as the counter electrode and glass fiber as the separator in an argon-filled glove box. 1 M sodium trifluoromethanesulfonate (NaSO_3CF_3) was dissolved in diglyme (DGM) as the electrolyte. Galvanostatically charging/discharging, cycling stability, galvanostatic intermittent titration technique (GITT), and rate performance measurements were conducted on a battery testing system (LAND CT2001A model,

Wuhan LAND Electronic., Ltd.) over a 0.3-3 V voltage range. Cyclic voltammetry (CV) at the same voltage range and electrochemical impedance spectroscopy (EIS) in a frequency range of 0.01 Hz-100 kHz measurements were recorded on an electrochemical workstation. Herein, all electrochemical tests were performed at ambient temperature.

4.3. Results and discussion

4.3.1. Characterizations of as-prepared materials

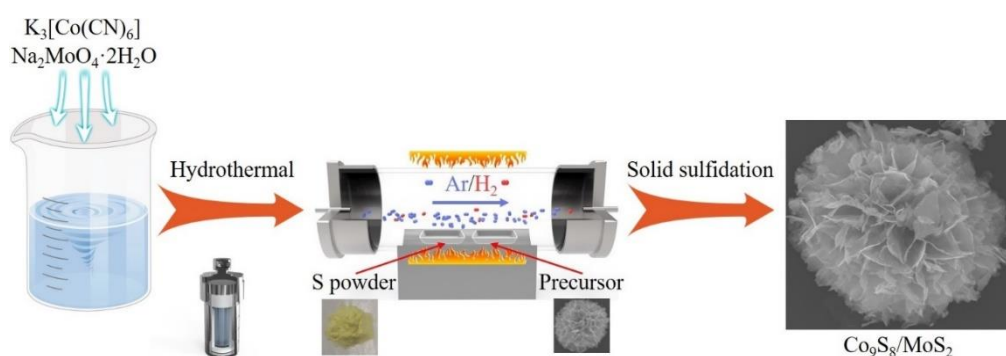


Figure 4.1 Schematic illustration of the synthesis of micro-flower-like Co_9S_8/MoS_2 heterostructure.

The process for the synthesis of the micro-flower-like Co_9S_8/MoS_2 heterostructure is schematically depicted in Fig. 4.1, which mainly includes two steps, i.e., (a) hydrothermal synthesis of precursors and (b) solid sulfidation at 500 °C to form TMSs. To investigate the formation mechanism of the micro-flower-like Co_9S_8/MoS_2 , as depicted in Fig. 4.2, it is found that the precursors prepared with different Co/Mo molar ratios exhibit different morphologies. Specifically, as shown in Fig. 4.2a, the precursors without Mo addition exhibits a sea urchin-like morphology with a large particle size of ~50 μm . With the increase in the Mo content to a molar ratio of Co/Mo=5/1, as shown in Fig. 4.2 b, the CM51 precursor exhibits a morphology assembled from nanosheets and nanoribbons. However, with further increasing Mo content (Co/Mo=5/3, Co/Mo=5/5), the morphologies of CM53 (Fig. 4.2c) and CM55 (Figs. 4.2d) precursors tend to be a uniform micro-flower structure assembled by nanosheets with particle sizes

in the range of 5-15 μm . Herein, the addition of $\text{Na}_2\text{MoO}_4 \cdot 2\text{H}_2\text{O}$, by which 2D-structured independent nanoribbons are gradually changed to 3D interconnected nanosheets. Specifically, a certain concentration of MoO_4^{2-} could bridge the independent nanoribbons to form a micro-flower structure during hydrothermal treatment.

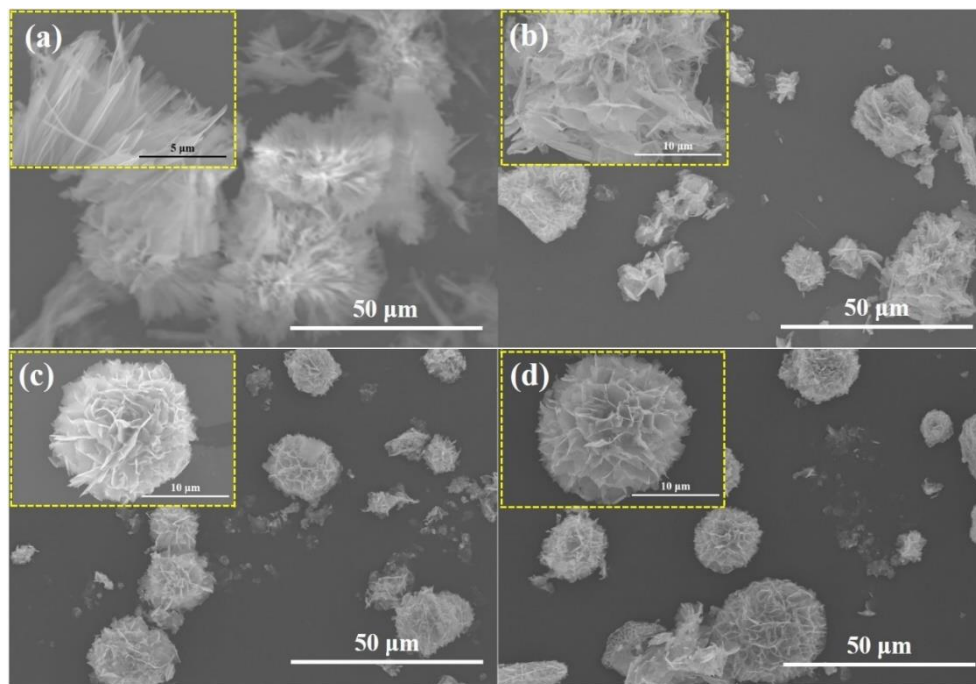


Figure 4.2 SEM images of precursors with different molar ratios of Co and Mo. (a) CM50, (b) CM51, (c) CM53, and (d) CM55.

ICP-OES was conducted to analyze the compositions of precursors with different Co/Mo molar ratios (Table 4.1). With the increase in the initial proportion of Mo in the precursor preparation process, the mass percentage of Mo in the final product gradually stabilizes at 20.3~21.5 wt%, which also results in the consistent morphologies of the CM53 and CM55 precursors. As such, only CM50, CM51, and CM55 are selected to be discussed in the following section. The SEM images of sulfurization products (CM51-S and CM55-S) are shown in Figs. 4.3c-f, which maintains the original morphologies of the precursors well. However, it should be noted that some pores are formed on the nanobelts of CM50-S (Figs. 4.3a and b), which may be resulted from the reaction between the carbon species in the precursor and H_2 in the gas flow to produce

NH₃ and CH₄ in the process of solid sulfidation. This phenomenon was also found in our previous work[30].

Table 4.1 ICP-OES analysis results of the precursors with different molar ratios of Co/Mo.

Element	Co/Mo.	
	Co wt%	Mo wt%
CM51	39.4	4.81
CM53	29.3	21.5
CM55	25.7	20.3

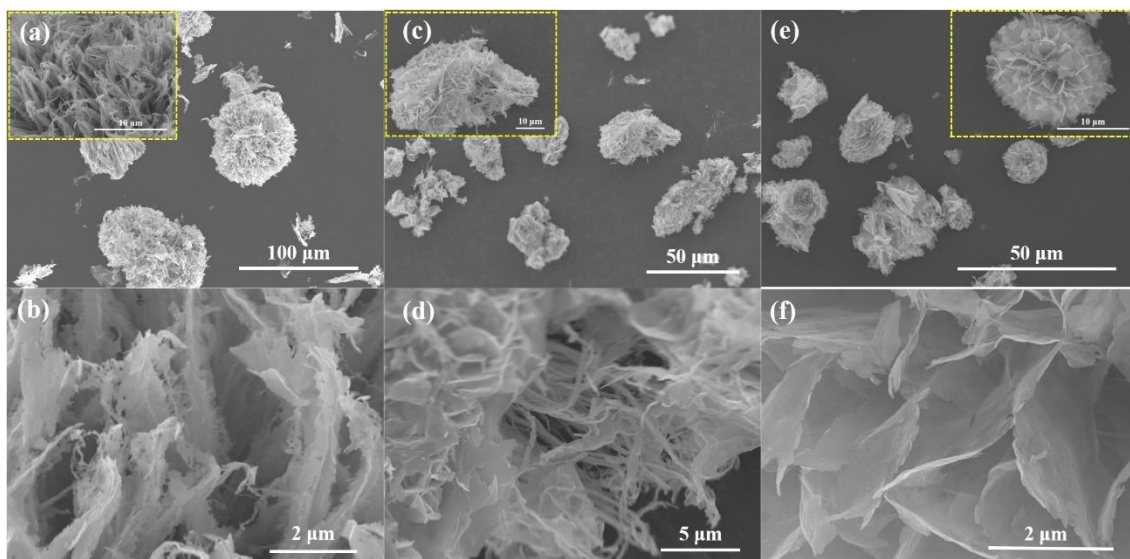


Figure 4.3 SEM images of sulfurization products with different molar ratios of Co and Mo, (a-b) CM50-S, (c-d) CM51-S and (e-f) CM55-S.

The nanostructure of CM55-S was further analyzed with TEM measurements (Fig. 4.4). As shown in Figs. 3a and b, there are almost no pores on the nanosheet, which is in agreement with the SEM observation. Figs. 4.4c-f depict the high-resolution TEM (HRTEM) images, which indicate that Co₉S₈ and layered MoS₂ (layer numbers range between 4 and 9) are well combined without obvious grain boundaries. The lattice fringe spacing of 0.625 nm is assigned to the MoS₂ (002) plane whereas the lattice fringe spacings of 0.30 and 0.35 nm just fit the Co₉S₈ (311) and Co₉S₈ (200) interplanar

distances, respectively. Several concentric circles are observed in the SAED pattern (Fig. 4.4g), which are well related to the (311), (331), (440), and (110) planes of Co_9S_8 , and (100) and (002) planes of MoS_2 , further verifying the polycrystalline characteristics and the formation of the heterostructure. EDS elements mappings (Fig. 4.4h) demonstrate that the distributions of C, S, Co, and Mo on the nanosheet are homogenous.

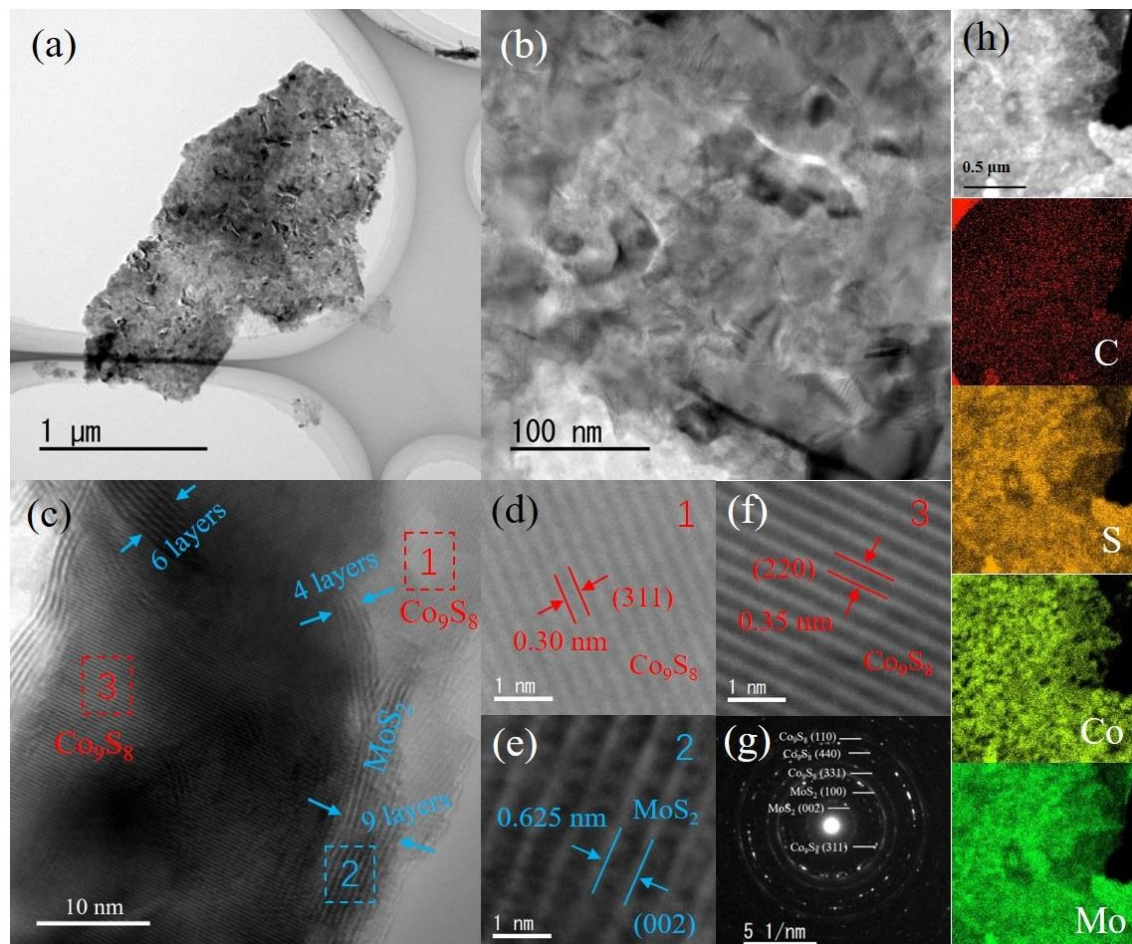


Figure 4.4 (a-b) TEM images; (c-f) HRTEM images; (g) SAED pattern; and (h) EDS elements mapping of CM55-S.

The phase purity and crystal structure of the samples were detected by XRD analysis. As displayed in Fig. 4.5a, the characteristic peaks of CM50-S are well indexed to those of Co_9S_8 (JCPDS Card No. 86-2273) without forming other impurities. The XRD characteristic peaks of CM51-S and CM55-S also correspond well to those of Co_9S_8 , and the predominant peaks located at 14.4° , 39.6° , and 58.4° can be ascribed to (002), (103), and (110) planes of 2H- MoS_2 (JCPDS Card No. 87-2416).

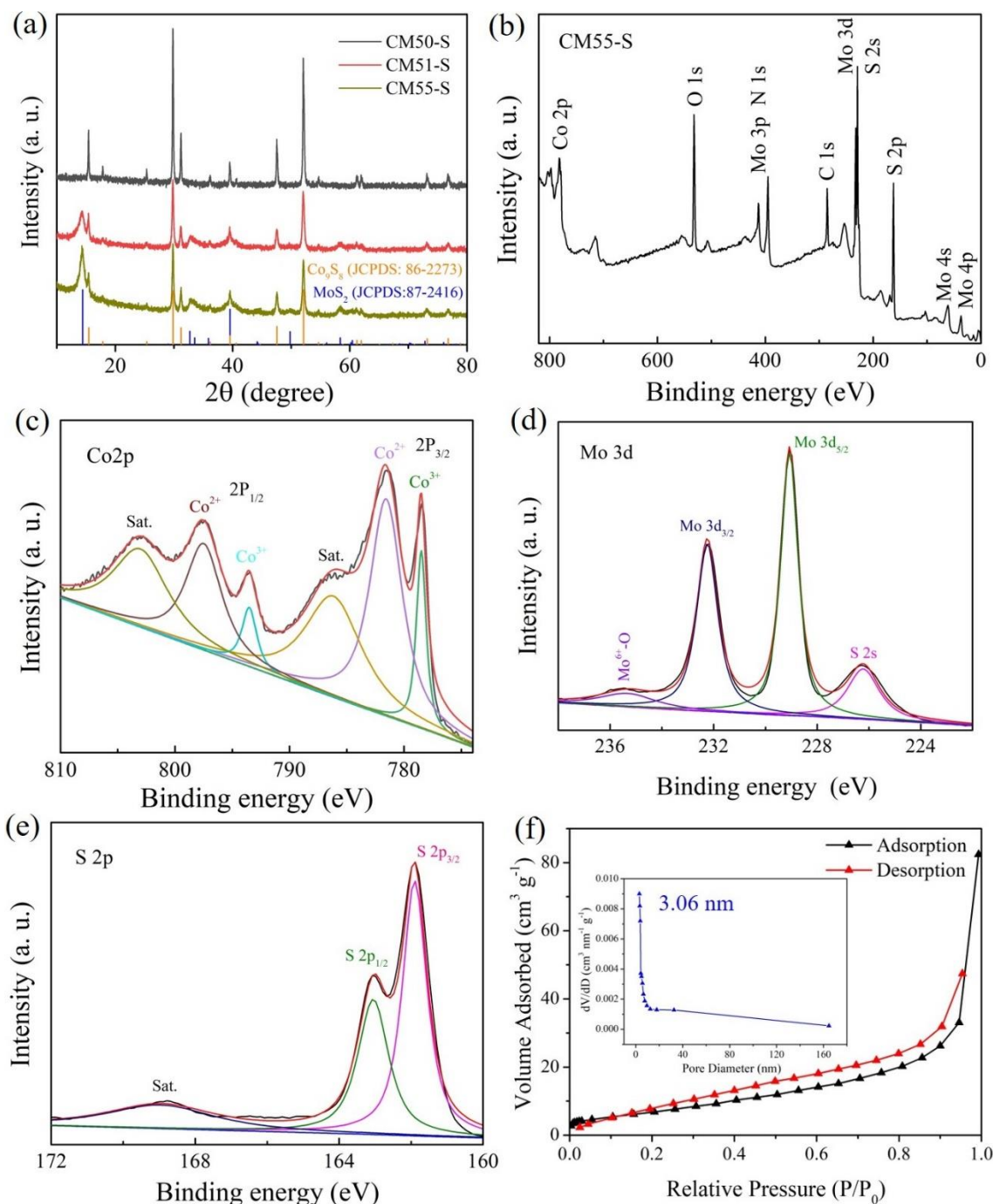


Figure 4.5 (a) XRD patterns of CM50-S, CM51-S, and CM55-S; High-resolution XPS spectra of (b) full XPS survey, (c) Co 2p, (d) Mo 3d, (e) S 2p for CM55-S; (f) Nitrogen desorption-adsorption isotherm and pore size distribution of CM55-S.

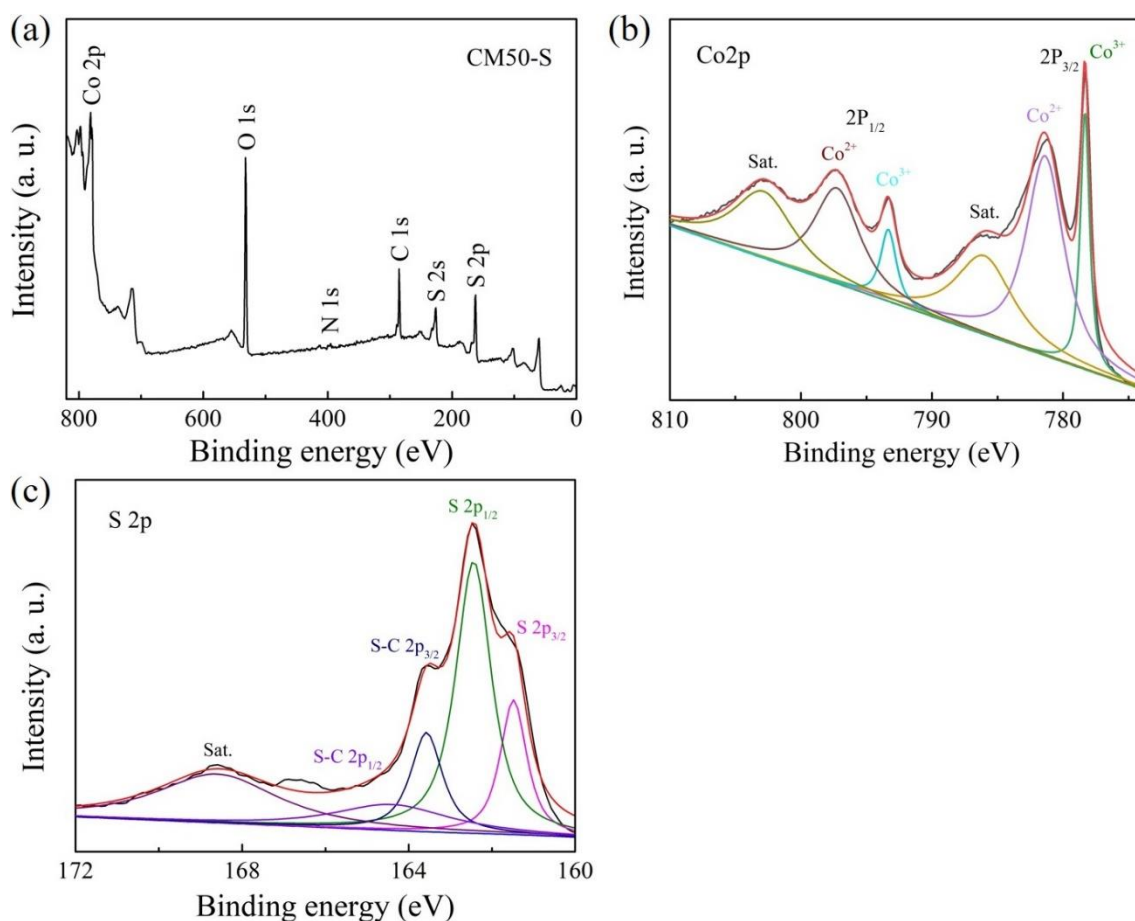


Figure 4.6 High-resolution XPS spectra of (a) full XPS survey, (b) Co 2p, and (c) S 2p for CM50-S.

Furthermore, the surface chemical compositions and valence states of the samples were determined via XPS measurement. Fig. 4.5b shows the full XPS survey of CM55-S, which indicates the coexistence of Co, Mo, S, C, N, and O species in the materials. For comparison, the full XPS survey of CM51-S (Fig. 4.7a) shows the same elemental composition as that of CM55-S. While the CM50-S (Fig. 4.6a) exhibits all other elemental compositions except Mo. The Co 2p XPS high-resolution spectrum in Fig. 4.5c is resolved into two pairs of spin-orbit doublets and two shakeup satellite peaks (denoted as sat.). Here, the two pairs of doublets (778.4/781.5 eV, 793.4/797.4 eV) should be ascribed to Co 2p_{3/2} and Co 2p_{1/2}, respectively, which are well in agreement with the data reported in the previous literature on Co₉S₈ [31]. In contrast, Co 2p XPS high-resolution spectra of CM50-S and CM51-S are shown in Figs. 4.6b and 4.7b, which exhibit almost the same peak positions as the CM55-S. The XPS high-resolution

spectra of Mo 3d (Figs. 4.5d and 4.7c) show two strong peaks centered at 229.1 and 232.2 eV, relating to $\text{Mo}^{4+} 3d_{5/2}$ and $\text{Mo}^{4+} 3d_{3/2}$, separately. While, the signal of 226.2 eV should be related to the Mo-S bond and the other weak peak at 235.3 eV can be indexed to Mo^{6+} , which can be ascribed to partial oxidation on the surface [32, 33]. Fig. 4.5e shows the S 2p XPS high-resolution spectrum of CM55-S with three peaks at 161.9, 163.1, and 169.9 eV, attributing to S $2p_{3/2}$, S $2p_{1/2}$, and one shakeup satellite, separately [34, 35]. The S 2p XPS high-resolution spectrum of CM51-S shows a similar peak distribution as the CM55-S due to their identical composition. However, the S 2p XPS high-resolution spectrum of CM50-S shows five characteristic peaks at 161.5, 162.4, 163.57, 164.4, and 168.6 eV, which can be assigned to S $2p_{3/2}$, S $2p_{1/2}$, S-C $2p_{3/2}$, S-C $2p_{1/2}$, and one shakeup satellite, separately[30].

Nitrogen desorption-adsorption properties were measured to determine specific surface areas and pore size distributions of the active materials. As displayed in Figs. 4.5f and 4.8, the isotherms of the samples exhibit a typical type-IV, implying the existence of abundant mesopores[36]. The main pore diameter distributions are concentrated at 3.36, 3.07, and 3.06 nm for CM50-S, CM51-S, and CM55-S, respectively. Besides, the BET specific surface areas of CM50-S, CM51-S, and CM55-S are 9.13, 21.82, and 26.41 $\text{m}^2 \text{g}^{-1}$, respectively. Generally, the larger specific surface area of the active material always endows a larger contact area with the electrolyte, which could accelerate mass transfer [37]. Therefore, it is expected that the CM55-S-based anode material could have a good performance for Na^+ storage.

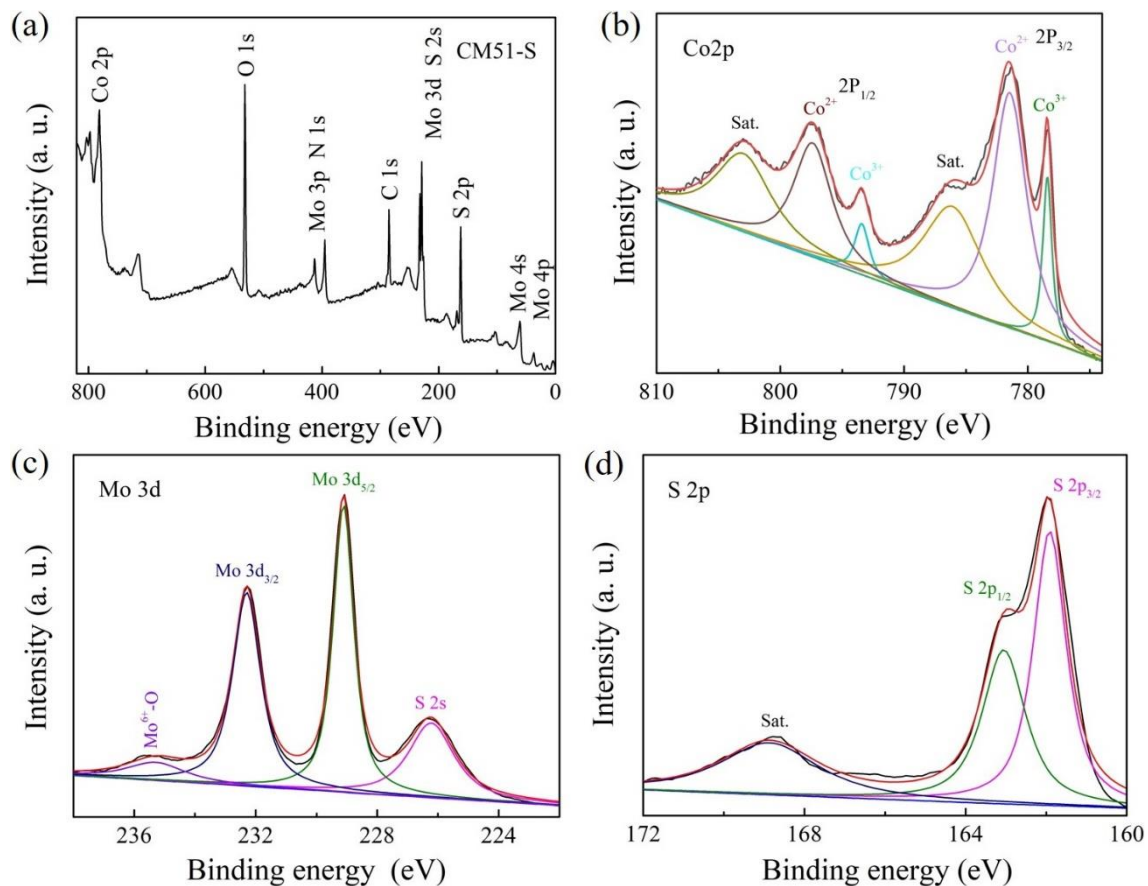


Figure 4.7 High-resolution XPS spectra of (a) full XPS survey, (b) Co 2p, (c) Mo 3d, and (d) S 2p for CM51-S.

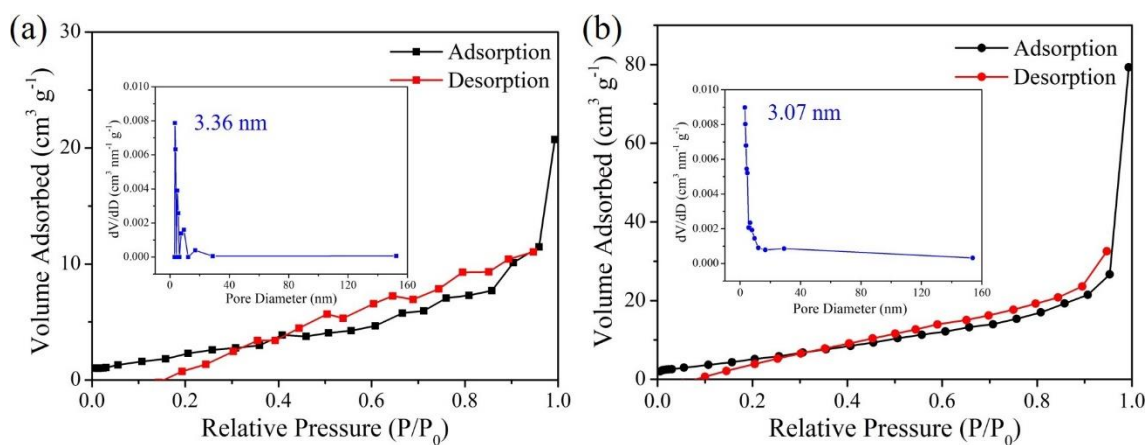


Figure 4.8 Nitrogen desorption-adsorption isotherms and pore size distributions of (a) CM50-S and (b) CM51-S.

4.3.2. Electrochemical performance

Fig. 4.9a displays the cyclic voltammetry (CV) profiles of the CM55-S-based anode for the first three cycles at a 0.1 mV s^{-1} scanning rate. Herein, two reductive peaks are observed in the 1st cathodic sweeping cycle, the peaks at 0.94 and 0.67 V can be ascribed to the phase transformations (i.e., MoS_2 to Na_xMoS_2 , Co_9S_8 to $\text{Na}_x\text{Co}_9\text{S}_8$), the solid electrolyte interface (SEI) layer formation and the corresponding conversion reactions. However, in the following two cycles, the cathodic peaks are divided into three peaks at 1.21, 0.91 and 0.64 V [33, 38]. In comparison, in the anodic sweeping, only one strong oxidation peak at 1.68 V appears, which should be assigned to the above-mentioned reversible reactions. It should be noted that the CV lines of the CM55-S-based anode almost overlap in the following two cycles, indicating that the CM55-S-based anode has high reversibility. In contrast, the CV curves of CM50-S- and CM51-S-based anodes were also investigated (Fig. 4.10). As displayed in Fig. 4.10b, only the CM51-S-based anode exhibits almost the similar curve as the CM55-S-based anode, attributing to its same composition.

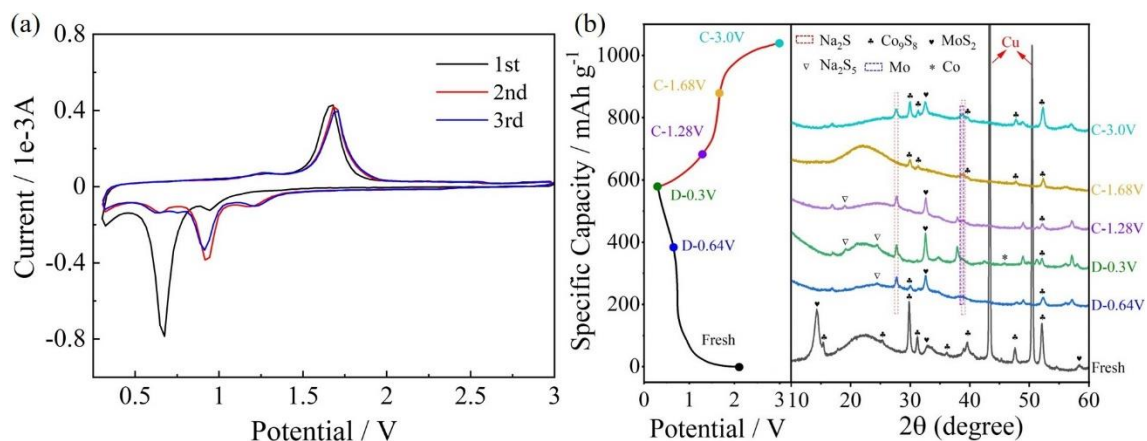


Figure 4.9 (a) CV curves of CM55-S-based anode at a scan rate of 0.1 mV s^{-1} in the potential window of 0.3-3V; (b) *Ex situ* XRD patterns of CM55-S-based anode at different charge/discharge states.

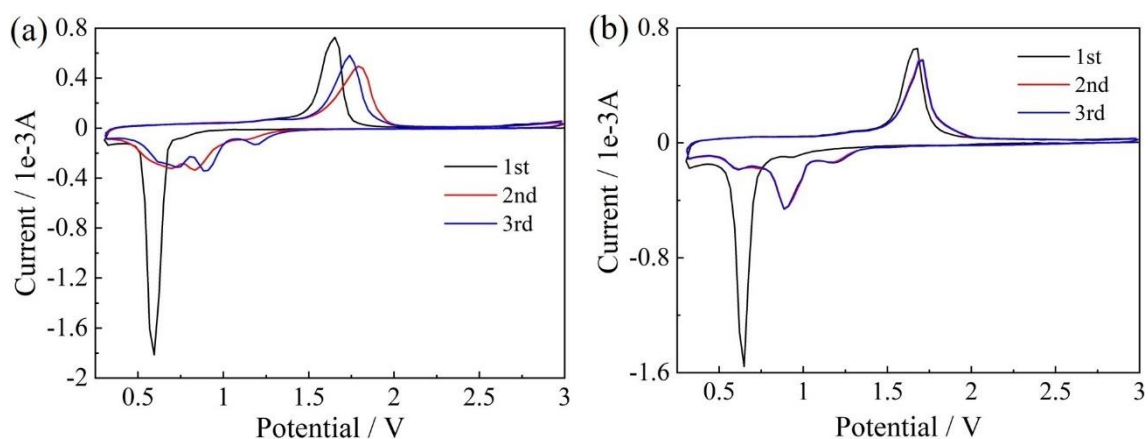


Figure 4.10 CV curves of (a) CM50-S- and (b) CM51-S-based anodes at a scan rate of 0.1 mV s^{-1} in the potential window of 0.3-3V.

To further investigate the reaction mechanism on the CM55-S-based anode, *ex situ* XRD analysis was performed to investigate the phase transformation in various discharging/charging (D/C) states (Fig. 4.9b). Before the testing, the XRD peaks of MoS_2 and Co_9S_8 are observed for the fresh electrode. During the discharge process, the number of signal peaks of MoS_2 and Co_9S_8 decreases obviously. In addition, four new reflections emerge at 19.1° , 24.5° , 27.4° , and 39.0° , which can be assigned to Na_2S_5 ((101) and (040) lattice planes, JCPDS card No. 77-0294) and Na_2S ((200) and (220) lattice planes, JCPDS card No. 77-2149), respectively. The existence of Na_2S_5 is also observed in other transition metal sulfide-based anodes, which can be attributed to its complex redox reactions [33, 39, 40]. Furthermore, Na_2S , as an intermediate product, reflects the typical conversion reactions (i.e., $\text{Na}_x\text{Co}_9\text{S}_8 + (16-x) \text{Na}^+ + (16-x) \text{e}^- \rightarrow 8 \text{Na}_2\text{S} + 9 \text{Co}$, $\text{Na}_x\text{MoS}_2 + (4-x) \text{Na}^+ + (4-x) \text{e}^- \rightarrow 2 \text{Na}_2\text{S} + \text{Mo}$). The presence of metallic Co and Mo also confirms the progress of the conversion reaction. Conversely, the number of XRD signal peaks of MoS_2 and Co_9S_8 increase, and the peak intensity of some peaks are enhanced when charging to 3.0 V, also representing the above reversible reactions. Based on these *ex-situ* XRD analysis results, it can know the high reversibility of CM55-S-based anode during the process for the inserting/extracting of Na^+ .

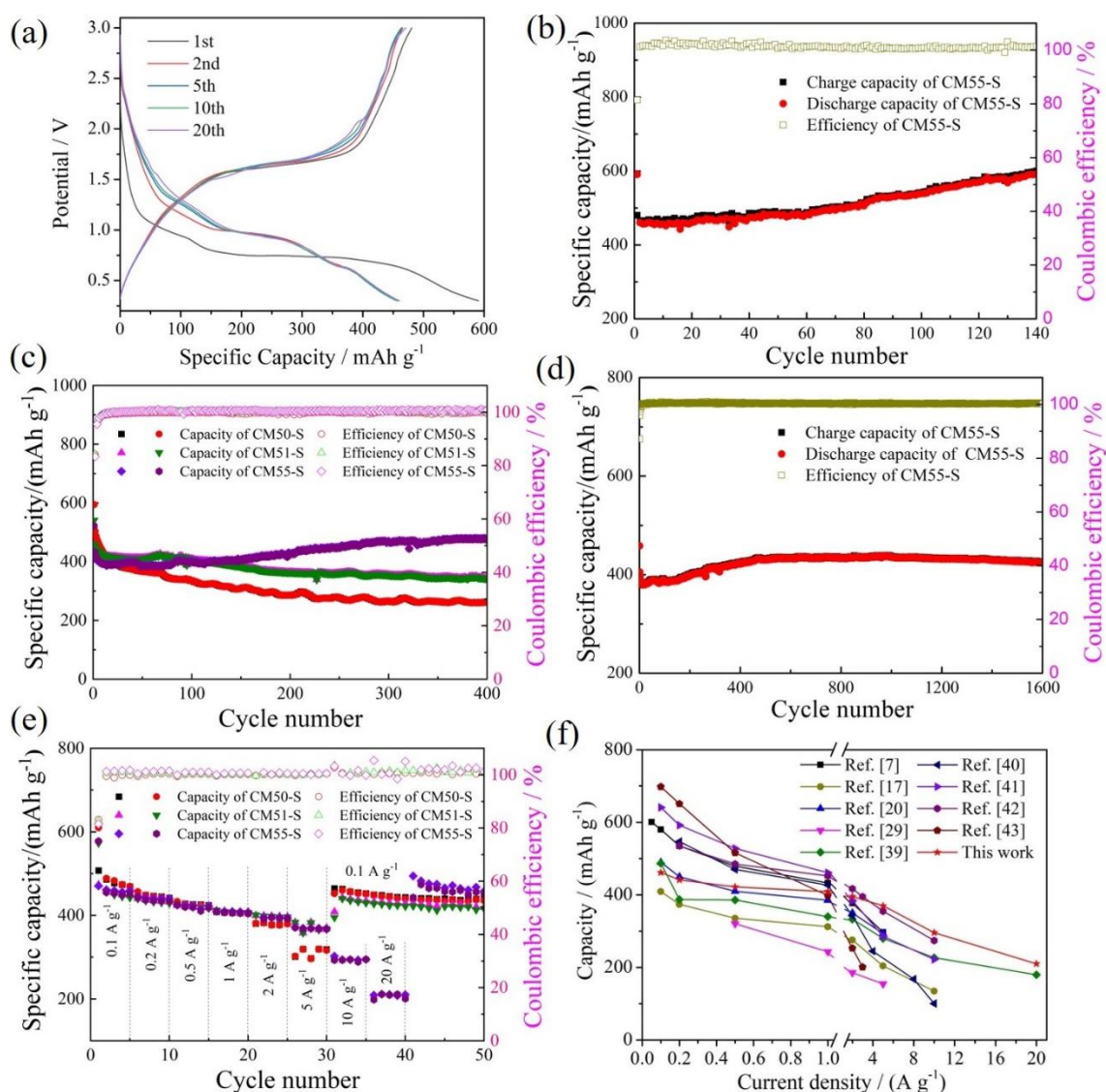


Figure 4.11 (a) Typical galvanostatic charge-discharge profiles of CM55-S-based anode at 0.1 A g⁻¹ with different cycles (1st, 2nd, 5th, 10th, and 20th); Cycling performance of CM55-S-based anode at current densities of (b) 0.1 A g⁻¹ and (d) 2 A g⁻¹; (c) Cycling performances of CM50-S-, CM51-S- and CM55-S-based anodes at the current density of 1 A g⁻¹; (e) Rate performances of CM50-S-, CM51-S- and CM55-S-based anodes; (f) Comparison of rate performance of the CM55-S-based anode with other Co₉S₈- and MoS₂-based anodes.

Fig. 4.11a exhibits the galvanostatically charging/discharging voltage profiles of the CM55-S-based anode at the current density of 0.1 A g⁻¹. One can see that the initial discharge/charge capacity is 590.7/480.6 mA h g⁻¹, corresponding to an initial Coulombic efficiency (CE) of 81.4%. Herein, it should be noted that irreversible

capacity loss occurs in the 1st cycle, which should be due to the SEI layer formation on the electrode [41]. The CE of 99.4% and $\sim 100\%$ are obtained for the 2nd and subsequent cycles, respectively. Furthermore, the CM55-S-based anode exhibits excellent reversibility with a higher capacity, delivering a discharge capacity of 599.8 mA h g⁻¹@ 0.1 A g⁻¹ even at the 140th cycle (Fig. 4.11b). For comparison, the galvanostatically charging/discharging voltage profiles of CM50-S- and CM51-S-based anodes were also obtained (Fig. 4.12), which show that the CM50-S- and CM51-S-based anodes have the initial CEs of 82.6% (602.3/497.8 mA h g⁻¹) and 80.1% (569.5/455.8 mA h g⁻¹), respectively. Generally, a larger specific surface area may result in more SEI layer formation on the active material, thereby exhibiting a lower initial CE. Therefore, the larger specific surface area leads to the lower initial CEs for CM51-S- and CM55-S-based anodes.

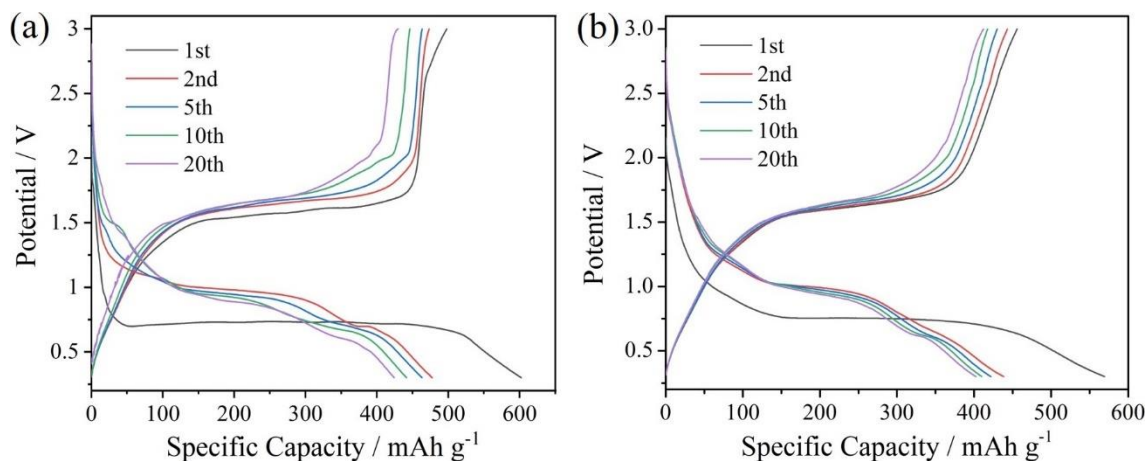


Figure 4.12 Typical galvanostatic charge/discharge profiles of (a) CM50-S- and (b) CM51-S-based anodes at 0.1 A g⁻¹ with different cycles (1st, 2nd, 5th, 10th, and 20th).

Fig. 4.11c shows the cycling performances of CM50-S-, CM51-S-, and CM55-S-based anodes tested at 1 A g⁻¹ in a cutoff voltage range of 0.3-3 V. The capacity of CM55-S-based anode decays rapidly in the first 20 cycles but gradually increases in the subsequent cycles, and as a result, the highest charge capacity of 473.2 mA h g⁻¹ is obtained even after 400 cycles, corresponding to a 109.5% capacity retention based on the second-cycle charge capacity. On the contrary, the capacities of CM50-S- and CM51-S-based anodes continue to decay during the cycling and only deliver the charge

capacities of 261.4 and 342.8 mA h g⁻¹ after 400 cycles, which are much lower than that of CM55-S-based anode. Fig. 4.11d exhibits the cycling performance of the CM55-S-based anode at 2 A g⁻¹, which displays the same trend as the test at 1 A g⁻¹. Specifically, the charge/discharge capacity stabilizes at approximately 431.9/430.7 mA h g⁻¹ after 460 cycles and maintained a considerable capacity of 426/424.5 mA h g⁻¹ even after 1600 cycles with a capacity retention of 104.7%. Furthermore, as shown in Fig. 4.13, the CM55-S-based anode also delivers an exceptional charge capacity of 401.1 mA h g⁻¹ even at 5 A g⁻¹ after 800 cycles (the first ten cycles were tested at 1 A g⁻¹). Thus, the CM55-S-based anode delivers excellent cycling stability.

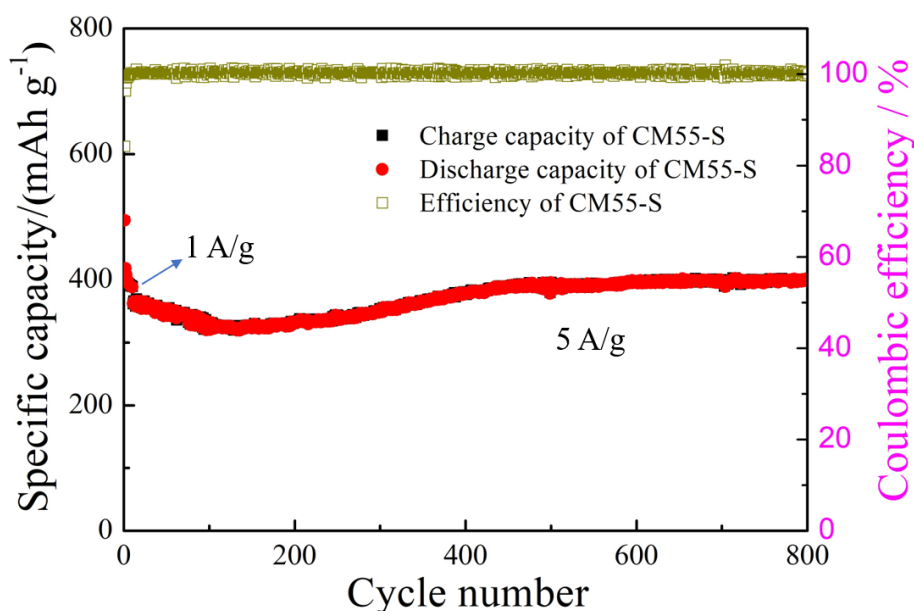


Figure 4.13 Cycling performance of CM55-S-based anode at a current density of 5 A g⁻¹ (the first ten cycles were tested at 1 A g⁻¹).

To better understand the main reasons for the enhanced electrochemical performance, HRTEM and SAED analyses were conducted for the CM55-S-based anode after 150 cycles at 0.2 A g⁻¹ (Fig. 4.14). As indicated in Fig. 4.14a, the interlayer spacing of MoS₂ is expanded from 0.625 to 0.72/0.74 nm, which should endow more active sites for Na⁺ storage and lower the energy barrier for Na⁺ inserting/extracting [25, 42]. The repeated insertion/extraction of Na⁺ with cycling is the main reason for the expansion of the interlayer spacing of MoS₂ [25, 43, 44]. While, the lattice fringe spacing of 0.375 nm is attributed to the (111) plane of Na₂S, and the diffraction rings

of Na_2S and Co_9S_8 are also found in the SAED pattern (Fig. 4.14b), which is in agreement with *ex-situ* XRD analysis result.

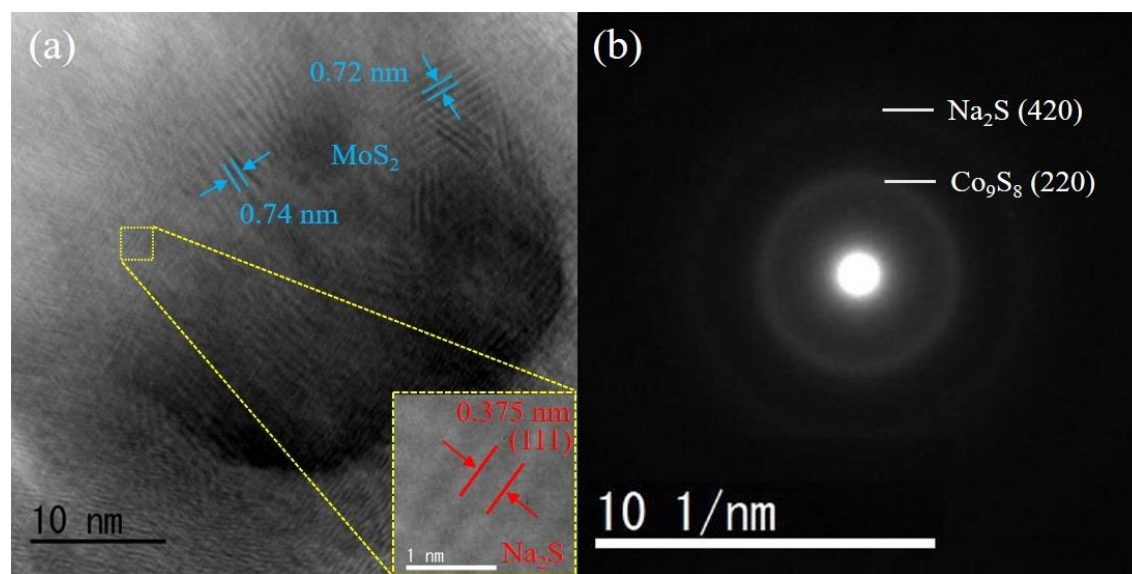


Figure 4.14 (a) HRTEM image and (b) SAED pattern of CM55-S-based anode after 150 cycles at the current density of 0.2 A g^{-1} .

The rate capabilities of CM50-S-, CM51-S-, and CM55-S-based anodes were investigated at various current densities from 0.1 to 20 A g^{-1} . As displayed in Fig. 4.11e, the CM55-S-based anode delivers average capacities around 461.5 , 441.5 , 422.0 , 409.1 , 395.4 , 369.7 , and $295.8 \text{ mA h g}^{-1}$ at 0.1 , 0.2 , 0.5 , 1.0 , 2.0 , 5.0 and 10.0 A g^{-1} , respectively. It also exhibits a considerable capacity of $210.1 \text{ mA h g}^{-1}$ even at 20 A g^{-1} . When the current density is set back to 0.1 A g^{-1} , its reversible capacity is also recovered to about $471.7 \text{ mA h g}^{-1}$, which is higher than those of the first five cycles. In contrast, the CM50-S- and CM51-S-based anodes exhibit worse rate performances, which only exhibit reversible capacities of 311.3 and $372.2 \text{ mA h g}^{-1}$ at 5 A g^{-1} , respectively. When the current density is returned to 0.1 A g^{-1} , their capacities are significantly less than that of the CM55-S-based anode. Furthermore, the typical galvanostatic charge-discharge profiles corresponding to the rate performance are shown in Fig. 4.15. The 1st, 3rd, 8th, 13th, 18th, 23rd, 28th, 33rd, 38th, and 43rd circles of the rate capacity test were selected to draw the curves, which correspond to different rate test conditions from 0.1 to 20 A g^{-1} and return to 0.1 A g^{-1} . It can be seen that with the

increase of the current density, the capacity gradually decays. The charge-discharge platform can be seen at 0.1-5 A g⁻¹, however, when the current density increases to 10 or 20 A g⁻¹, there is no obvious charge-discharge platform since only a few points were collected. When the current density returns to 0.1 A g⁻¹ again, the charge-discharge platform reappears and the capacity is slightly higher than that of the 3rd circle. As indicated in Fig. 4.11f, compared with the rate capabilities of other reported Co₉S₈-based and MoS₂-based anodes, the CM55-S-based anode exhibits more excellent rate performance, which can be assigned to the synergistic advantages of the Co₉S₈/MoS₂ heterostructure materials [7, 17, 32, 45-49].

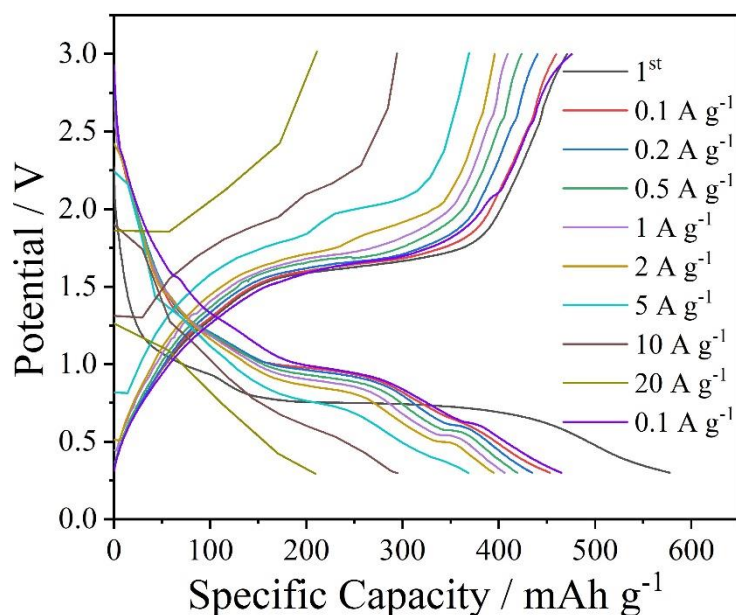


Figure 4.15 Typical galvanostatic charge/discharge profiles corresponding to rate performance for CM55-S-based anode.

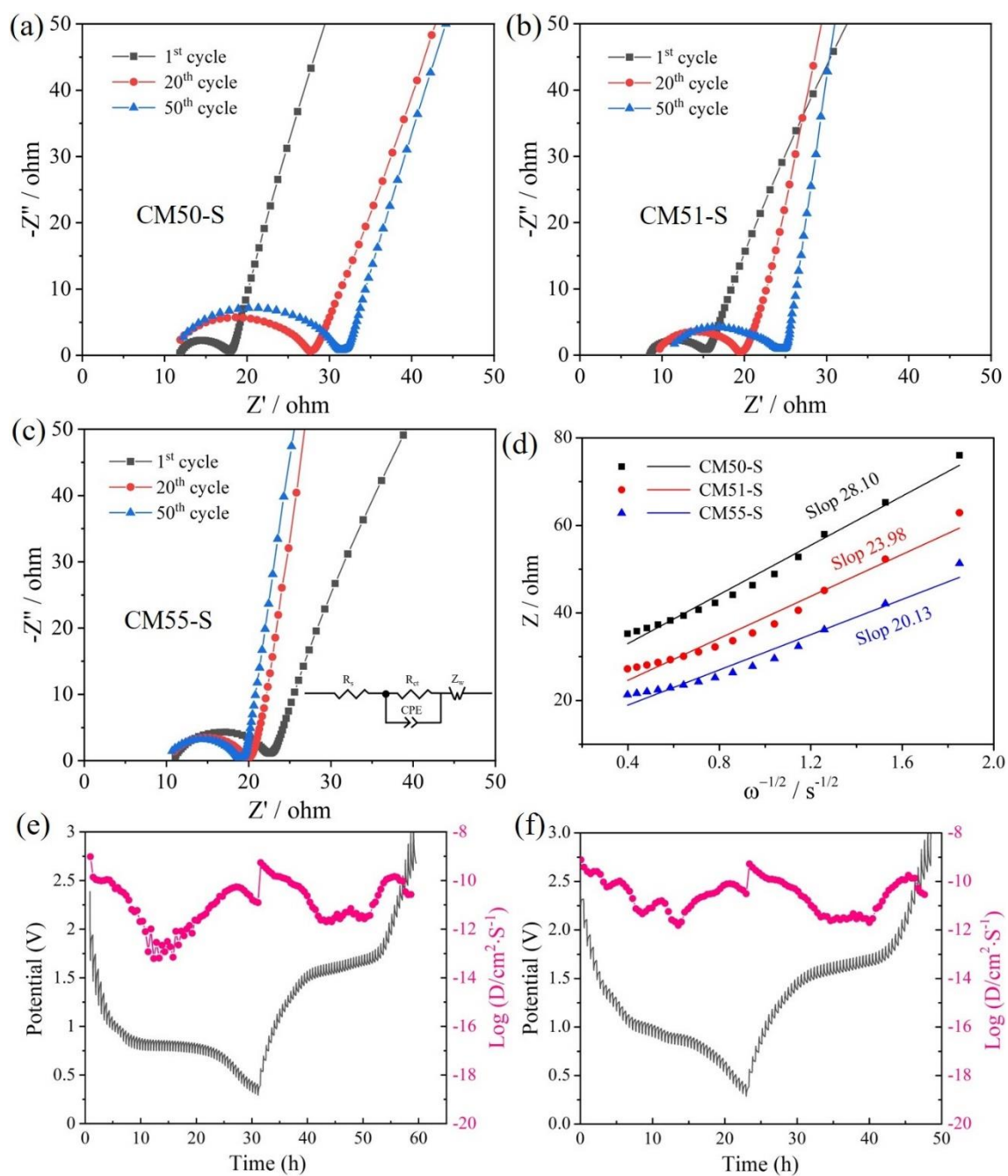


Figure 4.16 Nyquist plots of (a) CM50-S, (b) CM51-S, and (c) CM55-S based anodes after different cycles (1, 20, and 50); (d) Fitted straight lines between z' and $\omega^{-1/2}$ at the low-frequency region for CM50-S-, CM51-S- and CM55-S-based anodes after 50 cycles; The discharge/charge profiles and corresponding Na^+ diffusion coefficients of CM55-S-based anode in GITT measurements of (e) the first cycle, and (f) the 20th cycle.

Table 4.2 Fitting results of Nyquist plots based on the equivalent circuit after 1, 20 and 50 cycles.

Electrode	1 st cycle		20 th cycle		50 th cycle	
	R_s	R_{ct}	R_s	R_{ct}	R_s	R_{ct}
CM50-S	11.72	5.57	10.79	16.2	11.09	19.66
CM51-S	8.54	6.75	9.47	9.46	10.3	13.41
CM55-S	10.96	11.38	10.61	8.8	10.22	8.31

To further investigate Na^+ storage kinetics of the as-prepared electrodes (CM50-S, CM51-S, and CM55-S), electrochemical impedance spectroscopy (EIS) profiles were measured. Figs. 4.16a-c show the Nyquist plots after 1, 20, and 50 cycles at 0.2 A g^{-1} , which are composed of a compressive semicircle in the middle-to-high frequency range and a straight line in the low-frequency range. Herein, the semicircle corresponds to charge-transfer resistance (R_{ct}) at the interface of the electrolyte/electrode, and the straight line is attributed to the Warburg impedance (Z_w) during Na^+ diffusion[50]. Obviously, there is a decrease in the semicircle diameter for the CM55-S-based anode and an increased semicircle diameter for the CM50-S- and CM51-S-based anodes with the cycling, indicating an activation process for the CM55-S-based anode. The specific resistance values are evaluated by fitting those experimental data with an equivalent circuit model (inset of Fig. 4.16c). As shown in Table 4.2, the R_{ct} value of CM55-S-based anode gradually decreases with the cycling, indicating the enhanced charge transfer kinetics, which is one of the main reasons for its increased charge/discharge capacity with superior rate capability. Whereas, the R_{ct} values increase with the cycling for the CM50-S- and CM51-S-based anodes, which could be assigned to the slower charge transfer rate of the 2D nanoribbon structure than the 3D micro-flower structure. Especially, the lack of support structure in the nanoribbons makes it easier to pulverize during the sodiation/desodiation process, further weakening the charge transfer kinetics.

To explore Na^+ diffusion characteristics of CM50-S-, CM51-S- and CM55-S-based anodes, the Warburg impedance coefficient (σ_w) was evaluated by the following

equation:

$$Z' = R_s + R_{ct} + \sigma_w \omega^{-0.5} \quad (1)$$

where Z' and ω represent the real part of the impedance and the angular frequency, respectively, and σ_w can be evaluated by fitting the slope of Z' vs. $\omega^{-0.5}$ linearly. As depicted in Fig. 4.16d, the CM55-S-based anode exhibits a smaller slope after 50 cycles than the CM50-S- and CM51-S-based anodes, indicating its faster Na^+ diffusion ability.

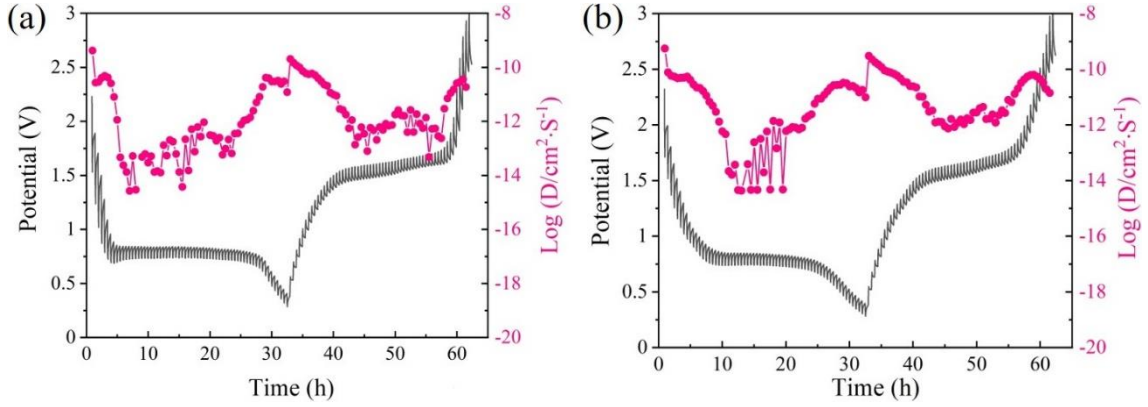


Figure 4.17 The discharge/charge profiles and corresponding Na^+ diffusion coefficients of (a) CM50-S-, and (b) CM51-S-based anodes in GITT measurements of the first cycle.

The diffusion coefficients of Na^+ (D_{Na^+}) at various discharge/charge states can be evaluated by galvanostatic intermittent titration technique (GITT) measurements. As such, the electrodes (CM50-S, CM51-S, and CM55-S) were tested with a series of pulse currents (0.1 A/g for 5 min) and an open-circuit stand for 25 min. For GITT measurement, the assembled battery before and after the cycling test for 20 cycles at 0.1A/g were investigated. Herein, the D_{Na^+} is calculated by the following equation:

$$D_{\text{Na}^+} = \frac{4}{\pi\tau} \left(\frac{nV_m}{S} \right)^2 \left(\frac{\Delta E_s}{\Delta E_\tau} \right)^2 \quad (2)$$

where τ is the pulse time of current; n and V_m denote the molar number and molar volume, respectively; S represents the electrode/electrolyte interface area; ΔE_s and ΔE_τ are respectively the voltage change during two adjacent steady-states and the constant-current pulse. As indicated in Figs. 4.16e and f, the CM55-S-based anode exhibits a higher D_{Na^+} in the 20th cycle compared to the first cycle. For comparison, the CM50-S- and CM51-S-based anodes were also investigated with the GITT measurement (Figs. 4.17 a and b), and the D_{Na^+} values in the first cycle are both smaller than that of the

CM55-S-based anode. This phenomenon is consistent with the fitting results of straight lines between z' and $\omega^{-1/2}$ in the low-frequency region, indicating faster Na^+ diffusion in the CM55-S-based anode.

4.3.3. Electrochemical kinetics

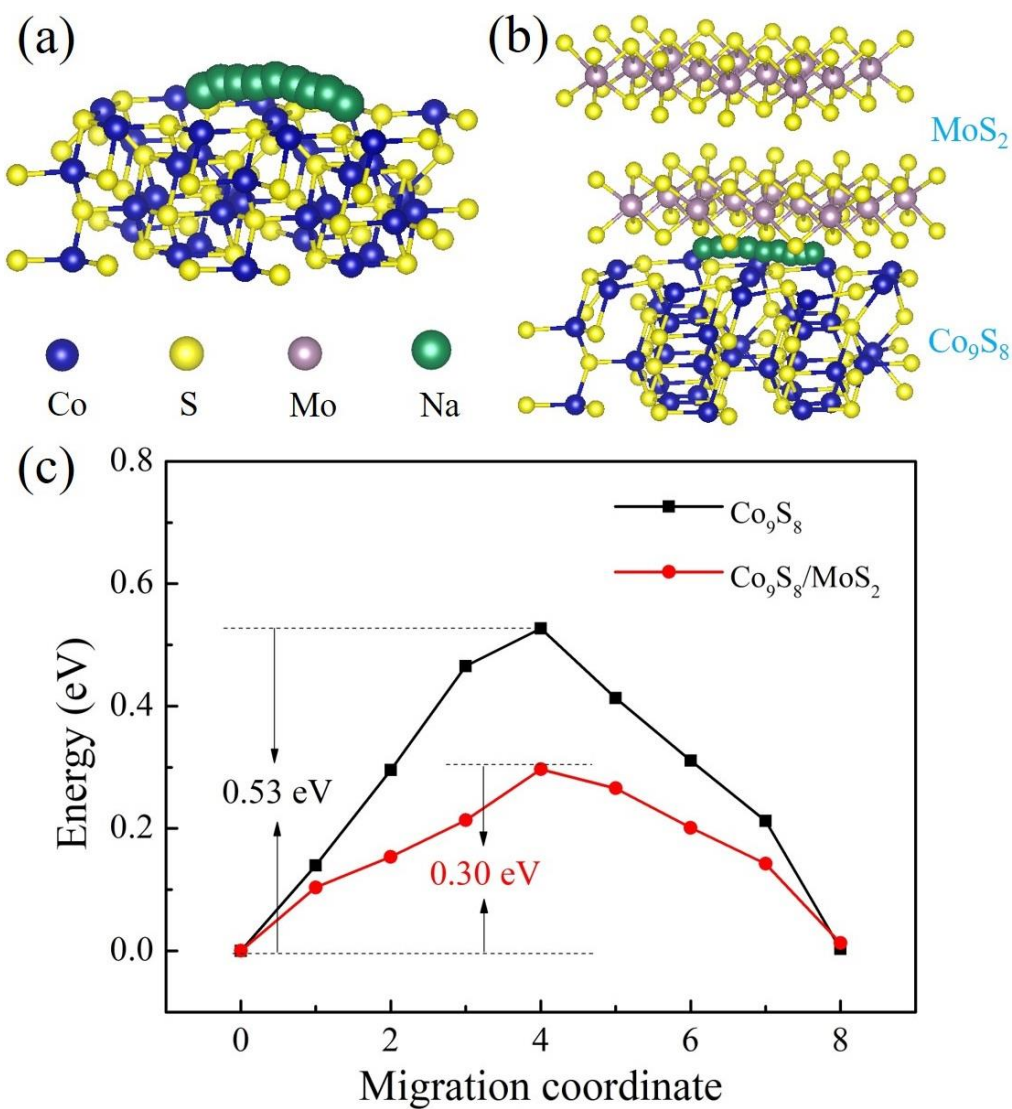


Figure 4.18 Schematic illustration of the diffusion path for Na^+ in (a) Co_9S_8 and (b) $\text{Co}_9\text{S}_8/\text{MoS}_2$ heterostructure, and (c) corresponding energy profiles between adjacent low-energy sites.

DFT calculations were also performed to further explore the interfacial diffusivity of the $\text{Co}_9\text{S}_8/\text{MoS}_2$ heterostructure. As shown in Figs. 4.18a and b, geometric models of

Co₉S₈ pure phase and Co₉S₈/MoS₂ heterostructure are established based on the HRTEM analysis results, in which the interface between the (220) plane of Co₉S₈ and (002) plane of MoS₂ is formed as the heterojunction. It is well known that such a heterojunction may introduce a built-in electric field, where the Na⁺ migration can be accelerated to some extent via the Coulomb force [34, 51]. The diffusion path between the adjacent lowing-energy sites and the corresponding energy profiles are shown in Fig. 4.18c, which are obtained by the climbing-image nudged elastic band method [52]. It is found that the Na⁺ diffusion energy barrier in the Co₉S₈/MoS₂ heterostructure (0.30 eV) is smaller than that of the Co₉S₈ pure phase (0.53 eV), indicating that the Na⁺ diffusion kinetics at the heterointerface is more favorable, which is in agreement with the GITT measurement results.

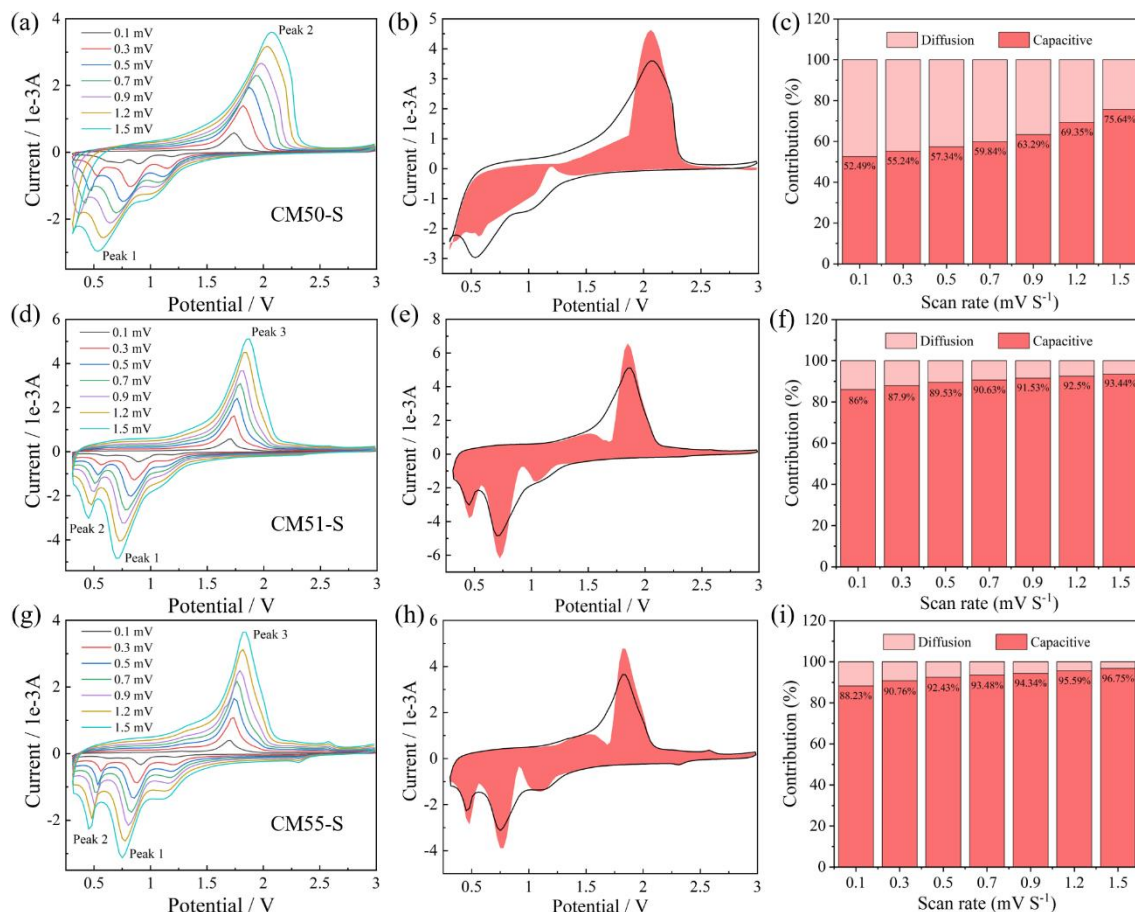


Figure 4.19 CV curves of (a) CM50-S-, (d) CM51-S-, and (g) CM55-S-based anodes in a voltage range of 0.3-3 V at different scan rates from 0.1 to 1.5 mV s⁻¹; Capacitive contributions of (b) CM50-S-, (e) CM51-S- and (h) CM55-S-based anodes compared with the total current at 1.5 mV s⁻¹; The capacitive contributions of (c) CM50-S-, (f)

CM51-S- and (i) CM55-S-based anodes at different scan rates from 0.1 to 1.5 mV s⁻¹.

To further explore the Na⁺ storage mechanism of the Co₉S₈/MoS₂-based anode, a set of CV curves were tested at different scan rates from 0.1 to 1.5 mV s⁻¹. One can see that the reduction peak shifts to the left whereas the oxidation peak shifts to the right with the increase of scan rate from 0.1 to 1.5 mV s⁻¹, which can be ascribed to the potential polarization [53]. As illustrated in Fig. 4.19 a, for the CM50-S-based anode, at low reduction potentials, the reduction peak gradually shifts to the left with the increasing of scan rates, even exceeding the low testing potential limitation of 0.3 V. However, for the CM51-S- and CM55-S-based anodes, the shapes of the CV curves (Figs. 4.19d and g) are well maintained with the increase in the scan rate, implying the high-rate capability and small potential polarization. Generally, the peak current (*i*) and scan rate (*v*) in the CV curve obey the equation as follows [54]:

$$i = av^b \quad (3)$$

Herein, the different values of *b* (ranging from 0.5 to 1) can reflect different Na⁺ storage mechanisms. Specifically, the *b*-value approaching 1.0 manifests a capacitive-controlled process. While the *b*-value closing to 0.5 indicates the diffusion-controlled process[55]. Herein, the *b* value can be quantified by fitting the log(*v*)-log(*i*) plot. As displayed in Fig. 4.20 c, the *b* values approaching 1 (i.e., *b* = 0.83, 1.04, and 0.82) indicate that the Na⁺ storage of CM55-S-based anode is predominantly determined by the surface-induced capacitance property. While the *b* values of the CM51-S-based anode approaching 1.0 (Fig. 4.20 b) suggest that it has a similar Na⁺ storage mechanism as the CM55-S-based anode. However, due to the absence of Mo modification, the *b* values of CM50-S-based anodes relating to the two peaks are 0.78 and 0.66 (Fig. 4.20 a), respectively, revealing that both surface capacity-controlling and diffusion-controlling behaviors should be the dominant processes for charge storage. Besides, the capacity contribution ratio of CM55-S-based anode can be evaluated via fitting and calculating the current (*i*) measured at a specific voltage (*V*) based on the following formulas:

$$i(V) = k_1 v + k_2 v^{1/2} \quad (4)$$

$$i(V)/v^{1/2} = k_1 v^{1/2} + k_2 \quad (5)$$

where, k_1 and k_2 are constants, $k_1 v$ and $k_2 v^{1/2}$ relate to surface-induced capacitance and diffusion-controlled processes, respectively. As displayed in Fig. 4.19h, the CM55-S-based anode exhibits a capacitive contribution of 96.75% at 1.5 mV s⁻¹. The capacitive contributions of other scan rates are displayed in Fig. 4.19i. One can see that the CM51-S-based anode exhibits capacitive contributions of 86%, 87.9%, 89.53%, 90.63%, 92.5%, and 93.44% with the scan rate increase from 0.1 to 1.5 mV s⁻¹ (Figs. 4.19e and f), which are slightly lower than those of the CM55-S-based anode due to their similar composition. However, as the scan rate increases, the capacitive contributions of 52.49%, 55.24%, 57.34%, 59.84%, 63.29%, 69.35 and 75.64% can be obtained for the CM50-S-based anode (Fig. 4.19c). Therefore, it can be concluded that the addition of MoS₂ can enhance the capacitive contribution of Co₉S₈ and facilitate charge transfer.

Based on the above material characterization and kinetic analysis results, the extraordinary sodium storage performance of the CM55-S-based anode should be ascribed to its special 3D micro-flower heterostructure, by which the charge transfer can be accelerated by the built-in electric field in the heterostructure. While the expanded interlayer spacing of MoS₂ during the reaction process provides more active sites for Na⁺ storage and lowers the energy barrier for Na⁺ intercalation/deintercalation. In addition, the unique 3D micro-flower-like CM55-S heterostructure assembled by nanosheets can enlarge the electrolyte/electrode contact area and maintain structural stability, thereby improving the cycling stability during the charge/discharge process.

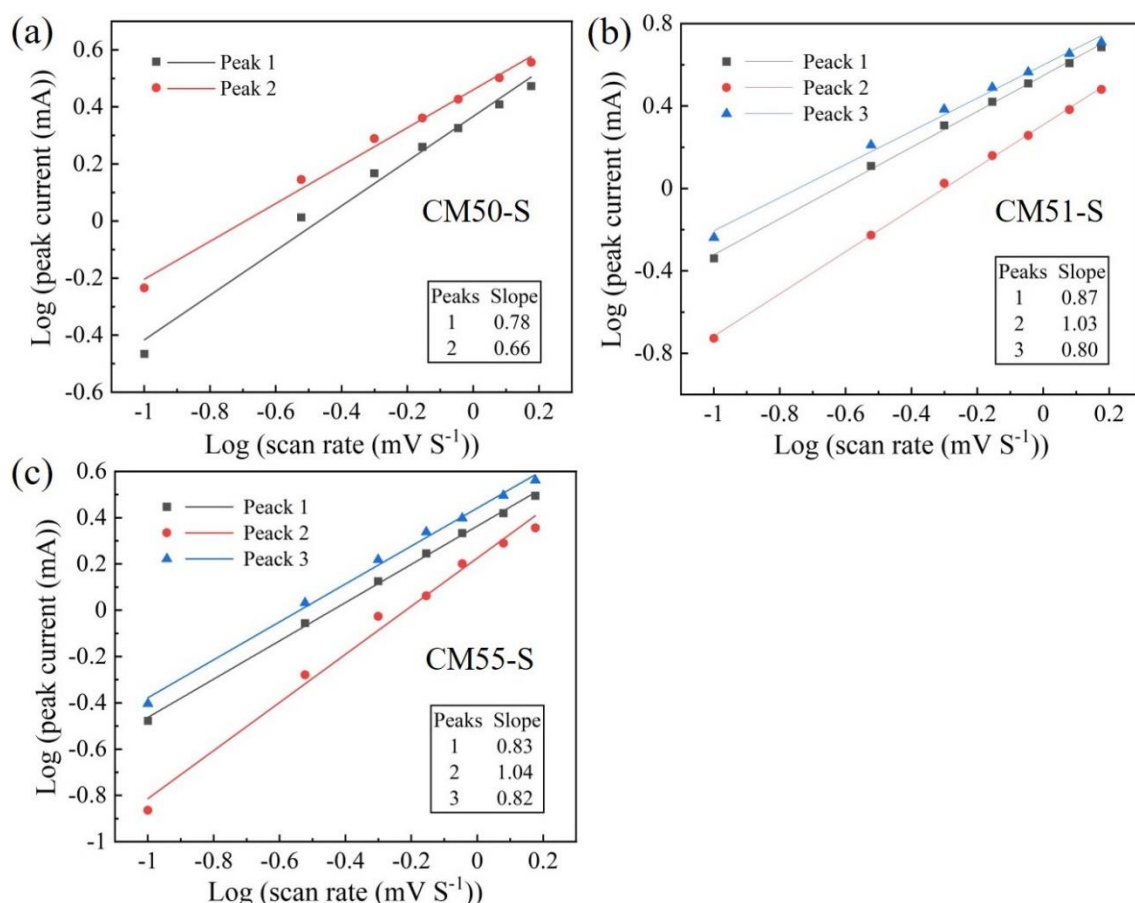


Figure 4.20 The fitting lines of $\log i$ vs $\log v$ of peaks in CV curves for (a) CM50-S, (b) CM51-S, and (c) CM55-S.

4.4. Conclusions

In summary, a 3D micro-flower-like $\text{Co}_9\text{S}_8/\text{MoS}_2$ heterostructure with rapid charge transfer and synergistic physicochemical properties was successfully designed and fabricated via a facile hydrothermal synthesis method followed by a solid sulfidation treatment process. It is found that the addition of Mo species during the synthesis process played a crucial role in the formation of 3D micro-flower-like morphology, and the overall morphology and the percentage ratio of Mo in the final product tended to be stable with the increase of initial Mo content. As the anode material for SIBs, the CM55-S-based anode exhibited enhanced capacity, excellent reversibility (424.5 mAh g^{-1} at 2 A g^{-1} for 1600 cycles, 401.1 mAh g^{-1} at 5 A g^{-1} for 800 cycles), and superior rate capacities (295.8 mAh g^{-1} at 10 A g^{-1} , 210.1 mAh g^{-1} at 20 A g^{-1}), which should be attributed to the rational design of 3D micro-flower-like heterostructure with more

active sites for Na^+ storage, high-speed charge transfer, and low energy barrier. This chapter provides a reliable way for designing sulfides with 3D heterostructures as electrodes for energy storage devices.

References

- [1] J.Y. Huang, L. Zhong, C.M. Wang, J.P. Sullivan, W. Xu, L.Q. Zhang, S.X. Mao, N.S. Hudak, X.H. Liu, A. Subramanian, H.Y. Fan, L.A. Qi, A. Kushima, J. Li, In Situ Observation of the Electrochemical Lithiation of a Single SnO₂ Nanowire Electrode, *Science* 330 (2010) 1515-1520.
- [2] B.L. Ellis, W.R.M. Makahnouk, Y. Makimura, K. Toghill, L.F. Nazar, A multifunctional 3.5 V iron-based phosphate cathode for rechargeable batteries, *Nature Mater.* 6 (2007) 749-753.
- [3] G.Q. Zou, H.S. Hou, P. Ge, Z.D. Huang, G.G. Zhao, D.L. Yin, X.B. Ji, Metal-Organic Framework-Derived Materials for Sodium Energy Storage, *Small* 14 (2018).
- [4] X. Ou, L. Cao, X.H. Liang, F.H. Zheng, H.S. Zheng, X.F. Yang, J.H. Wang, C.H. Yang, M.L. Liu, Fabrication of SnS₂/Mn₂SnS₄/Carbon Heterostructures for Sodium-Ion Batteries with High Initial Coulombic Efficiency and Cycling Stability, *Acs Nano* 13 (2019) 3666-3676.
- [5] Q.C. Pan, Q.B. Zhang, F.H. Zheng, Y.Z. Liu, Y.P. Li, X. Ou, X.H. Xiong, C.H. Yang, M.L. Liu, Construction of MoS₂/C Hierarchical Tubular Heterostructures for High-Performance Sodium Ion Batteries, *Acs Nano* 12 (2018) 12578-12586.
- [6] X.C. Hou, Y.Z. Zhang, Q.C. Dong, Y. Hong, Y.L. Liu, W.J. Wang, J.J. Shao, W.L. Si, X.C. Dong, Metal Organic Framework Derived Core-Shell Structured Co₉S₈@N-C@MoS₂ Nanocubes for Supercapacitor, *Acs Appl. Energ. Mater.* 1 (2018) 3513-+.
- [7] Y.H. Zhang, N.N. Wang, P. Xue, Y.L. Liu, B. Tang, Z.C. Bai, S.X. Dou, Co₉S₈@carbon nanospheres as high-performance anodes for sodium ion battery, *Chem. Eng. J.* 343 (2018) 512-519.
- [8] Y.G. Li, H.L. Wang, L.M. Xie, Y.Y. Liang, G.S. Hong, H.J. Dai, MoS₂ Nanoparticles Grown on Graphene: An Advanced Catalyst for the Hydrogen Evolution Reaction, *J. Am. Chem. Soc.* 133 (2011) 7296-7299.
- [9] Y.L. Zhou, D. Yan, H.Y. Xu, J.K. Feng, X.L. Jiang, J. Yue, J. Yang, Y.T. Qian, Hollow nanospheres of mesoporous Co₉S₈ as a high-capacity and long-life anode for advanced lithium ion batteries, *Nano Energy* 12 (2015) 528-537.

- [10] Z. Hu, Q.N. Liu, S.L. Chou, S.X. Dou, Advances and Challenges in Metal Sulfides/Selenides for Next-Generation Rechargeable Sodium-Ion Batteries, *Adv. Mater.* 29 (2017).
- [11] X.Y. Li, K.K. Li, S.C. Zhu, K. Fan, L.L. Lyu, H.M. Yao, Y.Y. Li, J.L. Hu, H.T. Huang, Y.W. Mai, J.B. Goodenough, Fiber-in-Tube Design of Co₉S₈-Carbon/Co₉S₈: Enabling Efficient Sodium Storage, *Angew. Chem. Int. Edit.* 58 (2019) 6239-6243.
- [12] W.L. Wang, W.J. Li, S. Wang, Z.C. Miao, H.K. Liu, S.L. Chou, Structural design of anode materials for sodium-ion batteries, *J. Mater. Chem. A* 6 (2018) 6183-6205.
- [13] W. Cha, I.Y. Kim, J.M. Lee, S. Kim, K. Ramadass, K. Gopalakrishnan, S. Premkumar, S. Umapathy, A. Vinu, Sulfur-Doped Mesoporous Carbon Nitride with an Ordered Porous Structure for Sodium-Ion Batteries, *Acs Appl. Mater. Inter.* 11 (2019) 27192-27199.
- [14] J.F. Ni, L. Li, J. Lu, Phosphorus: An Anode of Choice for Sodium-Ion Batteries, *Acs Energy Lett.* 3 (2018) 1137-1144.
- [15] J.M. Lee, G. Singh, W. Cha, S. Kim, J.B. Yi, S.J. Hwang, A. Vinu, Recent Advances in Developing Hybrid Materials for Sodium-Ion Battery Anodes, *Acs Energy Lett.* 5 (2020) 1939-1966.
- [16] Y.M. Chen, X.Y. Li, K. Park, L.M. Zhou, H.T. Huang, Y.W. Mai, J.B. Goodenough, Hollow Nanotubes of N-Doped Carbon on CoS, *Angew. Chem. Int. Edit.* 55 (2016) 15831-15834.
- [17] Y. Qi, T. Zhang, N.X. Wu, H.R. Ding, G.X. Yu, J.B.A. Lian, L. Xu, J.X. Qiu, S. Li, Rational Design of the CoS/Co₉S₈@NC Composite Enabling High-Rate Sodium-Ion Storage, *Acs Appl. Energ. Mater.* 4 (2021) 5574-5582.
- [18] S.P. Zhang, F.X. Ling, L.F. Wang, R. Xu, M.Z. Ma, X.L. Cheng, R.L. Bai, Y. Shao, H.J. Huang, D.J. Li, Y. Jiang, X.H. Rui, J.T. Bai, Y. Yao, Y. Yu, An Open-Ended Ni₃S₂-Co₉S₈ Heterostructures Nanocage Anode with Enhanced Reaction Kinetics for Superior Potassium-Ion Batteries, *Adv. Mater.* 34 (2022).
- [19] X.P. Hong, J. Kim, S.F. Shi, Y. Zhang, C.H. Jin, Y.H. Sun, S. Tongay, J.Q. Wu, Y.F. Zhang, F. Wang, Ultrafast charge transfer in atomically thin MoS₂/WS₂ heterostructures, *Nature Nanotech.* 9 (2014) 682-686.

- [20] Y.Y. He, C.F. Dong, S.J. He, H. Li, X.P. Sun, Y. Cheng, G.W. Zhou, L.Q. Xu, Bimetallic nickel cobalt sulfides with hierarchical coralliform architecture for ultrafast and stable Na-ion storage, *Nano Res.* 14 (2021) 4014-4024.
- [21] C.F. Dong, L.J. Guo, H.B. Li, B. Zhang, X. Gao, F. Tian, Y.T. Qian, D.B. Wang, L.Q. Xu, Rational fabrication of $\text{CoS}_2/\text{Co}_4\text{S}_3@\text{N-doped carbon microspheres}$ as excellent cycling performance anode for half/full sodium ion batteries, *Energy Storage Mater.* 25 (2020) 679-686.
- [22] S. Iqbal, L. Wang, Z. Kong, Y.J. Zhai, X.P. Sun, F.B. Wang, Z.X. Jing, X.Y. He, J.M. Dou, L.Q. Xu, In Situ Growth of CoS_2/ZnS Nanoparticles on Graphene Sheets as an Ultralong Cycling Stability Anode for Potassium Ion Storage, *Acs Appl. Mater. Inter.* 14 (2022) 15324-15336.
- [23] Y.Z. Huang, X. Hu, J.W. Li, J.S. Zhang, D.P. Cai, B.S. Sa, H.B. Zhan, Z.H. Wen, Rational construction of heterostructured core-shell $\text{Bi}_2\text{S}_3@\text{Co}_9\text{S}_8$ complex hollow particles toward high-performance Li- and Na-ion storage, *Energy Storage Mater.* 29 (2020) 121-130.
- [24] X.Q. Zhang, X.N. Li, J.W. Liang, Y.C. Zhu, Y.T. Qian, Synthesis of $\text{MoS}_2@\text{C}$ Nanotubes Via the Kirkendall Effect with Enhanced Electrochemical Performance for Lithium Ion and Sodium Ion Batteries, *Small* 12 (2016) 2484-2491.
- [25] Z. Hu, L.X. Wang, K. Zhang, J.B. Wang, F.Y. Cheng, Z.L. Tao, J. Chen, MoS_2 Nanoflowers with Expanded Interlayers as High-Performance Anodes for Sodium-Ion Batteries, *Angew. Chem. Int. Edit.* 53 (2014) 12794-12798.
- [26] H. Li, Y.Y. He, Y.X. Dai, Y.Q. Ren, T.T. Gao, G.W. Zhou, Bimetallic $\text{SnS}_2/\text{NiS}_2@\text{S-rGO}$ nanocomposite with hierarchical flower-like architecture for superior high rate and ultra-stable half/full sodium-ion batteries, *Chem. Eng. J.* 427 (2022).
- [27] Y.B. Xu, K. Wang, Z.P. Yao, J. Kang, D. Lam, D. Yang, W. Ai, C. Wolverton, M.C. Hersam, Y. Huang, W. Huang, V.P. Dravid, J.S. Wu, In Situ, Atomic-Resolution Observation of Lithiation and Sodiation of WS_2 Nanoflakes: Implications for Lithium-Ion and Sodium-Ion Batteries, *Small* 17 (2021).
- [28] S. Hwang, Z.P. Yao, L. Zhang, M.S. Fu, K. He, L.Q. Mai, C. Wolverton, D. Su, Multistep Lithiation of Tin Sulfide: An Investigation Using in Situ Electron Microscopy,

Acs Nano 12 (2018) 3638-3645.

- [29] M.S. Fu, Z.P. Yao, X. Ma, H. Dong, K. Sun, S. Hwang, E.Y. Hu, H. Gan, Y. Yao, E.A. Stach, C. Wolverton, D. Su, Expanded lithiation of titanium disulfide: Reaction kinetics of multi-step conversion reaction, *Nano Energy* 63 (2019).
- [30] Y. He, C.L. Liu, Z.K. Xie, J.W. Wang, G. Chen, Q. Zhao, A. Abudula, G.Q. Guan, Prussian Blue Analogue-Derived Cobalt Sulfide Nanoparticles Embedded in N/S-Codoped Carbon Frameworks as a High-Performance Anode Material for Sodium-Ion Batteries, *Acs Appl. Energy Mater.* 5 (2022) 8697-8708.
- [31] M.M. Yin, D. Zhao, C.H. Feng, W. Zhou, Q.Z. Jiao, X.T. Feng, S.S. Wang, Y. Zhao, H.S. Li, T.Y. Feng, Construction of Porous Co₉S₈ Hollow Boxes with Double Open Ends toward High-Performance Half/Full Sodium-Ion Batteries, *Acs Sustainable Chem. Eng.* 8 (2020) 6305-6314.
- [32] Y.L. Zhou, M. Zhang, Q. Han, Y. Liu, Y.F. Wang, X.Q. Sun, X.T. Zhang, C.F. Dong, F.Y. Jiang, Hierarchical 1 T-MoS₂/MoO_x@NC microspheres as advanced anode materials for potassium/sodium-ion batteries, *Chem. Eng. J.* 428 (2022).
- [33] F.Q. Luo, X.S. Feng, L.X. Zeng, L.X. Lin, X.Y. Li, B.Y. Kang, L.R. Xiao, Q.H. Chen, M.D. Wei, Q.R. Qian, In situ simultaneous encapsulation of defective MoS₂ nanolayers and sulfur nanodots into SPAN fibers for high rate sodium-ion batteries, *Chem. Eng. J.* 404 (2021).
- [34] C. Guo, W.C. Zhang, Y. Liu, J.P. He, S. Yang, M.K. Liu, Q.H. Wang, Z.P. Cuo, Constructing CoO/Co₃S₄ Heterostructures Embedded in N-doped Carbon Frameworks for High-Performance Sodium-Ion Batteries, *Adv. Funct. Mater.* 29 (2019).
- [35] H. Geng, J. Yang, Z. Dai, Y. Zhang, Y. Zheng, H. Yu, H. Wang, Z. Luo, Y. Guo, Y. Zhang, H. Fan, X. Wu, J. Zheng, Y. Yang, Q. Yan, H. Gu, Co₉S₈/MoS₂ Yolk-Shell Spheres for Advanced Li/Na Storage, *Small* 13 (2017).
- [36] H.K. Chae, D.Y. Siberio-Perez, J. Kim, Y. Go, M. Eddaoudi, A.J. Matzger, M. O'Keeffe, O.M. Yaghi, A route to high surface area, porosity and inclusion of large molecules in crystals, *Nature* 427 (2004) 523-527.
- [37] G.Q. Zou, X.N. Jia, Z.D. Huang, S.M. Li, H.X. Liao, H.S. Hou, L.P. Huang, X.B. Ji, Cube-shaped Porous Carbon Derived from MOF-5 as Advanced Material for

Sodium-Ion Batteries, *Electrochim. Acta* 196 (2016) 413-421.

[38] Q.B. Guo, Y.F. Ma, T.T. Chen, Q.Y. Xia, M. Yang, H. Xia, Y. Yu, Cobalt Sulfide Quantum Dot Embedded N/S-Doped Carbon Nanosheets with Superior Reversibility and Rate Capability for Sodium-Ion Batteries, *Acs Nano* 11 (2017) 12658-12667.

[39] X.M. Lin, J.H. Chen, J.J. Fan, Y. Ma, P. Radjenovic, Q.C. Xu, L. Huang, S. Passerini, Z.Q. Tian, J.F. Li, Synthesis and Operando Sodiation Mechanistic Study of Nitrogen-Doped Porous Carbon Coated Bimetallic Sulfide Hollow Nanocubes as Advanced Sodium Ion Battery Anode, *Adv. Energy Mater.* 9 (2019).

[40] L.P. Hou, X.Q. Zhang, B.Q. Li, Q. Zhang, Challenges and promises of lithium metal anode by soluble polysulfides in practical lithium-sulfur batteries, *Mater. Today* 45 (2021) 62-76.

[41] Y. Zhang, S.M. Yu, H. Wang, Z.F. Zhu, Q. Liu, E.Z. Xu, D.T. Li, G.Q. Tong, Y. Jiang, A novel carbon-decorated hollow flower-like MoS₂ nanostructure wrapped with RGO for enhanced sodium-ion storage, *Chem. Eng. J.* 343 (2018) 180-188.

[42] W.N. Ren, H.F. Zhang, C. Guan, C.W. Cheng, Ultrathin MoS₂ Nanosheets@Metal Organic Framework-Derived N-Doped Carbon Nanowall Arrays as Sodium Ion Battery Anode with Superior Cycling Life and Rate Capability, *Adv. Funct. Mater.* 27 (2017).

[43] H.L. Zhu, F. Zhang, J.R. Li, Y.B. Tang, Penne-Like MoS₂/Carbon Nanocomposite as Anode for Sodium-Ion-Based Dual-Ion Battery, *Small* 14 (2018).

[44] W. Ye, F.F. Wu, N.X. Shi, H. Zhou, Q.Q. Chi, W.H. Chen, S.Y. Du, P. Gao, H.B. Li, S. Xiong, Metal-Semiconductor Phase Twinned Hierarchical MoS₂ Nanowires with Expanded Interlayers for Sodium-Ion Batteries with Ultralong Cycle Life, *Small* 16 (2020).

[45] Y.X. Wang, Y.X. Wang, Y.X. Wang, X.M. Feng, W.H. Chen, J.F. Qian, X.P. Ai, H.X. Yang, Y.L. Cao, In Situ Formation of Co₉S₈ Nanoclusters in Sulfur-Doped Carbon Foam as a Sustainable and High-Rate Sodium-Ion Anode, *Acs Appl. Mater. Inter.* 11 (2019) 19218-19226.

[46] Y.Y. Zhao, Q. Fu, D.S. Wang, Q. Pang, Y. Gao, A. Missiul, R. Nemausat, A. Sarapulova, H. Ehrenberg, Y.J. Wei, G. Chen, Co₉S₈@carbon yolk-shell nanocages as a high performance direct conversion anode material for sodium ion batteries, *Energy*

Storage Mater. 18 (2019) 51-58.

[47] J. Xiang, T. Song, One-pot synthesis of multicomponent (Mo, Co) metal sulfide/carbon nanoboxes as anode materials for improving Na-ion storage, Chem. Commun. 53 (2017) 10820-10823.

[48] T. Zhang, Y. Feng, J. Zhang, C. He, D.M. Itkis, J. Song, Ultrahigh-rate sodium-ion battery anode enabled by vertically aligned (1T-2H MoS₂)/CoS₂ heteronanosheets, Mater. Today Nano 12 (2020).

[49] L. Bai, F.X. Liang, Hierarchical MoS₂/carbon composites as superior anode for advanced sodium-ion battery, Ionics 28 (2022) 3341-3345.

[50] S.H. Yang, S.K. Park, J.K. Kim, Y.C. Kang, A MOF-mediated strategy for constructing human backbone-like CoMoS₃@N-doped carbon nanostructures with multiple voids as a superior anode for sodium-ion batteries, J. Mater. Chem. A 7 (2019) 13751-13761.

[51] J.N. Hao, J. Zhang, G.L. Xia, Y.J. Liu, Y. Zheng, W.C. Zhang, Y.B. Tang, W.K. Pang, Z.P. Guo, Heterostructure Manipulation via in Situ Localized Phase Transformation for High-Rate and Highly Durable Lithium Ion Storage, Acs Nano 12 (2018) 10430-10438.

[52] G. Henkelman, B.P. Uberuaga, H. Jonsson, A climbing image nudged elastic band method for finding saddle points and minimum energy paths, J. Chem. Phys. 113 (2000) 9901-9904.

[53] X. Li, Y.G. Sun, X. Xu, Y.X. Wang, S.L. Chou, A.M. Cao, L.B. Chen, S.X. Dou, Lotus rhizome-like S/N-C with embedded WS₂ for superior sodium storage, J. Mater. Chem. A 7 (2019) 25932-25943.

[54] X.T. Lian, N. Xu, Y.C. Ma, F. Hu, H.X. Wei, H.Y. Chen, Y.Z. Wu, L.L. Li, D.S. Li, S.J. Peng, In-situ formation of Co_{1-x}S hollow polyhedrons anchored on multichannel carbon nanofibers as self-supporting anode for lithium/sodium-ion batteries, Chem. Eng. J. 421 (2021).

[55] L.H. Xu, P.X. Xiong, L.X. Zeng, Y.X. Fang, R.P. Liu, J.B. Liu, F.Q. Luo, Q.H. Chen, M.D. Wei, Q.R. Qian, Electrospun VSe_{1.5}/CNF composite with excellent performance for alkali metal ion batteries, Nanoscale 11 (2019) 16308-16316.

Chapter 5 Construction of Cobalt Sulfide/Molybdenum Disulfide Heterostructure as the Anode Material for Sodium Ion Batteries

5.1 Introduction

The increasingly burning of fossil fuels leads to serious environmental pollution, and nowadays more and more attention has been paid to renewable energy (e.g., solar-, wind- and hydro-power) [1, 2]. However, limited by natural conditions, these renewable energies cannot continuously provide stable power, which makes it difficult for wide applications. As such, the development of energy conversion/storage technologies including water splitting, supercapacitors, metal-ion batteries, and metal-air batteries becomes more and more important [3-9]. Especially, as an energy storage technology, the commercialization of lithium-ion batteries (LIBs) has made great progress since the 1990s [10-12]. In recent years, due to the uneven distribution of lithium resources, the limited crustal abundance, and the increasing cost, the advantages of LIBs as energy storage media are no longer obvious. Recently, since sodium-ion batteries (SIBs) have similar energy storage mechanisms as LIBs, and possess the advantages of high abundance, wide distribution, and low cost of sodium resources, it has become the most promising alternative to LIBs. However, in view of the larger ionic radius of sodium ion (Na^+ , 1.02 Å) compared to that of Li-ion (Li^+ , 0.76 Å). The electrode materials of SIBs face larger volume expansion and more sluggish reaction kinetics than those of LIBs in the charge/discharge operation, thereby hindering the stability of SIBs [13]. To date, although extensive research on the development of anode materials for SIBs such as carbon-, alloys-, and transition-metal-based ones have been performed, further research is still needed for the creation of anode materials with excellent rate-capability as well as cycle-stability.

In various possible active materials for the anode, transition metal chalcogenides always exhibit large sodium ion storage ability based on their conversion reaction mechanisms during the Na^+ charging/discharging process [14, 15]. In particular,

molybdenum disulfide (MoS_2) with a typical layered structure is considered a candidate material for the anode of SIBs due to the superior theoretical capacity (670 mAh g^{-1}) and the large interlayer spacing of the (002) plane (0.62 nm) [16, 17]. However, the low intrinsic conductivity (2H phase) and the large volume expansion of MoS_2 during repeated charge/discharge processes always lead to unsatisfactory rate capability as well as cycle stability [18-20]. To face these deficiencies, some effective solving approaches such as combining MoS_2 with various carbon matrices (e.g., graphene, carbon nanotube, or carbon network) [21-25] have been proposed. Even so, although the conductivity and cycling stability of the composite can be improved, the specific capacity always decreases due to the introduction of inactive material.

Constructing a heterostructure has been proven to be another efficient approach to promoting the electrochemical performances of various materials due to the favorable synergistic effect [26]. For instance, Cao et al. [27] fabricated a $\text{Bi}_2\text{S}_3/\text{MoS}_2$ heterostructure as the anode material of SIBs and found that the phase boundaries can boost charge transfer and enhance reaction kinetics. Specifically, the built-in electrical field existing at the interface of different phases can accelerate charge transfer owing to the Coulomb force and lower the diffusion barrier [28, 29]. Combining MoS_2 with cobalt sulfides (CoS_x) to create various heterostructures such as $\text{CoS}_2/\text{MoS}_2$ [30, 31], $\text{Co}_3\text{S}_4/\text{MoS}_2$ [32] and $\text{Co}_9\text{S}_8/\text{MoS}_2$ [33, 34] is also an effective way since the obtained materials always have high theoretical capacities as well as versatile structure properties. However, in-depth mechanism research on them is still lacking, and how to greatly improve cycle stability as well as rate capability is also full of challenges.

In recent years, two-dimensional (2D) material has attracted extensive attention in the field of energy storage and conversion due to its unique characteristics, especially for its large specific surface area, uniform surface plane, flexible stacking, and high carrier mobility [35-38]. Zhang et al. [39] synthesized 2D SnSe as the cathode material for lithium-oxygen batteries, which exhibited a superior specific capacity and cycle stability due to the unique electrocatalytic mechanism. Herein, CoS/MoS_2 composite with a heterostructure and a micro-flower morphology, which has never been reported as the anode material for SIBs, is successfully constructed via a one-pot hydrothermal route with a solid-state sulfidation step. As demonstrated, the obtained CoS/MoS_2

composite exhibits superior Na⁺ storage performance due to its enhanced reaction kinetics with cycling and facilitated surface capacity-controlled behavior.

5.2 Experimental

5.2.1 Synthesis of CoS/MoS₂

Firstly, the precursor was synthesized by a facial hydrothermal method following our previous work [33]. In brief, K₃[Co(CN)₆] (1 mmol, Sigma-Aldrich, ≥97%) and Na₂MoO₄·2H₂O (1 mmol, Sigma-Aldrich, ≥99.5%) were mixed in deionized (DI, 18.2 MΩ cm, 30 ml) water, respectively. Then, the above two solutions were mixed and stirred for 1 hour. The obtained solution was introduced into a Teflon-lined autoclave (100 mL) and maintained at 200 °C for 20 hours in a sealed state. After the autoclave was cooled down, the precipitate was collected by centrifugation and successively rinsed with DI water and ethanol and then freeze-dried for 24 hours. As such, a blue precursor was obtained.

The above-obtained precursor and C₂H₅NS (TAA, Wako, 99%) with a mass ratio of 1:8 were separately placed in two porcelain boats and sealed in a tube furnace with an Argon (Ar) gas flow. After that, the tube was evacuated to a certain negative pressure with a vacuum pump, and the inlet/outlet valves on both sides of the tube were closed at the same time. After holding at 300 and 500 °C, respectively, for 2 hours with a heating rate of 5 °C min⁻¹, a black powder, i.e., CoS/MoS₂ powder, was obtained. For comparison, pure CoS and pure MoS₂ powders were also synthesized following the reported methods [40, 41], which are specifically presented in Supplementary Materials. The characterizations of these prepared materials and electrochemical performance tests are also described in Supplementary Materials.

5.2.2 Synthesis of pure CoS and pure MoS₂

Pure CoS and pure MoS₂ were synthesized following the reported methods in the literature [40, 41]. For the pure CoS synthesis, in brief, 1 mmol of CoCl₂·6H₂O and 2.2

mmol of $\text{CH}_4\text{N}_2\text{S}$ were dissolved in 50 mL of ethylene glycol with continuous stirring for 30 min. Then, the solution was transferred to a stainless steel autoclave (100 mL) with Teflon-line, sealed, and maintained at 180 °C for 12 h. The black powder can be obtained after centrifugation, washing, and drying. While, for the synthesis of nanoflower-like MoS_2 , typically, Na_2MoO_4 (0.3 g) and $\text{CH}_4\text{N}_2\text{S}$ (0.4 g) were dissolved in 30 mL of deionized (DI) water, and the pH value of the solution was adjusted to 1 by using concentrated HCl. Then, the solution was transferred to a stainless steel autoclave (45 mL) with Teflon-line, sealed, and maintained at 180 °C for 24 h. The black precipitation was collected by centrifugation and then washed and dried. For comparison, the above obtained two kinds of products were further calcined at 500 °C for 2 h in an Ar atmosphere.

5.2.3 Characterizations

Structures and compositions of the as-prepared materials were determined with a Smartlab X-ray diffractometer (XRD, Japan). Raman spectra were detected by a Renishaw inVia Raman spectrometer with 532 nm laser excitation. Morphology, crystal lattice, and elemental distribution measurements were performed on a Hitachi SU8010 field-emission scanning electron microscopy (FE-SEM, Japan) and a JEM-2100F high-resolution transmission electron microscope (TEM, Japan). NOVA 4200e (Quantachrome Inc., USA) instrument was used to measure the specific surface area and pore size distribution. An inductively coupled plasma emission optical spectrometry (ICP-OES) was applied to analyze the ratio of metal species. The elemental compositions on the material surface and their valence states were investigated by an X-ray photoelectron spectrometer, (XPS, VG ESCALAB 250, UK).

5.2.4 Electrochemical measurements

The working electrode was fabricated as follows: firstly, a homogeneous slurry was formed by mixing the active material, conductive material (super P), and polyvinylidene fluoride (PVDF) binder with a mass ratio of 75:15:10 in N-methyl pyrrolidone (NMP). Subsequently, the slurry was coated on a copper sheet and dried overnight in a vacuum oven at 80 °C, which was later cut into discs (12 mm in diameter)

with an active material loading amount of about $1.0 \sim 1.1 \text{ mg cm}^{-2}$. CR2032 coin cell was assembled in an argon-filled glove box, in which the metallic sodium was used as the counter electrode and glass fiber (GFF) as the separator. The electrolyte was prepared by dissolving 1 M NaSO_3CF_3 in diethylene glycol dimethyl ether (DGM). Galvanostatic charge/discharge measurement, cycling stability test, rate performance test, and galvanostatic intermittent titration technique (GITT) were conducted on a battery testing system (LAND CT2001A model, Wuhan LAND Electronic., Ltd.) in a voltage range of 0.3-3 V. Cyclic voltammetry (CV) curve was obtained from an electrochemical workstation VersaSTAT 4. The electrochemical impedance spectrum (EIS) was determined on an electrochemical workstation (RST 5090F) in a frequency range of 0.01 Hz-100 kHz. All the electrochemical tests were performed at ambient temperature.

5.3 Results and discussion

5.3.1 Characterizations

Fabrication of CoS/MoS₂ composite with a heterostructure by a two-step process is schematically illustrated in Fig. 5.1, in which the synthesis of the precursor is performed by a facial hydrothermal synthesis method at first and then solid-sulfurization of it into CoS/MoS₂ heterostructure under a certain vacuum state with TAA as the sulfur source is carried out. Fig. 5.2a displays the XRD pattern of the obtained product, in which a few characteristic peaks corresponding to (002), (103), and (110) facets of 2H-MoS₂ (JCPDS Card No. 87-2416) are observed at 2θ of 14.4° , 39.6° , and 58.4° , respectively, and those main peaks at 30.7° , 35.4° , 46.9° , and 54.7° are ascribed to the (100), (101), (102) and (110) planes of CoS (JCPDS Card No. 75-0605). This preliminarily confirms the successful formation of the CoS/MoS₂ composite. For comparison, as shown in Fig. 5.2b, pure phases of CoS and MoS₂ have been also obtained as those reported in the literature [40, 41]. Raman spectroscopy was further conducted to confirm the MoS₂ phase composition in CoS/MoS₂. As indicated in Fig. 5.3, the vibrational peaks at 283, 372, and 402 cm^{-1} can be ascribed to E_{1g}, in-

plane (E_{1g}^1), and out-of-plane (A_{1g}), respectively, which are well indexed to 2H-MoS₂ phase [42]. Besides, there are three signals at 156, 217, and 327 cm⁻¹, which can be assigned to the J1, J2, and J3 vibration modes of the 1T-MoS₂ phase [43]. Therefore, MoS₂ in the CoS/MoS₂ heterostructure should be a hybrid of 1T and 2H phases.

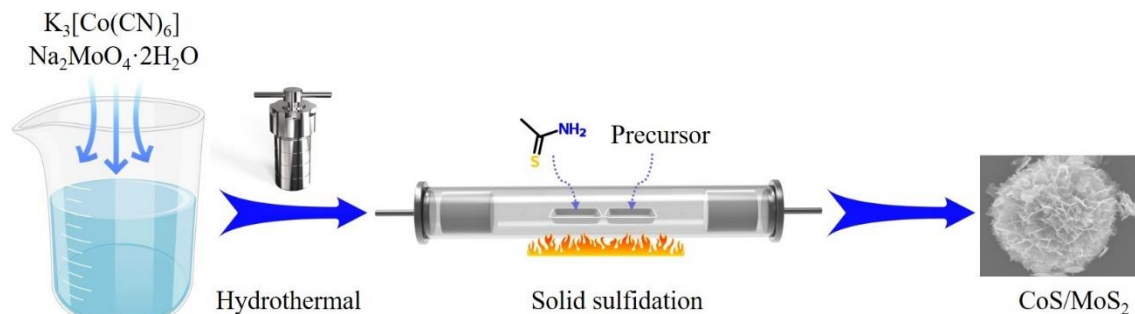


Figure 5.1 Schematic illustration of the fabrication CoS/MoS₂ heterostructure.

The SEM images of pure CoS and pure MoS₂ are shown in Figs. 5.2c and d, respectively. The pure CoS exhibits a microsphere structure with a particle size of $\sim 2 \mu m$ assembled by many nanosheets, and the pure MoS₂ demonstrates a nanoflower structure with a smaller particle size ($0.5 \sim 0.7 \mu m$), all of which are consistent with the morphologies reported in the literature[40, 41]. Furthermore, as shown in Figs. 5.2e and f, the obtained CoS/MoS₂ composite exhibits a micro-flower structure with a larger particle size of $12 \sim 15 \mu m$, which is also assembled by numerous nanosheets with a longitudinal length of $\sim 1 \mu m$. In our previous investigations, it is demonstrated that the existence of MoO_4^{2-} leads to the generation of a micro-flower-like particle during the hydrothermal synthesis process [33]. The specific surface areas and pore size distributions of as-prepared samples were conducted by using N₂ desorption-adsorption analysis. As indicated in Figs. 5.4, they all exhibit a typical type-IV curve, indicating that they have a mesoporous structure [44, 45]. Besides, the average pore sizes of pure CoS, CoS/MoS₂, and pure MoS₂ centered at 3.79, 3.82, and 3.87 nm, respectively, are confirmed. Herein, a larger specific surface area means more contact area at the active material/electrolyte interface, which also represents the formation of more solid electrolyte interface (SEI) layers during the initial charging/discharging process.

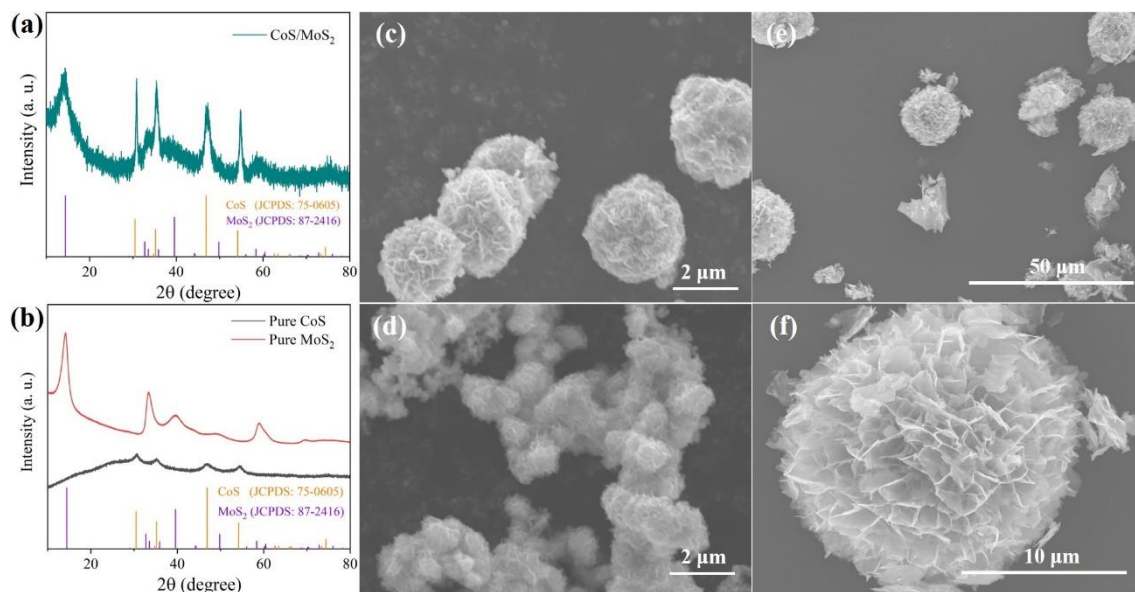


Figure 5.2 XRD patterns of (a) CoS/MoS₂ heterostructure, (b) pure CoS and pure MoS₂; and SEM images of (c) pure CoS, (d) pure MoS₂, and (e-f) CoS/MoS₂ composite.

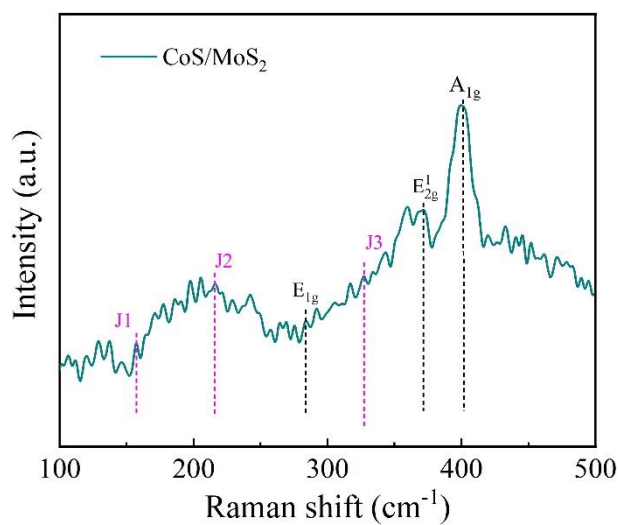


Figure 5.3 Raman spectrum of CoS/MoS₂.

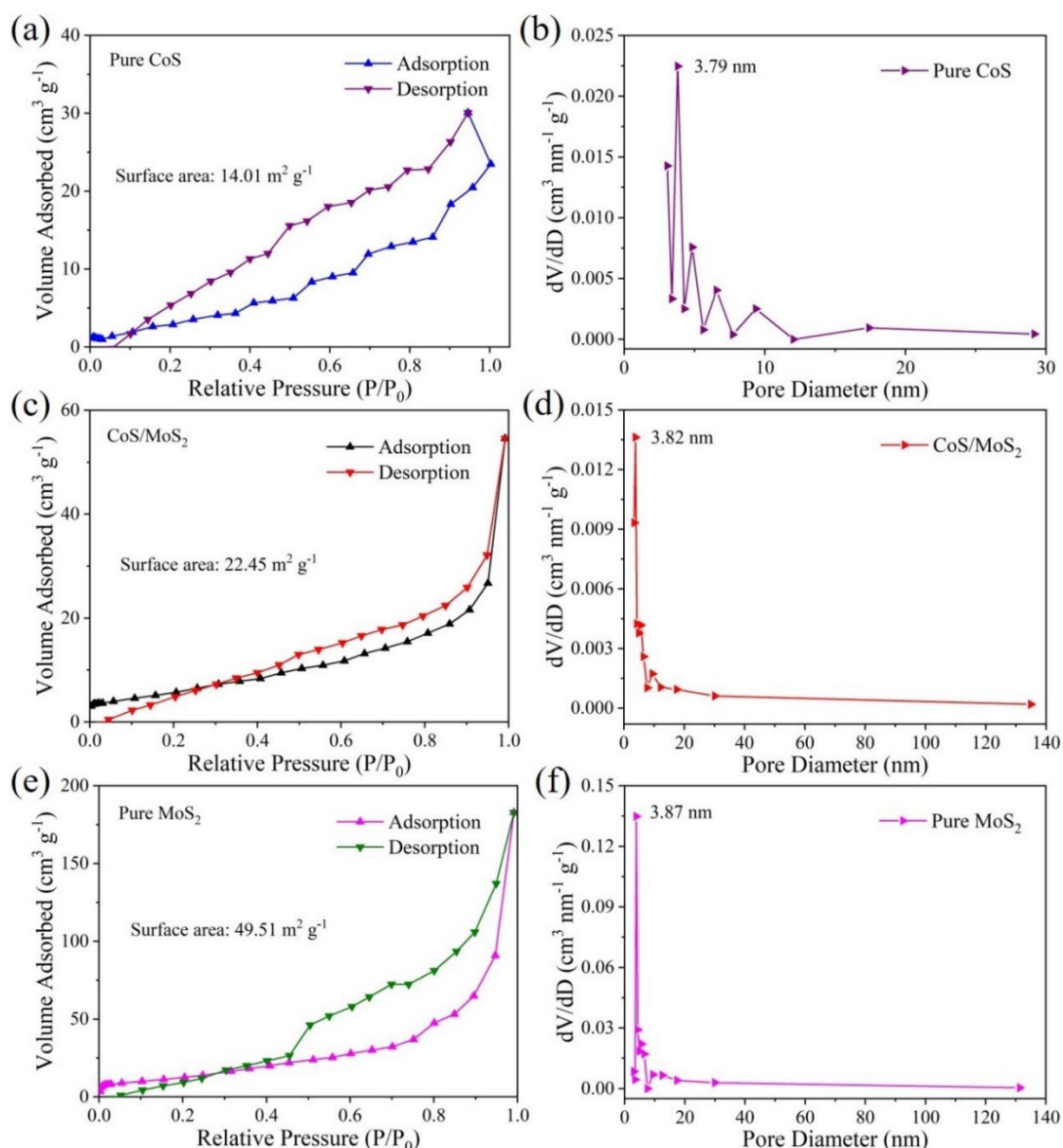


Figure 5.4 Nitrogen desorption-adsorption isotherms and pore size distributions of (a-b) pure CoS, (c-d) CoS/MoS₂, and (e-f) pure MoS₂.

The micro-flower-like CoS/MoS₂ heterostructure was further characterized by TEM observation. As displayed in Figs. 5.5a and b, the micro-flower is composed of nanosheets, which is consistent with the SEM observations. As depicted in Fig. 5.5c, the (002) plane of MoS₂ with an interlayer spacing of 0.624 nm exists and there are layer numbers in a range from 3 to 8 exposed, which should offer abundant effective channels for Na^+ diffusion. While the (101) plane of CoS with an interlayer spacing of 0.255 nm embedded in the composite can also be found. The SAED pattern (Fig. 5.5d)

exhibits multiple concentric circles, representing the (002), (110) planes of MoS₂ and the (101), (103) planes of CoS, respectively, which confirms the hybrid heterojunctions in the CoS/MoS₂ composite. EDS elemental mappings (Fig. 5.5e) indicate uniform distributions of Co, Mo, S, C, and N elements in the composite.

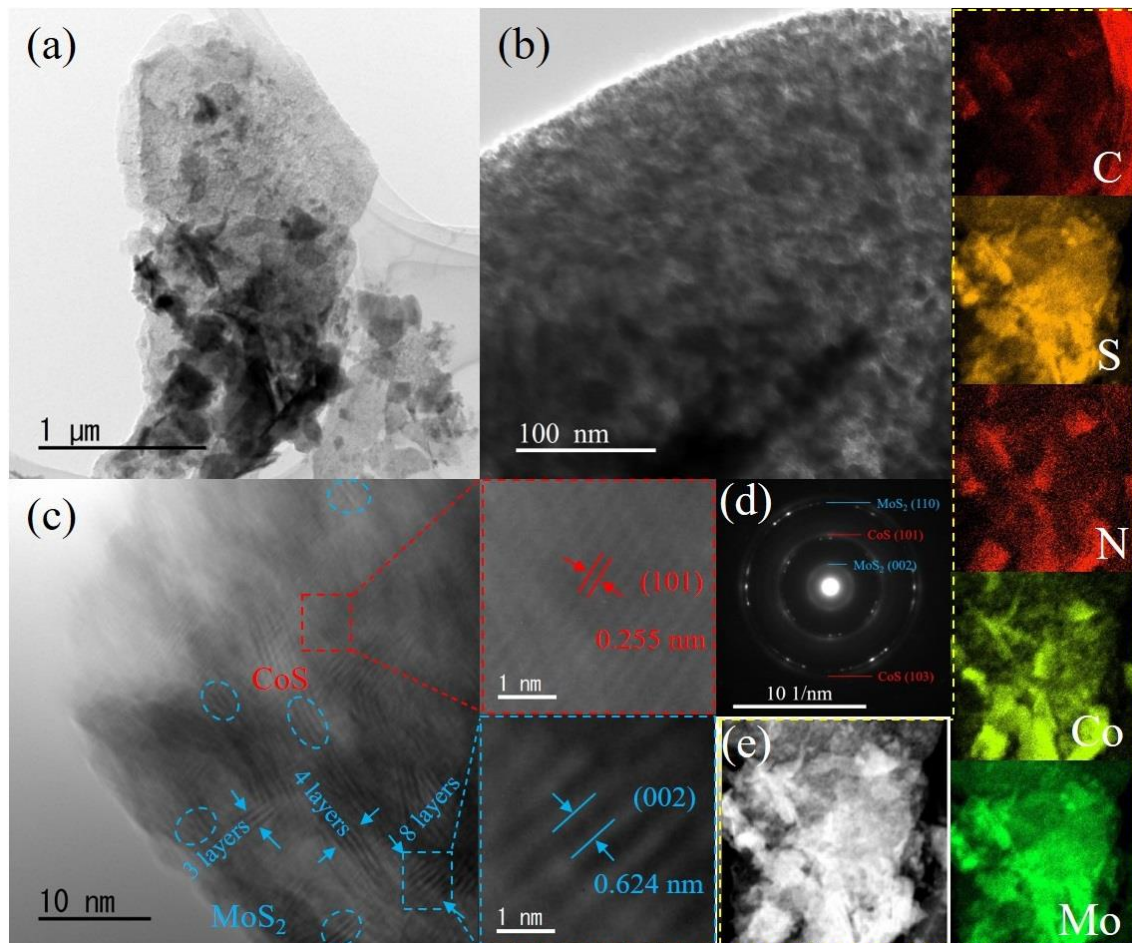


Figure 5.5 (a-b) TEM images; (c) HRTEM images; (d) SAED pattern; and (e) the area for EDS analysis of CoS/MoS₂ powder.

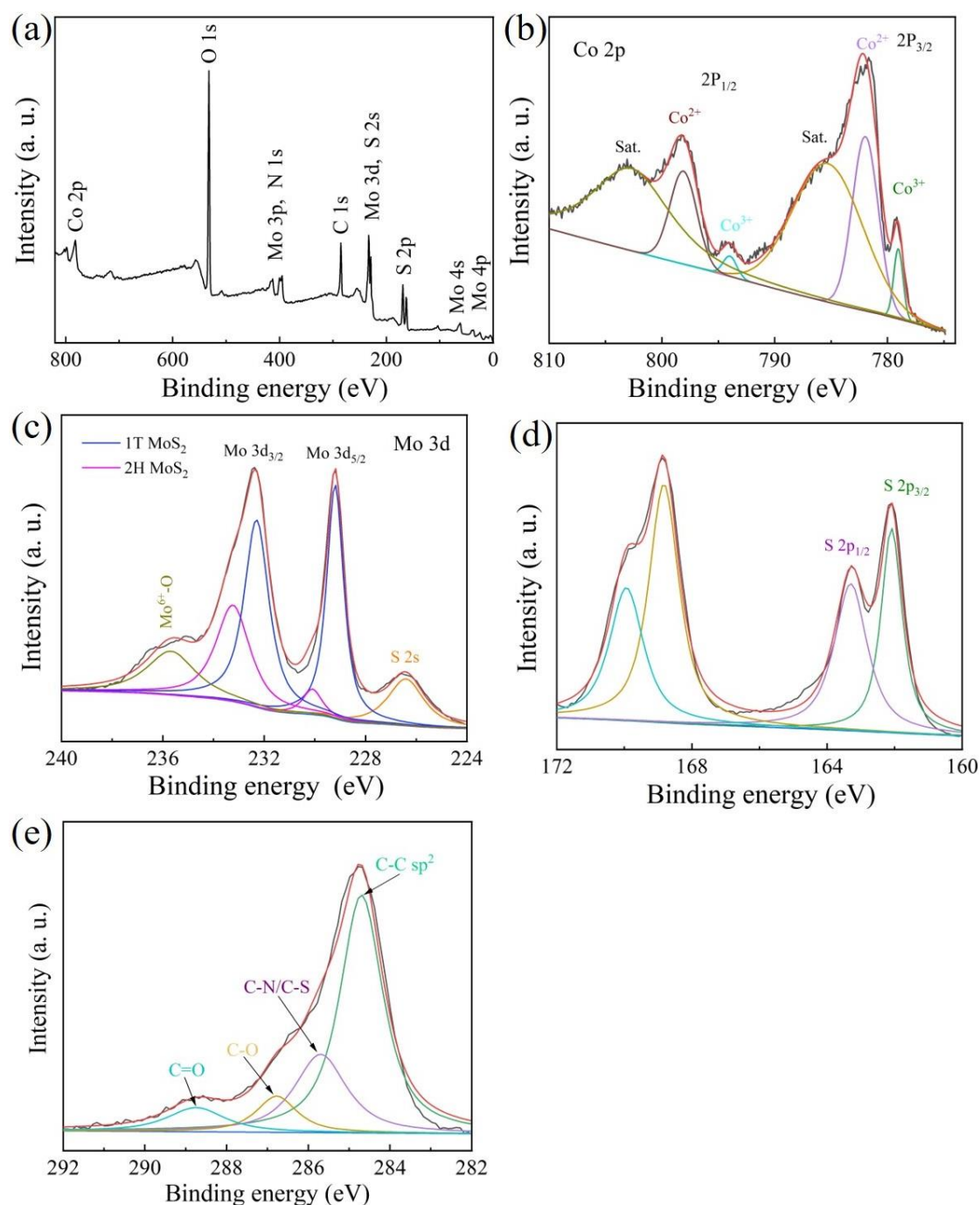


Figure 5.6 High-resolution XPS spectra of (a) full XPS survey, (b) Co 2p, (c) Mo 3d, (d) S 2p, and (e) C 1s for CoS/MoS₂ composite.

Fig. 5.6a displays the full XPS survey of the CoS/MoS₂ composite. It demonstrates the presence of C, N, O, S, Co, and Mo. Fig. 5.6b shows the Co 2p XPS spectrum, which can be divided into two shakeup satellites (i.e., 785.3/802.7 eV, identified as “sat.”) and two pairs of spin-orbit doublets (i.e., 779.1/782.0 eV for Co 2p_{3/2} and 794.0/798.1 eV for Co 2p_{1/2}). Herein, the pair of peaks at 782.0 and 798.1 eV can be

assigned to Co^{2+} , whereas two small peaks at 779.1 and 794.0 eV are well indexed to Co^{3+} . The high-resolution Mo 3d XPS spectrum (Fig. 5.6c) depicts two predominant peaks at 229.2 and 232.3 eV, corresponding to Mo 3d_{5/2} and Mo 3d_{3/2} of 1T MoS₂. Meanwhile, two signals at 230.1 and 233.2 eV are related to the 2H phase of MoS₂ [30]. In addition, the peak at 226.4 eV can be indexed to the Mo-S bond while the signal at a higher binding energy of 235.3 eV should be related to Mo⁶⁺. The coexistence of Co^{3+} and Mo⁶⁺ can be ascribed to the partial oxidation of CoS/MoS₂ after long-term exposure to air [46-49]. Fig. 5.6d displays the S 2p XPS spectrum, the pair of peaks at 162.1 and 163.3 eV are attributed to Co-S 2p_{3/2} and 2p_{1/2} while two satellite peaks at 168.8 and 169.9 eV are assigned to C_xSO_y 2p_{3/2} and 2p_{1/2} [50]. The C1s XPS spectrum (Fig. 5.6e) exhibits four fitted peaks at 287.7, 285.7, 286.8, and 288.7 eV, indexing to C-C, C-N/C-S, C-O, and C=O, respectively [51, 52]. Based on ICP-OES analysis, the specific molar ratio Co/Mo in this CoS/MoS₂ composite is 1.43/1.

5.3.2 Electrochemical performance

Cyclic voltammetry (CV) spectra were tested at 0.1 mV s⁻¹ with a potential range of 0.3-3 V (vs Na⁺/Na). As demonstrated in Fig. 5.7a, three peaks at 0.97, 0.75, and 0.46 V are observed in the initial cathodic sweep. Herein, the peak at 0.97 V in the initial cathodic sweep can be assigned to the insertion of Na⁺ (i.e., CoS to Na_xCoS, MoS₂ to Na_xMoS₂), which shifts to a higher voltage (1.34 V) after the initial cathodic sweep. Then, there are a strong peak (0.75 V) and a broad peak (0.46 V), which can be ascribed to the establishment of the solid electrolyte interface (SEI) layer with the corresponding conversion processes (Na_xCoS/Na_xMoS₂ to Co, Mo, and Na₂S). As a result, the peaks shift to 0.91 and 0.59 V in the following two cycles [53, 54]. While, in an anodic scan, the peaks at 1.71 and 1.98 V are observed, which should be ascribed to the re-formation of CoS and MoS₂. It should be noted that the CV curve of the third cycle coincides with the second one, demonstrating the high reversibility of the CoS/MoS₂-based anode. In contrast, CV measurements of pure CoS- and pure MoS₂-based anodes were also performed. As depicted in Fig. 5.8 a, the CV profile of pure

CoS-based anode exhibits three cathodic peaks (1.29, 0.94, and 0.53 V) and two anodic peaks (1.71 and 1.93 V), which are almost identical to those of CoS/MoS₂-based anode. Fig. 5.8b shows the CV profiles of pure MoS₂-based anode, in which two anodic peaks (1.53 and 0.82 V) and three cathodic peaks (1.55, 1.74, and 2.12 V) can be observed in the 2nd and 3rd cycles, and the peak intensity gets stronger at the subsequent higher scan rates. Fig. 5.7b displays the galvanostatic charging/discharging curves at 0.1 A g⁻¹. Three discharge plateaus appeared at \sim 1.4, \sim 0.92, and \sim 0.61 V, and two charge plateaus at \sim 1.68 and \sim 2.0 V are found in the sodiation process, which corresponds well to the CV curves. Furthermore, the CoS/MoS₂-based anode delivers a high starting discharging/charging capacity of 662.3/554.1 mA h g⁻¹ and a beginning Coulombic efficiency (CE) of 83.67%, which gradually recovers to \sim 100% in the subsequent cycles. The irreversible capacity loss in the first cycle is well-indexed to the establishment of the SEI layer [55]. For comparison, the galvanostatic charge/discharge profiles of pure CoS- and pure MoS₂-based anodes are shown in Fig. 5.9, which only exhibit the beginning CEs of 79.12% (679.2/537.4 mA h g⁻¹) and 71.36% (310.1/221.3 mA h g⁻¹), respectively.

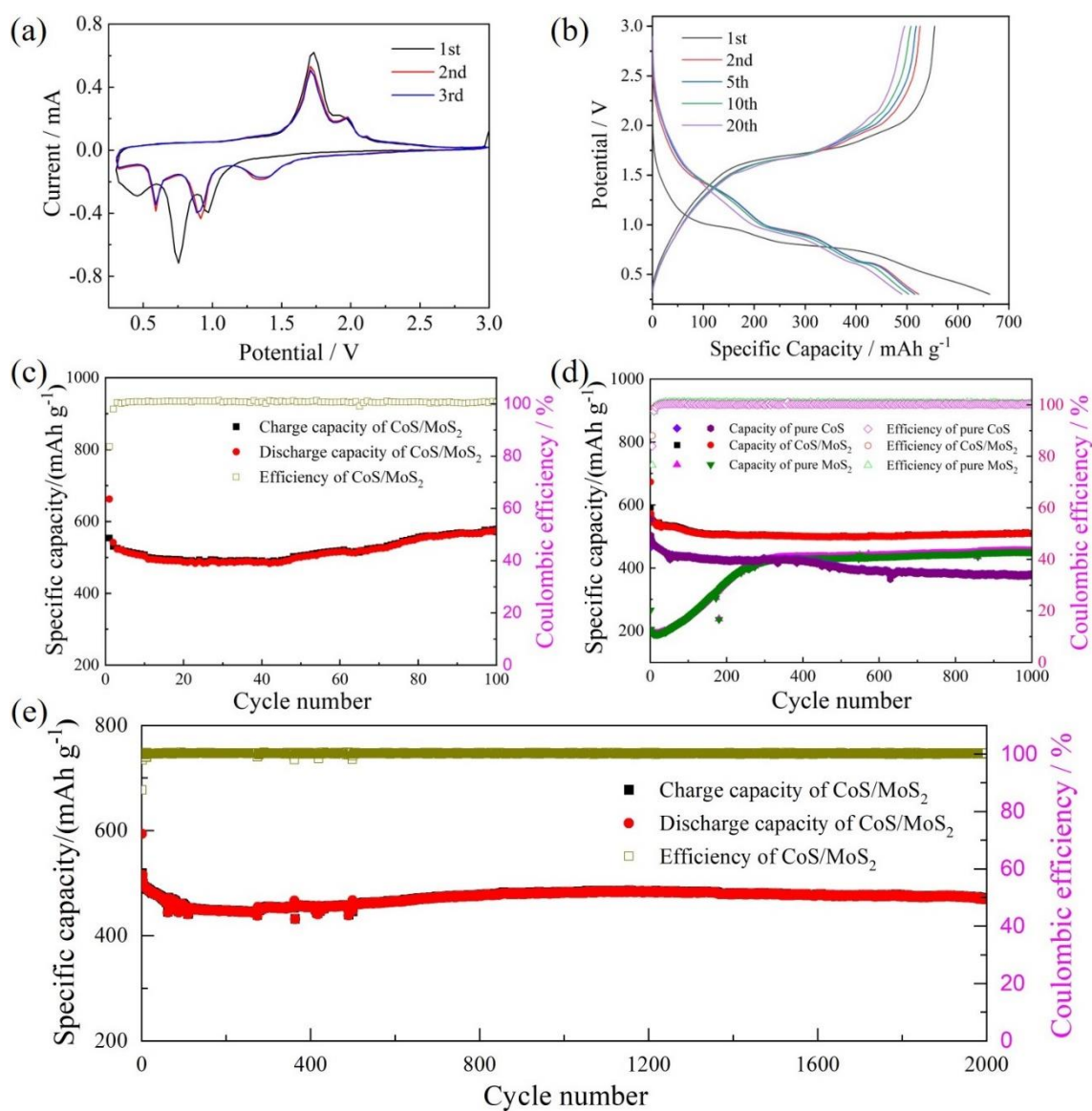


Figure 5.7 (a) CV curves of CoS/MoS₂-based anode at a scan rate of 0.1 mV s⁻¹ in the potential window of 0.3-3V; (b) galvanostatic charge/discharge profiles of CoS/MoS₂-based anode at 0.1 A g⁻¹; (c) Cycling performance of CoS/MoS₂-based anode at 0.1 A g⁻¹; (d) Cycling performances of pure CoS-, pure MoS₂- and CoS/MoS₂-based anodes at the current density of 1 A g⁻¹; (e) The long-term cycling stability of CoS/MoS₂-based anode at a higher current density of 2 A g⁻¹.

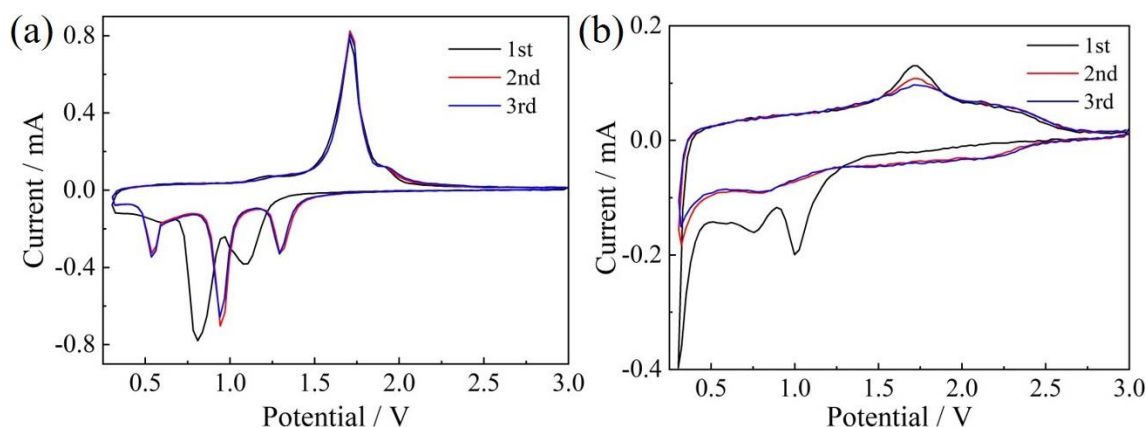


Figure 5.8 CV curves of (a) pure CoS- and (b) pure MoS₂-based anodes at a scan rate of 0.1 mV s⁻¹ in the potential window of 0.3-3V.

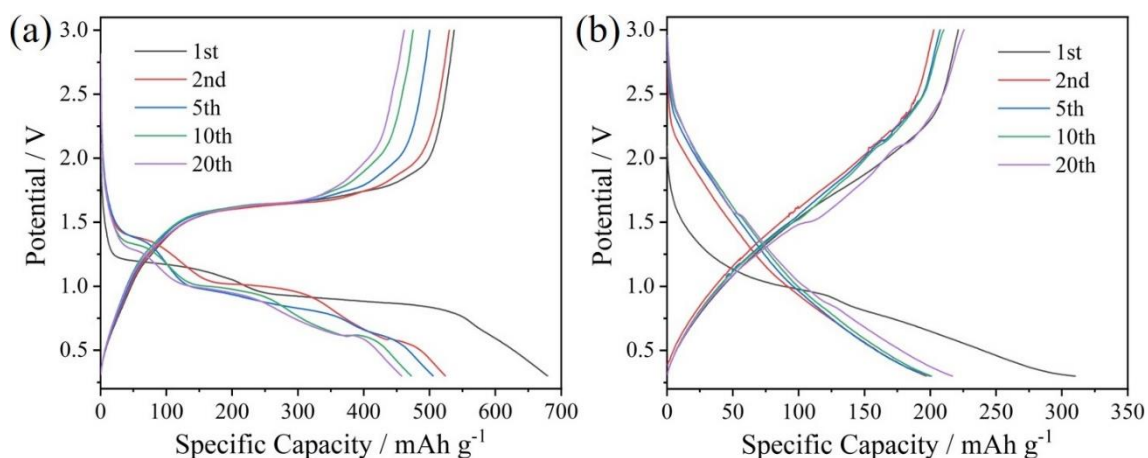


Figure 5.9 Typical galvanostatic charge/discharge profiles of (a) pure CoS- and (b) pure MoS₂-based anodes at 0.1 A g⁻¹ with different cycles (1st, 2nd, 5th, 10th, and 20th).

Fig. 5.7c displays the cycle performance of the CoS/MoS₂-based anode at 0.1 A g⁻¹. It is obvious that the discharging/charging capacity is gradually decreased in the beginning 25 cycles and then slowly recovered in the following cycles, and high discharge/charge capacities of 575.3/579 mA h g⁻¹ are reached at the 100th cycle with a capacity retention of 108.4% based on the 2nd cycle. The cycling performances of pure CoS-, CoS/MoS₂- and pure MoS₂-based anodes at 1 A g⁻¹ are displayed in Fig. 5.7d, in which the CoS/MoS₂-based anode exhibits the most excellent cycle performance with a high charge capacity of 510.9 mA h g⁻¹ after 1000 cycles. In contrast, the pure CoS-based anode displays a gradually decreasing in charge/discharge capacity, and the charge capacity is reduced to 378.3 mA h g⁻¹ after 1000 cycles. It is much lower than

that of CoS/MoS₂-based anode. Furthermore, the pure MoS₂-based anode exhibits a low discharge/charge capacity at the beginning of the cycling, but then it is gradually increased and stabilized at about the 650th cycle, and the charge capacity of 453.6 mA h g⁻¹ is achieved at the 1000th cycle. The long-term cycle stability of the CoS/MoS₂-based anode at 2 A g⁻¹ is depicted in Fig. 5.7e. One can see that a large charge capacity of 470.5 mA h g⁻¹ is delivered with an excellent capacity retention rate of 91.1%. More significantly, it also can maintain a considerable charge capacity of 441.7 mA h g⁻¹ at the 750th cycle even at 5 A g⁻¹ (Fig. 5.10).

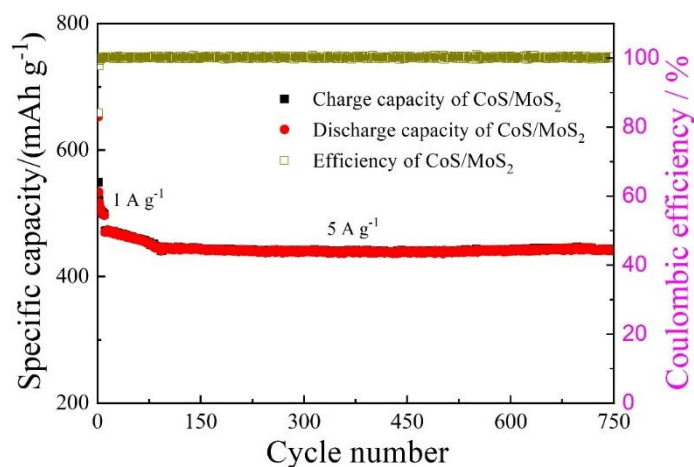


Figure 5.10 Cycling performance of the CoS/MoS₂-based anode at a current density of 5 A g⁻¹ (the first ten cycles were tested at 1 A g⁻¹).

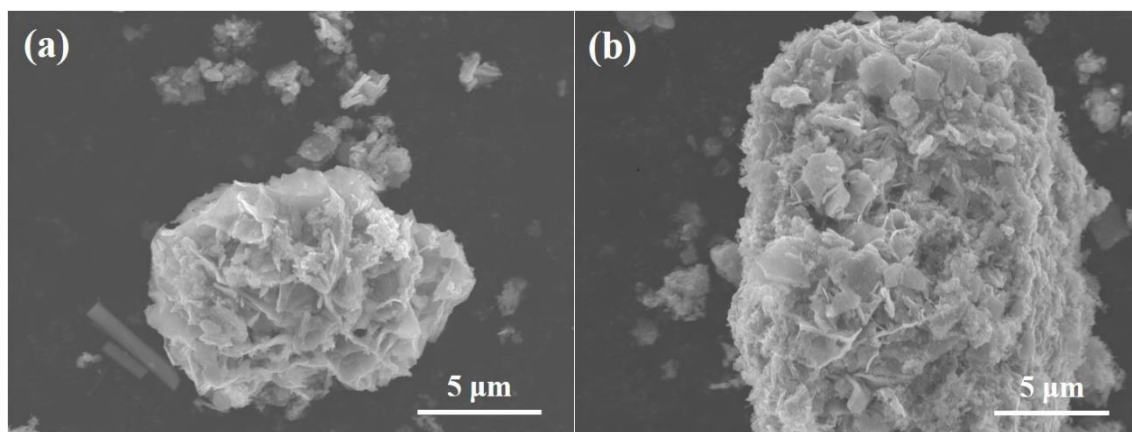


Figure 5.11 SEM images of CoS/MoS₂-based anode (a) after 5 cycles and (b) after 20 cycles at a current density of 0.2 A g⁻¹.

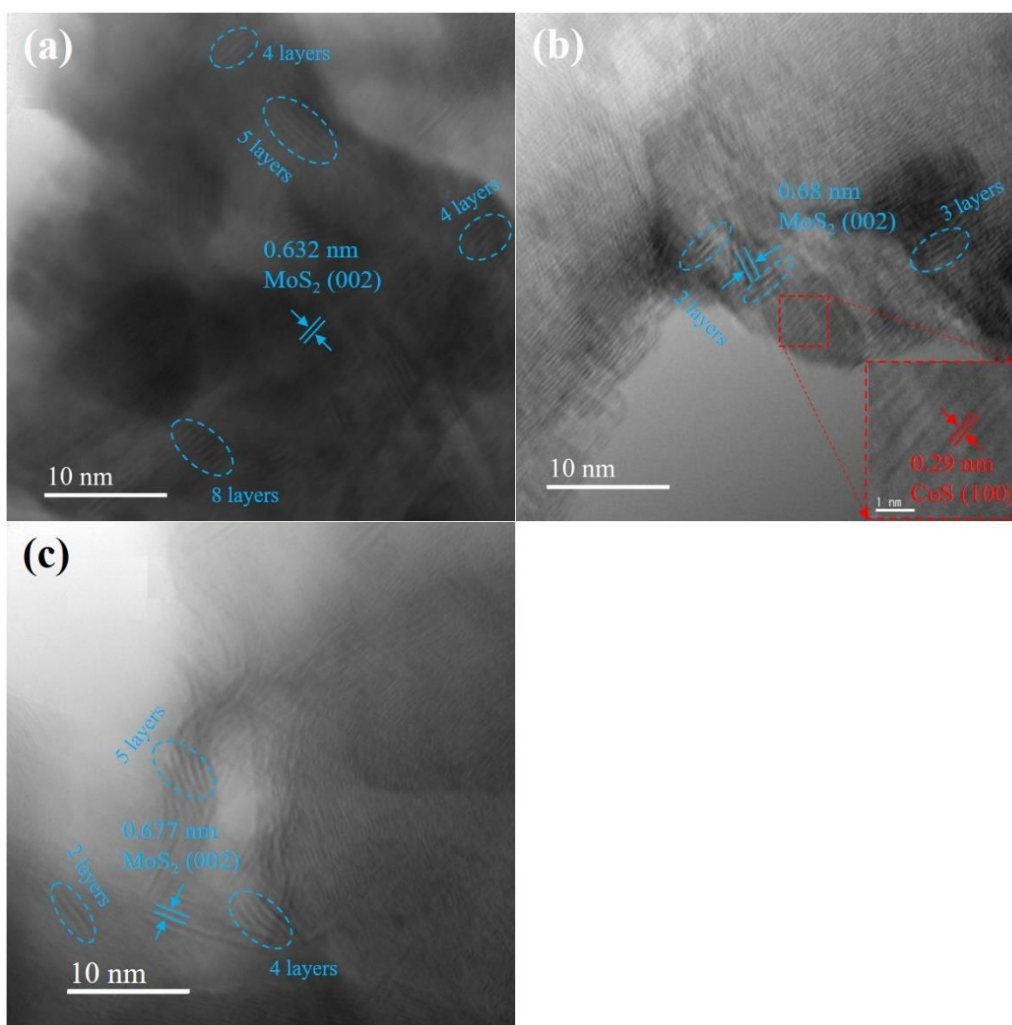


Figure 5.12 (a) HRTEM images of (a) the CoS/MoS₂ composite after 100 cycles, (b) the CoS/MoS₂ composite after 500 cycles, and (c) pure MoS₂ after 100 cycles at the current density of 0.2 A g⁻¹.

To explore the mechanism of the excellent cycle performance of MoS₂-based anode, SEM observations were conducted for CoS/MoS₂-based anode after different cycles (5 and 20). As shown in Fig. 5.11a, the overall structure of the micro-flower is maintained after 5 cycles. However, when the battery is charged/discharged to the 20th cycle, the material retains part of the micro-flower morphology, and some nanosheets are scattered around (Fig. 5.11b). Furthermore, HRTEM observations were also conducted for pure MoS₂ and CoS/MoS₂ after different cycles. As depicted in Fig. 5.12a, the interlayer spacing of MoS₂ in CoS/MoS₂-based anode has a small expansion (from 0.624 to 0.632 nm) after 100 cycles and the number of layers maintains almost

unchanged when compared with that of the fresh one (Fig. 5.5c). However, the interlayer spacing of MoS₂ is further expanded to 0.68 nm and the number of layers is decreased to 2-3 after 500 cycles (Fig. 5.12b). The same phenomenon also occurs in the pure MoS₂-based anode as displayed in Fig. 5.12c, in which the interlayer spacing MoS₂ reaches 0.677 nm and the number of layers is 2-5 after 100 cycles. Therefore, the delamination and interlayer spacing expansion could be the key reasons for the superior performance of the MoS₂-based anode since it has more active sites for Na⁺ storage [41, 56-58].

The reason for the capacity change of the CoS/MoS₂-based anode during the cycling is explained in the following by taking the cycling performance of the CoS/MoS₂-based anode at 2 A g⁻¹ as an example. Firstly, the rapid capacity fading in the first few cycles is attributed to the irreversible capacity loss caused by the establishment of the SEI layer. In the subsequent cycling performance test (from the 10th to the 260th cycles), the nanosheets in the active material fall off, resulting in the formation of a new SEI layer again, which is accompanied by capacity decay. Moreover, the interlayer spacing expansion of MoS₂ and capacity enhancement during the repeated charge/discharge process occur simultaneously. However, the rate of capacity increase (caused by the expansion of the MoS₂ interlayer spacing) is much smaller than that of capacity decay (caused by the newly formed SEI layer), and thus capacity decay dominates in the first 260 cycles. Subsequently, the structural change of the active material gradually tends to be stable and the capacity increase rate becomes greater than that of capacity decay and as a result, the capacity shows an overall upward trend and reaches the maximum in the 1177th cycle. As the interlayer spacing expansion of MoS₂ reaches the limit, the charge/discharge capacity of the CoS/MoS₂-based anode can be gradually stabilized, and finally, the capacity fading is only 14 mA h g⁻¹ in the subsequent 800 cycles, which is almost negligible. It is worth noting that some data points have a significant deviation in Fig. 5.7e, which should be attributed to multiple factors including electrode structure change, SEI layer establishment/destruction, testing condition change and cell structure change, and so on. That is, it may be resulted from a factor and/or multiple factors superimposed, and this phenomenon always

occurs from time to time during the battery testing.

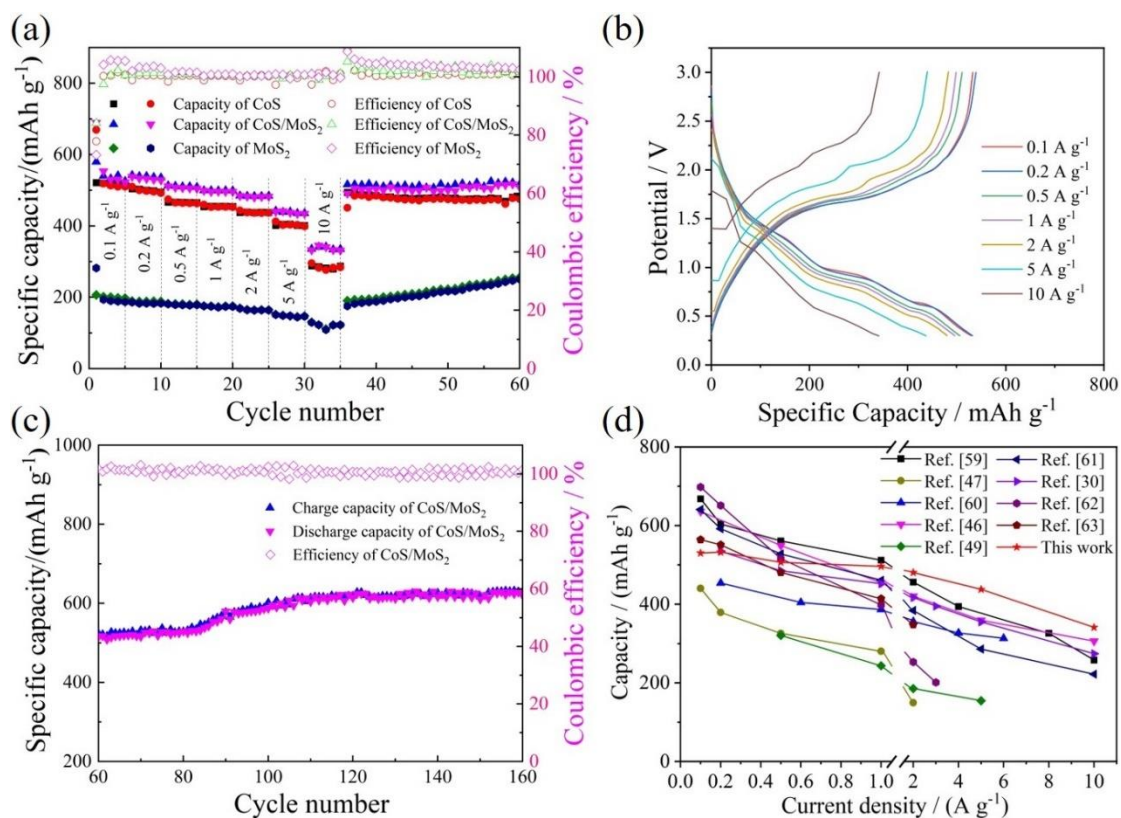


Figure 5.13 (a) Rate performances of pure CoS-, pure MoS₂- and CoS/MoS₂-based anodes; (b) Charge-discharge curves corresponding to rate performance for CoS/MoS₂-based anode; (c) Cycling performance of CoS/MoS₂-based anode after rate performance test at 0.1 A g⁻¹. (d) Comparison of rate performance of the CoS/MoS₂-based anode with other CoS- and MoS₂-based anodes reported in the literatures.

The rate capabilities of pure CoS-, CoS/MoS₂-, and pure MoS₂-based anodes are further compared at various current densities in the range of 0.1-10 A g⁻¹. As indicated in Fig. 5.13a, with the increasing of current density from 0.1 to 10 A g⁻¹, the CoS/MoS₂-based anode exhibits the best rate capacities of 530.3, 532.4, 506.6, 496.3, 480.5, 437.6 and 341 mA h g⁻¹ at 0.1, 0.2, 0.5, 1, 2, 5 and 10 A g⁻¹, successively. As the current density is subsequently decreased to 0.1 A g⁻¹, the reversible capacity is also recovered to 516.2 mA h g⁻¹. The charge-discharge curves corresponding to the rate performance are shown in Fig. 5.13b. Herein, the different circles (3rd, 8th, 13th, 18th, 23rd, 28th, and 33rd) of the rate capacity test are selected to draw the curves, which correspond to the different rate test conditions from 0.1 to 10 A g⁻¹. Obviously, the CoS/MoS₂-based anode exhibits a

higher charging capacity of 629.7 mA h g⁻¹ at the 160th cycle (Fig. 5.13c) after the rate capacity test, which is consistent with the cycle performance test at 0.1 A g⁻¹. In contrast, the pure CoS- and pure MoS₂-based anodes deliver lower rate capabilities with only 282.6 and 123.1 mA h g⁻¹ at 10 A g⁻¹, respectively. It is worth noting that the rate-capability of CoS/MoS₂-based anode is superior to those of most reported CoS- and MoS₂-based anodes (Fig. 5.13d), especially at high current densities [30, 46, 47, 49, 59-63].

5.3.3 Electrochemical kinetics

The Na⁺ storage kinetics of pure CoS-, pure MoS₂-, and CoS/MoS₂-based anodes were further investigated by electrochemical impedance spectroscopy (EIS). As shown in Figs. 5.14a-c, the Nyquist plots were obtained after different cycles (1, 20, and 50) with a current density of 0.2 A g⁻¹, all of which consist of a semicircle and a straight line. Herein, the semicircle in the middle-to-high frequency range represents the charge-transfer resistance (R_{ct}) whereas the straight line in the low frequency corresponds to the Warburg impedance (Z_w) for Na⁺ diffusion [64]. Table 5.1 displays specific resistance values, which were obtained via the fitting of the Nyquist plots with the equivalent circuit model (inset, in Fig. 5.14c). The R_{ct} value for the pure CoS-based anode increases with the cycling whereas those of CoS/MoS₂- and pure MoS₂-based anodes first increase and then decrease due to the enhancement of electronic conductivity [65], demonstrating the accelerated reaction rates for the CoS/MoS₂- and pure MoS₂-based anodes. This is one main reason why the charging/discharging capacities of the pure CoS-based anode decrease with the cycling whereas the CoS/MoS₂- and pure MoS₂-based anodes first decrease and then increase with the cycling. While the Warburg impedance coefficient (σ_w) corresponding to Na⁺ diffusion characteristics of the CoS/MoS₂-based anode obeys the following equation:

$$Z' = R_s + R_{ct} + \sigma_w \omega^{-0.5} \quad (1)$$

where σ_w is evaluated by linearly fitting the slope of Z' (the real part of impedance) vs. $\omega^{-0.5}$ (ω represents the angular frequency). As shown in Fig. 5.14d, the CoS/MoS₂-based

anode shows the smallest slope in the 20th cycle and it slightly increases in the 50th cycle, indicating a faster Na⁺ diffusion than that at the 1st cycle.

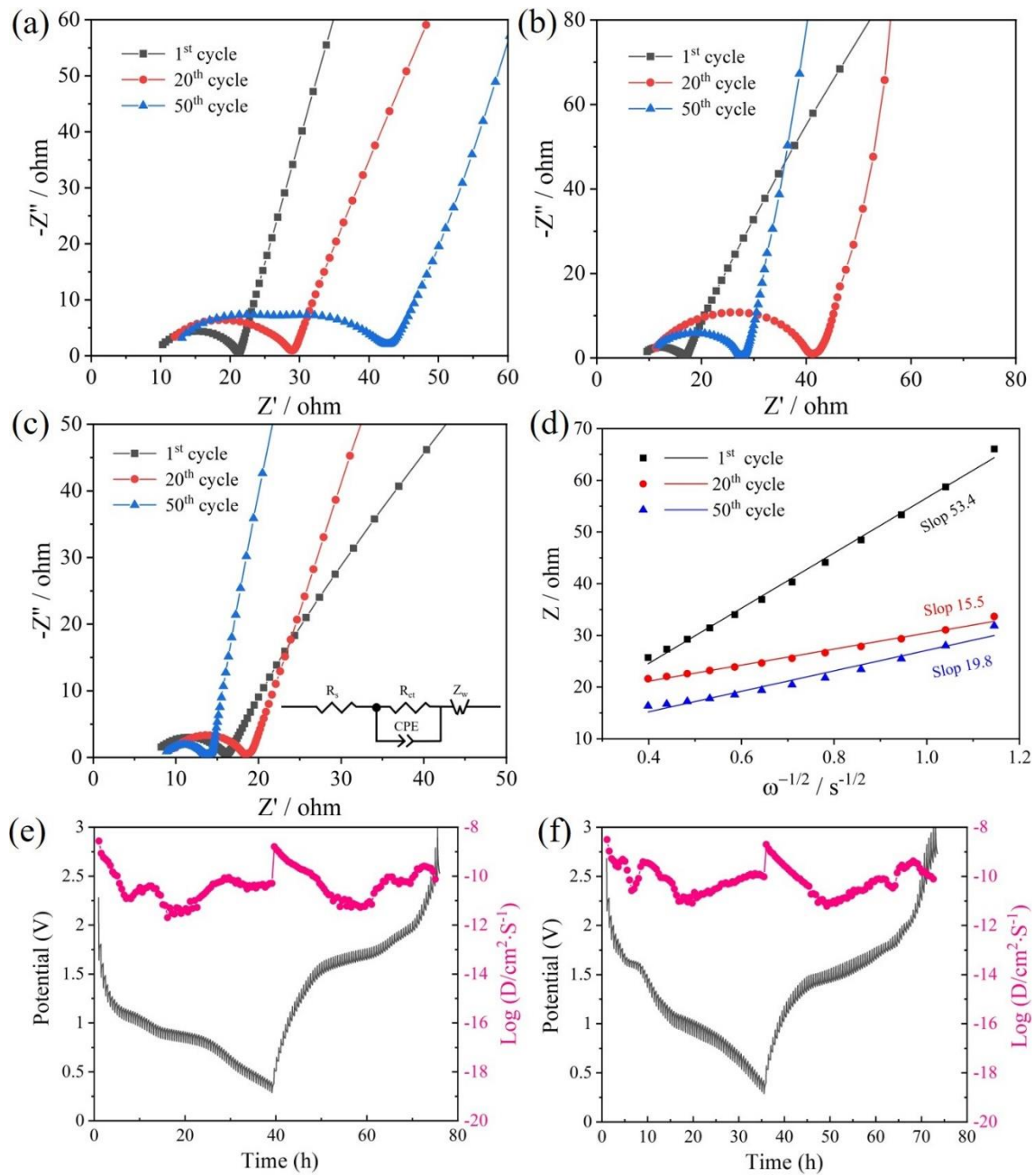


Figure 5.14 Nyquist plots of (a) CoS-, (b) MoS₂-, and (c) CoS/MoS₂-based anodes after different cycles (1, 20, and 50); (d) Fitted straight lines between z' and $\omega^{-1/2}$ at the low-frequency region for the CoS/MoS₂-based anode after different cycles (1, 20, and 50); The discharge/charge profiles and corresponding Na⁺ diffusion coefficients of the CoS/MoS₂-based anode in GITT measurements of (e) the first cycle, and (f) the 100th cycle.

The specific Na⁺ diffusion coefficients (D_{Na^+}) at different charge/discharge states were evaluated by a galvanostatic intermittent titration technique (GITT), which was investigated by continuous galvanostatic pulses (0.1 A g⁻¹ for 5 min) with a rest interval of 25 min. In this regard, the D_{Na^+} can be evaluated by the following equation [66]:

$$D_{Na^+} = \frac{4}{\pi\tau} \left(\frac{nV_m}{S} \right)^2 \left(\frac{\Delta E_s}{\Delta E_\tau} \right)^2 \quad (2)$$

where τ represents the current plus time; n is the molar number and V_m is the molar volume of active material; S denotes the interface area of electrode/electrolyte; ΔE_s and ΔE_τ are the voltage variations during the galvanostatic pulse and steady state of the single-step GITT curve. As shown in Figs. 5.14e and f, the CoS/MoS₂-based anode delivers a higher average D_{Na^+} in the 100th cycle ($1.77 \times 10^{-10} \text{ cm}^2 \text{ s}^{-1}$) than that of the 1st cycle ($1.32 \times 10^{-10} \text{ cm}^2 \text{ s}^{-1}$), which is identical with the law of σ_w linearly fitted by Z' vs $\omega^{-0.5}$.

Table 5.1 Fitting results of Nyquist plots based on the equivalent circuit after 1, 20 and 50 cycles.

Electrode	1 st cycle		20 th cycle		50 th cycle	
	R _s	R _{ct}	R _s	R _{ct}	R _s	R _{ct}
Pure CoS	9.76	10.75	10	18.74	9.02	34.67
CoS/MoS ₂	7.55	8.20	9.39	8.58	8.26	5.73
Pure MoS ₂	8.38	8.29	10.56	30.06	10.14	17.11

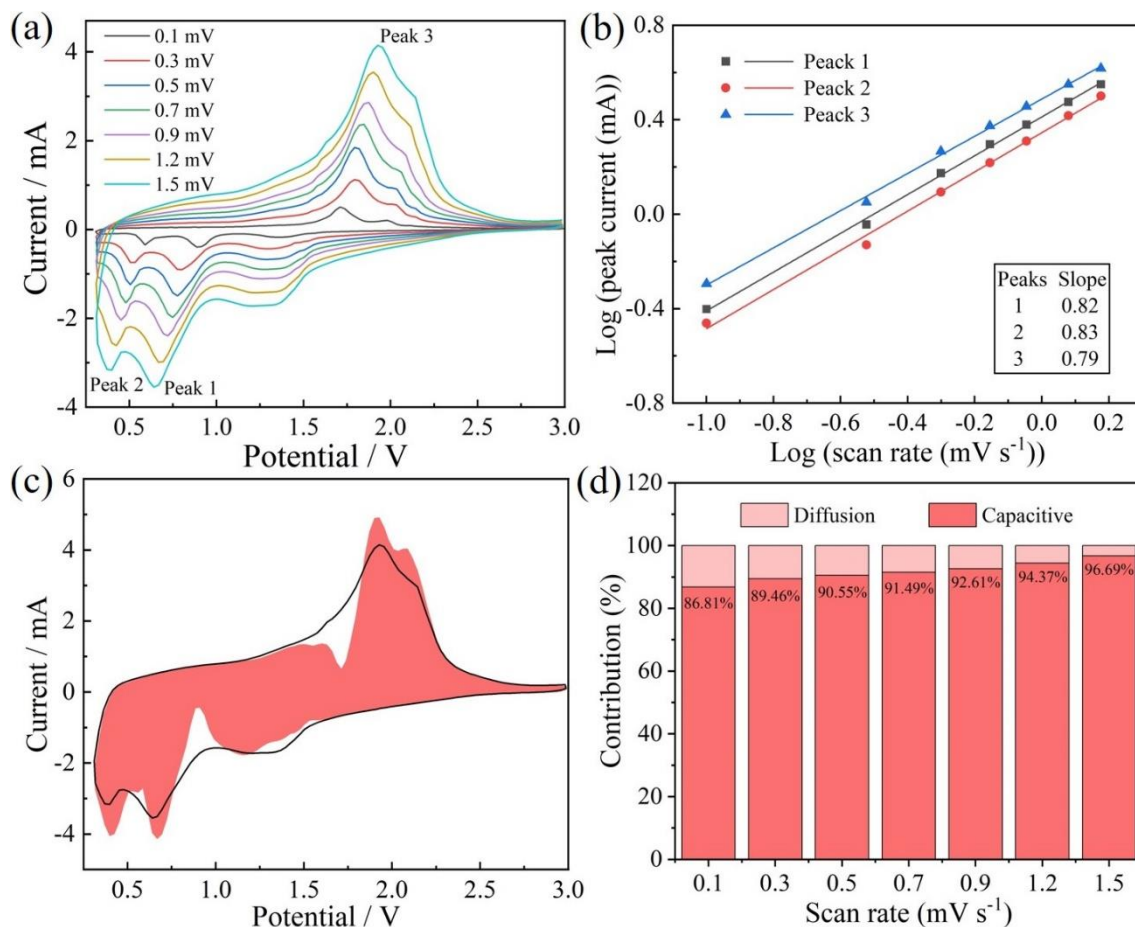


Figure 5.15 (a) CV curves of the CoS/MoS₂-based anode in a voltage range of 0.3-3 V at different scan rates from 0.1 to 1.5 mV s⁻¹; (b) The fitting lines of log i vs log v of peaks in CV curves for the CoS/MoS₂-based anode; (c) Capacitive contributions of CoS/MoS₂-based anode compared with the total current at 1.5 mV s⁻¹; The capacitive contributions of the CoS/MoS₂-based anode at different scan rates from 0.1 to 1.5 mV s⁻¹.

For more insight into the mechanism of Na⁺ storage, CV tests were performed at various scan rates (0.1-1.5 mV s⁻¹) (Fig. 5.15a). One can see that the CV curves maintain the original shape as the scan rate increases, demonstrating that voltage polarization has little effect on the CoS/MoS₂-based anode, which is the main reason for its high-rate capability. In comparison, the CV curves of pure CoS- and pure MoS₂-based anodes are displayed in Figs. 5.16a and 5.17a. The correction of the peak current (i) and scan rate (v) follows the equations [67]:

$$i = av^b \quad (3)$$

$$\log(i) = \log(a) + b \log(v) \quad (4)$$

in which, a and b parameters are adjustable, and the b value is obtained by linearly fitting of $\log(i)$ - $\log(v)$. Notably, b value close to 0.5 reflects a diffusion-controlled process. Whereas, the b value ≈ 1 indicates a capacitive-controlled process. As illustrated in Fig. 5.15b, the b values are 0.82 (peak 1), 0.83 (peak 2), and 0.79 (peak 3), indicating that the Na^+ storage mechanism is a predominantly surface capacitive-controlled process. For comparison, the b values of the pure CoS and pure MoS_2 are shown in Figs. 5.16b and 5.17b, respectively, where the pure MoS_2 exhibits that the b value is much closer to 1. Moreover, the capacity contributions of two components (capacitive- and diffusion-controlled process) can be quantitatively evaluated by fitting current (i) at a fixed voltage (V) through the following equations:

$$i(V) = k_1V + k_2V^{1/2} \quad (5)$$

$$i(V)/V^{1/2} = k_1V^{1/2} + k_2 \quad (6)$$

Herein, the k_1V and the $k_2V^{1/2}$ can be respectively ascribed to the capacitive- and diffusion-controlled steps. As indicated in Fig. 5.15c, the CoS/ MoS_2 -based anode delivers a high capacitive contribution of 96.69% at the scan rate of 1.5 mV s^{-1} . Besides, the capacitive contributions of 86.81%, 89.46%, 90.55%, 91.49%, 92.61%, and 94.37% can be obtained over the scan rate range of 0.1-1.2 mV s^{-1} (Fig. 5.15d). In contrast, the pure CoS- and pure MoS_2 -based anodes (Figs. 5.16c-d and 5.17c-d) deliver smaller capacitive contribution values than the CoS/ MoS_2 . In general, MoS_2 is considered as an attractive material for pseudocapacitive charge storage because of its relatively large van der Waals gap with electrochemically active metallic 1T phase [68]. While, those conversion reactive materials (e.g., TiS_2 nanocrystals) with typical layered structures have also demonstrated excellent pseudocapacitive behavior, and sometimes a high capacitive contribution of 85% could be obtained from the potentiostatic cycling [69]. Herein, the built-in electric field in the CoS/ MoS_2 heterostructure is found to accelerate charge transfer, which further improves the electrochemical kinetics. Therefore, compared with pure CoS and pure MoS_2 , CoS/ MoS_2 heterostructure exhibits a higher

proportion of pseudocapacitive contribution, and the reasonable design of CoS/MoS₂ heterostructure can facilitate surface capacity-controlled behavior.

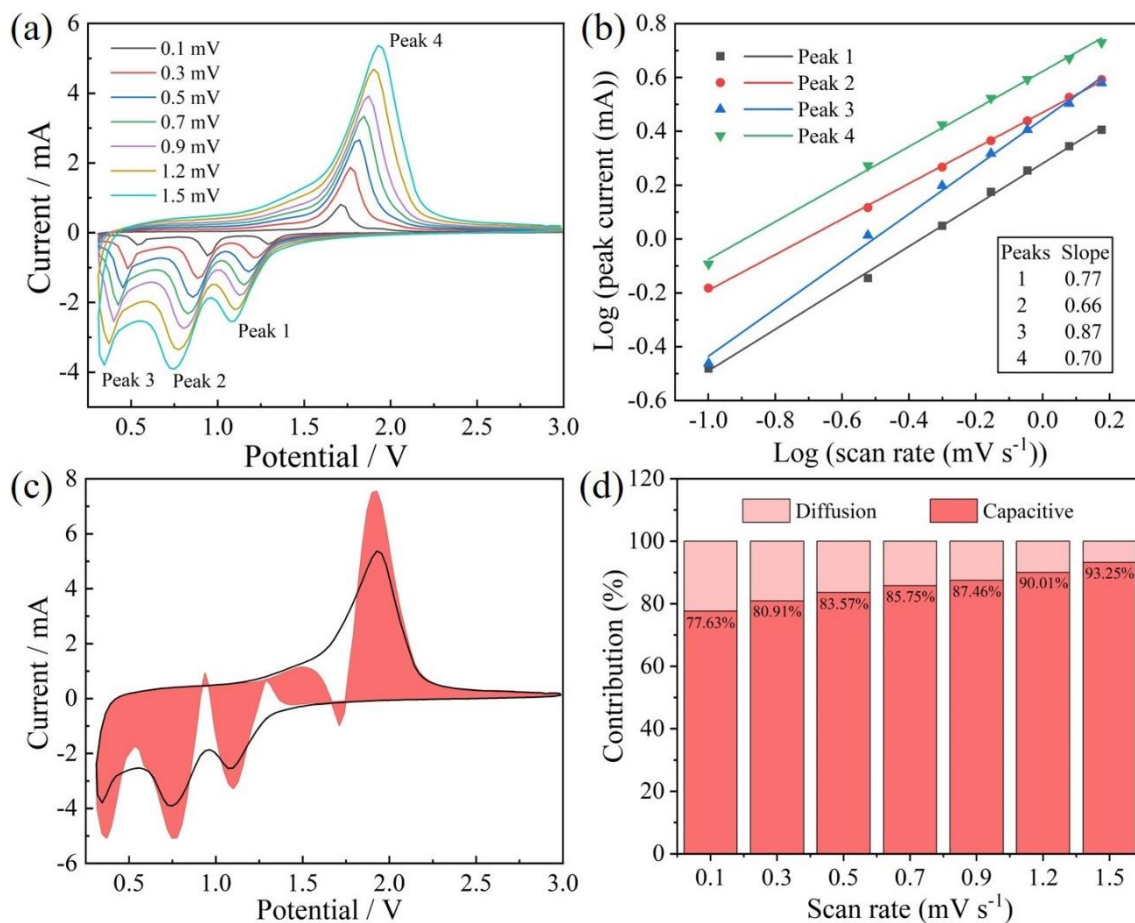


Figure 5.16 (a) CV curves of pure CoS-based anode in a voltage range of 0.3-3 V at different scan rates from 0.1 to 1.5 mV s⁻¹; (b) The fitting lines of log i vs log v of peaks in CV curves for the pure CoS-based anode; (c) Capacitive contribution of the pure CoS-based anode compared with the total current at 1.5 mV s⁻¹; The capacitive contributions of pure CoS-based anode at different scan rates from 0.1 to 1.5 mV s⁻¹.

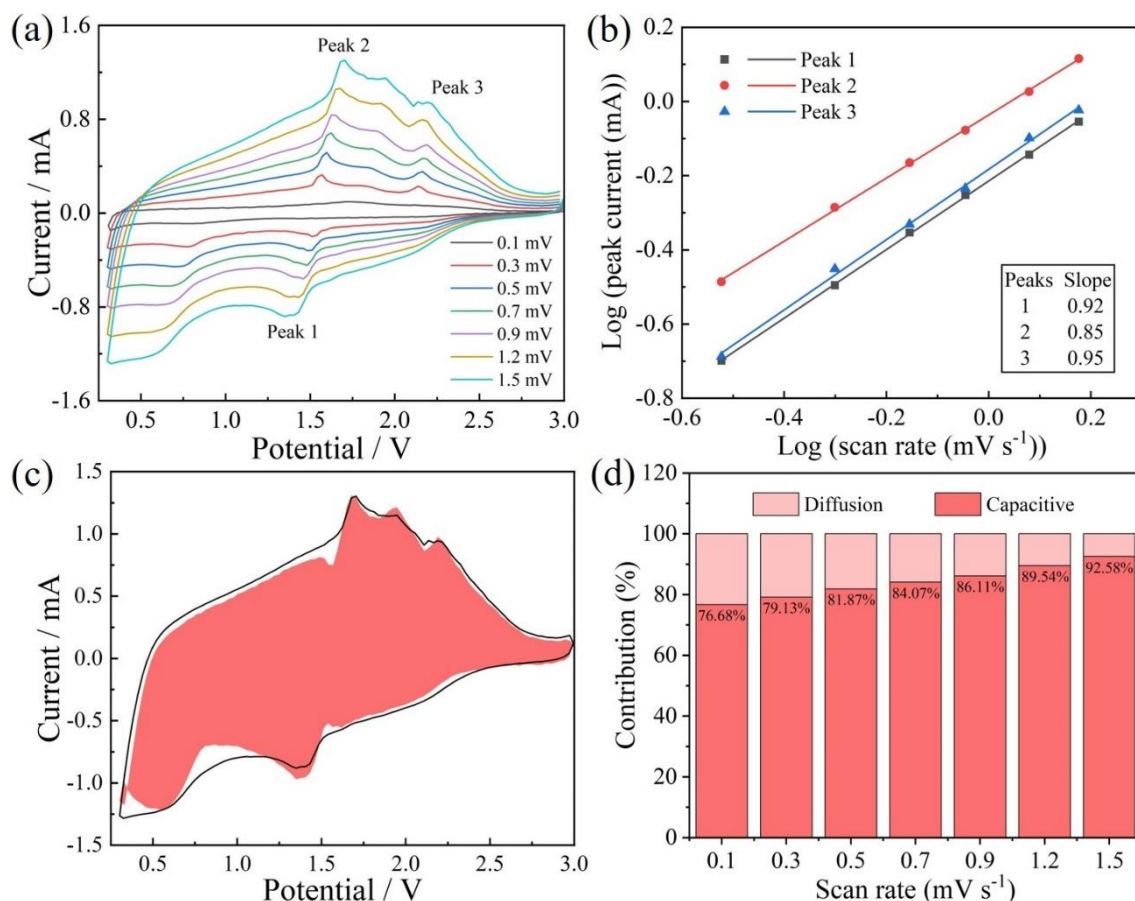


Figure 5.17 (a) CV curves of pure MoS₂-based anode in a voltage range of 0.3-3 V at different scan rates from 0.1 to 1.5 mV s⁻¹; (b) The fitting lines of log *i* vs log *v* of peaks in CV curves for the pure MoS₂-based anode; (c) Capacitive contributions of the pure MoS₂-based anode compared with the total current at 1.5 mV s⁻¹; The capacitive contributions of the pure MoS₂-based anode at different scan rates from 0.1 to 1.5 mV s⁻¹.

From the characterization and kinetic analysis results mentioned above, it can be concluded that the reasonable design of micro-flower-like CoS/MoS₂ heterostructure could result in an exceptional sodium storage performance. Specifically, as stated above, creating micro-flower morphology with an abundance of mesopores is beneficial to promote Na⁺ diffusion. While the delamination and interlayer spacing expansion of MoS₂ can provide more active sites for Na⁺ storage. In addition, the obtained CoS/MoS₂ heterostructure can enhance reaction kinetics with the decreased charge transfer resistance and the increased Na⁺ diffusion coefficient, thereby leading to a superior Na⁺

storage performance. Finally, the intrinsic pseudocapacitive properties of 1T MoS₂ and the rational design of the heterostructure lead to the facilitated surface pseudocapacitive behavior of CoS/MoS₂-based anode compared to the pure phases (i.e., the pure CoS and pure MoS₂).

5.1 Conclusion

In summary, the micro-flower-like CoS/MoS₂ composite with a heterostructure was successfully synthesized by a one-pot hydrothermal route with a solid-state sulfidation step, which exhibited superior Na⁺ storage performance than those of the pure CoS and pure MoS₂. Specifically, the CoS/MoS₂-based anode delivered high cycling stability (510.9 mAh g⁻¹ @1 A g⁻¹ at the 1000th cycle, 470.5 mAh g⁻¹ @2 A g⁻¹ at the 2000th cycle, and 441.7 mAh g⁻¹ @5 A g⁻¹ at the 750th cycle) with an exceptional rate performance (341 mAh g⁻¹ @10 A g⁻¹). It can be ascribed to the reasonable design of CoS/MoS₂ heterostructure with the enhanced reaction kinetics (decreased R_{ct} and increased D_{Na^+} with the cycling), facilitated surface capacity-controlled behavior and abundant active sites for Na⁺ storage. This work provides a novel Co/Mo sulfide composite as a promising anode material for SIBs, which also gives useful insights for the design of heterogeneous electrode materials.

References

- [1] Y. He, G. Chen, X.B. Zhang, L.L. Zhang, D. Yang, M.I. Asghar, S.J. Geng, P.D. Lund, Mechanism for Major Improvement in SOFC Electrolyte Conductivity When Using Lithium Compounds as Anode, *Acs Appl. Energy Mater.* 3 (2020) 4134-4138.
- [2] S.L. Gao, X.H. Zhao, Q. Fu, T.C. Zhang, J. Zhu, F.H. Hou, J. Ni, C.J. Zhu, T.T. Li, Y.L. Wang, V. Murugadoss, G.A.M. Mersal, M.M. Ibrahim, Z.M. El-Bahy, M.N. Huang, Z.H. Guo, Highly transmitted silver nanowires-SWCNTs conductive flexible film by nested density structure and aluminum-doped zinc oxide capping layer for flexible amorphous silicon solar cells, *J. Mater. Sci. Technol.* 126 (2022) 152-160.
- [3] Y.P. Ma, X.B. Xie, W.Y. Yang, Z.P. Yu, X.Q. Sun, Y.P. Zhang, X.Y. Yang, H. Kimura, C.X. Hou, Z.H. Guo, W. Du, Recent advances in transition metal oxides with different dimensions as electrodes for high-performance supercapacitors, *Adv. Compos. Hybrid. Ma.* 4 (2021) 906-924.
- [4] A.L. Chen, C.Y. Wang, O.A.A. Ali, S.F. Mahmoud, Y.T. Shi, Y.X. Ji, H. Algadi, S.M. El-Bahy, M.A. Huang, Z.H. Guo, D.P. Cui, H.G. Wei, MXene@nitrogen-doped carbon films for supercapacitor and piezoresistive sensing applications, *Compos. Part. A-Appl.* 163 (2022) 107174.
- [5] C.C. Dang, Q. Mu, X.B. Xie, X.Q. Sun, X.Y. Yang, Y.P. Zhang, S. Maganti, M.N. Huang, Q.L. Jiang, I. Seok, W. Du, C.X. Hou, Recent progress in cathode catalyst for nonaqueous lithium oxygen batteries: a review, *Adv. Compos. Hybrid. Ma.* 5 (2022) 606-626.
- [6] R. Wang, Z.H. Meng, X.M. Yan, T. Tian, M. Lei, R.A. Pashameah, H.M. Abo-Dief, H. Algadi, N.N. Huang, Z.H. Guo, H.L. Tang, Tellurium intervened Fe-N codoped carbon for improved oxygen reduction reaction and high-performance Zn-air batteries, *J. Mater. Sci. Technol.* 137 (2023) 215-222.
- [7] R. Ma, B. Cui, D.W. Hu, S.M. El-Bahy, Y. Wang, I.H. El Azab, A.Y. Elnaggar, H.X. Gu, G.A.M. Mersal, M.N. Huang, V. Murugadoss, Enhanced energy storage of lead-free mixed oxide core double-shell barium strontium zirconate titanate@magnesium aluminate@zinc oxide-boron trioxide-silica ceramic nanocomposites, *Adv. Compos.*

Hybrid. Ma. 5 (2022) 1477-1489.

[8] X. Hu, H. Wu, S. Liu, S. Gong, Y. Du, X. Li, X. Lu, J.J.E.S. Qu, Fabrication of Organic Shape-stabilized Phase Change Material and Its Energy Storage Applications, Eng. Sci. 17 (2022) 1-27.

[9] W. W, a. Qiu, Q. Hao, S.H.K. Annamareddy, B.B. Xu, J. Zhang, Z. Guo, Q.J.E.S. Jiang, Electric Vehicle Revolution and Implications: Ion Battery and Energy, Eng. Sci. 20 (2022) 100-109.

[10] J.B. Goodenough, K.S. Park, The Li-Ion Rechargeable Battery: A Perspective, J. Am. Chem. Soc. 135 (2013) 1167-1176.

[11] C. Hou, B. Wang, V. Murugadoss, S. Vupputuri, Y. Chao, Z. Guo, C. Wang, W.J.E.S. Du, Recent Advances in Co_3O_4 as Anode Materials for High-Performance Lithium-Ion Batteries, Eng. Sci. 11 (2020) 19-30.

[12] Y.M. Zhang, L.Y. Liu, L.L. Zhao, C.X. Hou, M.N. Huang, H. Algadi, D.Y. Li, Q. Xia, J. Wang, Z.R. Zhou, X. Han, Y.X. Long, Y.B. Li, Z.D. Zhang, Y. Liu, Sandwich-like $\text{CoMoP}_2/\text{MoP}$ heterostructures coupling N, P co-doped carbon nanosheets as advanced anodes for high-performance lithium-ion batteries, Adv. Compos. Hybrid. Ma. 5 (2022) 2601-2610.

[13] K.S. Cao, Q.L. Ma, F. Tietz, B.B. Xu, M. Yan, Y.Z. Jiang, A robust, highly reversible, mixed conducting sodium metal anode, Sci. Bull. 66 (2021) 179-186.

[14] L.B. Fang, N. Bahlawane, W.P. Sun, H.G. Pan, B.B. Xu, M. Yan, Y.Z. Jiang, Conversion-Alloying Anode Materials for Sodium Ion Batteries, Small 17 (2021) 2101137.

[15] Y.Z. Jiang, M.J. Hu, D. Zhang, T.Z. Yuan, W.P. Sun, B. Xu, M. Yan, Transition metal oxides for high performance sodium ion battery anodes, Nano Energy 5 (2014) 60-66.

[16] W. Wang, H. Bi, C. Li, J. Zhang, J. Feng, Y. Wang, X. Huang, Y. Sun, L. Sun, Edge-terminated few-layer MoS_2 nanoflakes supported on TNAs@C with enhanced electrocatalysis activity for iodine reduction reaction, Mater. Today Nano 6 (2019) 100033.

[17] Y.L. Zhou, Y. Liu, M. Zhang, Q. Han, Y.F. Wang, X.Q. Sun, X.Y. Zhang, C.F. Dong,

- J.C. Sun, Z.K. Tang, F.Y. Jiang, Rationally designed hierarchical N, P co-doped carbon connected 1T/2H-MoS₂ heterostructures with cooperative effect as ultrafast and durable anode materials for efficient sodium storage, *Chem. Eng. J.* 433 (2022) 133778.
- [18] Y.F. Wang, K. Wang, C. Zhang, J.X. Zhu, J.S. Xu, T.X. Liu, Solvent-Exchange Strategy toward Aqueous Dispersible MoS₂ Nanosheets and Their Nitrogen-Rich Carbon Sphere Nanocomposites for Efficient Lithium/Sodium Ion Storage, *Small* 15 (2019) 1903816.
- [19] Q.C. Pan, Q.B. Zhang, F.H. Zheng, Y.Z. Liu, Y.P. Li, X. Ou, X.H. Xiong, C.H. Yang, M.L. Liu, Construction of MoS₂/C Hierarchical Tubular Heterostructures for High-Performance Sodium Ion Batteries, *Acs Nano* 12 (2018) 12578-12586.
- [20] D.W. Su, S.X. Dou, G.X. Wang, Ultrathin MoS₂ Nanosheets as Anode Materials for Sodium-Ion Batteries with Superior Performance, *Adv. Energy Mater.* 5 (2015) 1401205.
- [21] J.F. Li, W.X. Gao, L.Y. Huang, Y.C. Jiang, X.T. Chang, S.B. Sun, L.K. Pan, In situ formation of few-layered MoS₂@N-doped carbon network as high performance anode materials for sodium-ion batteries, *Appl. Surf. Sci.* 571 (2022) 151307.
- [22] M.G. Wu, J.Q. Liao, L.X. Yu, R.T. Lv, P. Li, W.P. Sun, R. Tan, X.C. Duan, L. Zhang, F. Li, J. Kim, K.H. Shin, H.S. Park, W.C. Zhang, Z.P. Guo, H.T. Wang, Y.B. Tang, G. Gorgolis, C. Galiotis, J.M. Ma, 2020 Roadmap on Carbon Materials for Energy Storage and Conversion, *Chem-Asian J.* 15 (2020) 995-1013.
- [23] M.K. Sarwar, Z. Xu, K. Yao, X. Liu, Y. Wang, J. Yang, J. Huang, Constructing N-Doped graphene supported MoS₂@Ni₃S₄ for pseudocapacitive sodium-ion storage with high rate and long life, *Mater. Today Chem.* 23 (2022) 100713.
- [24] X.C. Hao, J.F. Zhang, J. Wang, B. Zhao, M.M. Qian, R. Wang, Q. Yuan, X.Y. Zhang, X.W. Huang, H.L. Li, C.G. Yu, J. Xie, F. Wu, G.Q. Tan, Metallothermic-synchronous construction of compact dual-two-dimensional MoS₂-graphene composites for high-capacity lithium storage, *Nano Energy* 103 (2022) 107850.
- [25] F. Niu, Z. Bai, Y. Mao, S. Zhang, H. Yan, X. Xu, J. Chen, N. Wang, Rational design of MWCNTs@amorphous carbon@MoS₂: Towards high performance cathode for aqueous zinc-ion batteries, *Chem. Eng. J.* 453 (2023) 139933.

- [26] X.Y. Zhang, H.T. Shi, L.S. Liu, C.Y. Min, S.T. Liang, Z.W. Xu, Y.L. Xue, C.X. Hong, Z.J. Cai, Construction of MoS₂/Mxene heterostructure on stress-modulated kapok fiber for high-rate sodium-ion batteries, *J. Colloid Interf. Sci.* 605 (2022) 472-482.
- [27] L. Cao, X.H. Liang, X. Ou, X.F. Yang, Y.Z. Li, C.H. Yang, Z. Lin, M.L. Liu, Heterointerface Engineering of Hierarchical Bi₂S₃/MoS₂ with Self-Generated Rich Phase Boundaries for Superior Sodium Storage Performance, *Adv. Funct. Mater.* 30 (2020) 1910732.
- [28] C. Guo, W.C. Zhang, Y. Liu, J.P. He, S. Yang, M.K. Liu, Q.H. Wang, Z.P. Cuo, Constructing CoO/Co₃S₄ Heterostructures Embedded in N-doped Carbon Frameworks for High-Performance Sodium-Ion Batteries, *Adv. Funct. Mater.* 29 (2019) 1901925.
- [29] C.X. Hou, W.Y. Yang, H. Kimura, X.B. Xie, X.Y. Zhang, X.Q. Sun, Z.P. Yu, X.Y. Yang, Y.P. Zhang, B. Wang, B.B. Xu, D. Sridhar, H. Algadi, Z.H. Guo, W. Du, Boosted lithium storage performance by local build-in electric field derived by oxygen vacancies in 3D holey N-doped carbon structure decorated with molybdenum dioxide, *J. Mater. Sci. Technol.* 142 (2023) 185-195.
- [30] T. Zhang, Y. Feng, J. Zhang, C. He, D.M. Itkis, J. Song, Ultrahigh-rate sodium-ion battery anode enabled by vertically aligned (1T-2H MoS₂)/CoS₂ heteronanosheets, *Mater. Today Nano* 12 (2020) 100089.
- [31] Y. Su, C.X. Wu, H. Li, F.J. Chen, Y. Guo, L. Yang, S.L. Xu, MoS₂ nanoplatelets scaffolded within CoS₂ nanobundles as anode nanomaterials for sodium-ion batteries, *J. Alloy Compd.* 845 (2020) 156229.
- [32] J. Liu, D. Li, G. Yang, F. Cai, G. Li, Synthesis of Honeycomb-Like Co₃S₄/MoS₂ Composites with Hollow Structure As Anode Materials for High-Performance Lithium-Ion and Sodium-Ion Batteries, *J. Electron. Mater.* 49 (2020) 6519-6527.
- [33] Y. He, C. Liu, S. Peng, J. Zhang, G. Chen, Z. Feng, Q. Zhao, A. Abudula, G. Guan, Micro-flower-like MoS₂-modified Co₉S₈ heterostructure as anode material for sodium-ion batteries with superior reversibility and rate capacity, *J. Mater. Sci. Technol.* (2022) 210-220.
- [34] Y.Y. Wang, W.P. Kang, D.W. Cao, M.H. Zhang, Z.X. Kang, Z.Y. Xiao, R.M. Wang,

D.F. Sun, A yolk-shelled Co₉S₈/MoS₂-CN nanocomposite derived from a metal-organic framework as a high performance anode for sodium ion batteries, *J. Mater. Chem. A* 6 (2018) 4776-4782.

[35] B. He, G. Li, J. Li, J. Wang, H. Tong, Y. Fan, W. Wang, S. Sun, F. Dang, MoSe₂@CNT Core–Shell Nanostructures as Grain Promoters Featuring a Direct Li₂O₂ Formation/Decomposition Catalytic Capability in Lithium–Oxygen Batteries, *Adv. Energy Mater.* 11 (2021) 2003263.

[36] L. Guo, L.W. Tan, A.L. Xu, G.Y. Li, G.L. Zhang, R.W. Liu, J.C. Wang, Y. Du, F. Dang, Highly efficient two-dimensional Ag₂Te cathode catalyst featuring a layer structure derived catalytic anisotropy in lithium–oxygen batteries, *Energy Storage Mater.* 50 (2022) 96-104.

[37] G. Zhang, C. Liu, L. Guo, R. Liu, L. Miao, F. Dang, Electronic “Bridge” Construction via Ag Intercalation to Diminish Catalytic Anisotropy for 2D Tin Diselenide Cathode Catalyst in Lithium–Oxygen Batteries, *Adv. Energy Mater.* 12 (2022) 2200791.

[38] Y. Qiu, G.Y. Li, H.M. Zhou, G.L. Zhang, L. Guo, Z.H. Guo, R.A. Yang, Y.Q. Fan, W.L. Wang, Y. Du, F. Dang, Highly Stable Garnet Fe₂Mo₃O₁₂ Cathode Boosts the Lithium–Air Battery Performance Featuring a Polyhedral Framework and Cationic Vacancy Concentrated Surface, *Adv. Sci.* (2023) 2300482.

[39] G. Zhang, G. Li, J. Wang, H. Tong, J. Wang, Y. Du, S. Sun, F. Dang, 2D SnSe Cathode Catalyst Featuring an Efficient Facet-Dependent Selective Li₂O₂ Growth/Decomposition for Li–Oxygen Batteries, *Adv. Energy Mater.* 12 (2022) 2103910.

[40] Y. Gu, Y. Xu, Y. Wang, Graphene-Wrapped CoS Nanoparticles for High-Capacity Lithium-Ion Storage, *Acs. Appl. Mater. Interfaces* 5 (2013) 801-806.

[41] Z. Hu, L.X. Wang, K. Zhang, J.B. Wang, F.Y. Cheng, Z.L. Tao, J. Chen, MoS₂ Nanoflowers with Expanded Interlayers as High-Performance Anodes for Sodium-Ion Batteries, *Angew. Chem. Int. Edit.* 53 (2014) 12794-12798.

[42] N.T. Xuyen, J.M. Ting, Hybridized 1T/2H MoS₂ Having Controlled 1T Concentrations and its use in Supercapacitors, *Chem.-Eur. J.* 23 (2017) 17348-17355.

- [43] S. Wang, D. Zhang, B. Li, C. Zhang, Z.G. Du, H.M. Yin, X.F. Bi, S.B. Yang, Ultrastable In-Plane 1T-2H MoS₂ Heterostructures for Enhanced Hydrogen Evolution Reaction, *Adv. Energy. Mater.* 8 (2018) 1801345.
- [44] F. Li, Q. Li, H. Kimura, X. Xie, X. Zhang, N. Wu, X. Sun, B.B. Xu, H. Algadi, R.A. Pashameah, A.K. Alanazi, E. Alzahrani, H. Li, W. Du, Z. Guo, C. Hou, Morphology controllable urchin-shaped bimetallic nickel-cobalt oxide/carbon composites with enhanced electromagnetic wave absorption performance, *J. Mater. Sci. Technol.* 148 (2023) 250-259.
- [45] W.Y. Yang, D.N. Peng, H. Kimura, X.Y. Zhang, X.Q. Sun, R.A. Pashameah, E. Alzahrani, B. Wang, Z.H. Guo, W. Du, C.A.X. Hou, Honeycomb-like nitrogen-doped porous carbon decorated with Co₃O₄ nanoparticles for superior electrochemical performance pseudo-capacitive lithium storage and supercapacitors, *Adv. Compos. Hybrid. Ma.* 5 (2022) 3146-3157.
- [46] S.J. Peng, X.P. Han, L.L. Li, Z.Q. Zhu, F.Y. Cheng, M. Srinivansan, S. Adams, S. Ramakrishna, Unique Cobalt Sulfide/Reduced Graphene Oxide Composite as an Anode for Sodium-Ion Batteries with Superior Rate Capability and Long Cycling Stability, *Small* 12 (2016) 1359-1368.
- [47] X.M. Zhu, X.Y. Jiang, X.L. Liu, L.F. Xiao, X.P. Ai, H.X. Yang, Y.L. Cao, Amorphous CoS nanoparticle/reduced graphene oxide composite as high-performance anode material for sodium-ion batteries, *Ceram. Int.* 43 (2017) 9630-9635.
- [48] F.Q. Luo, X.S. Feng, L.X. Zeng, L.X. Lin, X.Y. Li, B.Y. Kang, L.R. Xiao, Q.H. Chen, M.D. Wei, Q.R. Qian, In situ simultaneous encapsulation of defective MoS₂ nanolayers and sulfur nanodots into SPAN fibers for high rate sodium-ion batteries, *Chem. Eng. J.* 404 (2021) 126430.
- [49] Y.L. Zhou, M. Zhang, Q. Han, Y. Liu, Y.F. Wang, X.Q. Sun, X.T. Zhang, C.F. Dong, F.Y. Jiang, Hierarchical 1 T-MoS₂/MoO_x@NC microspheres as advanced anode materials for potassium/sodium-ion batteries, *Chem. Eng. J.* 428 (2022) 131113.
- [50] Q.B. Guo, Y.F. Ma, T.T. Chen, Q.Y. Xia, M. Yang, H. Xia, Y. Yu, Cobalt Sulfide Quantum Dot Embedded N/S-Doped Carbon Nanosheets with Superior Reversibility and Rate Capability for Sodium-Ion Batteries, *Acs Nano* 11 (2017) 12658-12667.

- [51] T.Z. Liu, Y.P. Li, S. Hou, C.H. Yang, Y.Y. Guo, S. Tian, L.Z. Zhao, Building Hierarchical Microcubes Composed of One-Dimensional CoSe_2 @Nitrogen-Doped Carbon for Superior Sodium Ion Batteries, *Chem.-Eur. J.* 26 (2020) 13716-13724.
- [52] Y. Zhao, Y.L. Liu, C. Wang, E. Ortega, X.M. Wang, Y.F. Xie, J.N. Shen, C.J. Gao, B. Van der Bruggen, Electric field-based ionic control of selective separation layers, *J. Mater. Chem. A* 8 (2020) 4244-4251.
- [53] Y.C. Jiao, A. Mukhopadhyay, Y. Ma, L. Yang, A.M. Hafez, H.L. Zhu, Ion Transport Nanotube Assembled with Vertically Aligned Metallic MoS_2 for High Rate Lithium-Ion Batteries, *Adv. Energy Mater.* 8 (2018) 1702779.
- [54] Q.L. Wei, M.R. Gao, Y. Li, D.T. Zhang, S.Y. Wu, Z.H. Chen, Y.G. Sun, Directionally assembled MoS_2 with significantly expanded interlayer spacing: a superior anode material for high-rate lithium-ion batteries, *Mater. Chem. Frontiers* 2 (2018) 1441-1448.
- [55] X.J. Hu, X.J. Liu, K. Chen, G. Wang, H. Wang, Core-shell MOF-derived N-doped yolk-shell carbon nanocages homogenously filled with ZnSe and CoSe_2 nanodots as excellent anode materials for lithium- and sodium-ion batteries, *J. Mater. Chem. A* 7 (2019) 11016-11037.
- [56] W.N. Ren, H.F. Zhang, C. Guan, C.W. Cheng, Ultrathin MoS_2 Nanosheets@Metal Organic Framework-Derived N-Doped Carbon Nanowall Arrays as Sodium Ion Battery Anode with Superior Cycling Life and Rate Capability, *Adv. Funct. Mater.* 27 (2017) 1702116.
- [57] H.L. Zhu, F. Zhang, J.R. Li, Y.B. Tang, Penne-Like MoS_2 /Carbon Nanocomposite as Anode for Sodium-Ion-Based Dual-Ion Battery, *Small* 14 (2018) 1703951.
- [58] W. Ye, F.F. Wu, N.X. Shi, H. Zhou, Q.Q. Chi, W.H. Chen, S.Y. Du, P. Gao, H.B. Li, S. Xiong, Metal-Semiconductor Phase Twinned Hierarchical MoS_2 Nanowires with Expanded Interlayers for Sodium-Ion Batteries with Ultralong Cycle Life, *Small* 16 (2020) 1906607.
- [59] J.Y. Yu, X.L. Li, Y.P. Sun, X.G. Liu, CoS @sulfur doped onion-like carbon nanocapsules with excellent cycling stability and rate capability for sodium-ion batteries, *Ceram. Int.* 44 (2018) 17113-17117.

- [60] Y. Wu, J. Cheng, Z. Liang, T. Qiu, Y. Tang, J. Shi, S. Gao, R. Zhong, R. Zou, Construction of CoS-encapsulated in ultrahigh nitrogen doped carbon nanofibers from energetic metal-organic frameworks for superior sodium storage, *Carbon* 198 (2022) 353-363.
- [61] J. Xiang, T. Song, One-pot synthesis of multicomponent (Mo, Co) metal sulfide/carbon nanoboxes as anode materials for improving Na-ion storage, *Chem. Commun.* 53 (2017) 10820-10823.
- [62] L. Bai, F.X. Liang, Hierarchical MoS₂/carbon composites as superior anode for advanced sodium-ion battery, *Ionics* 28 (2022) 3341-3345.
- [63] Y.D. Liu, C. Tang, W.W. Sun, G.J. Zhu, A.J. Du, H.J. Zhang, In-situ conversion growth of carbon-coated MoS₂/N-doped carbon nanotubes as anodes with superior capacity retention for sodium-ion batteries, *J. Mater. Sci. Technol.* 102 (2022) 8-15.
- [64] S.H. Yang, S.K. Park, J.K. Kim, Y.C. Kang, A MOF-mediated strategy for constructing human backbone-like CoMoS₃@N-doped carbon nanostructures with multiple voids as a superior anode for sodium-ion batteries, *J. Mater. Chem. A* 7 (2019) 13751-13761.
- [65] X. Wang, B.Q. Wang, Y.X. Tang, B.B. Xu, C. Liang, M. Yan, Y.Z. Jiang, Manganese hexacyanoferrate reinforced by PEDOT coating towards high-rate and long-life sodium-ion battery cathode, *J. Mater. Chem. A* 8 (2020) 3222-3227.
- [66] Q. Mu, R.L. Liu, H. Kimura, J.C. Li, H.Y. Jiang, X.Y. Zhang, Z.P. Yu, X.Q. Sun, H. Algadi, Z.H. Guo, W. Du, C.X. Hou, Supramolecular self-assembly synthesis of hemoglobin-like amorphous CoP@N, P-doped carbon composites enable ultralong stable cycling under high-current density for lithium-ion battery anodes, *Adv. Compos. Hybrid Ma.* 6 (2023).
- [67] X.T. Lian, N. Xu, Y.C. Ma, F. Hu, H.X. Wei, H.Y. Chen, Y.Z. Wu, L.L. Li, D.S. Li, S.J. Peng, In-situ formation of Co_{1-x}S hollow polyhedrons anchored on multichannel carbon nanofibers as self-supporting anode for lithium/sodium-ion batteries, *Chem. Eng. J.* 421 (2021) 127755.
- [68] J.B. Cook, T.C. Lin, H.S. Kim, A. Siordia, B.S. Dunn, S.H. Tolbert, Suppression of Electrochemically Driven Phase Transitions in Nanostructured MoS₂

Pseudocapacitors Probed Using Operando X-ray Diffraction, *Acs Nano* 13 (2019) 1223-1231.

[69] G.A. Muller, J.B. Cook, H.S. Kim, S.H. Tolbert, B. Dunn, High Performance Pseudocapacitor Based on 2D Layered Metal Chalcogenide Nanocrystals, *Nano Lett.* 15 (2015) 1911-1917.

Chapter 6 Conclusion and Prospects

6.1 Conclusion

Based on the unique advantages of SIBs including high abundance, wide distribution, and low cost of sodium resources, which are expected to replace LIBs as the next generation of energy storage devices. TMSs have attracted extensive attention as anodes for SIBs based on their excellent comprehensive properties. In this dissertation, three kinds of anodes were fabricated for SIBs, which exhibited excellent electrochemical properties due to their unique material structure design. The conclusions are summarized as follows:

(1) PBA-derived $\text{Co}_3\text{S}_4@\text{C-N/S}$ and $\text{Co}_9\text{S}_8@\text{C-N/S}$ with tremella-like micro-flower structure were successfully prepared as the anode materials for SIBs by two steps (hydrothermal followed with solid sulfidation), which inherits the carbon/nitrogen framework in the precursor to form an N/S co-doped carbon frameworks during the solid sulfidation process. The obtained anode possesses high-speed ion/electron transfer ability and more active sites for sodium storage, ultimately resulting in a high specific capacity as well as cycling stability when used as the anode material for the SIBs. The optimum $\text{Co}_3\text{S}_4@\text{C-N/S}$ -based anode delivers excellent initial charge/discharge specific capacities of 685.3/745.2 mA h g⁻¹ with a high initial Coulombic efficiency of 91.97% at 0.1 A g⁻¹ and superior cycling performance (599.1 mA h g⁻¹ even in the 600th cycle at 1 A g⁻¹ with a capacity retention of 89.4%). While the optimum $\text{Co}_9\text{S}_8@\text{C-N/S}$ -based anode also exhibits considerable initial Coulombic efficiency (86.1% at 0.1 A g⁻¹) and cycling stability (391.9 mA h g⁻¹ even in the 1200th cycle at 2 A g⁻¹ with a capacity retention of 78.1%). This novel hydrothermally synthesized PBA-driven cobalt-based sulfides ($\text{Co}_3\text{S}_4@\text{C-N/S}$ and $\text{Co}_9\text{S}_8@\text{C-N/S}$) provide a new material preparation strategy, and their excellent electrochemical performance indicates that can be promising anodes for SIBs.

(2) A 3D micro-flower-like $\text{Co}_9\text{S}_8/\text{MoS}_2$ heterostructure with rapid charge transfer and synergistic physicochemical properties was successfully designed and fabricated

via a facile hydrothermal synthesis method followed by a solid sulfidation treatment process. It is found that the addition of Mo species during the synthesis process played a crucial role in the formation of 3D micro-flower-like morphology, and the overall morphology and the percentage ratio of Mo in the final product tended to be stable with the increase of initial Mo content. As the anode material for SIBs, the CM55-S-based anode exhibited enhanced capacity, excellent reversibility (424.5 mAh g⁻¹ at 2 A g⁻¹ for 1600 cycles, 401.1 mAh g⁻¹ at 5 A g⁻¹ for 800 cycles), and superior rate capacities (295.8 mAh g⁻¹ at 10 A g⁻¹, 210.1 mAh g⁻¹ at 20 A g⁻¹), which should be attributed to the rational design of 3D micro-flower-like heterostructure with more active sites for Na⁺ storage, high-speed charge transfer, and low energy barrier. It provides a reliable way for designing sulfides with 3D heterostructures as energy materials for energy storage devices.

(3) The micro-flower-like CoS/MoS₂ composite with a heterostructure was successfully synthesized by a one-pot hydrothermal route with a solid-state sulfidation step, which exhibited superior Na⁺ storage performance than those of pure CoS and pure MoS₂. Specifically, the CoS/MoS₂-based anode delivered high cycling stability (510.9 mAh g⁻¹ @1 A g⁻¹ at the 1000th cycle, 470.5 mAh g⁻¹ @2 A g⁻¹ at the 2000th cycle, and 441.7 mAh g⁻¹ @5 A g⁻¹ at the 750th cycle) with an exceptional rate performance (341 mAh g⁻¹ @10 A g⁻¹). It can be ascribed to the reasonable design of CoS/MoS₂ heterostructure with enhanced reaction kinetics (decreased R_{ct} and increased D_{Na^+} with cycling), facilitated surface capacity-controlled behavior, and abundant active sites for Na⁺ storage. This work provides a novel Co/Mo sulfide composite as a promising anode material for SIBs, which gives useful insights for the design of heterogeneous electrode materials.

6.2 Prospects

Although many efforts have been performed in this dissertation on TMSs as anodes for SIBs, there are still some challenges that require more in-depth investigations. Such as various in-situ characterization methods, full battery assembly,

exploration of electrolyte solution and additives, etc. At the same time, to realize the commercialization of SIBs, it is necessary to give full play to its advantages of low cost. More researches need to be paid attention to anode materials with low raw material cost and high specific capacity. In a summary, future follow-up researches should be carried out from the following aspects:

(1) The sodium storage mechanisms of some electrode materials are still unclear, and various in-situ characterization methods (in-situ SEM, TEM, XRD, XPS, XRD, and FTIR, etc.) are needed to monitor electrode transient response including atomic structure, intermediates, morphology, oxidation or reduction products, coordination atom migration, etc.

(2) The excellent electrochemical performance of the TMSs-based anode in the half-battery system does not represent its performance in the full-battery system. The full battery system of sodium-ion batteries is more complicated, and a lot of empirical research is still needed, which is also the most critical step for the commercialization of sodium-ion batteries.

(3) The electrolyte solution and additives in SIBs are also the key factors for electrode materials to fully exert their capacity. A well-matched electrolyte system with the electrode material can form a stable SEI film on the surface of the electrode material, which can suppress the consumption of the electrolyte and stabilize the output capacity.

(4) Most of the current development of anode materials for sodium-ion batteries uses precious metals, which will undoubtedly weaken the cost advantage of sodium-ion batteries. The development of low-cost transition metal sulfide anode materials that can still maintain high specific capacity output is the key to the commercial application of sodium-ion batteries.

List of publications and presentations

Publications

- (1) **Yang He**, Changlin Liu, Zhengkun Xie, Jiwei Wang, Gang Chen, Qiang Zhao, Abuliti Abudula, Guoqing Guan, "Prussian Blue Analogue-Derived Cobalt Sulfide Nanoparticles Embedded in N/S Co-doped Carbon Frameworks as a High-Performance Anode Material for Sodium-ion Batteries," ACS Applied Energy Materials, 5 (2022) 8697-8708.
- (2) **Yang He**, Changlin Liu, Shang Peng, Juan Zhang, Gang Chen, Zhongbao Feng, Qiang Zhao, Abuliti Abudula, and Guoqing Guan, "Micro-flower-like MoS₂-modified Co₉S₈ heterostructure as anode material for sodium-ion batteries with superior reversibility and rate capacity," Journal of Materials Science & Technology. 135 (2022), 210-220.
- (3) **Yang He**, Changlin Liu, Zhengkun Xie, Pairuzha Xiaokaiti, Gang Chen, Zhongbao Feng, Yutaka Kasai, Abuliti Abudula, and Guoqing Guan, "Construction of cobalt sulfide/molybdenum disulfide heterostructure as the anode material for sodium ion batteries," Advanced Composites and Hybrid Materials, 6 (2023) 85.
- (4) Changlin Liu, **Yang He**, Xiaowei An, Nutthaphak Kitiphatpiboon, Xiao Du, Xiaogang Hao, Abuliti Abudula, and Guoqing Guan "A poly(ether block amide) based solid polymer electrolyte for solid-state lithium metal batteries", Journal of Colloid & Interface Science, 630(2023), 595-603.
- (5) Changlin Liu, **Yang He**, Xiaowei An, Zhijun Wu, Xiaogang Hao, Qiang Zhao, Abuliti Abudula, and Guoqing Guan "Effect of nano Al₂O₃ addition on cycling performance of poly(ether block amide) based solid-state lithium metal batteries," Resources Chemicals and Materials, 2 (2023) 167-176.
- (6) Xiyan Yue, Jiajia Wang, Zhengkun Xie, **Yang He**, Zhao Liu, Changlin Liu, Xiaogang Hao, Abuliti Abudula and Guoqing Guan, "Controllable Synthesis of Novel Orderly Layered VMoS₂ Anode Materials with Super Electrochemical Performance for Sodium Ion Batteries," ACS Applied Materials & Interfaces, 13

(2021) 26049-26054.

International presentations

- (1) **Yang He**, Changlin Liu, Shang Peng, Juan Zhang, Katsuki Kusakabe, Abuliti Abudula, and Guoqing Guan, "MoS₂-modified Co₉S₈ Heterostructure as Anode Material for Sodium-ion Batteries," International Symposium on Chemical Engineering (ISChE) 2022, Fukuoka, Japan, December 2-4, 2022
- (2) **Yang He**, Changlin Liu, Juan Zhang, Abuliti Abudula, and Guoqing Guan, "CoS/MoS₂ heterostructure as Anode Material for Sodium-ion Batteries with Superior Reversibility and Rate Capacity", International Chemical Engineering Symposia 2023, Tokyo University of Agriculture and Technology (TUAT), March 15-17, 2023.
- (3) Changlin Liu, Xiaowei An, Natthaphak Kitiphatpiboon, **Yang He**, Abuliti Abudula, Guoqing Guan, "Electrochemical Characteristics of Solid-state Lithium Metal Batteries Based on PEBAX Electrolyte," 19th Asia Pacific Confederation of Chemical Engineering (APCCHE 2022) Congress, August 9-12, Kuala Lumpur Convention Centre, Kuala Lumpur, Malaysia.
- (4) Changlin Liu, **Yang He**, Abuliti Abudula, Guoqing Guan, "Electrochemical Characteristics of All Solid-state Lithium Metal Batteries Based on Poly(ether block amide) 4033 Electrolyte," International Chemical Engineering Symposia 2023, Tokyo University of Agriculture and Technology (TUAT), March 15-17.

Domestic presentations

- (1) **Yang He**, Jiajia Wang, Abuliti Abudula, and Guoqing Guan, "Co₃S₄ Embedded in N-doped Carbon Frameworks as High Performance Anode Materials for Sodium-ion Batteries", 第 52 東北電気化学セミコンファレンスおよび第 34 回若手の会 November 22-23, 2021.
- (2) **Yang He**, Abuliti Abudula, and Guoqing Guan, "Co₃S₄ Embedded in N, S co-doped Carbon Frameworks as Anode Materials for Sodium-ion Batteries with High Capacity and Long-term Cycle Life", The Society of Chemical Engineers, Japan (SCEJ) 87th Annual Meeting, Tokyo, Japan, (on-line), March 16-18, 2022.
- (3) **Yang He**, Abuliti Abudula, and Guoqing Guan, "MoS₂-modified Co₉S₈ 3D micro-

flower as Anode Material for Sodium-ion Batteries with Superior Reversibility and Rate Capacity", 令和4年度化学系学協会東北大会, 岩手大学 September 17-18, 2022.

List of patents

- (1) 何楊、官国清、王佳佳、関和治、阿布里提、“負極活物質、負極材料及び該負極材料を備えるアルカリイオン電池、並びに、負極活物質の製造方法”、日本特許、出願番号：特願 2021-202012、出願日：2021 年 12 月 13 日.
- (2) 何楊、官国清、関和治、阿布里提、“ナトリウムイオン電池用負極活物質及びその製造方法、負極材料並びにナトリウムイオン電池”、日本特許、出願番号：特願 2022-095279、出願日：2022 年 6 月 13 日.
- (3) 何楊、官国清、関和治、阿布里提 “ナトリウムイオン電池用負極活物質及びその製造方法、負極材料並びにナトリウムイオン電池”、特願 2023-060417、出願日：2023 年 4 月 3 日.